

FIRST PRINCIPLES STUDY OF GA-STABILIZED  $\delta$ -PU  
BULK AND SURFACES

Sarah Christine Hernandez

Presented to the Faculty of the Graduate School of  
The University of Texas at Arlington in Partial Fulfillment  
of the Requirements  
for the Degree of

DOCTOR OF PHILOSOPHY

THE UNIVERSITY OF TEXAS AT ARLINGTON

May 2015

Copyright © by Sarah Christine Hernandez 2015

All Rights Reserved



*This work is dedicated to my husband, Samir El-Darazi, and to my beautiful, always smiling children, Celeste and Maximus.*

## Acknowledgements

I would like to thank Dr. Asok Ray, who took a whim on me and believed in me. He provided valuable guidance, encouraged me to do an internship at LANL and inspired me to be the best I can be. He will be missed. Dr. Muhammad Huda, I would like to thank him for graciously mentoring me to completing this work, for his invaluable knowledge, guidance, and advice. Dr. Raymond Atta-Fynn has been an amazing mentor and friend and I am grateful for his generosity. I would like to express my gratitude to Dr. Chris Taylor for providing support, encouragement, and advice, and without his continued support this work would not have moved forward. Thank to you Dr. Tom Venhaus, for mentoring, support, and encouragement during this project. Without Dr. Venhaus support for this work, it would not have continued throughout my last year at UTA and I am grateful for your belief in my work.

Thank you to Drs. Dan Schwartz and Marianna Wilkerson, for the support for this work and continued support thereafter. Thank you to Dr. Steve Valone, for his wisdom, encouragement, advice, and listening to the frustrations of a PhD student. My sincere gratitude to my committee members, Drs. C. Jackson, Z. Musielak, A. Weiss, and Q. Zhang, who have been supportive during my time here at UTA. Thank you to Dr. Dave Moore, for introducing me to the many wonders of experimental surface science during my first internship at LANL and the continued support and encouragement. Thank you to Dr. Ted Holby for his support, encouragement, and belief in my work. I would also like to acknowledge additional support from LANL,

Drs. F. Freibert and D. Korzekwa. I would like to acknowledge my fellow group members for enduring my weekly group presentations, Dr. Adhikari, Dr. Chen, Ms. Duesman, Ms. Morrosion-Sherrell, Mr. Wanaguru, Ms. Hoover, Ms. Moten, Ms. Sterrett, Mr. Mayfield, Mr. Sarker, Mr. Barman, and Mr. Khatri. I would like to acknowledge the Physics Department staff.

I would like to recognize my mother, father, and brothers who have always encouraged me to achieve anything and who have been with me throughout this journey.

Finally, this work was supported by the US Department of Energy through the Los Alamos National Laboratory LDRD Program.

February 16, 2015

Abstract

FIRST PRINCIPLES STUDY OF GA-STABILIZED  $\delta$ -PU  
BULK AND SURFACES

Sarah Christine Hernandez, PhD

The University of Texas at Arlington, 2015

Supervising Professor: Muhammad N. Huda

Plutonium (Pu) metal is highly reactive toward environmental gases and corrodes at a high rate. Due to this inevitable process, containers used to store Pu-based materials may experience catastrophic failure, subsequently releasing Pu particulates into the environment. Such interactions can be probed at the atomic scale using ab initio methods such as density functional theory (DFT). However, previous theoretical studies only examined these reactions with a pure  $\delta$ -Pu surface. This is not realistic since  $\delta$ -Pu exists at a high temperature (600K), therefore most technological applications of  $\delta$ -Pu employ the alloyed form. The alloyed form is achieved with the addition of as little as 1 atomic percent (at. %) concentration of an alloying impurity such as elemental gallium (Ga) and aluminum (Al); this stabilizes  $\delta$ -Pu from 600 K to 300 K. Thus, corrosion of  $\delta$ -Pu may be affected by the alloying impurities and therefore realistic theoretical calculations must include such impurities.

In this work, atomic oxygen and hydrogen adsorptions on the  $\delta$ -Pu (111) surfaces with experimentally relevant Ga concentrations of 3.125 and 9.375 at. %. Ga concentrations were studied using DFT. The goals of the studies were to elucidate the role played by Ga in the reaction of  $\delta$ -Pu surfaces with oxygen and hydrogen, particularly the geometric and electronic factors which dictate surface  $\delta$ -Pu oxide and hydride formation. The results of the studies are summarized as follows: (i) Both hydrogen and oxygen preferred on-surface Pu-rich regions with three-fold coordination. (ii) Unfavorable chemisorption energies were realized when an adatom was coordinated with Ga or when it is adsorbed at interstitial sites. (iii) Electronic properties indicated that for both concentrations, Ga influenced the hybridization of the Pu  $6d$ -O  $2p$  states. However the degree of hybridization of the Pu  $5f$ -O  $2p$  states was dependent on the Ga concentration. (iv) Hydrogen slightly influenced the electronic properties.

## Table of Contents

Acknowledgements.....	iv
Abstract.....	vi
List of Illustrations.....	xii
List of Tables.....	xx
Chapter 1 Introduction.....	1
1.1 Overview of Plutonium.....	1
1.2 DFT and beyond applied to $\delta$ -Pu.....	5
1.3 $\delta$ -Pu-Ga alloy properties: Experimental and Theoretical overview.....	6
1.4 Corrosion of $\delta$ -Pu.....	11
1.4.1 Oxidation of $\delta$ -Pu.....	13
1.4.2 Hydride Formation in $\delta$ -Pu.....	18
1.4.2.1 Defects and Vacancies.....	22
1.5 Overview of Theoretical Surface Studies on $\delta$ -Pu.....	22
1.6 Motivation.....	24
Chapter 2 Computational Methodologies.....	26
2.1 Density Functional Theory.....	26
2.1.1 Hohenberg-Kohn Theorems.....	29
2.1.2 Kohn-Sham auxiliary system.....	33
2.2 Exchange-Correlation Approximations.....	40

2.2.1 Local density approximation.....	40
2.2.2 Generalized gradient approximation.....	42
2.3 WIEN2K.....	43
2.3.1 LAPW + LO method.....	43
2.3.2 APW+lo method .....	46
2.3.3 Spin-orbit coupling in WIEN2k.....	48
Chapter 3 Pu-Ga bulk alloys and H-vacancy .....	51
3.1 Computational Details .....	51
3.2 Results and Discussions $\delta$ -Pu with and without Ga impurities .....	54
3.2.1 Structural effects due to Ga.....	54
3.2.2 Electronic properties of $\delta$ -Pu with Ga impurities .....	76
3.3 Hydrogen-vacancy complex within a $\delta$ -Pu 3.125 at. % Ga.....	85
Chapter 4 Atomic O adsorption on Ga stabilized $\delta$ -Pu (111) surface .....	95
4.1 Computational Details .....	95
4.2 Results and Discussions Oxygen adsorption on 3.125 at. % Ga stabilized $\delta$ -Pu (111) surface .....	106
4.2.1 Relaxation and stability of 3.125 at. % Ga $\delta$ -Pu (111) surface.....	106
4.2.2 Adsorption on Pu-terminated surface .....	110
4.2.3 Adsorption on PuGa-terminated surface.....	115
4.2.4 Interstitial adsorption .....	117

4.2.5 Adsorption Probabilities .....	121
4.2.6 Adsorbate-induced work function changes.....	121
4.2.7 Electronic structure analysis .....	124
4.3 Results and Discussions Oxygen adsorption on 9.375 at. % Ga stabilized $\delta$ -Pu (111) surface .....	136
4.3.1 Relaxation and stability of 9.375 at. % Ga $\delta$ -Pu (111) surface .....	136
4.3.2 Adsorption on Pu-terminated surface .....	139
4.3.3 Adsorption on PuGa-terminated surface.....	144
4.3.4 Interstitial adsorption .....	151
4.3.5 Adsorption Probabilities .....	154
4.3.6 Electronic structure analysis .....	155
Chapter 5 Atomic H adsorption on Ga stabilized $\delta$ -Pu (111) surface .....	169
5.1 Computational Details .....	169
5.2 Results and Discussions.....	171
5.2.1 Adsorption on Pu-terminated surface .....	171
5.2.2 Adsorption on PuGa-terminated surface.....	173
5.2.3 Interstitial adsorption .....	177
5.2.4 Electronic structure analysis .....	181
Chapter 6 Conclusions .....	194
Appendix A Program Flow of <i>WIEN2k</i> .....	200

Appendix B Three-Dimensional Charge Density Difference Plot .....	202
Appendix C Initial and final positions for O adsorption on 3.125 at. %	
Ga $\delta$ -Pu (111) surface .....	206
Appendix D Initial and final positions for O adsorption on 9.375 at. %	
Ga $\delta$ -Pu (111) surface .....	212
Appendix E Initial and final positions for H adsorption on 3.125 at. %	
Ga $\delta$ -Pu (111) surface .....	220
Appendix F Initial and final positions for H adsorption on 9.375 at. %	
Ga $\delta$ -Pu (111) surface .....	226
References .....	233
Biographical Information.....	243

## List of Illustrations

Figure 1.1: Pu has six solid state phase transitions. Shown here is a comparison with the phase transitions of iron. Image from Ref. 3. ....	3
Figure 1.2: Phase transition with respect to temperature for pure $\delta$ -Pu and $\delta$ -Pu alloyed with a Ga impurity. Image from Ref. 31. ....	7
Figure 1.3: Schematic depiction of catastrophic failure of Pu within a metal food-pack can. Image from Ref. 48. ....	12
Figure 1.4: Left picture shows a plutonium metal button and right picture shows stabilized plutonium-oxide. Image from Ref. 54. ....	13
Figure 1.5: Kinetics of $\text{Pu}_2\text{O}_3$ and $\text{PuO}_2$ in dry air at room temperature. Image from Ref. 49. ....	15
Figure 1.6: Oxide layer formation for Pu under different environment conditions. Image from Ref. 49. ....	16
Figure 1.7: Images showing the sequence of hydriding spots. The numbers are the seconds that the sample was exposed to hydrogen. Image from Ref. 63. ....	20
Figure 1.8: Generalized model for hydrogen interactions with metals. Image from Ref. 71. ....	21
Figure 2.1: DFT self-consistency loop flow chart. ....	39
Figure 2.2: Illustration of system divided into two regions, muffin-tin (MT) around atoms and interstitial region. Interstitial regions have planewave	

solutions, while inside MT solutions are rapidly varying. Image obtained from Ref. 100. ....	45
Figure 2.3: Flow chart of the implantation of SOC in <i>WIEN2k</i> . ....	50
Figure 3.1: (a) The 32-atom supercell for $\delta$ -Pu <i>fcc</i> structure (yellow atoms are Pu atoms). (b) $E$ vs. $V$ curves for each magnetic configuration (inserts show expanded $E$ vs. $V$ curves for the FM and AFM). (c) The $5f$ PDOS with SOC for AFM configuration. Image from Ref. 108. ....	56
Figure 3.2: All cases studied for the Pu-Ga alloys. Pu atoms are yellow and Ga atoms are purple. 3.125 at. % Ga is shown in (a), while (b-f) are the cases for 6.25 at. % Ga, and (g-l) are the cases for 9.375 at. % Ga. Atoms shared by periodic cells are also shown. Image from Ref. 108. ....	60
Figure 3.3: Relative $E$ vs. $V$ curves for the NM, FM, and AFM ordering for (a) 3.125, (b) 6.25, and (c) 9.375 at. % Ga. Inserts show expanded $E$ vs. $V$ curves for the FM and AFM magnetic ordering. Image from Ref. 108. ....	61
Figure 3.4: $E$ vs. $V$ curves for the 6.25 at. % Ga concentration for different Ga cases. Image from Ref. 108. ....	68
Figure 3.5: $E$ vs. $V$ curves for the 9.375 at. % Ga concentration for all Ga cases. Side panel illustrates 9.375 at. % Ga concentration cases of the different distances of the Ga atoms within the 32-atom supercell. Image from Ref. 108. ....	72
Figure 3.6: Lattice constant vs. Ga concentration for the NM, FM, and AFM at the NSOC level of theory. AFM data that was plotted includes the lattice constants	

for the lowest energy structures for all Ga concentrations and cases. The inserts are expanded NM and AFM graphs. Experimental data obtained from Ref. 27. Image from Ref. 108. .... 73

Figure 3.7: PDOS for the SOC calculation of the lowest energy structure for (a) 3.125, (b) 6.25, and (c) 9.375 at. % Ga concentration for a Pu atom located at 1nn and 4nn from the Ga atom within the cell. Image from Ref. 108. .... 79

Figure 3.8: PDOS of Pu  $7s6d$  and Ga  $4p$  for the SOC relax lowest energy structure for (a) 3.125, (b) 6.25, and (c) 9.375 at. % Ga concentration. Pu atoms were located at 1nn and 4nn from the Ga atom. Image from Ref. 108. .... 80

Figure 3.9: Three-dimensional  $\Delta n(r)$  for Pu (yellow) in 1nn shell around Ga (purple) atom for (a) 3.125, (b) 6.25, and (c) 9.375 at. % Ga concentrations. Red are regions of charge accumulation, while blue indicates regions of charge depletion. (a), (b), and (c) are shown with an isosurface level of 0.0270, 0.0270, and 0.0324 e-/cubic Å, respectively. Image from Ref. 108. .... 83

Figure 3.10: H□ at 1nn (a), 2nn (b), and 4nn (c) from Ga atom. Hydrogen atom is green and periodic images are shown. .... 87

Figure 3.11: Initial position of H□ located at quasi-1nn distance to Ga (purple) atom (a), after relaxation (b) a three-dimensional  $\Delta n(r)$  is plotted. Red indicates regions of charge accumulation, while blue indicates regions of charge depletion. The isosurface level is 0.0270 e-/cubic-Å. Image (b) is from Ref. 108. .... 92

Figure 3.12: PDOS for a Pu atom located at 1nn distance relative to the H atom (H-vac) and vacancy (vac) for the final quasi-1nn distance to the Ga atom SOC relaxed structure. Insert shows expanded PDOS to amplify the hybridization of the H *1s* and Pu-1nn *5f6d7s*. Image from Ref. 108..... 94

Figure 4.1: 3.125 at. % Ga stabilized  $\delta$ -Pu surface, with Ga located in the topmost surface. Pu atoms are yellow, while Ga atoms are purple. .... 97

Figure 4.2: 9.375 at. % Ga stabilized  $\delta$ -Pu surface, with Ga located in the topmost surface and in the sub-surface..... 98

Figure 4.3: 3.125 at. % Ga slab initial sites for adsorbate (blue) on PuGa-terminated surface. On top of Ga (a), bridge between Pu and Ga (b), and hollow sites, hcp (c) and fcc (d), with Ga as a nearest neighboring atom. Similar sites for the adsorbate were also taken into consideration for a Pu-rich environment for both the Pu-terminated and PuGa-terminated surface, which can be seen in Appendix C..... 101

Figure 4.4: Initial octahedral interstitial sites with O adatom for 3.125 at. % Ga surface. Sites include positions where the O atom regressed further away from the Ga atom [(a)-(c)]. A similar regression of the O atom from the Ga atom was also studied for the tetrahedral sites, which can be observed in Appendix C..... 102

Figure 4.5: 9.375 at. % Ga initial sites for O atom for PuGa-terminated surface. On top of Ga (a), bridge between Pu and Ga (b), and hcp (c) and fcc (d) sites, with Ga as a nearest neighboring atom. Similar sites were also investigated for the Pu-

rich environment for the Pu-terminated and PuGa-terminated surface, which may be viewed in Appendix D. ....	104
Figure 4.6: 9.375 at. % Ga surface initial octahedral interstitial sites when O atom is far from Ga (a) and near Ga (b). Initial tetrahedral interstitial sites when O atom is far from Ga (c) and near Ga (d).....	105
Figure 4.7: Top (a) and side (b) view of the final geometries after O adsorption for the Pu-terminated bridge-to-fcc site. Pu atoms are yellow, Ga atom is purple, and O atom is blue. ....	114
Figure 4.8: PDOS for the SOC level of theory for the least favorable site, top site (a), and most favorable site, bridge-to-fcc site (b), for when the O adsorbate is approaching the Pu-terminated surface.....	125
Figure 4.9: PDOS for the SOC level of theory for the least favorable site, top-Ga and top-Pu site [(a) and (c), respectively], and most favorable site, fcc-PuGa and bridge-Pu site [(b) and (d), respectively], for when the O adsorbate is approaching the PuGa-terminated surface.....	128
Figure 4.10: PDOS of Pu <i>5f</i> and <i>6d</i> states and nearest neighboring Ga atom <i>4p</i> states before and after O adsorption. O <i>4p</i> states are also plotted. ....	130
Figure 4.11: PDOS for the SOC level of theory for the least favorable interstitial site, tetrahedral-1 and octahedral-1 [(a) and (c), respectively], and most favorable site, tetrahedral-3 and octahedral-3 site [(b) and (d), respectively], for when the O adsorbate is initially placed in an interstitial site. ....	132

Figure 4.12: Three-dimensional  $\Delta n(r)$  for the bridge-to-fcc site (a) for the Pu-terminated surface, and for the PuGa-terminated surface the bridge-PuGa-to-four-fold site (b). Only the coordination environment around the O-atom is shown. Regions of red indicate charge accumulation, while regions of blue indicate charge depletion. Isosurface level is 0.0337 e<sup>-</sup>/cubic Å..... 135

Figure 4.13: Two Ga atoms located in the second layer (a) and fourth layer (b) with respect to the PuGa-terminated surface. .... 149

Figure 4.14: PDOS for the SOC level of theory for the least favorable site, top site (a), and most favorable site, fcc site (b), for when the O adsorbate is approaching the Pu-terminated surface. .... 157

Figure 4.15: PDOS for the Pu *5f* and *6d* state and nearest neighboring Ga atom *4s* and *4p* states, and O *2p* states for the Pu-terminated top site after adsorption. .. 158

Figure 4.16: PDOS for the SOC level of theory for the least favorable site, top-Ga (a), and most favorable site, hcp-PuGa-to-fcc (b), for when the O adsorbate is approaching the PuGa-terminated surface. .... 160

Figure 4.17: PDOS for hcp-PuGa to fcc site before and after O adsorption with nearest neighboring Ga atom plotted. Pu-Ga bond is 3.18 Å and Ga-O bond was 4.09 Å..... 161

Figure 4.18: PDOS for the SOC level of theory for the most favorable interstitial site, tetrahedral-1 and octahedral-1 [(a) and (c), respectively], and least favorable

site, tetrahedral-2 and octahedral-2 site [(b) and (d), respectively], for when the O adsorbate is initially placed in an interstitial site. ....	164
Figure 4.19: Three-dimensional $\Delta n(r)$ for the Pu-terminated fcc site (a), and for the interstitial tetrahedral-2 site (b). Only the coordination environment around the O-atom is shown. Red indicates charge accumulation (positive), blue indicates charge depletion (negative). Isosurface level is $0.0337 e^-/\text{cubic } \text{\AA}$ . ....	166
Figure 5.1: PDOS for the SOC level of theory for the least favorable site, top site [(a) and (c)], and most favorable site, hcp (b) and fcc (d) sites, for the 3.125 and 9.375 at. % Ga surfaces, respectively. PDOS is for the case when the H atom is approaching the Pu-terminated surface. ....	183
Figure 5.2: PDOS for the SOC level of theory for the least favorable site, top-Ga [(a) and (c)], and most favorable site, hcp-Pu (b) and fcc-Pu (d), for the 3.125 and 9.375 at. % Ga surfaces for when the H atom is approaching the PuGa-terminated surface. ....	185
Figure 5.3: PDOS for the SOC level of theory for the least favorable interstitial site, tetrahedral-1 [(a) and (c)], and most favorable site, octahedral-3 and octahedral-2 site [(b) and (d)] for the 3.125 and 9.375 at. % Ga surfaces for when the H adsorbate is initially placed in an interstitial site. ....	188
Figure 5.4: PDOS for Pu $5f$ and $6d$ for the pure $\delta$ -Pu (111) surface and 3.125 and 9.375 at. % Ga $\delta$ -Pu (111) surface. Only a Pu atom for the Pu-terminated surface was plotted. The Pu $6d$ have been amplified (x10) to see features. ....	190

Figure 5.5: Three-dimensional  $\Delta n(r)$  for the hcp site (a) and fcc site for the Pu-terminated surface, and the fcc-PuGa site [(b)-(d)] for the PuGa-terminated 3.125 and 9.375 at. % Ga surface, respectively. Only the coordination environment around the H-atom is shown. Red indicates charge accumulation, while blue indicates charge depletion. Isosurface level is  $0.0121 \text{ e}^-/\text{cubic } \text{\AA}$ . Green is Pu atoms, orange is Ga atom, and H is the center atom. .... 192

## List of Tables

<p>Table 3.1: Equilibrium lattice constant (<math>a_o</math>), bulk modulus (<math>B</math>), and the spin polarization energy (<math>E_{sp}</math>) results for NM, FM, and AFM at the NSOC level of theory. In the 6.25% and 9.375% cells, Ga atoms are at nearest neighbor distances from each other. Experimental data was obtained from Ref. 106 and 107.....</p>	58
<p>Table 3.2: Relaxation energy (<math>E_r</math>), spin-orbit coupling energy (<math>E_{SOC}</math>), and formation energy (<math>E_f</math>) calculated for NSOC and SOC level of theory. Results shown are for the lowest energy structure (AFM magnetic configuration) for each Ga concentration. Formation energies in units of kJ/mol are shown in parentheses.....</p>	64
<p>Table 3.3: The average Pu-Ga and Pu-Pu bond lengths for the 1nn shell around a Ga atom was calculated by dividing the distance in the final relaxed structure by the distance in the perfect <i>fcc</i> lattice and averaging. <math>\sigma</math> is the standard deviation of the bond lengths.....</p>	65
<p>Table 3.4: Equilibrium lattice constants (<math>a_o</math>) and bulk moduli (<math>B</math>) for the NSOC AFM calculations for different Ga cases (see text). Experimental data was obtained from Ref. 106 and 107. ....</p>	74
<p>Table 3.5: Partial charges of a Pu and Ga atom at first nearest neighboring distance from each other for each Ga concentration. <math>\Delta</math>-Pu is the difference between the partial charge for the Pu atom in the Pu-Ga cell and in the Pu-only</p>	

cell, and $\Delta$ -Ga is the difference between the partial charge for the Ga atom in the Pu-Ga cell and the isolated Ga.....	84
Table 3.6: NSOC and SOC relaxation ( $E_r$ ) and formation energies ( $E_f$ ) for a vacancy ( $\square$ ) and hydrogen-vacancy complex ( $H\square$ ) when located at a quasi 1nn, 2nn, and 4nn position with respect to the Ga atom.....	88
Table 3.7: Partial charges for a Pu and H atom at 1nn distance to each other for the final relaxed structure when the $H\square$ complex is located at a quasi-1nn distance from the Ga atom. $\Delta$ -Pu or $\Delta$ -H is the difference between the partial charge for the Pu or H atom in the Pu-Ga+ $H\square$ cell and the Pu-Ga cell or isolated H. ....	93
Table 4.1: Structural analysis of the first nearest neighboring shell around the Ga atom in the 3.125 at. % Ga bulk and surface systems. The division of the bond length distance in the final relaxed structure by the bond length distance of the pristine structure is defined by $d_{relax}/d_{fcc}$ , $\sigma$ is the standard deviation of the normalized bond lengths, and the average bond length contractions are tabulated. Bulk data was obtained from Ref. 108.....	108
Table 4.2: Results for the Pu-terminated surface which includes relaxation energy, $E_r$ , chemisorption energy, $E_c$ , at the NSOC and SOC level of theory, and distance of the adatom from the surface, $r_{slab-O}$ , and distance of the adatom to the nearest neighboring atoms, $r_{Pu-O}$ . ....	113
Table 4.3: Results for the PuGa-terminated surface which includes relaxation energy, $E_r$ , chemisorption energy, $E_c$ , at the NSOC and SOC level of theory, and	

distance of the adatom from the surface,  $r_{slab-O}$ , and distance of the adatom to the nearest neighboring atoms,  $r_{X-O}$ , where  $X$  is the atom that is nearest to the adatom. If atom is not designated by parenthesis it is assumed that it is a Pu atom. .... 116

Table 4.4: Results for the interstitials sites which includes relaxation energy,  $E_r$ , chemisorption energy,  $E_c$ , at the NSOC and SOC level of theory, and distance of the adatom from the surface,  $r_{slab-O}$ , and distance of the adatom to the nearest neighboring atoms,  $r_{X-O}$ , where  $X$  is the atom that is nearest to the adatom. If atom is not designated by parenthesis it is assumed that it is a Pu atom. .... 120

Table 4.5: Changes in work function,  $\Delta\phi$ , at the NSOC and SOC levels of theory. The work function for the clean relaxed Pu slab was 3.29 eV and 3.37 eV, respectively, at the NSOC and SOC level of theory. Experimental work function for Ga stabilized  $\delta$ -Pu is 3.2 eV [116]. ..... 123

Table 4.6: Net valance partial charges for the Pu-terminated bridge-to-fcc site and PuGa-terminated bridge-PuGa-to-four-fold site. .... 134

Table 4.7: Structural analysis of the first nearest neighboring shell around the Ga atom in the 9.375 at. % Ga bulk and surface system. The division of the bond length distance in the final relaxed structure by the bond length distance of the pristine structure is defined by  $d_{relax}/d_{fcc}$ ,  $\sigma$  is the standard deviation of the bond lengths, and the average bond length contractions are tabulated. Bulk data was obtained from Ref. 108. .... 138

Table 4.8: Relaxation energy, $E_r$ , chemisorption energy, $E_c$ , at the NSOC and SOC level of theory, and distance of the adatom from the surface, $r_{slab-O}$ , and distance of the adatom to the nearest neighboring Pu atoms, $r_{Pu-O}$ , for the Pu-terminated surface sites.....	141
Table 4.9: Results for PuGa-terminated surface sites, which include relaxation energy, $E_r$ , chemisorption energy, $E_c$ , at the NSOC and SOC level of theory, and distance of the adatom from the surface, $r_{slab-O}$ , and distance of the adatom to the nearest neighboring atoms, $r_{X-O}$ , where $X$ is the atom that is nearest to the adatom. In the last column if atom is not designated by parenthesis it is assumed that it is a Pu atom. ....	145
Table 4.10: SOC chemisorption energies for when two Ga atoms are located in a different layer.....	150
Table 4.11: Relaxation energy, $E_r$ , chemisorption energy, $E_c$ , at the NSOC and SOC level of theory, and distance of the adatom from the surface, $r_{slab-O}$ , and distance of the adatom to the nearest neighboring atoms, $r_{X-O}$ , where $X$ is the atom that is nearest to the adatom, for the interstitials sites. In last column, if atom is not designated by parenthesis it is assumed that it is a Pu atom.....	153
Table 4.12: Changes in work function, $\Delta\phi$ , at the NSOC and SOC levels of theory. The work function for the clean relaxed Pu-Ga slab was 3.32 eV and 3.39 eV, respectively, at the NSOC and SOC level of theory. Experimental work function is 3.2 eV for stabilized $\delta$ -Pu [36].....	168

Table 5.1: Relaxation energy,  $E_r$ , chemisorption energy,  $E_c$ , at the NSOC and SOC level of theory, and distance of the H atom from the surface,  $r_{slab-H}$ , and bond length of H atom to the nearest neighboring Pu atoms,  $r_{Pu-H}$ , for the Pu-terminated surface sites on the 3.125 and 9.375 at. % Ga slabs. .... 172

Table 5.2: Relaxation energy,  $E_r$ , chemisorption energy,  $E_c$ , at the NSOC and SOC level of theory, and distance of the H atom from the surface,  $r_{slab-H}$ , and bond length of the H atom to the nearest neighboring atoms,  $r_{X-H}$ . In the last column if atom is not designated by parenthesis it is assumed that it is a Pu atom. .... 174

Table 5.3: Relaxation energy,  $E_r$ , chemisorption energy,  $E_c$ , at the NSOC and SOC level of theory, and distance of the H atom from the surface,  $r_{slab-H}$ , and bond length of the H atom to the nearest neighboring atoms,  $r_{X-O}$ , for the interstitials sites. In last column, if atom is not designated by parenthesis it is assumed that it is a Pu atom. .... 179

Table 5.4: Changes in work function,  $\Delta\phi$ , at the NSOC and SOC levels of theory. The work function for the clean relaxed Pu-Ga slab was 3.32 eV and 3.39 eV, respectively, at the NSOC and SOC level of theory. Experimental work function is 3.2 eV for stabilized  $\delta$ -Pu [116]. .... 193

## Chapter 1

### Introduction

#### 1.1 Overview of Plutonium

Discovered by bombarding uranium-238 by deuterons, Dr. G. T. Seaborg and collaborators discovered plutonium (Pu) in 1941[1] and Pu is the most intriguing and complex element in the periodic table. This is due to its very complicated electronic and nuclear structure that arises from the  $5f$  electrons. Thus, Pu is often considered to be a “physicist’s dream, but an engineer’s nightmare [2].” Pu is located amongst the actinides, which are characterized by the gradual filling of the  $5f$  electrons in the periodic table and is considered the boundary between itinerant (Ac – Np) and localized valence electrons (Am – No). This special location has given rise to some of the most unusual properties seen in Pu, such as undergoing six phase transitions from room temperature to its melting point of 913 K and a negative thermal expansion in its high temperature phase ( $\delta$ -Pu) [3,4,5]. The low-temperature phases of Pu are complex in crystal structure, such as the room-temperature low symmetry  $\alpha$ -phase. The  $\alpha$ -phase is a monoclinic crystal with a 16 atom unit cell. The high temperature phases have compact, high symmetry crystal structures, such as the  $\delta$ -phase, which is a face-centered-cubic ( $fcc$ ) crystal. Between these two phases a 25% increase in volume is observed, along with a negative coefficient of thermal expansion in the  $\delta$ -phase in the range of  $\sim 593$  K – 735 K. Figure 1.1 shows Pu phase

transitions with increasing temperatures. Note that a seventh phase, known as the  $\zeta$ -phase, appears when Pu undergoes pressure and high temperatures [6].

In addition, although Pu is located at the boundary between delocalized and localized electronic behavior, this boundary is also apparent within its own phases. For instance,  $\alpha$ -Pu is well known to be delocalized in nature, while  $\delta$ -Pu has a dual nature of delocalized/localized behavior. Even though there are these abrupt phase transitions of Pu, the origin of magnetism still remains an open question amongst the theorists that study Pu.

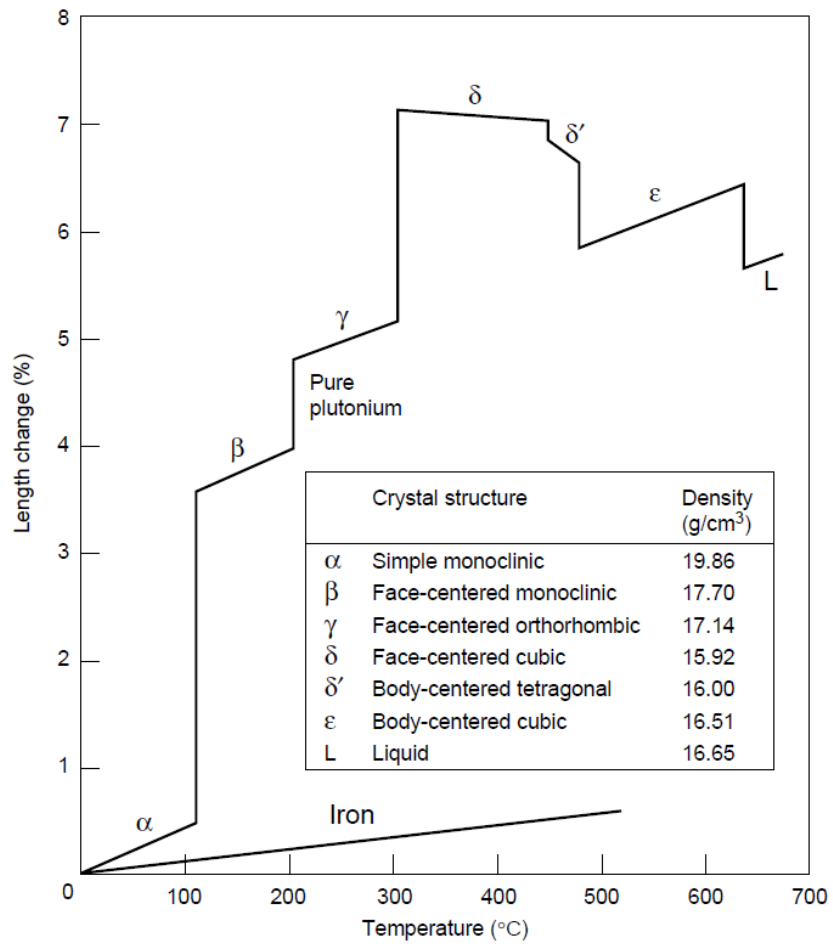


Figure 1.1: Pu has six solid state phase transitions. Shown here is a comparison with the phase transitions of iron. Image from Ref. 3.

Among the experimental community, the question of magnetism remains answered by the fact that Pu does not have magnetism. Lashley *et al.* [7] determined that Pu has no ordered magnetic moments, thus a non-magnetic arrangement within Pu. This claim is still being determined experimentally, which recently there were findings of an existence of high energetic magnetic fluctuations that might help understand the “missing” magnetism in Pu [8]. While on the other hand, modeling or simulating Pu with *ab initio* theories, such as density functional theory (DFT- will be discuss later), an anti-ferromagnetic arrangement is always the lowest energy structure. This discrepancy that exists among theory and experimental has opened up a slew of theoretical methodological approaches that go beyond DFT to obtain the holy grail of a non-magnetic ground state. Overall the successes of DFT are not limited to all the phases of Pu. In fact it is well known that DFT accurately describes  $\alpha$ -Pu [9], due to the delocalized nature of the *5f* electrons in this phase, but  $\delta$ -Pu is problematic, specifically the localized/delocalized nature of the *5f* electronic behavior. We will now provide a brief overview of the successes and drawbacks of DFT and beyond as they are applied to understanding the electronic behavior of  $\delta$ -Pu.

## 1.2 DFT and beyond applied to $\delta$ -Pu

Past studies indicated that DFT with or without the inclusion of spin-orbit coupling and orbital polarization provides good agreement with the equilibrium volume and bulk modulus, but an anti-ferromagnetic ground state is obtained [10, 11, 12, 13, 14, 15 16], which is contrary to experimental results by Lashley et. al. [7], which indicated that there is an absence of magnetic moments in Pu. Extensions to DFT, namely, DFT with the addition of a Hubbard U parameter (DFT+U) and DFT with dynamical mean-field theory (DFT+DMFT) have been used to study  $\delta$ -Pu [17]. Past DFT+U studies have shown that  $\delta$ -Pu is highly sensitive to the selection of the U parameter [18] and a non-magnetic ground state can be obtained by a complete cancellation of the spin and orbital moments [19]. More recently, the around-the-mean-field version of DFT+ U was used to obtain a non-magnetic ground state for  $\delta$ -Pu [20]. It has been also shown, using a hybrid density with functional 55% Hartree-Fock exchange, that a non-magnetic ground state of  $\delta$ -Pu may be attained, but all other properties were not consistent with experimental results (such as lattice constant and partial density of states) [21]. On the other hand, DFT+DMFT calculations yielded a non-magnetic ground state of  $\delta$ -Pu, along with good agreement with the photoemission spectra [22, 23, 24]. Although these methods acquire the non-magnetic ground state, computational expense increases, and so these methods may not be the most ideal.

### 1.3 $\delta$ -Pu-Ga alloy properties:

#### Experimental and Theoretical overview

During the Manhattan project, it was quickly discovered that the room-temperature  $\alpha$ -phase is known to be brittle, similar to glass, and extremely difficult to cast. The high temperature  $\delta$ -phase is ductile and therefore more suitable for applications. Such applications include Pu being used as a nuclear energy source. For instance, the isotope Pu-239 can also be used as a nuclear mixed oxide fuel, where Pu oxide is mixed with depleted uranium [25]. The desire to use mixed oxide fuels in nuclear reactors will take advantage of the excess Pu that is currently available from disarmed nuclear warheads and spent nuclear reactor fuel. Also, recently Pu-238 was used to supply energy to the Cassini mission [26] and may be the promised energy source for future space missions to Mars and beyond. Therefore, in order to use the more desirable  $\delta$ -Pu phase, it is often alloyed with an element from the IIIA metal group, such as aluminum and gallium (Ga). These alloying impurities are known to stabilize the ductile  $\delta$ -phase down to room temperature (Figure 1.2) [27, 28, 29, 30]. In Figure 1.2 the  $\delta$ -Pu phase alloyed with Ga shows that the stability of the  $\delta$ -phase is retained at room-temperatures and below, but at higher temperatures a phase transition is noticed. Also the disappearance of the negative thermal expansion is noted when  $\delta$ -Pu is alloyed with Ga.

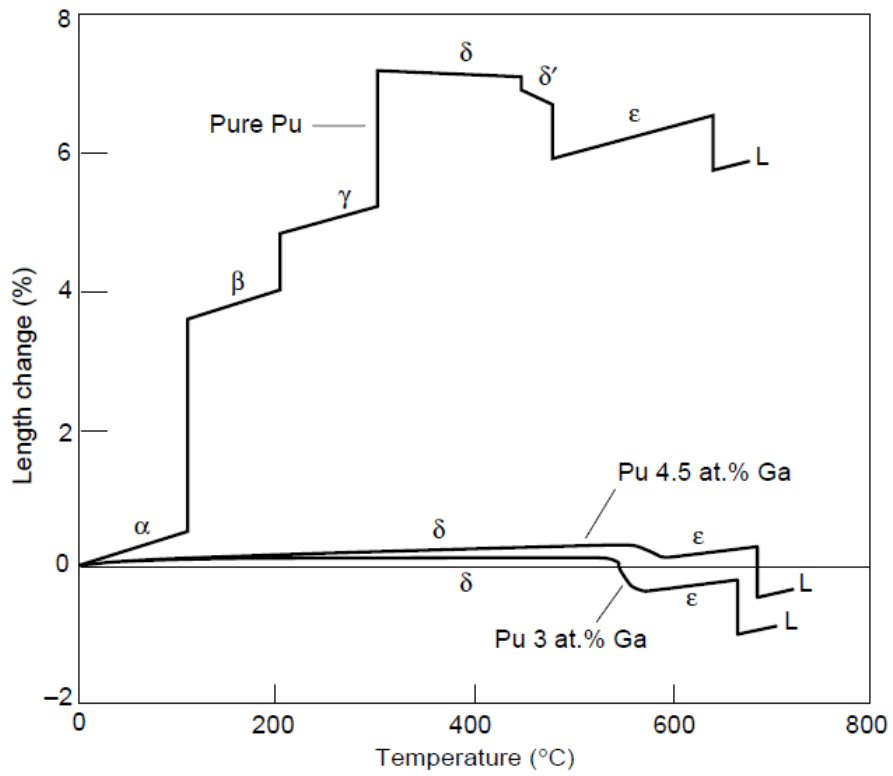


Figure 1.2: Phase transition with respect to temperature for pure  $\delta$ -Pu and  $\delta$ -Pu alloyed with a Ga impurity. Image from Ref. 31.

The Pu-Ga system has been studied experimentally and these studies have concluded that  $\delta$ -Pu may be stabilized at room temperature with as low as 1 atomic (at.) % Ga [27]. Studies have indicated that with increasing Ga concentrations the lattice constant decreases and the Ga occupies a substitutional site in the  $\delta$ -Pu *fcc* lattice [27, 28, 29, 30]. Upon cooling,  $\delta$ -Pu alloyed with 2.5 at. % Ga or lower will undergo a phase transformation into the martensitic  $\alpha'$ -phase (isostructural of  $\alpha$ -Pu that has an expanded unit cell) [32, 33, 34]. X-Ray absorption fine structure spectroscopy (EXAFS) has also shown that there is a local collapse around the Ga atom, along with short-range order that is close to the *fcc* arrangement, but there was an increase in strong disorder of the surrounding Pu atoms around the Ga when the Ga content increased [35]. Recent EXAFS also observed Ga-induced distortions in the second coordination sphere around the Ga impurity in  $\delta$ -Pu [36]. Therefore, there are local structural distortions around the Ga in  $\delta$ -Pu. Along with studying the phase stability of Pu-Ga alloys, the electronic and magnetic structures of the alloys are of great interest, particularly the roles played by the Pu  $7s^2 5f^5 6d^1$  and Ga  $4s^2 4p^1$  valence electrons.

The understanding of the structural and geometric effects that Ga induced in the  $\delta$ -phase has been explored by theoretical techniques, such as an earlier DFT study performed by Sadigh and Wolfer [37] that explored the effect of a Ga impurity in both the  $\alpha$  and  $\delta$ -phase. Key findings from their study are that within the  $\alpha$ -phase, Ga will reside in a site-8 location in the monoclinic structure, while Ga in the  $\delta$ -phase

has a negative heat of mixing (exothermic) for alloys with concentration of 3.125 and 6.25 at. % Ga. In addition, Sadigh and Wolfer [37] analyzed the local Pu structure environment around the Ga impurity and found that the first nearest neighbor Pu atoms around the Ga contract inward and the Pu-Pu bond distances decrease with increasing Ga concentration. Studies by Robert *et al.* [38] indicated that there was an increase in short range disorder in the first nearest neighbor shell around the Ga, even though the Pu-Ga and Pu-Pu distances retain the *fcc* structure with increasing Ga concentration. A more recent theoretical study by Söderlind *et al.* [39] examined the elastic properties of Pu-Ga alloys and predicated a linear behavior for the atomic volume and bulk modulus as a function of Ga concentration. Other theoretical works have also investigated the relaxation of the *fcc*  $\delta$ -Pu lattice around a Ga atom to help explain the stabilization of the  $\delta$ -phase [40, 41]. Becker *et al.* [40] performed full-potential linear-muffin-tin-orbital DFT-local density approximation force calculations on the relaxation of Pu atoms around a Ga atom in an *fcc*-based  $\text{Pu}_{31}\text{Ga}$  supercell (with Ga located at the center). They also observed that the nearest neighbor shell of Pu atoms around Ga relaxes inward by 1.04% of the initial theoretical bond length, which is significantly less than the measured EXAFS value of 3.7% [28, 29]. Moore *et al.* [41] performed DFT calculations for a pure  $\delta$ -Pu and  $\delta$ -Pu alloyed with 3.7 at. % Ga. by computing the forces on the 12 nearest neighbor Pu atoms of the central Pu atom in a  $\text{Pu}_{27}$  *fcc* supercell and on the central Ga atom in a  $\text{Pu}_{26}\text{Ga}$  *fcc* supercell. In the  $\text{Pu}_{27}$  supercell, the forces on the 12 nearest neighbors of

the central Pu displayed a large degree of anisotropy, while in the  $\text{Pu}_{26}\text{Ga}$  supercell the forces display some uniformity. The authors concluded that the non-uniformity of the magnitude of the forces in pure Pu somewhat explain why the ground state of Pu is monoclinic and also the uniformity of the magnitude of the forces in the presence of Ga explains why Ga stabilizes the high temperature  $\delta$  phase to room temperature or below.

To understand the mechanisms of how Ga stabilizes the  $\delta$ -phase, it is of great importance to understand the electronic properties behavior of these alloys. Without the presence of Ga, previous theoretical studies showed that there exist strong hybridized  $d$ - $f$  character [42, 43]. With the inclusion of Ga, it was postulated that Ga stabilizes  $\delta$ -Pu to room-temperature by the fact that the presence of Ga tends to shift the Fermi level in such a way that decreases the  $f$ -bonding nature, subsequently enhancing the  $d$ -bonding characteristics [44]. This enhancement of the  $d$ -bonding with the weakening of the  $f$ -bonding in turn leads to the stability of Ga-containing  $\delta$ -Pu [45]. In  $\text{Pu}_3\text{Ga}$ , where the concentration of Ga is greater than 12.5 at. % Ga and one Ga atom is present per two  $\delta$  unit cells [30], it was observed that there was covalent bonding in the Pu  $d$ - $f$  state and the Ga  $p$  state [46]. Therefore, the Ga impurity plays an important role of influencing the electronic structure of  $\delta$ -Pu. Even though it was mentioned above that DFT does not describe magnetism in  $\delta$ -Pu well, recent calculations by Söderlind *et al.* [47] have shown that DFT describes Pu-Ga

alloys quite well, including magnetism. Söderlind *et al.* [47] claimed that Pu-Ga alloys were anti-ferromagnetic.

#### 1.4 Corrosion of $\delta$ -Pu

Evaluating the ageing and corrosion effects of plutonium is one of the leading challenges for scientists today, because of environmental concerns and waste disposal issues. Plutonium metal is known to be highly reactive when exposed to environmental gases, particularly hydrogen, oxygen, and water [48, 49, 50, 51, 52]. Catastrophic failure has been seen in early storage cases for Pu (Figure 1.3). In 1992, a 2.2 kg Pu casting was stored in a screw-lid metal can, and two-layers of plastic served as an inner barrier for contamination within a rim-seal closure metal food-pack [48]. Unfortunately a pin hole developed on the outer can and as the reaction with oxygen and hydrogen on Pu occurred, the Pu metal oxidized and expanded, causing catastrophic failure of the storage unit within seven years [48]. Scientists are concerned about the future applications and storage of Pu from the nuclear stockpile or spent nuclear fuel, but also the environmental issue of corroded Pu is of grave importance. When Pu metal reacts with air, moisture, hydrogen, or oxygen, the surface corrodes very rapidly into a powder of small plutonium particles, which can be easily airborne and inhaled (Figure 1.4) [49]. Due to the toxic nature of Pu, inhaling Pu is considered extremely dangerous, because a chance of 5% - 25% of Pu will be retained and absorbed by the blood; thus posing as an extremely great threat to the environment and life forms [53]. Therefore, understanding the corrosion of Pu

is crucial for the safe maintenance and storage of excess Pu. Ageing will not be discussed furthermore, but the importance of ageing of Pu is of importance to actinide science.

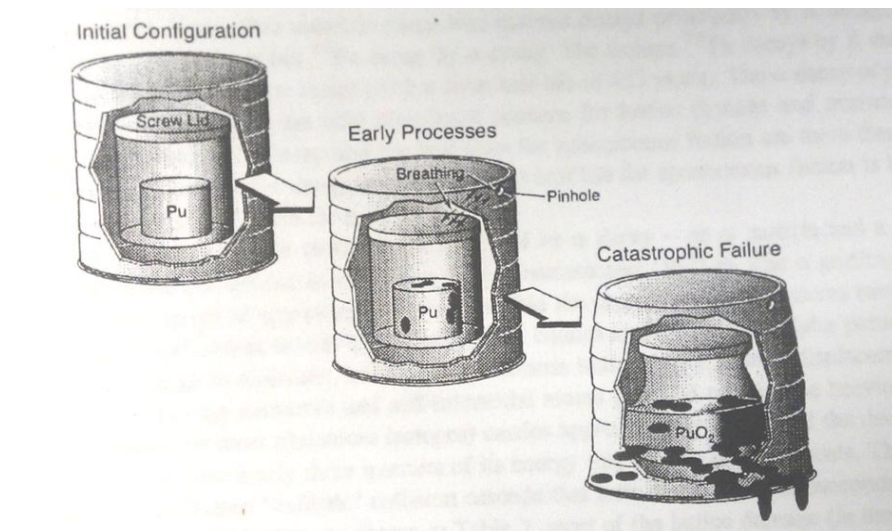


Figure 1.3: Schematic depiction of catastrophic failure of Pu within a metal food-pack can. Image from Ref. 48.



Figure 1.4: Left picture shows a plutonium metal button and right picture shows stabilized plutonium-oxide. Image from Ref. 54.

#### *1.4.1 Oxidation of $\delta$ -Pu*

It is well known from experiments that oxidation of plutonium metal will passivate the surface by forming a thin oxide layer; however the oxidation kinetics is quite complicated [49, 55]. These experiments suggest that when Pu metal is exposed to air, it forms a layer of plutonium dioxide ( $\text{PuO}_2$ ) at the air-oxide interface, while a layer of the sesquioxide ( $\text{Pu}_2\text{O}_3$ ) will form at the oxide-metal interface over time. The formation of  $\text{Pu}_2\text{O}_3$  is determined by the rapid kinetics of the  $\text{PuO}_2$  formation. Also an increase in temperature or decrease in oxygen concentration yields an increase in the  $\text{Pu}_2\text{O}_3$ . Indicated in Figure 1.5, the steady-state oxide layer is  $\text{PuO}_2$  but the oxidation of  $\text{Pu}_2\text{O}_3$  is the predominant surface reaction. This is because when  $\text{O}_2$  is absorbed by  $\text{PuO}_2$ , the oxygen dissociates to form ions, and these ions diffuse through the  $\text{PuO}_2$  layer. Furthermore, with the combination of auto-reduction of the

$\text{PuO}_2$  by Pu, this phenomenon continually produces  $\text{Pu}_2\text{O}_3$ .  $\text{Pu}_2\text{O}_3$  then reacts with the oxygen ions to produce  $\text{PuO}_2$ . Therefore, both  $\text{PuO}_2$  and  $\text{Pu}_2\text{O}_3$  are stable at room temperature and in dry air. After a certain oxide thickness is reached, about 4-5  $\mu\text{m}$ , localized oxide particles start to spall from the surface due to surface stresses that is induced by the different densities of the oxide and plutonium, 11.40  $\text{g/cm}^3$  and 19.86  $\text{g/cm}^3$ , respectively [48]. Therefore, steady-state corrosion is reached because further oxidation is counter balanced by the spallation of the surface.

In an ultra-high-vacuum (UHV) environment, Pu undergoes spontaneous auto-reduction of the  $\text{PuO}_2$  into the  $\text{Pu}_2\text{O}_3$  [56]. Eventually,  $\text{PuO}_2$  will be completely converted to  $\text{Pu}_2\text{O}_3$ . This suggests that  $\text{PuO}_2$  does not coexist with Pu metal thermodynamically [49, 55]. Also as mentioned above, this reaction can occur when increasing the temperature in dry air (not in UHV). Varying environmental conditions for the oxidation of Pu are shown in Figure 1.6.

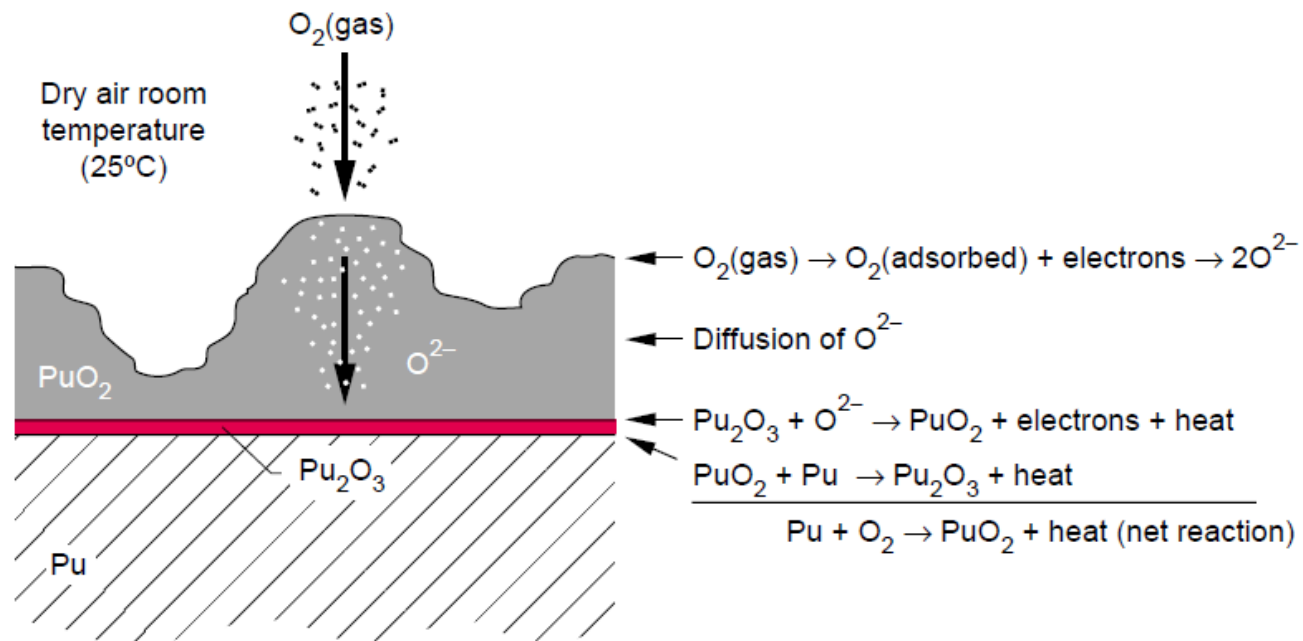


Figure 1.5: Kinetics of  $Pu_2O_3$  and  $PuO_2$  in dry air at room temperature. Image from Ref. 49.

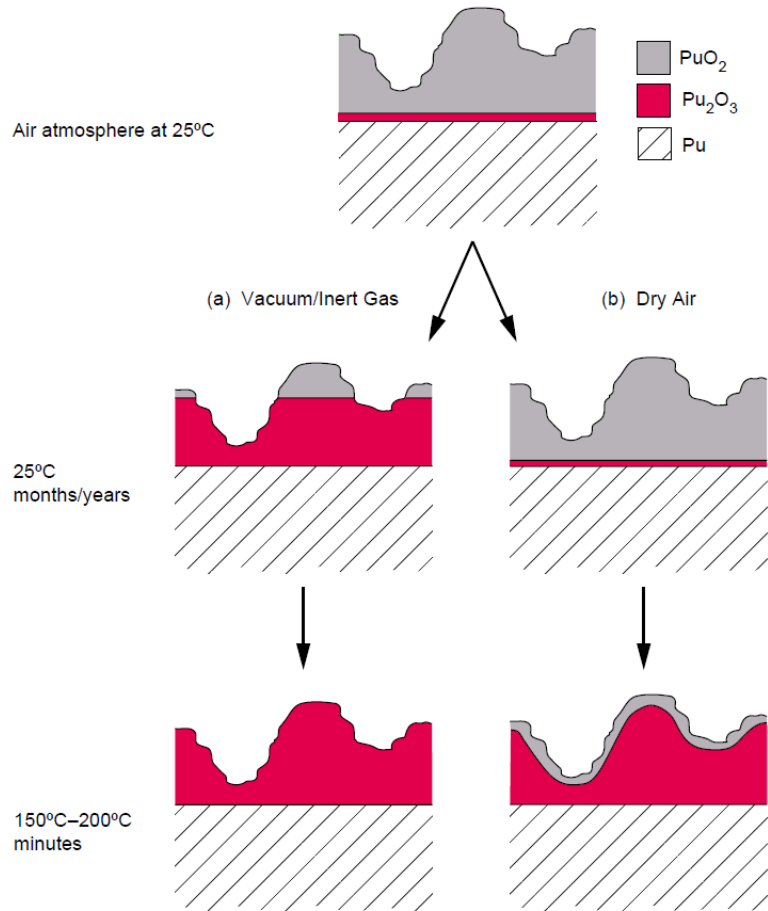


Figure 1.6: Oxide layer formation for Pu under different environment conditions.

Image from Ref. 49.

Recent surface corrosion studies have challenged some of these historical results. For instance, Nelson and Roussel [57] performed UHV experiments that involved dosing of oxygen at low temperatures on a 2.08 at. % Ga stabilized  $\delta$ -Pu sample and they observed that a layer of Pu<sub>2</sub>O<sub>3</sub> formed rapidly and then was

followed by a formation of a  $\text{PuO}_2$  layer. Upon heating the sample, the  $\text{PuO}_2$  quickly reduces to the  $\text{Pu}_2\text{O}_3$ . These results were similar to the photoemission spectroscopy studies done by Butterfield *et al.* [58], but the key results from Nelson and Roussel [57] was that the activation energy for the auto-reduction of  $\text{PuO}_2$  to  $\text{Pu}_2\text{O}_3$  was 38.8 kJ/mol and that the oxide that was formed at room temperature, x-ray diffraction measurements taken after 40 days from the formation of the oxide indicated that the oxide growth is amorphous. The initial growth of the oxide being amorphous has been recently discussed [59]. Finally, the roles of impurities may change the stoichiometry of the oxide and effect the formation of the oxide. For instance, Garcia Flores *et al.* [56] reported that the level of carbon contamination introduces a sub-stoichiometric Pu oxide ( $\text{Pu}_2\text{O}_{3-y}$ ), therefore challenging the accepted belief of the stoichiometric stability of  $\text{Pu}_2\text{O}_3$ . Also Haschke *et al.* [49] reported that in dry air that the ratio of the rate of corrosion between  $\alpha$ -Pu and Ga-stabilized  $\delta$ -Pu was 1:1, but in moist air or a moist inert environment this ratio changes. In moist air,  $\alpha$ -Pu corroded at a rate of 2.6 nm/hr, while Ga-stabilized  $\delta$ -Pu was 1.5 nm/hr [60], thus indicating that the inclusion of Ga made  $\delta$ -Pu corrosion resistant, when compared to unalloyed Pu. On the other hand, in an inert moist environment, the rate of corrosion for  $\alpha$ -Pu became 16 nm/hr, while Ga-stabilized  $\delta$ -Pu was 105 nm/hr [60], which indicates that in this particular environment Ga hindered the resilience of  $\delta$ -Pu to corrosion.

#### 1.4.2 Hydride Formation in $\delta$ -Pu

At low temperatures, the reaction of hydrogen (H) with Pu metal may be used in purifying the metal of impurities or to make Pu powder [61]. The formation of a hydride in Pu metal is dependent on the environmental conditions (i.e. temperature, pressure, atmospheric conditions). Once Pu hydrides are formed, they may be a catalyst in further corroding Pu metal [49, 50, 62, 63]. It is known that  $\delta$ -Pu may absorb hydrogen to form cubic and hexagonal hydrides  $\text{PuH}_x$ , where  $x = 2.0$  to  $3.0$  [62, 64, 65, 66] and are known to be pyrophoric in air at room temperature [49, 61]. The process for hydride formation is as follows [63]: (1) Induction occurs when the metal is exposed to hydrogen and no apparent reaction is taking place. (2) Nucleation of the hydrogen within the metal begins when the first hydride spot is noticeable and depending on the nucleation rate, acceleration of hydride spots are formed and in turn increasing the reacting surface area. (3) The bulk hydride has formed, since the surface is completely covered with hydride and the rate of hydriding decreases. (4) Once the metal is consumed and completely converted to a hydride, the rate falls to zero. The induction period is highly dependent on the amount of impurities that may exist on the surface of the metal or near the surface-bulk interface, since once nucleation occurs the reaction period is rapid and seem to be a barrier-less process [67, 68]. Figure 1.7 shows how after induction has occurred visually, hydride pits formed after 100 seconds and significantly more hydrides formed on the Pu surface at 150 seconds [63], thus showing how hydrides behave as a catalyst for more

hydride formation. The hydriding of Pu metal has been shown to occur even if an apparent oxide is formed on the surface. The sesquioxide,  $\text{Pu}_2\text{O}_3$ , is extremely reactive and is considered a catalyst for further hydrogen corrosion of Pu, since formation of the hydride occurred over the entire surface at once. The growing of isolated nucleation sites materialize after an incubation period that occurred for a lengthy and unpredictable time was observed when the surface was known to be the oxide,  $\text{PuO}_2$  [49, 50, 69].

The solubility of hydrogen has been shown to be dependent on the purity level of the metal and whether the metal was alloyed [70]. Richmond *et al.* [70] observed that there were significant differences in hydrogen solubility between unalloyed and Ga alloyed Pu, which they concluded that in the temperature range of 400-525°C the heat of solution for hydrogen was more exothermic for unalloyed Pu than 2 at. % Ga stabilized  $\delta$ -Pu sample. Therefore, the existence of the alloyed impurity affected the hydrogen solubility, which subsequently may affect the rate of hydrides forming at the surface.

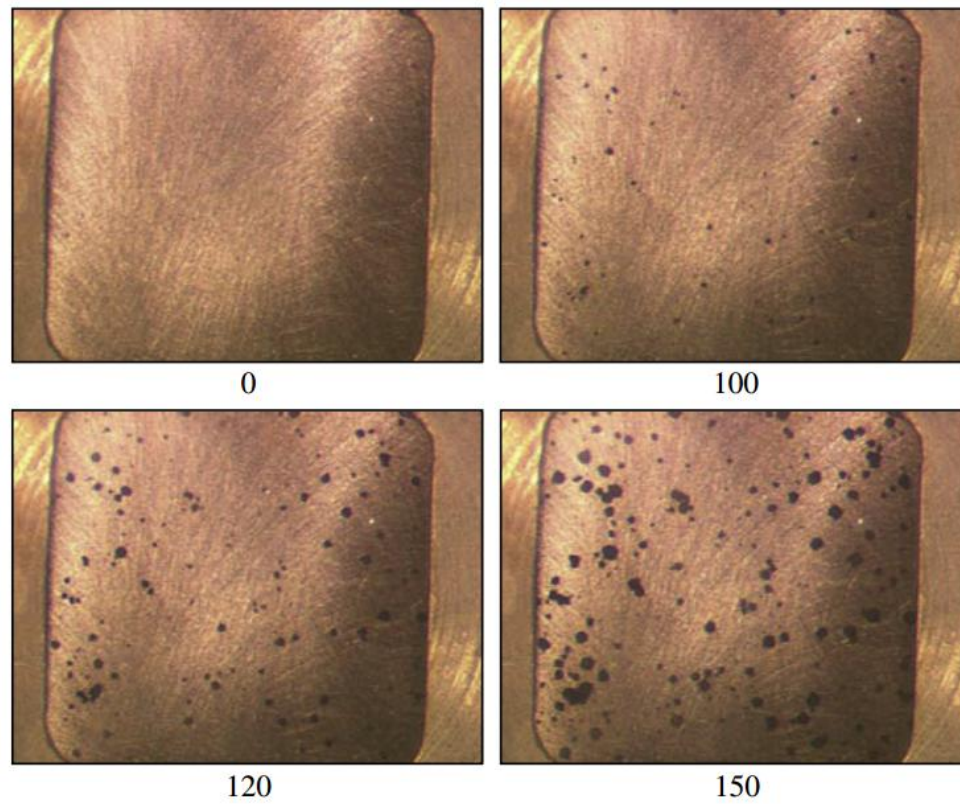


Figure 1.7: Images showing the sequence of hydriding spots. The numbers are the seconds that the sample was exposed to hydrogen. Image from Ref. 63.

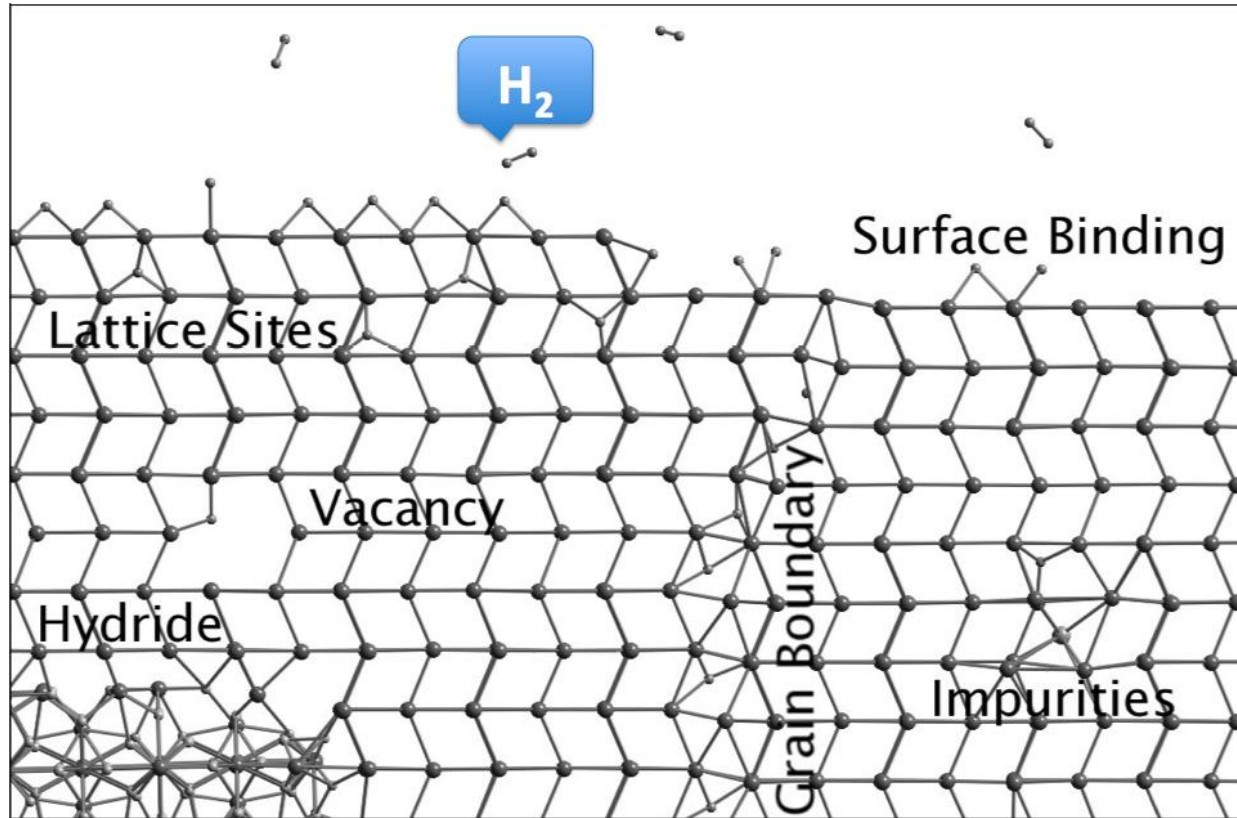


Figure 1.8: Generalized model for hydrogen interactions with metals. Image from Ref. 71.

#### 1.4.2.1 Defects and Vacancies

Formation of the hydride can occur in multiple ways, since hydrogen may interact with the metal in different manners (Figure 1.8). One mechanism for diffusion and binding of hydrogen into the *fcc* bulk lattice is through defects and vacancies. Theoretical studies have shown that isolated mono-vacancies and di-vacancies yielded formation energies that are equally the same and endothermic in  $\delta$ -Pu [38, 72]. Also defect formation and migration energies are dependent on the local Ga environment [73]. Recent experimental data by Schwartz *et al.* and Richmond *et al.* for the solubility of hydrogen in  $\delta$ -Pu (unalloyed and alloyed) metal leads to indications of hydrogen induced vacancies, since Pu shows no discontinuity in hydrogen solubility for the phase transitions from the  $\delta$  (*fcc*) to  $\delta'$  (*bct*) to  $\epsilon$  (*bcc*) phase [70, 74, 75], unlike other metals such as zirconium or titanium [76]. DFT studies that complemented the experimental results of Schwartz *et al.* [74] showed that the hydrogen-vacancy complex energy decreased with an increasing number of hydrogen atoms in the Pu lattice, thus supporting the idea that hydrogen stabilizes vacancies in  $\delta$ -Pu.

#### 1.5 Overview of Theoretical Surface Studies on $\delta$ -Pu

DFT calculations provide a way to probe these interactions with the surface. These calculations are ideal to perform, since the radioactive toxicity of Pu makes it difficult to do experimental work. Therefore, experimental work is performed at

limited facilities. We will give a brief overview of some of the theoretical surface adsorption studies on  $\delta$ -Pu. Previous theoretical studies of oxygen adsorption on the  $\delta$ -Pu (111) surface have given initial insight into the electronic effects [77, 78, 79, 80], and more recently the possible reconstruction of the surface [81]. To briefly summarize some key findings, molecular oxygen does dissociate as it approaches the Pu surface [77], and when the oxygen adatom approaches the surface, it binds to the surface with a three-fold coordination (preferably the hollow hexagonal-closed-pack site) with adsorption energy of  $\sim 8$  eV. This is associated with an increase in work function due to ionic bonding between the Pu and O atom. Also, hybridization of Pu  $6d$  and O  $2p$  orbitals with some mixture of Pu  $5f$  states are noted [77, 78, 79, 80]. In addition, Taylor [81] concluded that initial oxidation coverage is a local environmental phenomenon, but at 1.0 monolayer (ML) coverage of oxygen, significant reconstruction of the surface (up to three atomic layers) of a  $\text{PuO}_2$ -like structure on the topmost surface was observed. The O atoms were four-fold coordinated with the Pu atoms that had been “lifted” out of the plane of the surface.

DFT have also been implemented to elucidate the electronic interactions of hydrogen with a Pu surface [82, 83, 84, 85, 86, 87]. Some of the key findings have shown that on both the (100) and (111) surface, atomic hydrogen prefers to be adsorb at a hollow site [84], while molecular hydrogen will need to overcome an activation energy, 0.778 eV for the (100) surface and 0.305 eV for the (111) surface, to dissociate [85, 86]. Most recently, theoretical attempts have shown the pathway of

hydrogen from the surface to hydride formation, which concluded that in all states hydrogen binds exothermically to Pu. The hydride was more exothermic than adsorption on the surface and a dissociation barrier of 0.02 eV indicates a barrier-less process [87]. Methods beyond DFT, such as atomistic theories, have also been implemented to modeling the reactions of hydrogen with Pu [88], which such methods are beyond the scope of this work.

## 1.6 Motivation

Since  $\delta$ -Pu actually exists at room temperature in an alloyed state with a Ga impurity, the Ga impurity is not only present in the bulk but also at the surface. Therefore, a realistic surface model of  $\delta$ -Pu at ambient conditions should include the alloy materials at concentrations consistent with experiment. In this regard, this work will explore the effects of oxygen and hydrogen adsorption on the  $\delta$ -Pu (111) surface when a Ga impurity is present in the surface. This is the first theoretical attempt to elucidate the effects of Ga on atomic oxygen and hydrogen interaction with the  $\delta$ -Pu (111) surface.

This work will include an initial investigation using DFT for the Pu-Ga bulk alloy systems, along with an additional study of hydrogen-vacancy complexes. The Pu-Ga bulk study will provide the theoretical lattice constants, and the location of the Ga atoms when one or more Ga atoms are present within the bulk supercell. In addition, we will explore the magnetic and electronic properties of these systems. Results for the Pu-Ga bulk work are discussed in Chapter 3. Afterwards, two Ga

concentrated surfaces will be modeled from the bulk study, a low and high concentrated Ga surface, which will be used for the adsorption study. The oxygen adsorption results will be discussed in Chapter 4 and the hydrogen adsorption results will be discussed in Chapter 5.

## Chapter 2

### Computational Methodologies

#### 2.1 Density Functional Theory

The fundamental and accurate description of condensed phases of matter at the atomic and molecular scales is based on quantum mechanics. This requires the solution to the many-body Schrodinger or Dirac equation:

$$\hat{H}\Psi = E\Psi \quad (2.1)$$

Here,  $\Psi = \Psi(\mathbf{r}_1, \dots, \mathbf{r}_N)$  is the many body wave function, which contains all the information about the system and depends on  $3N$  electronic spatial variables,  $N$  electronic spin variables, and  $3N_N$  nuclear spatial variables.  $\hat{H}$  is the Hamiltonian operator. The non-relativistic Hamiltonian is given by

$$H = -\sum_{i=1}^N \frac{\hbar^2}{2m} \nabla_i^2 - \sum_{I=1}^{N'} \frac{\hbar^2}{2M_I} \nabla_I^2 - \frac{1}{4\pi\epsilon_0} \sum_{I=1}^{N'} \sum_{i=1}^N \frac{Ze^2}{r_{iI}} + \frac{1}{4\pi\epsilon_0} \sum_{i<j}^n \frac{e^2}{r_{ij}} + \frac{1}{4\pi\epsilon_0} \sum_{I<J}^{N'} \frac{Z_I Z_J e^2}{R_{IJ}}, \quad (2.2)$$

where the first term is the kinetic energy of the electrons, the second term is the kinetic energy of the nuclei, the third term is the electron-nuclei interaction, the fourth term is the electron-electron interaction, and the last term is the nucleus-nucleus interaction. Solving Equation 2.1 with the Hamiltonian in Equation 2.2 to obtain  $\Psi$  is an arduous task. In fact,  $\Psi$  can only be calculated exactly for the

hydrogen atom, which is only a two particle system (one electron system). As we move down the periodic table to heavier elements, Equation 2.1 and 2.2 become troublesome even for the helium atom, which is a two-electron system. In general, the term in Equation 2.2 that becomes the most difficult to compute is the electron-electron interaction, due to the fact that to solve for the individual wave function, it cannot be found without simultaneously considering the individual electron wave function that is associated with the interaction with all other electrons in the system. However, solving for the wave function is only one part of the many-body problem. The other part of the problem is to understand and predict the properties of the system and compute experimentally measurable properties, such as bond dissociation and formation energies, optical properties, etc.

It is obvious that practical solutions to the many-body problem require formalisms, approximations, or assumptions which reduce the complexities of the problem. Density functional theory (DFT) is a ground state theory, many-body formalism, which is *exact* in principle, and allows for the computation of properties of large system sizes with significantly less computational effort. In a nutshell, DFT takes the many-body Hamiltonian and transforms it into a more effective and efficient way to solve for the electronic ground state properties of the system by using the electron density as the key variable. DFT is the *de facto* method for quantum mechanical description and prediction of properties of condensed matter systems.

Why use the electron density? This question can be simply answered by the fact that in reality the wave function cannot be observe directly, thus the probability of  $N$  electrons at a particular set of coordinates,  $\mathbf{r}_1, \dots, \mathbf{r}_N$ , in principle can be measured. Therefore, the probability of finding one electron at  $\mathbf{r}_1$ , another electron at  $\mathbf{r}_2$ , and so on is defined by

$$\Psi^*(\mathbf{r}_i)\Psi(\mathbf{r}_i) = |\Psi(\mathbf{r}_i)|^2, \quad (2.3)$$

and by multiplying this equation by  $e$ , this will essential give use the electron density. If we integrate Equation 2.3, this will yield the number of electrons

$$N = \int |\Psi(\mathbf{r}_i)|^2 d\mathbf{r}_1 d\mathbf{r}_2 \dots d\mathbf{r}_N. \quad (2.4)$$

Thus the probability of an electron at position  $\mathbf{r}_1$  is defined by the electron density and by using the constraint from Equation 2.4, the electron density is defined by

$$\int \rho(\mathbf{r}) d\mathbf{r} = N. \quad (2.5)$$

Before we begin discussing the aspects of DFT relevant to this work, it must be stated that Equation 2.2 may be furthered simplified by using the Born-Oppenheimer Approximation (BOA) [89]. BOA states that the motion of the nuclei

is significantly slower than the electrons that surround it, hence the many-body wave function can be decoupled in the electronic wave function and nuclear wave function and the second term in Equation 2.2, which deals with the kinetic energy of the nuclei, may be approximated to zero. Also, the last term in Equation 2.2, i.e. nucleus-nucleus interaction, is a constant classical term that can be omitted from the Hamiltonian, but must be computed separately and added to the total energy at the end of the calculation (any constant added to an operator only adds to the operator eigenvalues and therefore has no effect on the operator eigenfunctions). In essence, BOA yields the electronic Hamiltonian operator

$$H = -\sum_{i=1}^N \frac{\hbar^2}{2m} \nabla_i^2 - \frac{1}{4\pi\epsilon_0} \sum_{I=1}^{N'} \sum_{i=1}^N \frac{Ze^2}{r_{iI}} + \frac{1}{4\pi\epsilon_0} \sum_{i<j}^N \frac{e^2}{r_{ij}}. \quad (2.6)$$

Equation 2.6 will provide the basis of obtaining the ground state energy of many electron systems.

### 2.1.1 Hohenberg-Kohn Theorems

The earliest form of DFT was based on the Thomas-Fermi model [90]. However, its applications were limited due to the inaccurate representation of the kinetic energy functional and exchange energy, and the exclusion of the electron correlation effects. The formulation of DFT as an *exact* ground state theory of many-body systems began with a seminal work by Hohenberg and Kohn in 1964 [91]. We will state the theorems and corollary here as written from Ref. [92].

**Theorem I:**

For any system of interaction particles in an external potential, the external potential is determined uniquely, except for a constant, by the ground state particle density  $\rho(r)$ .

**Corollary I:**

Since the Hamiltonian is thus fully determined, except for a constant shift of the energy, it follows that the many-body wave functions for all states (ground and excited) are determined. Therefore all properties for the system are completely determined given only the ground state density  $\rho(r)$ .

**Theorem II:**

A universal functional for the energy  $E[\rho]$  in terms of the density  $\rho(r)$  can be defined, valid for any external potential. For any particular external potential, the exact ground state energy of the system is the global minimum value of this functional, and the density  $\rho(r)$  that minimizes the functional is the exact ground state density  $\rho_0(r)$ .

**Corollary II:**

The functional  $E[\rho]$  alone is sufficient to determine the exact ground state energy and density. In general, excited states of the electrons must be determined by other means.

The significance of the Hohenberg-Kohn theorems is that two different systems will never have the same ground state density and that  $\rho(r)$  determines all the

properties of the ground state. Furthermore, we can write a universal energy functional  $E[\rho]$ .

Referring back to Equation 2.6 and considering atomic units, Equation 2.6 may be re-written as

$$H = \sum_{i=1}^N \left(-\frac{1}{2}\nabla_i^2\right) + \sum_{i=1}^N v_{ext}(r_i) + \sum_{i<j}^N \frac{1}{r_{ij}}, \quad (2.7)$$

where  $v_{ext}(r)$  is the external potential of a system of interacting particles and is defined by

$$v_{ext}(r) = Z \sum_{I=1}^{N'} \frac{1}{|r - r_I|}. \quad (2.8)$$

In this form, Equation 2.7 is in atomic units and can be expressed in terms of the electronic density. The third term in Equation 2.7 is known as the Hartree potential. Hohenberg-Kohn reduced the many-body  $3N$  dimensional function of  $\Psi$  to a function with three spatial variables. Thus, the Hamiltonian operator may be re-written as the universal energy functional in terms of the electronic density, which is written as

$$E[\rho] = T[\rho] + V_{ne}[\rho] + V_{ee}[\rho], \quad (2.9)$$

where each term now corresponds to its respective term in Equation 2.7 and  $V_{ee}[\rho]$  may be written as

$$V_{ee}[\rho] = J[\rho] + \text{non-classical term} \quad (2.10)$$

The non-classical term will be discussed later, while  $J[\rho]$  is the classical electronic repulsion term and defined by

$$J[\rho] = \frac{1}{2} \iint \frac{1}{r_{12}} \rho(r_1) \rho(r_2) dr_1 dr_2, \quad (2.11)$$

which is also written in atomic units.  $T[\rho]$  and  $V_{ee}[\rho]$  may be combined to become the Hohenberg-Kohn functional,  $F_{HK}[\rho]$ , which is defined by

$$F_{HK}[\rho] = T[\rho] + V_{ee}[\rho]. \quad (2.12)$$

The beauty of DFT is that it took the many-body Hamiltonian equation as seen in Equation 2.2 and simplified it in terms of electronic density (Equation 2.9), while retaining the integrity of the electronic properties of the system. Although Hohenberg and Kohn proved a way to reduce the  $3N$  dimensional problem we have for solving the full electronic wave function to instead proving the electron density, with only three spatial variables and have the same ground state properties as the full electronic wave function, the theorem never states what exactly this functional is or

how to solve for it. Kohn and Sham will help solve this issue by introducing the single electronic orbitals in a non-interacting system instead of an interacting system. Kohn and Sham will also provide a means to determine the kinetic energy functional  $T[\rho]$  and the non-classical piece of  $V_{ee}[\rho]$ . In another seminal work, Kohn and Sham introduced an auxiliary system which allows for a simpler computation of these terms but at the expense of introducing the so-called exchange-correlation term (this would be elucidated later) [93].

### 2.1.2 Kohn-Sham auxiliary system

Kohn-Sham developed an *ansatz*, which states, “the ground state density of the original interaction system is equal to that of some chosen non-interacting system [92, 93].” Not only is this system non-interacting, but it also retains all the ground state properties, and it is a self-consistent method that involves independent particles that interact through its density. In other words, the non-interacting system has the same  $\rho(r)$  as the interacting system. Kohn-Sham made it possible to solve the many electron problem *exactly* in principle if provided a term, which is difficult to evaluate, known as the exchange-correlation functional is *exactly* known.

The approach of Kohn-Sham begins by viewing the kinetic energy as

$$\langle \Psi | \hat{T} | \Psi \rangle = T_{KS}[\rho] + \Delta T, \quad (2.13)$$

where  $T_{KS}[\rho]$  is the kinetic energy of the non-interacting system and  $\Delta T$  is the difference in the kinetic energy between the many-body kinetic energy and non-interacting kinetic energy. Now  $T_{KS}[\rho]$  is defined by

$$T_{KS}[\rho] = \sum_{i=1}^N \left\langle \phi_i \left| -\frac{1}{2} \nabla^2 \right| \phi_i \right\rangle, \quad (2.14)$$

where each  $\phi_i$  is a single particle orbitals, and  $\rho(r)$  is defined by the following

$$\rho(r) = \sum_{i=1}^{\text{Occupied states}} |\phi_i|^2 = |\psi|^2. \quad (2.15)$$

This means that  $\rho(r)$  is the charge density of all the occupied orbital states in the non-interacting system, which is equivalent to the probability of the wave functions in an interacting system. Equation 2.12 may be re-written with the substitution of Equation 2.13, thus yielding

$$F_{HK}[\rho] = T_{KS}[\rho] + \Delta T + J[\rho] + \text{non-classical term}, \quad (2.16)$$

which may be written as

$$F_{HK}[\rho] = T_{KS}[\rho] + J[\rho] + E_{xc}[\rho], \quad (2.17)$$

where  $E_{xc}[\rho]$  is defined as the exchange-correlation functional and where

$$E_{xc}[\rho] = \Delta T + \text{non-classical term.} \quad (2.18)$$

The terms in the exchange-correlation functional are by far the most difficult and greatest challenge within DFT. In Equation 2.18, it is here that the non-classical term, which is all the quantum mechanical properties of the system, along with the electron correlation, and the difference in energy between an interacting system and a non-interacting system are not well defined *exactly*. Practical DFT involves approximation to the exchange-correlation functionals. Such approximations will be discussed in a later section.

The exchange-correlation functional is essentially two energy terms combined. The exchange energy arises from the anti-symmetry of the wave function under the permutation of the electrons. Due to the Pauli exclusion principle, the exchange energy prevents two electrons from occupying the same one-electron state and it also prevents two electrons of the same spin to be in close proximity to each other. Therefore, this lowers the total electrostatic energy, when there are two electrons anti-parallel to each. The electron exchange energy is defined by

$$E_{ex} = -2J_{ex} \mathbf{S}_i \cdot \mathbf{S}_j, \quad (2.19)$$

where  $\mathbf{S}_i$  and  $\mathbf{S}_j$  are the angular momenta of the electrons and  $J_{ex}$  is the exchange integral. A method known as the Hartree-Fock method provides an exact

description of the electron exchange. The correlation energy is simply the influence that electrons have on each other. In other words, due to the Coulomb repulsion of electrons, electrons will avoid each other and move according. Since the development of DFT, the exchange-correlation functional has eluded theorist to come up with a functional that may describe every chemical system in the universe. Unfortunately not all approximations have been able to do quite so, and in the next section we will discuss just a few of these approximations.

Finally, Kohn-Sham enabled to determine, in principle, an *exact* solution to the ground state density, but does not provide a prescription in obtaining the “right” exchange-correlation functional. Although this was not ideal, Kohn-Sham provided a set of equations in solving for the electronic charge density. These equations are known as the Kohn-Sham equations and this is where  $\varphi_i(r)$  is solved and the kinetic energy is solved partially. The Kohn-Sham equations are

$$\left[-\frac{1}{2}\nabla^2 + v_{eff}(r)\right]\varphi_i = \varepsilon_i\varphi_i, \quad (2.20)$$

$$v_{eff}(r) = v(r) + \int \frac{\rho(r')}{|r-r'|} dr' + \frac{\delta E_{xc}[\rho]}{\delta \rho(r)}, \quad (2.21)$$

$$\rho(r) = \sum_i |\varphi_i(r)|^2. \quad (2.23)$$

Equation 2.20 is the one-electron Hamiltonian and  $\varphi_i$  is the lowest eigenstates, as referred to in Equation 2.15. Equation 2.21 is the Kohn-Sham

effective potential, whereas the  $E_{xc}[\rho]$  will be defined as an approximation, and Equation 2.23 is the electron density of the non-interacting systems. The first term in Equation 2.21 is the potential defined by the interaction between an electron and the atomic nuclei. The second term in Equation 2.21 is the Hartree potential, which describes the Coulomb repulsion between one electron and the total electron density. It is in this term that the self-interaction contribution arises, due to the fact that the one electron that is being considered from the system is also part of the total electron density, so this invokes a Coulomb interaction between the electron and itself. The self-interaction is unphysical and partially is corrected in the third term in Equation 2.21. The third term is a functional derivative of the exchange-correlation contributions to the single electron equation and is usually approximated with approximations such as local density approximation (LDA), generalized gradient approximation (GGA), etc.

Although Kohn-Sham provided a method in solving for the electronic density, an issue arises when trying to solve Kohn-Sham equations. This issue is first you need to define a Hartree potential, but to define the Hartree potential you need to know the electron density. To find the electron density you need to know the single-electron wave functions, which to obtain the single electron wave functions we must solve Kohn-Sham equations. Therefore, Equations 2.20, 2.21, and 2.23 may be combine, with an initial guess to the electron density, to form a method that is known as the DFT self-consistency loop. A flow chart of the DFT self consistency loop is

illustrated in Figure 2.1. In Figure 2.1, we begin with an initial guess of the charge density, from there an effective potential is calculated, which is then used to solve Equation 2.21. From the obtained eigenstates, a new density is calculated. Finally, if the magnitude difference in density between the new density and the initial density is less than the convergence criteria, the total energy and other physical quantities are calculated. Otherwise, it repeats the process with a new initial guess. Usually the initial electronic density is calculated via classically by solving for summation of the atomic densities using Poisson's Equation.

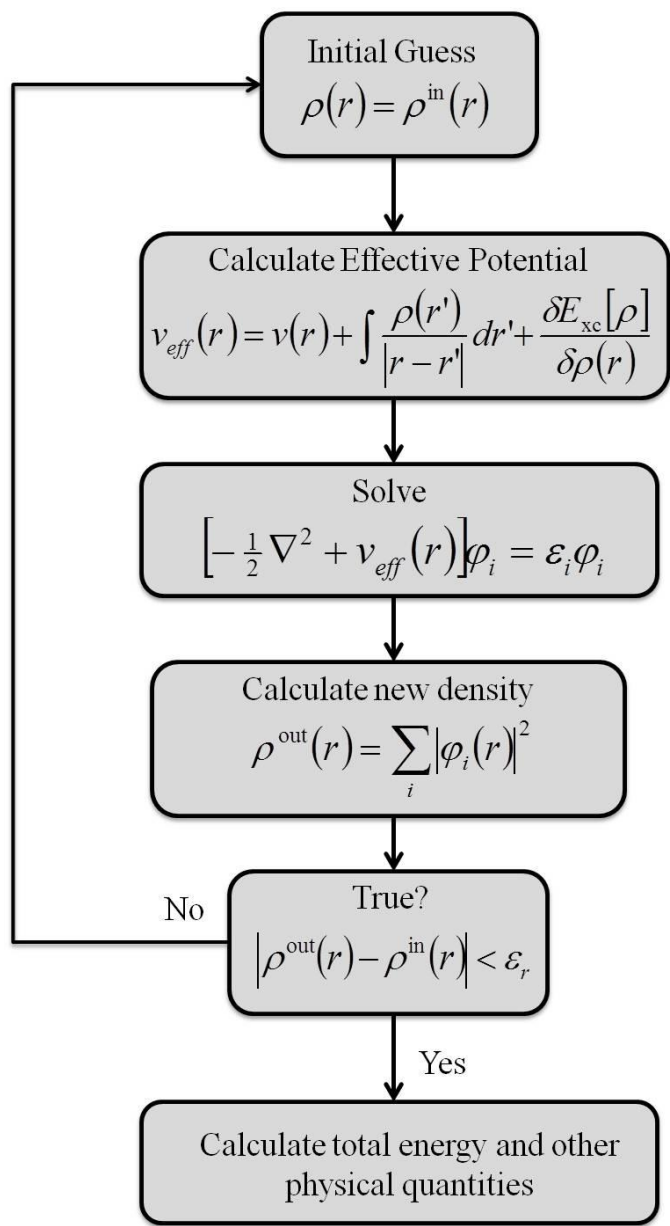


Figure 2.1: DFT self-consistency loop flow chart.

## 2.2 Exchange-Correlation Approximations

### 2.2.1 Local density approximation

The Hohenberg-Kohn theorems and Kohn-Sham equations provided a way to determine the electronic properties of any system in an elegant and computational efficient manner, but the elusive exchange-correlation,  $E_{xc}[\rho]$ , was unknown and therefore must be approximated. In 1965, Kohn and Sham proposed the simplest of approximations for the exchange-correlation, local density approximation (LDA) [93]. LDA assumes a hypothetical uniform electron gas with slowly varying densities. LDA is described by the following equations:

$$E_{xc}^{LDA}[\rho] = \int \rho(r) \varepsilon_{xc}(\rho) dr, \quad (2.24)$$

$$v_{xc}^{LDA}(r) = \frac{\delta E_{xc}^{LDA}}{\delta \rho(r)} = \varepsilon_{xc}(\rho(r)) + \rho(r) \frac{\partial \varepsilon_{xc}}{\partial \rho}, \quad (2.25)$$

$$\left[ -\frac{1}{2} \nabla^2 + v(r) + \int \frac{\rho(r')}{|r-r'|} dr' + v_{xc}^{LDA}(r) \right] \varphi_i = \varepsilon_i \varphi_i, \quad (2.26)$$

where Equation 2.24 is the LDA exchange-correlation energy, Equation 2.25 is the LDA exchange-correlation potential found by taking the partial derivative of Equation 2.24 with respect to the density, and finally, Equation 2.26 is the Kohn-Sham one-electron Hamiltonian equation (similar to Equation 2.20) with LDA. Equation 2.24 describes that the exchange-correlation energy is the integration over all space of the exchange-correlation density and each point is assumed to be the

same in a homogeneous electron gas with the same electron density [92]. Within Equation 2.24, the term  $\varepsilon_{xc}(\rho)$  is simply the addition of the exchange and correlation terms,

$$\varepsilon_{xc}(\rho) = \varepsilon_x(\rho) + \varepsilon_c(\rho). \quad (2.27)$$

Furthermore, the term for the exchange energy is described by the Dirac exchange-energy functional [94]

$$\varepsilon_x(\rho) = -C_x[\rho(r)]^{1/3}, \quad (2.28)$$

where

$$C_x = \frac{3}{4} \left( \frac{3}{\pi} \right)^{1/3}, \quad (2.29)$$

and  $\varepsilon_c(\rho)$  may be found by numerical methods, such as quantum Monte Carlo calculations. Although the equations that make up LDA seem crude, it has been proven to work [95] and is consistently a good model to describe simple elements like sodium.

LDA has been successful, since a uniform electron gas is the only system for which the form of the exchange and correlation energy functionals are known exactly or to very high accuracy, but in any realistic system consisting of atoms or molecules

the electron density is usually characterized by a rapidly varying density. Therefore, some of the fundamental properties of a system, which for a crystal is lattice constant, band gap, etc., may be incorrect and a higher level of approximation may be needed.

### 2.2.2 Generalized gradient approximation

Generalized gradient approximation (GGA) is widely used, since it takes into account the gradient expansion of the exchange hole [96] and is considered to be more accurate than LDA. The exchange-correlation hole may be explained by the fact that due to the exchange-correlation (in essence is to keep the electrons of the same spin as far apart as possible). The exchange-correlation induces a deficiency of the same spin electron surrounding the electron, thus creating a hole. GGA express the exchange-correlation energy as

$$E_{xc}[\rho] = \int \rho(r) \varepsilon_{xc}[\rho(r)] dr + \int F_{xc}[\rho(r), \nabla \rho(r)] dr, \quad (2.30)$$

where the function  $F_{xc}$  is used to satisfy a number of formal conditions for the exchange-correlation hole, which may be calculated in a number of ways. GGA was an improvement over LDA by improvement of binding and atomic energies, and bond length and angles were also improved. In hydrogen bonded systems, GGA improved the energetic, geometries, and dynamical properties. Using GGA provided some improvement for the gap, but it wasn't significant. Finally, GGA did

overestimate the lattice constants for noble metals, such as gold and silver, whereas LDA values were extremely close to experimental, therefore depending on the type of system, consideration of the exchange approximation is extremely important. In this work we used the Pedrew-Burke-Ernzerhof (PBE) [97] formulation of GGA, which improved PW91 [98]. PBE included an accurate description of the linear response of the uniform electron gas, correct behavior under uniform scaling, and a smoother potential.

## 2.3 WIEN2K

### 2.3.1 LAPW + LO method

*WIEN2k* [99] is a highly accurate and efficient all-electron *ab initio* electronic-structure code. It is based on the linearized augmented plane wave (LAPW) method. Consider a system comprised of atoms within a lattice, LAPW partitions the cell into two parts, spheres known as the radius muffin-tin (RMT) around each atom and the interstitial region (Figure 2.2). Inside the spheres or RMT the solutions are rapidly varying and atomic-like near the atoms and outside the spheres, the solutions are smoothly varying and not atomic-like (Figure 2.2). These two regions are connected by plane waves within the interstitial region ( $I$ ) to linear combinations of atomic-like functions in the spheres. These equations are

$$\phi_{\vec{K}}^{\vec{k}}(\vec{r}, E) = \begin{cases} \frac{1}{\sqrt{V}} e^{i(\vec{k}+\vec{K})\cdot\vec{r}} & \vec{r} \in I \quad (2.31) \\ \sum_{l,m} [A_{lm} u_l(r, E_l) + B_{lm} u'_l(r, E_l)] Y_{lm}(\hat{r}) & \vec{r} \in S \quad (2.32) \end{cases}$$

were the vectors  $K$  and  $k$  are the reciprocal lattice vector and vector in first Brillouin zone, respectively,  $V$  is the volume of the unit cell,  $u_l(r, E_l)$  is the solution to the radial Schrödinger equation atom,  $l$  is the angular quantum number,  $m$  is the magnetic quantum number,  $E_l$  is the energy,  $u_l'$  is the energy derivative of  $u_l$ ,  $Y_{lm}$  are solutions to the spherical harmonics, and  $A_{lm}$  and  $B_{lm}$  are determined by the requirement of the basis functions to be continuous and smooth within the sphere boundaries of size  $S$  and depend on the  $k$  and  $K$ . The accuracy of the planewave basis (Equation 2.31) is determined by  $K_{max}$ , where  $K_{max}^2$  is the plane wave kinetic energy cutoff. The RMT also determines how far the planewave is from the nucleus. For instance, if the RMT is large, the planewave is far from the nucleus, but if the RMT is too large the spherical harmonics may not be described accurately within the RMT since it is too far away from the nucleus. RMT is determined by the smallest atomic sphere radius within the unit cell.

For a given RMT, partitioning inside the sphere is determined by an energy cut-off criterion, which is used to determine the separation between the core and valence states. Core electrons do not participate in chemical bonding and are therefore confined within the muffin-tin sphere. In *WEIN2k*, the core states are described as a spin-compensated Dirac equation, thus core states are considered to be fully relativistic. Valence electrons are states that have leaked out of the muffin-tin sphere and do participate in chemical bonding. *WEIN2k* will treat the valence states as scalar relativistic, with the inclusion of spin-orbit coupling may be added to these

states. The implementation of spin-orbit coupling within *WEIN2k* will be discussed later.

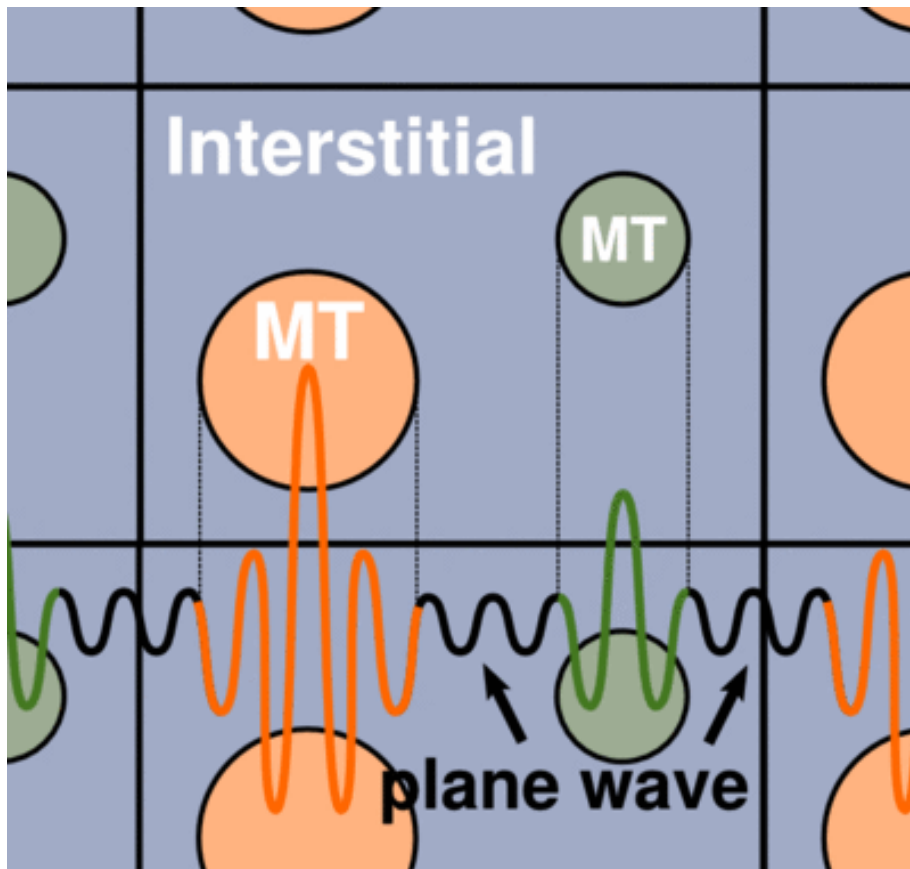


Figure 2.2: Illustration of system divided into two regions, muffin-tin (MT) around atoms and interstitial region. Interstitial regions have planewave solutions, while inside MT solutions are rapidly varying. Image obtained from

Ref. 100.

To ensure orthogonality, linearization, and consistent treatment between the semi-core and valence states, additional basis states, that are independent of reciprocal lattice vector and vector in Brillouin zone,  $K$  and  $k$ , respectively, may be added. This is called “local orbitals (LO).” LO consist of a linear combination of two radial functions at two different energy levels and one energy derivative taken at one of the energy levels. Usually LO are applied to low energy valence states, known as semi-core states. In the case of Pu, semi-core states are defined as the  $6s$  and  $6p$  states. LO is defined as

$$\phi_{LO}^{lm}(\vec{r}) = \begin{cases} 0 & \vec{r} \notin S \quad (2.32) \\ [A_{lm}^{LO} u_l(r, E_{1,l}) + B_{lm}^{LO} \dot{u}_l^\alpha(r, E_{1,l}) + C_{lm}^{LO} u_l(r, E_{2,l})] Y_{lm}(\hat{r}) & \vec{r} \in S \quad (2.33) \end{cases}$$

where  $E_1$  and  $E_2$  are the energy values for the highest energy state (i.e. Pu  $6p$  states) and the lower valence state before core states (i.e. Pu  $6s$  states), a particular  $l$  and  $m$  are defined by the chosen atom species (Equation 2.33) and is zero in the interstitial region (Equation 2.32). The coefficients  $A$ ,  $B$ , and  $C$  in Equation 2.33 are determined by the requirement that the LO are normalized, zero at the sphere boundary of radius  $R$  and have zero slope at  $R$ .

### 2.3.2 APW+lo method

Using LAPW+LO can be computationally expensive due to the large size of the basis set. It has been shown by Sjöstedt *et al.* [101] a more effective way in

ensuring the linearization of the planewaves of the interstitial region value to the slope of the solution inside in the muffin tin sphere. This new method would provide a more resourceful way to linearize Slater's augmented planewave (APW) method. APW is defined by

$$\phi_{\vec{K}}^{\vec{k}}(\vec{r}) = \begin{cases} \frac{1}{\sqrt{V}} e^{i(\vec{k}+\vec{K})\cdot\vec{r}} & \vec{r} \in I \\ A_{lm}^{\vec{k}+\vec{K}} u_l(r', E_{1,l}) Y_{lm}(\hat{r}') & \vec{r} \in S \end{cases} \quad (2.34)$$

which shows in the interstitial region planewave solutions (Equation 2.34) and atomic-like solutions within the sphere, but in comparison to Equation 2.32, the derivative term is missing. Thus, the derivative term in Equation 2.32 provided the linearization between the interstitial region and RMT region, hence LAPW.

Sjöstedt *et al.* [101] introduced a new type of local orbitals (lo), which added in enough variational flexibility in the radial basis functions, since the fixed energies in Equation 2.34 would not give a good description of the eigenfunctions. APW+lo is defined by

$$\phi_{lo}^{lm}(\vec{r}) = \begin{cases} 0 & \vec{r} \notin S \\ [A_{lm}^{lo} u_l(r, E_{1,l}) + B_{lm}^{lo} \dot{u}_l(r', E_{1,l})] Y_{lm}(\hat{r}') & \vec{r} \in S \end{cases} \quad (2.36)$$

where outside the RMT-sphere, solutions are zero, and inside the sphere, solutions are similar to Equation 2.32, but the coefficients  $A$  and  $B$  are determined by the requirement that  $l_0$  is zero at the RMT boundary and normalized. Therefore, both APW and  $l_0$  are continuous at the sphere's boundary, but the first derivative is discontinuous. Using APW+ $l_0$  for a particular electronic state will add  $2l+1$  local orbitals per atom to the basis set. It has been shown by Madesen *et al.* [102] that APW+ $l_0$  and LAPW practically give identical results, but allows to reduce the basis set by 50%, thus reducing the computational expense drastically.

In the end, the importance of both LAPW, LO, APW+ $l_0$  is dependent on the system that is being studied. For instance, for valence atoms that contain  $d$  and  $f$  states, using LAPW would require a higher  $K_{max}$  value than using APW+ $l_0$ , therefore it is more effective to treat the higher valence energy states with APW+ $l_0$ , while treating other lower valence energy states with LAPW. This leads to a mixed LAPW/APW+ $l_0$  basis set, which can be used for different atomic species within the system and different  $l$ -values for the same atom. In addition, a second LO can be added at different energy levels, therefore semi-core and valence states are *accurately* and *simultaneously* described.

### 2.3.3 Spin-orbit coupling in WIEN2k

For heavy fermions, such as Pu, the addition of spin-orbit coupling is extremely important, since the electrons in Pu are strongly correlated and relativistic. Spin-orbit coupling is defined by the interaction of the spin magnetic moment of an

electron with the magnetic field induced by its own orbital motion. In *WIEN2k*, implementation of spin-orbit coupling (SOC) is provided by an *ad hoc/perturbation* means through a second variational scheme and is only calculated inside the atomic spheres and it mixes the up and down spin scalar relativistic eigenstates. Essentially SOC in *WIEN2k* is calculated by solving scalar relativistic wave functions and then expanding the spin-orbit wave functions into a linear combination of the scalar relativistic wave functions by using the lowest  $N$  relativistic eigenfunctions, which is determined by a given energy criteria. This energy criterion includes all eigenstates below a chosen energy cut-off.  $N$  is chosen to be much smaller than the basis size used to solve the scalar relativistic wave functions. In addition, the  $p_{1/2}$  with LO state is added to account for the missing  $p_{1/2}$  radial basis functions in the scalar-relativistic basis (i.e.  $p_{3/2}$  state).

Figure 2.3 shows a flow chart of calculating SOC in *WIEN2k*. For further information on the reduction of the Dirac Equation to mass-velocity and Darwin terms and the implementation of SOC within the APW method, the reader is referred to the articles by Koelling and Harmon [103] and A. H. MacDonald *et al.* [104]. To see the full implementation of DFT and Kohn-Sham equations, via a flow chart, within *WIEN2k* see Appendix A on page 200.

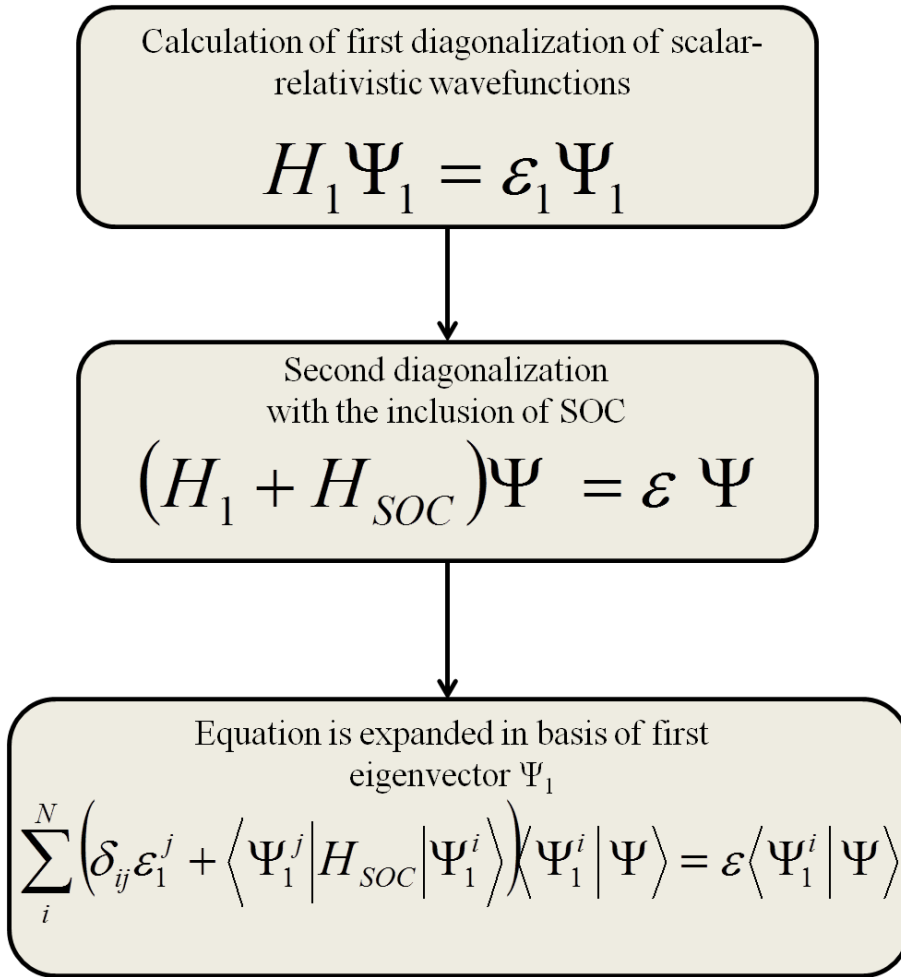


Figure 2.3: Flow chart of the implantation of SOC in *WIEN2k*.

## Chapter 3

### Pu-Ga bulk alloys and H-vacancy<sup>i</sup>

#### 3.1 Computational Details

Computations were based on density functional theory with the PBE exchange-correlation functional [97] to GGA have been performed using the all-electron full-potential linearized augmented-planewave plus local orbital (FP-L/APW+lo) basis method as implemented in the *WIEN2k* code [99]. APW+lo is used to describe all  $s$ ,  $p$ ,  $d$ , and  $f$  states ( $l=0,1,2,3$ ), and the LAPW basis is used for all other higher orders of angular momentum states up to  $l_{wf}^{max} = 10$  in the expansion of the wave functions. Additional local orbitals (LO) were added to the Pu  $6s$  and  $6p$  semi-core states.

The  $\delta$ -Pu  $fcc$  crystal was modeled as a 32 atom ( $2 \times 2 \times 2$   $fcc$  unit cells) supercell, so it may support 3.125, 6.25, and 9.375 at. % Ga concentrations (see Figure 3.1(a) on page 56). This was done by replacing a Pu atom within the  $fcc$  lattice site with a Ga atom, as discussed in Ref. 27, 28, 29, and 30. It should be noted that Söderlind *et al.* [12, 13, 14, 47] has shown a tetragonally distorted structure for  $\delta$ -Pu and Pu-Ga alloys is slightly energetically favorable compared to the cubic  $fcc$  structure. However, our interests are focused on probing the stability and retention of the  $fcc$  structure by the presence of Ga within the cell and hence our use of the cubic structure.

---

<sup>i</sup> This work has been published in *Journal of Physics: Condensed Matter* in 2014.

The *WIEN2k* parameters comprised of a radius muffin tin (RMT) of 1.32 Å for Pu and 1.22 Å for Ga, a planewave kinetic energy cutoff of  $K_{\max}^2 = 165$  eV for the expansion of the wave function in the interstitial region. A k-point mesh of 5x5x5 and a temperature broadening parameter of  $k_B T = 0.068$  eV were chosen. The convergence criterion was set to an energy convergence of  $1.36 \times 10^{-4}$  eV and charge convergence of  $1 \times 10^{-3}$  e<sup>-</sup>. The parameters used for the hydrogen-vacancy (H□) complex were set to keep the ratio of RMT: $K_{\max}^2$  consistent with the previous parameters for the bulk Pu-Ga system and the RMT were elected by considering the nearest neighboring atoms RMTs surrounding the H (Pu and/or Ga), thus yielding an RMT of H at 0.64 Å.

All structures were computed at three magnetic configurations, non-magnetic (NM), ferromagnetic (FM), and anti-ferromagnetic (AFM). To reduce the computational cost, we adopted a two-step optimization scheme for each magnetic system at the scalar relativistic level and then spin-orbit coupling (SOC) was included in a later step. They are as followed:

**Step 1:** The atoms (both Pu and Ga) were kept at their *fcc* positions and the total energy,  $E$ , of the cell was minimized with respect to the cell volume,  $V$ . This, in essence, is a constrained  $E$ - $V$  optimization because the energy minimization was performed by preserving the *fcc* symmetry (and therefore it is not necessarily the lowest energy structure).

**Step 2:** The cell volume of the lowest energy optimized structure in Step 1 was kept fixed and the total energy was further minimized with respect to the atomic positions until the maximum Hellman-Feynman force on each atom was less than  $0.051 \text{ eV/\AA}$ .

**Step 3:** Using the structure in Step 2, a single point total energy calculation was performed with the inclusion of SOC. The use of the scalar relativistic equilibrium geometry for a single point SOC-inclusive total energy is supported by the fact that the equilibrium scalar relativistic and SOC-inclusive geometries are quite similar [105]. We should also mention that currently *WIEN2k* cannot perform a Hellman-Feynman force computation with the inclusion of SOC. SOC interactions were included via a second variational scheme using the scalar relativistic eigenstates as a basis with all eigenstates with energies below  $61.2 \text{ eV}$  included [103]. Here SOC effects were added to Pu only. The atomic H total energy was calculated in a  $15.9 \text{ \AA}$  box and at the  $\Gamma$  point and a bulk Ga orthorhombic crystal cell was also optimized with the same respective parameters described above for both elements; these are required to compute the formation energies.

## 3.2 Results and Discussions

### $\delta$ -Pu with and without Ga impurities

#### 3.2.1 Structural effects due to Ga

A  $\delta$ -Pu 32-atom supercell was used to model concentrations of 3.125, 6.25, and 9.375 at. % Ga and to also ensure that the general trends of previous work from our group are consistent with the present 32-atom supercell, we investigated the basic physical properties of the  $\delta$ -Pu 32-atom supercell without Ga doping. The constrained  $E$ - $V$  optimization calculations with no-spin-orbit-coupling (NSOC), shown in Figure 3.1(b), indicates that the ground state is AFM, with an equilibrium lattice constant of 4.54 Å and bulk modulus of 31.83 GPa (calculated using the Birch-Murnaghan equation of state); this is in agreement with the experimental bulk modulus of 30-35 GPa [106, 107]. The results are also consistent with previous DFT calculations, all of which have predicted an anti-ferromagnetic ground state [9, 10, 11, 12, 13, 14, 15, 16, 20]; this is contrary to experimental results which indicate the absence of magnetic moments in Pu [7]. Our lattice constant is consistent with previous work done recently by Islam and Ray [16], but our bulk modulus is significantly improved in comparison to their work. The discrepancy could be due to a number of factors, such as different muffin tin sphere radii, plane wave cut-off energy, k-point density and the number of data points used to fit the equation of state. The equilibrium calculated lattice parameter was 2.10% less than the experimental value of 4.64 Å [106, 107], the significance in contraction could be potentially due to

the selection of RMT sizes. Previous works done by Söderlind *et al.* [12, 13, 14] have shown that the inclusion of orbital polarization and spin-orbit-coupling, particularly in a non-magnetic configuration, resulted in an equilibrium volume and bulk modulus consistent with experimental data. However, even with the inclusion of orbital polarization the non-magnetic configuration does not give the lowest energy structure; it is still AFM [16]. Also Islam and Ray [16] indicated that the AFM configuration with or without orbital polarization made little difference in the equilibrium lattice parameters. For this reason, orbital polarization was not considered in this work.

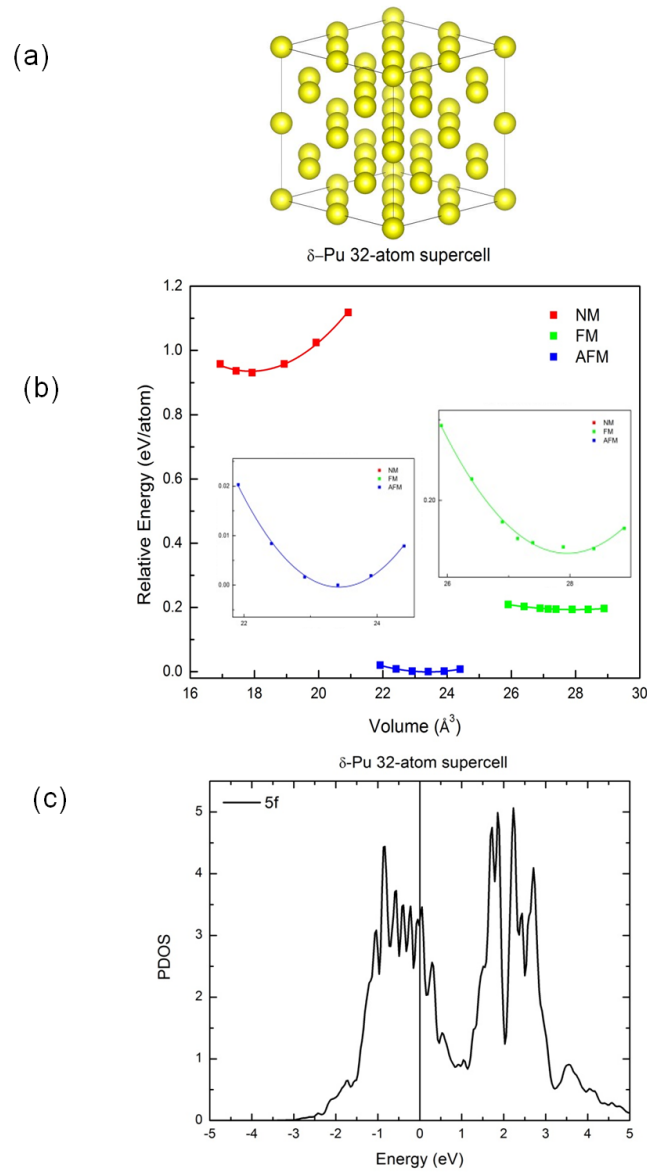


Figure 3.1: (a) The 32-atom supercell for  $\delta$ -Pu *fcc* structure (yellow atoms are Pu atoms). (b)  $E$  vs.  $V$  curves for each magnetic configuration (inserts show expanded  $E$  vs.  $V$  curves for the FM and AFM). (c) The  $5f$  PDOS with SOC for AFM configuration. Image from Ref. 108.

Table 3.1 shows a summary of the equilibrium lattice constant,  $a_o$ , the bulk modulus,  $B$ , and the spin polarization energy,  $E_{sp}$ , for each different magnetic order at the scalar relativistic level of theory. The spin polarization energy,  $E_{sp}$ , is calculated by  $E_{sp} = E_{NM} - E_{FM/AFM}$ , where  $E_X$  is the total energy at the equilibrium volume for magnetic configuration  $X$ . The partial density of states (PDOS) based on the SOC energy eigenvalues are depicted in Figure 3.1(c) for the lowest energy structure (AFM). We observe that the  $5f$  electrons show some localization below the Fermi energy, which does not quite match experimental data for  $\delta$ -Pu [109]. Overall however, it thus appears that the 32-atom supercell is a sufficient model for alloying with Ga, since the overall physical properties of  $\delta$ -Pu are preserved.

Table 3.1: Equilibrium lattice constant ( $a_0$ ), bulk modulus ( $B$ ), and the spin polarization energy ( $E_{sp}$ ) results for NM, FM, and AFM at the NSOC level of theory. In the 6.25% and 9.375% cells, Ga atoms are at nearest neighbor distances from each other. Experimental data was obtained from Ref. 106 and 107.

at. % Ga	Magnetic configuration	$a_0$ (Å)	B (GPa)	$E_{sp}$ (eV)
0	NM	4.150	81.78	-
	FM	4.816	14.78	0.74
	AFM	4.539	31.83	0.93
3.125	NM	4.145	82.40	-
	FM	4.772	14.37	0.70
	AFM	4.523	28.60	0.90
6.25	NM	4.141	79.96	-
	FM	4.745	14.54	0.68
	AFM	4.511	28.58	0.87
9.375	NM	4.137	78.82	-
	FM	4.724	15.65	0.66
	AFM	4.500	29.05	0.84
Expt. $\delta$ -Pu	NM	4.64	30-35	

With the addition of one Ga atom by replacing a Pu atom in the  $\delta$ -Pu 32 atom supercell [Figure 3.2(a)], we observe from the constrained  $E$  vs.  $V$  curves [Fig. 3(a)] that the AFM is the lowest energy structure compared to the NM and FM cases. In Table 3.1, the  $E_{sp}$  for both the FM and AFM decreases slightly for this Ga concentration when compared to the pure  $\delta$ -Pu cell, from 0.74 eV to 0.70 eV for NM to FM and 0.93 eV to 0.90 eV for NM to AFM. We would like to note that we do recognize that due to the substitution of Ga into a Pu site, the system is no longer a true AFM magnetic configuration, since there is no magnetic moment on Ga. Therefore, when Ga is present in the  $\delta$ -Pu cell, AFM is really AFM-like, but for our purposes here we will continue to use AFM. This decrease in spin polarization energy may be explained by the fact that  $E_{sp}$  is proportional to the number of Pu atoms and that the Ga atom makes a negligible contribution to  $E_{sp}$ , hence with the addition of each Ga atom (that is, for each Pu atom that is replaced)  $E_{sp}$  decreases. Table 3.1 also shows that for all magnetic cases that the lattice constant decreases from 0 at. % Ga to 3.125 at. % Ga, along with a slight change in the bulk modulus.

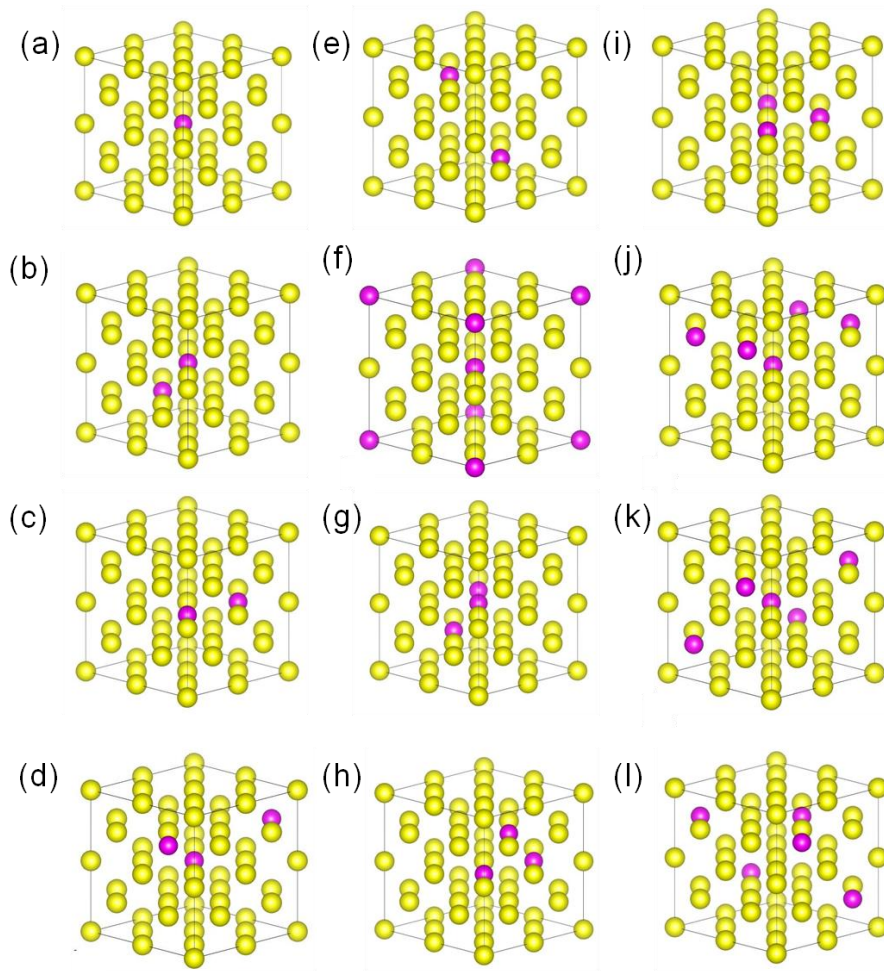


Figure 3.2: All cases studied for the Pu-Ga alloys. Pu atoms are yellow and Ga atoms are purple. 3.125 at. % Ga is shown in (a), while (b-f) are the cases for 6.25 at. % Ga, and (g-l) are the cases for 9.375 at. % Ga. Atoms shared by periodic cells are also shown. Image from Ref. 108.

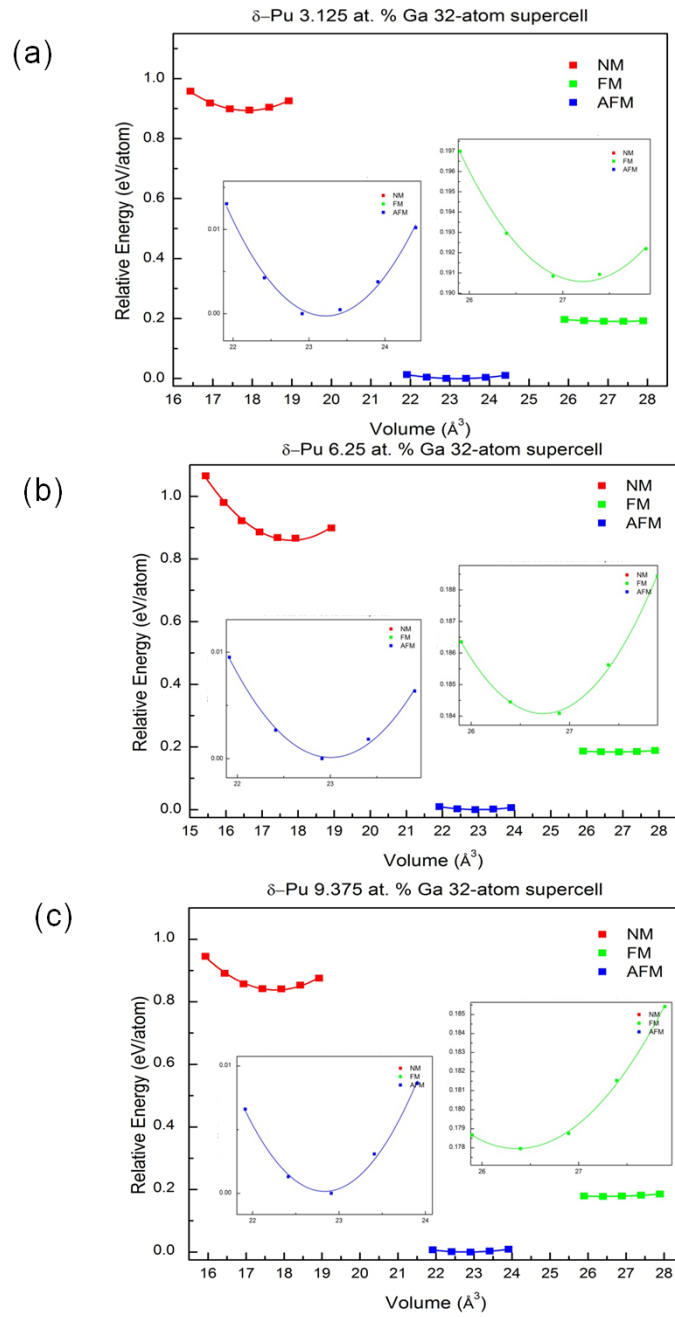


Figure 3.3: Relative  $E$  vs.  $V$  curves for the NM, FM, and AFM ordering for (a) 3.125, (b) 6.25, and (c) 9.375 at. % Ga. Inserts show expanded  $E$  vs.  $V$  curves for the FM and AFM magnetic ordering. Image from Ref. 108.

We now discuss the effects of the total energy minimization of the 3.125 at. % Ga structure with respect to the atomic positions. The minimizations employed the constrained  $E$ - $V$  optimized structure as the starting structure. Table 3.2 outlines the results for the relaxation energy,  $E_r$ , the spin-orbit coupling energy,  $E_{SOC}$ , and the formation energy,  $E_f$ , at both the NSOC and SOC level of theory. The relaxation energy is defined as  $E_r = E_{relax} - E_{unrelax}$ , where  $E_{unrelax}$  is the total energy of the structure prior to the minimization (that is, the constrained  $E$ - $V$  optimized structure) and  $E_{relax}$  is the total energy of the optimized structure. The spin-orbit coupling and formation energies will be discussed later in this paper. The relaxation energy for the 3.125 at. % was -0.14 eV/Ga-atom; therefore, indicating that breakage of the  $fcc$  symmetry is small. Further examination of the bond lengths around the first nearest neighbor (1nn) shell around the Ga provides additional information about the local structure around the Ga atom. Table 3.3 reports the ratio of the average nearest neighbor Pu-Ga bond distance,  $d_{relax}/d_{fcc}$ , where  $d_{relax}$  is the average Pu-Ga bond distance after the atomic position optimization, where  $d_{fcc}$  is the atomic positions of the Pu-Ga bond distance before the optimization (this is the distance in the constrained  $E$ - $V$  optimized structure). Similarly, this has been computed for the average nearest neighbor Pu-Pu bond distances. Also reported in Table 3.3 is the standard deviation,  $\sigma$ . The standard deviation of the bond distances for a given nearest-neighboring shell is a useful measure of the amount of structural disorder in that shell. We observe that in the 3.125 at. % Ga, the Pu atoms tend to contract

inward towards the Ga atom with a Pu-Ga and Pu-Pu average distance ratio of both at 0.978 and the distance between the Pu and Ga/Pu atoms is kept constant in the 1nn shell since the standard deviation is nearly zero. The contractions of the Pu-Ga and Pu-Pu bond length was 0.069 Å. Therefore, the *fcc* symmetry break is due to the misfitting of the Ga atom within the  $\delta$ -Pu cell. It should be noted here that only the AFM configurations were considered because the AFM-FM and AFM-NM energy differences in the constrained optimizations far exceeds the relaxation energies that are obtained.

Table 3.2: Relaxation energy ( $E_r$ ), spin-orbit coupling energy ( $E_{SOC}$ ), and formation energy ( $E_f$ ) calculated for NSOC and SOC level of theory. Results shown are for the lowest energy structure (AFM magnetic configuration) for each Ga concentration. Formation energies in units of kJ/mol are shown in parentheses.

at. % Ga	Case	$E_r$ (eV/Ga-atom)	$E_{SOC}$ (eV/Pu-atom)	$E_{f-NSOC}$ (eV/atom)	$E_{f-SOC}$ (eV/atom)
3.125	1	-0.14	-7.206	-0.028 (-2.71)	-0.029 (-2.81)
6.25	4	-0.11	-7.207	-0.062 (-5.94)	-0.064 (-6.17)
9.375	6	-0.05	-7.206	-0.099 (-9.52)	-0.100 (-9.66)

Table 3.3: The average Pu-Ga and Pu-Pu bond lengths for the 1nn shell around a Ga atom was calculated by dividing the distance in the final relaxed structure by the distance in the perfect *fcc* lattice and averaging.  $\sigma$  is the standard deviation of the bond lengths.

at. % Ga	Case	Bond Type	$d_{\text{relax}}/d_{\text{fcc}}$	$\sigma$
3.125	1	Pu-Ga	0.978	0.000
		Pu-Pu	0.978	0.001
6.25	4	Pu-Ga	0.987	0.010
		Pu-Pu	0.984	0.009
9.375	6	Pu-Ga	0.993	0.012
		Pu-Pu	0.996	0.010

For the 6.25 at. % Ga concentration (2 Ga atoms per 32 atoms), this system now provides an opportunity for different arrangements of the Ga within the 32-atom supercell. We examined 5 arrangements: case 1, where the two Ga atoms are located at 1nn positions relative to each other, case 2, where they are at second nearest neighbor distance apart (2nn), case 3, where they are at third nearest neighbor distance apart (3nn), case 4, where they are at fourth nearest neighbor distance apart (4nn), and case 5, where they are at sixth nearest neighbor distance apart (6nn). These arrangements are shown in Figure 3.2(b-f).

We would like to briefly discuss how the various arrangements were chosen based on the nearest neighbor coordination shells. Within an infinite *fcc* crystal there are of course an infinite number of nearest neighbor shells from a central atom. In our 32-atom supercell however, periodic boundary conditions and finite size effects allows up to five distinct nearest neighbor shells. These are the first, second, third, fourth, and sixth nearest neighbor shells. The fifth nearest neighboring shell is not present in the 32-atom supercell due primarily to symmetry reasons. Specifically within the supercell, only the first nearest neighbor shell is full (with 12 nearest neighbor atoms). For the remaining shells, only a fraction of the full set of nearest neighbors are present: 3 second nearest neighbor atoms (a complete shell has 6 atoms), 12 third nearest neighbor atoms (a complete shell has 24 atoms), 3 fourth nearest neighbor atoms (a complete shell has 12 atoms), 0 fifth nearest neighbor atoms (a complete shell has 24 atoms), and 1 sixth nearest neighbor atom (a complete

shell has 8 atoms). Therefore, due to our 32-atom supercell we were only allowed 5 distinct configurations of the Ga atoms within the cell.

We first begin with the case where the Ga are located at 1nn [Figure 3.2(b)] to each other to determine the lowest energetically magnetic configuration. The constrained  $E$  vs.  $V$  curves in Figure 3.3(b) show that the AFM is the ground state once again. The  $E_{sp}$  is further reduced from the unalloyed  $\delta$ -Pu  $E_{sp}$  and the 3.125 at. % Ga concentration values, because of the addition of a second Ga atom within the cell. Table 3.1 shows a reduction from 0.74 eV to 0.68 eV for the NM to FM and 0.93 eV to 0.87 eV for the NM to AFM case. Further contraction of the lattice constant in the NM, FM, and AFM is observed, and as seen in the 3.125 at. % Ga concentration results there is a small difference in the bulk modulus. For the additional 6.25 at. % cases, the constrained  $E$  vs.  $V$  curves obtained with an AFM arrangement in Figure 3.4 show that case 4 (Ga at 4nn apart) is the lowest energy structures for the 6.25 at. % Ga concentration. Using the case 4 structure, further minimization of the energy with respect to the atomic positions yielded a relaxation energy of -0.11 eV/Ga-atom (Table 3.2), which is a slight decrease from the relaxation energy of 3.125 at. %. Table 3.3 shows that the average ratio of Pu-Ga and Pu-Pu bond distances is 0.987 and 0.984, respectively, and the standard deviation shows that the Pu-Ga and Pu-Pu bond distances are not constant with 0.010 and 0.009, respectively. Therefore, although the *fcc* structure is better retained than the

3.125 at. % structure, a slight short range disorder is seen around the Ga atom. This effect will be more evident in the 9.375 at. % Ga concentration.

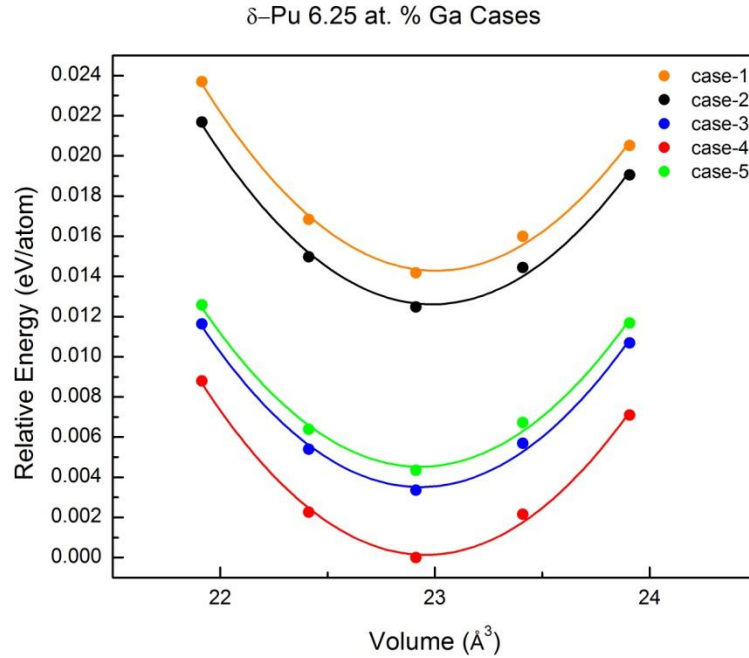


Figure 3.4:  $E$  vs.  $V$  curves for the 6.25 at. % Ga concentration for different Ga cases. Image from Ref. 108.

We also further minimized the energy with respect to the atomic positions for the case where the Ga atoms are 6nn distance apart (case 5; this is the maximum Ga-Ga separation within the supercell). We observed that the average ratio of the Pu-Ga and Pu-Pu bond distances are both coincidentally 0.977, which is slightly lower than the 3.125 at. % Ga case. Therefore, this indicates that at this point the Ga atoms are no longer or weakly interacting with each other. Thus locally, each Ga atom has an

environment similar to the 3.125 at. % Ga concentration case. In other words, the range within which the Ga atoms begin to behave independently is of the order of the 6nn distance ( $\sim 8 \text{ \AA}$ ). Therefore the *fcc* structural distortion is pronounced at 3.125 at. % Ga and the 6nn case for 6.25 at. % Ga. The latter is somewhat contrary to experimental results that the stability of the *fcc* structure should increase with increasing Ga concentrations [20-22]. We thus infer that the Ga atom separations also plays an important role in the preservation of the *fcc* symmetry. For this reason, the cases considered in the 9.375 at. % Ga concentration did not include any 6nn distances.

For the 9.375 at. % Ga concentration (3 Ga atoms per 32 atoms), there are a total of six cases in this system. All the different cases are graphically depicted in Figure 3.2(g-l). To determine the lowest magnetic structure, only the case where the Ga are at 1nn was considered [Figure 3.2(g)]. Figure 3.3(c) indicates that the AFM is the lowest energy structure, which was seen for all previous concentrations. The spin-polarization energy decreases further than the 6.25 at. % Ga concentration with an energy of 0.84 eV. The lattice constant contracts further than the 6.25 at. % for all magnetic orders, with a value of 4.500  $\text{\AA}$  for the AFM case and the bulk modulus shows little difference from the previous Ga concentrations. Figure 3.5 shows that when considering the different arrangements of Ga within the 32-atom supercell with an AFM arrangement, that case 6, where the Ga atoms are located at 4nn distance apart, is significantly lower in energy than all other cases. Therefore, when

considering the supercells with more than one Ga atom, namely the 6.25 and 9.375 at. % Ga structures, our current results show that Ga prefers to be within the 4nn distance from each other and not cluster together within the *fcc*  $\delta$ -Pu structure. A summary of lattice constant and bulk modulus is shown for the most stable structures in Table 3.4, which demonstrates that the lattice constant for each Pu-Ga system shows a small contraction with respect to that of the unalloyed  $\delta$ -Pu cell. Again, the bulk modulus exhibits no well-defined trend, even among the most stable structures. This is at odds with the results by Söderlind *et al.* [27], where a linear behavior in the bulk modulus was predicted. Further investigations on the pressure derivative of the bulk modulus, elastic constants, and shear modulus for varying Ga concentrations will provide more insights into the elastic properties. However, this is outside the scope of the present work. Figure 3.6 also shows the most stable AFM cases in comparison to the NM, FM, and experimental results [18] for lattice constant versus Ga concentration. We reiterate here that each magnetic order shows a decrease in lattice constant with increasing Ga concentration, which is consistent with experimental results. Söderlind *et al.* [27] showed that by using DFT-exact-muffin-tin orbitals method that the volumes were 2% greater than experimental volumes with increasing Ga concentrations, but still showed the decreasing trend observed experimentally. On the other hand our present work shows that our lowest energy structures (AFM arrangement and Ga located at 4nn for the 6.25 and 9.375 at. % Ga) display a contraction of the lattice constant for all Ga concentrations from the

experimental lattice constant (~1%-2%), therefore a contraction in volume. The discrepancy between the observed lattice contraction in this work and the expansion in the work by Söderlind *et al.*[27] is due to employed computational methodology; overall the trends are consistent with each other.

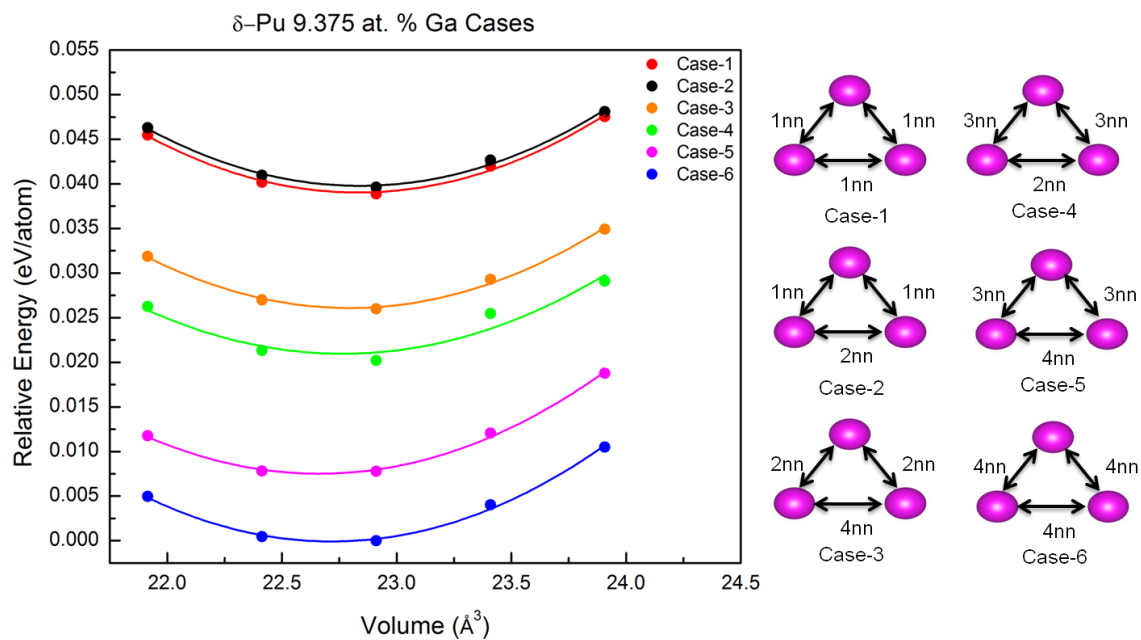


Figure 3.5:  $E$  vs.  $V$  curves for the 9.375 at. % Ga concentration for all Ga cases. Side panel illustrates 9.375 at. % Ga concentration cases of the different distances of the Ga atoms within the 32-atom supercell. Image from Ref. 108.

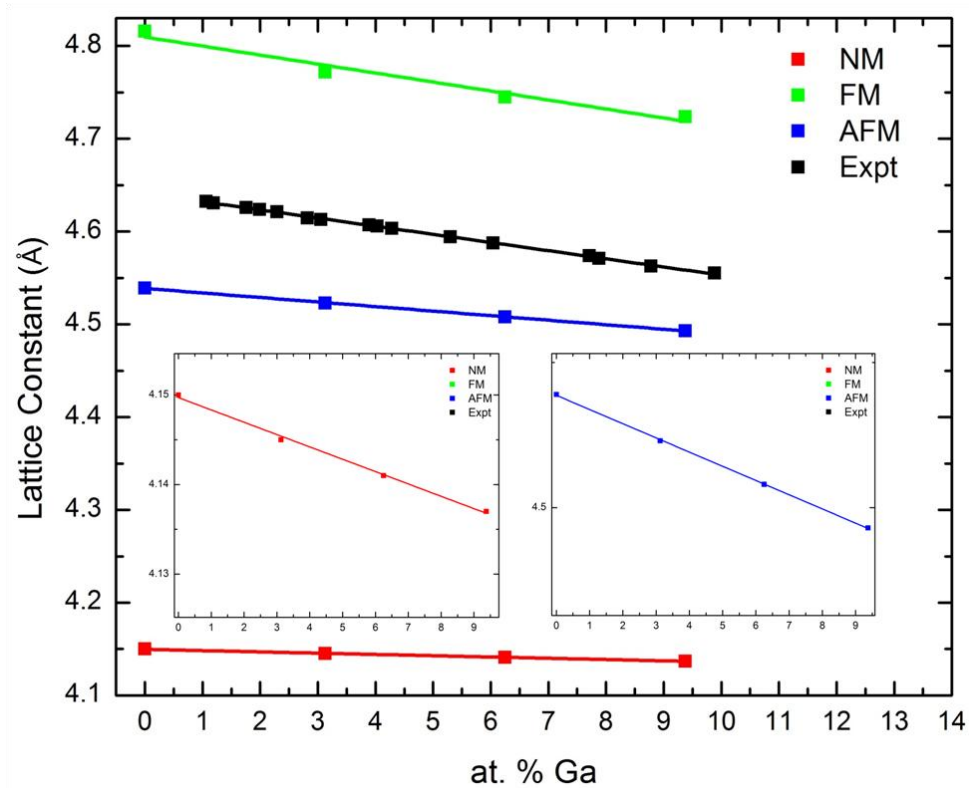


Figure 3.6: Lattice constant vs. Ga concentration for the NM, FM, and AFM at the NSOC level of theory. AFM data that was plotted includes the lattice constants for the lowest energy structures for all Ga concentrations and cases. The inserts are expanded NM and AFM graphs. Experimental data obtained from Ref. 27. Image from Ref. 108.

Table 3.4: Equilibrium lattice constants ( $a_0$ ) and bulk moduli ( $B$ ) for the NSOC AFM calculations for different Ga cases (see text). Experimental data was obtained from Ref. 106 and 107.

at. % Ga	Case	$a_0$ (Å)	B (GPa)
0	1	4.539	31.83
3.125	1	4.523	28.60
6.25	1	4.511	28.58
	2	4.510	28.58
	3	4.506	28.86
	4	4.508	29.14
	5	4.506	28.72
9.375	1	4.500	29.05
	2	4.500	28.92
	3	4.497	28.60
	4	4.488	36.24
	5	4.489	30.16
	6	4.493	30.69
Expt. $\delta$ -Pu	NM	4.64	30-35

The case 6 structure for the 9.375 at. % Ga energy was further minimized with respect to the atomic positions, which yielded a relaxation energy of -0.05 eV/Ga-atom (Table 3.2). This is a notable decrease from the relaxation energy of 3.125 and 6.25 at. % Ga. Table 3.3 shows that the average ratio of Pu-Ga and Pu-Pu bond distances is 0.993 and 0.996, respectively, and  $\sigma$  shows that the Pu-Ga and Pu-Pu bond distances are not constant with 0.012 and 0.010, respectively. Therefore in the 9.375 at. % Ga, the *fcc* crystal is practically stable but again the  $\sigma$  shows that the distances between the Pu and Ga atoms is not moving inward at a constant rate, thus indicating short range disorder. Recent extended x-ray absorption fine-structure

technique data observed Ga-induced distortions in the second coordination sphere around the Ga impurity in  $\delta$ -Pu [36]. These observations for all concentrations can be explained as follows: in the 3.125 at. % Ga there is only one Ga atom present, therefore the Pu atoms symmetrically contract toward the Ga atom; in the 6.25 at. % and 9.375 at. % structures there are competing effects between the local Pu interactions around the Ga atoms, and hence the Pu contractions are somewhat limited, and the symmetry is broken. We must also mention that the second, third, and fourth Pu-Ga and Pu-Pu nearest neighboring distances remain unchanged in all concentrations in comparison to the optimized cell with *fcc* symmetry. These observations are in agreement with Robert et al.'s DFT study [38], which also indicated a short range disorder with increasing Ga concentrations. The spin-orbit coupling energy is calculated by  $E_{SOC} = E_{relax-SOC} - E_{relax-NSOC}$ , where  $E_{relax-NSOC}$  is the total energy of the scalar relativistic optimized structure and  $E_{relax-SOC}$  is the single point SOC total energy computed using the scalar relativistic structure. For all Ga concentrations,  $E_{SOC}$  is constant with a value of around -7.21 eV/Pu-atom (Table 3.2). Also,  $E_{SOC}$  for unalloyed  $\delta$ -Pu was -7.205 eV/Pu-atom. This implies while SOC interactions definitely lower the total energy, the relative effects are the same in each system.

### 3.2.2 Electronic properties of $\delta$ -Pu with Ga impurities

The formation energy of the Pu-Ga alloys,  $E_f$ , was calculated by  $E_f = E_{Pu-Ga} - (m/32)*E_{Pu-bulk} - (n/8)*E_{Ga-bulk}$ , where  $E_{Pu-Ga}$  is the total energy for the Pu-Ga system,  $E_{Pu-bulk}$  is the total energy for the 32-atom *fcc* supercell  $\delta$ -Pu bulk,  $E_{Ga-bulk}$  is the total energy for the orthorhombic eight atom Ga bulk, and  $m$  and  $n$  are the number of Pu and Ga atoms within the Pu-Ga system, respectively. The computed formation energies for the most stable structures are reported in columns five and six of Table 3.2. The formation energy is negative implying an exothermic reaction, which agrees with Sadigh and Wolfer results [37]. The formation energy magnitude increases with increasing Ga concentration, implying that with the addition of more Ga atoms within the *fcc*  $\delta$ -phase, the stability of the *fcc* lattice increases. This is in agreement with the preservation of the *fcc* lattice structure discussed above for the 9.375 at. % Ga case. The formation energy slightly decreases from the NSOC to SOC calculations, and when comparing the formation energy difference between the SOC 3.125 and 6.25 at. % Ga we get -0.035eV/atom or -3.36kJ/mol, which agrees well with Sadigh's and Wolfer's values for their energy difference (-3.37kJ/mol) [37]. A couple of distinctions between this work and that of Sadigh and Wolfer [37] are: First, our calculations include SOC; Sadigh's and Wolfer's calculations do not include SOC. Second, we used a single supercell with increasing Ga concentrations; Sadigh and Wolfer used a single Ga atom in varying supercell sizes to yield the desired concentration (e.g. 1 Ga per 32 Pu atom supercell for 3.125 at. % Ga and 1

Ga per 16 Pu atom supercell for 6.25 at. % Ga). Due to the constant supercell size for all Ga concentrations we believe that our work provides keen details into the interactions between the Ga atoms and structural stability of the *fcc* crystal.

Depicted in Figure 3.7 is the partial density of states (PDOS) for each Pu-Ga system with the inclusion of SOC. The PDOS was calculated for a Ga atom and a first and fourth nearest neighboring Pu atom from the Ga atom, so we may be able to probe the effect of Ga on a Pu atom. In the 3.125 at. % Ga PDOS, we see that the Ga atom has little effect on the first nearest neighbor Pu atoms (1nn) because the Pu *5f*, *7s*, and *6d* states show a small perturbation relative to the corresponding states in the fourth nearest neighbor Pu atoms (4nn). In the case for the 6.25 at. % Ga concentration, we see a small decrease in the density of the *7s*, *6d*, and *5f* states in comparison to the Pu atom located at the 4nn distance from the Ga atom. This decrease in the density of the *7s* and *6d* states becomes even more prominent for the 9.375 at. % Ga concentration. At this concentration there is no change in the *5f* PDOS and also at approximately 1.7 eV below the Fermi energy, slight hybridization is seen between the Pu *6d* and Ga *4p* electrons. This is clearly seen in Figure 3.8, which shows that the Pu *6d* and Ga *4p* PDOS does not hybridize at the 3.125 at. % Ga concentration, but slowly increases to hybridizing at 9.375 at. % Ga concentration. Therefore, the Pu atom tends to have a slight *d* bonding with the Ga *4p* electrons. The Pu *7s* shows little change in the 3.125 at. % Ga concentration between the Pu atom at first and fourth distance from the Ga but delocalizes at the

higher concentrations. Overall, the preservation of the *fcc* lattice which occurs with increasing Ga concentration manifests in the electronic spectrum in the form of *6d* (and *7s*) electron state delocalization. This implies that there is sufficient overlap between the Ga and the neighboring Pu electronic states, leading to a more stable structure.

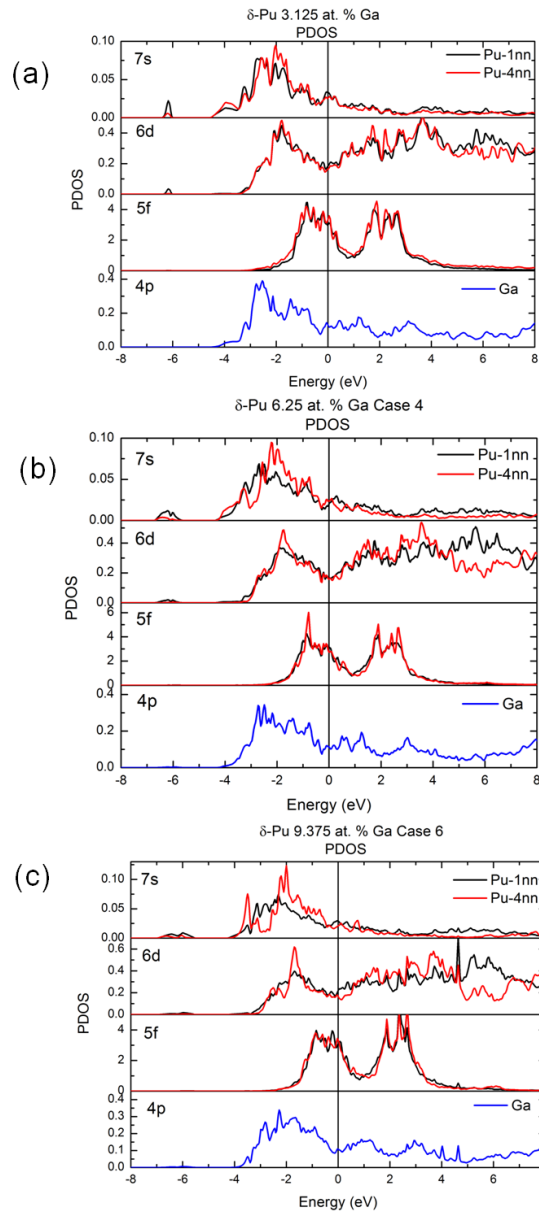


Figure 3.7: PDOS for the SOC calculation of the lowest energy structure for (a) 3.125, (b) 6.25, and (c) 9.375 at. % Ga concentration for a Pu atom located at 1nn and 4nn from the Ga atom within the cell. Image from Ref. 108.

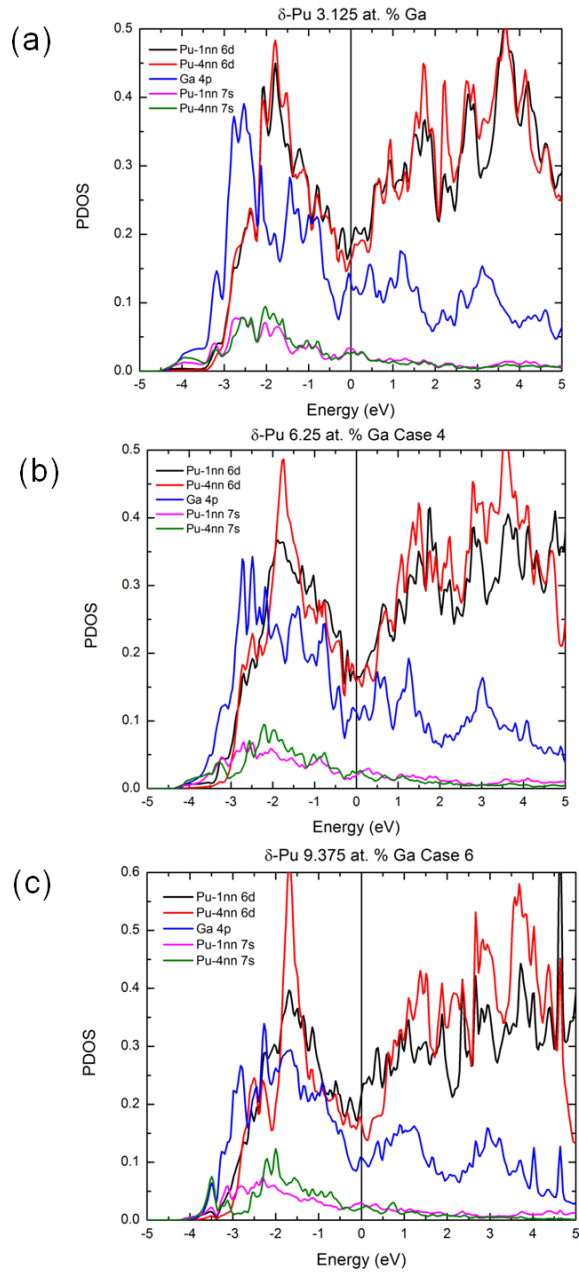


Figure 3.8: PDOS of Pu  $7s6d$  and Ga  $4p$  for the SOC relax lowest energy structure for (a) 3.125, (b) 6.25, and (c) 9.375 at. % Ga concentration. Pu atoms were located at 1nn and 4nn from the Ga atom. Image from Ref. 108.

To further probe the nature of the Pu-Ga interactions, a three-dimensional charge density difference was calculated by using  $\Delta n(r) = n(\text{Pu-Ga}) - n(\text{Pu}) - n(\text{Ga})$ , where  $n(\text{Pu-Ga})$  is the total electron charge density of the entire Pu-Ga system,  $n(\text{Pu})$  is the total charge density of the Pu atoms, and  $n(\text{Ga})$  is the total charge density of the Ga atoms. In computing  $n(\text{Pu})$  and  $n(\text{Ga})$ , the Pu and Ga atoms are kept in the exact same position as the Pu-Ga system. For more information on this computation, see Appendix B on page 202. Figure 3.9<sup>ii</sup> shows a three-dimensional charge density difference for the lowest energy structure for each Pu-Ga system; the visualization software was VESTA [110]. Each plot consists of a Ga atom surrounded by the first nearest neighbor Pu atoms. From these plots, we noticed that while the interaction seems to increase with increasing Ga concentration, the overall interaction in each system is quite small; this is in agreement with the PDOS plots. What is interesting from Figure 3.9 is the hybridization between the  $s$  and  $p$  orbitals in the Ga atom. To confirm the Ga  $sp$  hybridizations, the partial charges of each Ga atom in the Pu-Ga system are compared to those in the isolated Ga atom and the partial charges of the Pu atoms in the Pu-Ga system to that of the corresponding atoms in a Pu-only system (that is, Pu-Ga without the Ga atoms). The partial charges were computed inside the muffin tin sphere of each atom per angular momentum channel; the interstitial charge contribution is not included and hence the term “partial charge.” The interstitial charges are difficult to partition into exact atomic contributions. In Table 3.5, the

---

<sup>ii</sup> This figure was chosen as front cover figure for *Journal of Physics: Condensed Matter* June 11, 2014 printed issue. <http://ej.iop.org/pdf/jpcm/covers/2014/cm2623-webcover.pdf>

partial charges for the Ga atom and Pu atoms (1nn Pu atoms only) are reported. For each concentration there are little or no changes in the Pu partial charges. For each Pu-Ga system however, there is a decrease in the Ga  $4s$  charge relative to the isolated case, while there is an increase in the Ga  $4p$  partial charge relative to the isolated case; this is a signature of the Ga  $4s4p$  hybridization. The origin of the hybridization is attributed to the induced polarization of the Ga orbitals by the strong electric field of the Pu atoms. Therefore, the blue sphere surrounding the Ga atom in Figure 3.9 is the  $s$ -orbital, which is losing charge to the  $p$ -orbitals (red lobe-like shape around the Ga atom).

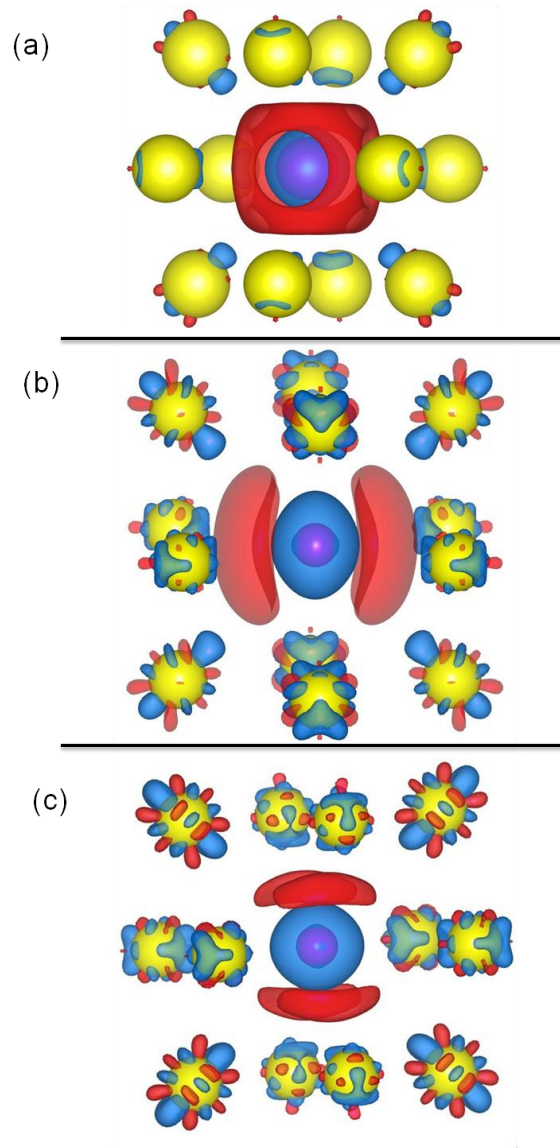


Figure 3.9: Three-dimensional  $\Delta n(r)$  for Pu (yellow) in 1nn shell around Ga (purple) atom for (a) 3.125, (b) 6.25, and (c) 9.375 at. % Ga concentrations. Red are regions of charge accumulation, while blue indicates regions of charge depletion. (a), (b), and (c) are shown with an isosurface level of 0.0270, 0.0270, and 0.0324 e-/cubic Å, respectively. Image from Ref. 108.

Table 3.5: Partial charges of a Pu and Ga atom at first nearest neighboring distance from each other for each Ga concentration.  $\Delta$ -Pu is the difference between the partial charge for the Pu atom in the Pu-Ga cell and in the Pu-only cell, and  $\Delta$ -Ga is the difference between the partial charge for the Ga atom in the Pu-Ga cell and the isolated Ga.

at. % Ga			s	p	d	f
3.125	Pu-Ga cell	Pu	2.119	5.334	0.764	4.864
		Ga	0.877	0.734	9.912	0.009
	Pu-only cell		2.121	5.325	0.753	4.878
		isolated Ga		1.093	0.251	9.884
	$\Delta$ -Pu		-0.002	0.009	0.011	-0.014
	$\Delta$ -Ga		-0.216	0.482	0.028	0.009
6.25	Pu-Ga cell	Pu	2.120	5.336	0.779	4.845
		Ga	0.877	0.725	9.910	0.009
	Pu-only cell		2.122	5.327	0.771	4.856
		isolated Ga		1.097	0.237	9.885
	$\Delta$ -Pu		-0.002	0.009	0.009	-0.011
	$\Delta$ -Ga		-0.219	0.488	0.025	0.009
9.375	Pu-Ga cell	Pu	2.121	5.337	0.780	4.840
		Ga	0.876	0.724	9.908	0.008
	Pu-only cell		2.122	5.328	0.774	4.850
		isolated Ga		1.098	0.231	9.885
	$\Delta$ -Pu		-0.001	0.009	0.006	-0.009
	$\Delta$ -Ga		-0.222	0.493	0.023	0.008

### 3.3 Hydrogen-vacancy complex within a $\delta$ -Pu 3.125 at. % Ga

For the remainder of this article, the symbol “ $\square$ ” will be used to denote a Pu-Ga vacancy complex and the symbol “H $\square$ ” will be used to denote a complex consisting of a hydrogen atom associated with a Pu-Ga vacancy. Starting with the optimized 3.125 at. % Ga AFM structure, a Pu atom was removed to create a vacancy in a *quasi* first nearest neighbor (1nn), second nearest neighbor (2nn), and fourth nearest neighbor (4nn) shells from the Ga atom. The term “quasi” is used since the *fcc* symmetry has been broken in the structure, but the vacancy was placed at a position that closely resembles the atomic position in the constrained optimized structure. The next step was to perform a total energy minimization with respect to atomic positions in the  $\square$  complexes. After the energy minimization, a hydrogen atom is placed inside the vacancy in each  $\square$  complex and the energy is minimized again to yield the optimized H $\square$  complex (Figure 3.10). From the relaxation energies of the vacancy complex, reported in Table 3.6, we observe that the structure becomes more stable when the vacancy was located at either the 2nn or 4nn shell from the Ga atom. However, the largest relaxation energy of -0.13 eV indicates that the movements of the Pu atoms are quite small. When calculating the standard deviation of the bond lengths between the Pu-Ga, we see that when the vacancy is at the quasi 1nn, 2nn, and 4nn positions, we get 0.0, 0.005, and 0.006, respectively. Therefore, when the vacancy is greater than 1nn distance from the Ga, the Pu atoms show more movement towards the Ga atom and a slight short range disordering is observed. The

vacancy formation energy was calculated by  $E_f = E_{\square} - (m/32)*E_{Pu-bulk} - (n/8)*E_{Ga-bulk}$ , where  $E_{\square}$  is the total energy of the Pu-Ga system plus vacancy,  $E_{Pu-bulk}$  is the total energy of the 32-atom supercell for  $\delta$ -Pu,  $E_{Ga-bulk}$  is the total energy of the orthorhombic structure for Ga, m, and n are the number of Pu and Ga atoms in the Pu-Ga cell, respectively. According to Table 3.6,  $E_f$  is  $>0$  at the scalar relativistic (NSOC) and spin-orbit inclusive (SOC) levels for the  $\square$  complexes, implying that vacancy formation in the vicinity of the Ga atom is endothermic in nature and unstable.

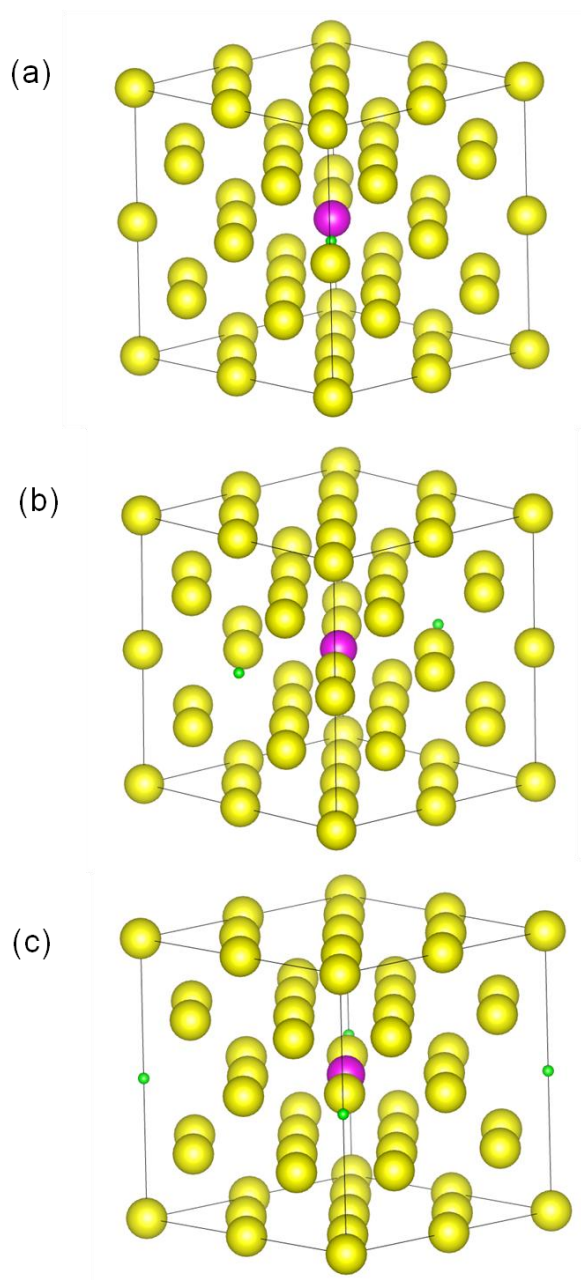


Figure 3.10:  $H_{\square}$  at  $1nn$  (a),  $2nn$  (b), and  $4nn$  (c) from Ga atom. Hydrogen atom is green and periodic images are shown.

Table 3.6: NSOC and SOC relaxation ( $E_r$ ) and formation energies ( $E_f$ ) for a vacancy ( $\square$ ) and hydrogen-vacancy complex ( $H\square$ ) when located at a quasi 1nn, 2nn, and 4nn position with respect to the Ga atom.

Location from Ga atom	<i>NSOC</i>				<i>SOC</i>	
	$E_r(\square)$ (eV)	$E_r(H\square)$ (eV)	$E_f(\square)$ (eV)	$E_f(H\square)$ (eV)	$E_r(\square)$ (eV)	$E_r(H\square)$ (eV)
quasi-1nn	-0.02	-0.74	0.76	-3.82	0.92	-3.88
quasi-2nn	-0.13	-0.02	1.05	-3.21	1.12	-3.17
quasi-4nn	-0.13	-0.02	0.76	-3.33	0.89	-3.27

We now discuss the results for the optimized H $\square$  complexes. Table 3.6 indicates that the relaxation energy at the NSOC level is minimal when the H $\square$  complex is either at the 2nn or 4nn position from the Ga, and the lowest energy structure corresponds to the 1nn H $\square$  complex. The standard deviation of the bond lengths between the Pu-Ga in the 1nn shell was 0.006, therefore there was slightly more short-range disorder. The formation energy for the H $\square$  complex was calculated by  $E_f = E_{H\square} - E_{\square} - E_{H-atom}$ , where  $E_{H\square}$  is the total energy for the Pu-Ga with H $\square$  complex,  $E_{\square}$  is the total energy for the Pu-Ga with vacancy, and  $E_{H-atom}$  is the total energy of the H atom. The formation energies are all negative for the NSOC and SOC. This transition from a positive value with a vacancy within the cell to a negative value with hydrogen in the vacancy has been discussed in Schwartz *et. al* [74] recent work, where the DFT calculations indicate that with the addition of hydrogen inside a vacancy, the system becomes more exothermic and could possibly drive super-abundant vacancy formation. We observe a significant energetic change from a mono-vacancy to a hydrogen-vacancy complex as seen in Table 3.6. In the H $\square$  complex, the most preferred site is when it is located at a 1nn distance to the Ga, with formation energies of -3.88eV, compared to -3.17eV and -3.27eV for the 2nn and 4nn, respectively. This larger formation energy could be due to the considerable relaxation energy. We note that after the geometry optimization, the H atom relaxes toward the nearest neighbor Pu atom and the equilibrium Pu-H bond distance is 2.22 Å, while the equilibrium Ga-H bond distance is 4.35 Å. Shown in Figure 3.11(a) is

that before optimization H was equidistant from Pu and Ga at a distance of 3.2 Å. The other nearest neighbor Pu atoms were at an average distance of 2.56 Å from H. This significant relaxation also induced another vacancy between the H□ complex and Ga atom, since the difference in distance between the final and initial distance of the H□ and the Ga is 1.15 Å.

Figure 3.11 illustrates the charge density difference of the optimized H□ complex when located at a starting position of a quasi-1nn distance to the Ga atom. The goal here is to probe the local charge density redistribution induced by the presence of the hydrogen vacancy. The difference charge density was computed using  $\Delta n(r) = n(\text{Pu-Ga} + \text{H}\square) - n(\text{Pu-Ga}) - n(\text{H})$ , where  $n(\text{Pu-Ga} + \text{H}\square)$  is the charge density of the Pu-Ga system with H□ complex,  $n(\text{Pu-Ga})$  is the charge density of the Pu-Ga with vacancy, and  $n(\text{H})$  is the charge density of the H atom. The figure indicates that the H atom *s*-orbital (red sphere) is interacting with the nearest neighboring Pu atom (accumulating charge from the Pu atom), where  $f_z^3$  characteristic orbitals are observed. Therefore the charge density difference plots indicates a strong Pu-H interaction, which is in good agreement with the strong binding energy of H in the Pu-Ga matrix (-3.88 eV). Shown in Table 3.7, the partial charges show an increase in the H *1s* charge when the H atom is located within the Pu-Ga cell from the isolated H case; therefore, validating the results seen for the charge density difference plot.

The PDOS are plotted for the nearest neighbor (1nn) Pu atom to the H atom within this final optimized structure with SOC in Figure 3.12. For comparison, in Figure 3.12 the PDOS for the Pu atom when only a vacancy is located at 1nn to the Ga atom is also plotted. We clearly see that for the Pu atom at 1nn from the H atom the *5f* electrons exhibit a decrease in intensity when compared to the *5f* electrons for a Pu atom with only a vacancy. This is expected since the missing Pu atom in the vacancy structure implies the availability of *5f* electrons from the neighboring Pu. On the other hand, the presence of hydrogen implies Pu-H interactions and hence reduced Pu *5f* electron states intensity; the Pu-H interactions comprise weak hybridization between the H *1s* and the Pu *5f6d7s* electrons.

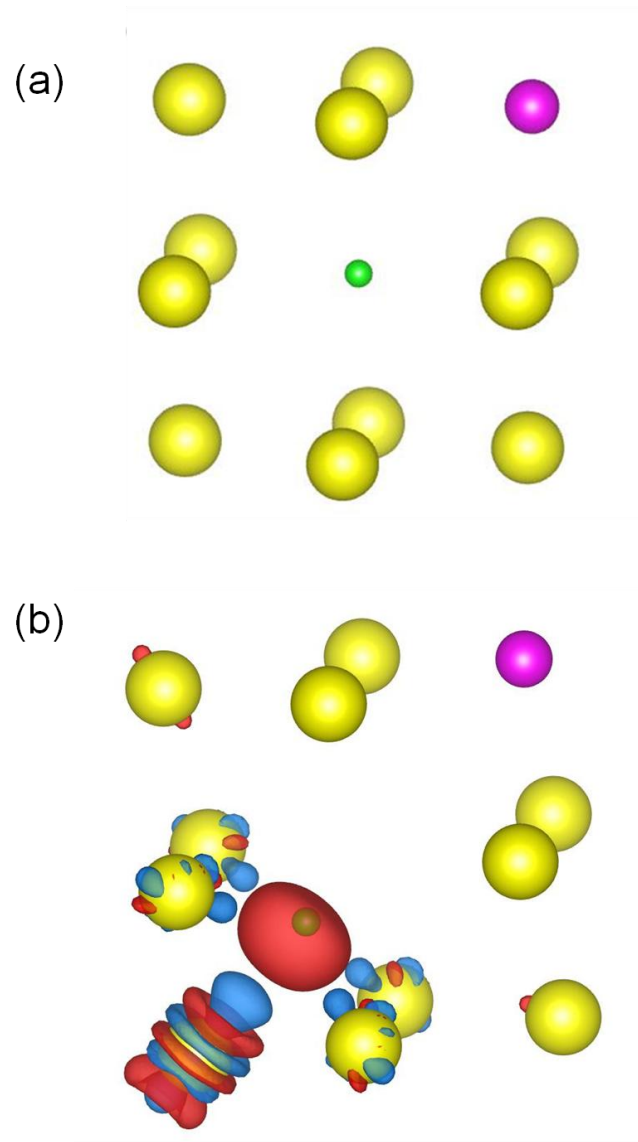


Figure 3.11: Initial position of H□ located at quasi-1nn distance to Ga (purple) atom (a), after relaxation (b) a three-dimensional  $\Delta n(r)$  is plotted. Red indicates regions of charge accumulation, while blue indicates regions of charge depletion.

The isosurface level is  $0.0270 \text{ e}^-/\text{cubic-}\text{\AA}$ . Image (b) is from Ref. 108.

Table 3.7: Partial charges for a Pu and H atom at 1nn distance to each other for the final relaxed structure when the H $\square$  complex is located at a quasi-1nn distance from the Ga atom.  $\Delta$ -Pu or  $\Delta$ -H is the difference between the partial charge for the Pu or H atom in the Pu-Ga+ H $\square$  cell and the Pu-Ga cell or isolated H.

at. % Ga			s	p	d	f
3.125	Pu-Ga + H $\square$ cell	Pu	2.122	5.332	0.799	4.865
		H	0.548	0.017	0.001	0.000
	Pu-Ga cell	Pu	2.127	5.317	0.792	4.874
		isolated H		0.423	0.000	0.000
	$\Delta$ -Pu		-0.004	0.016	0.008	-0.009
	$\Delta$ -H			0.125	0.017	0.001

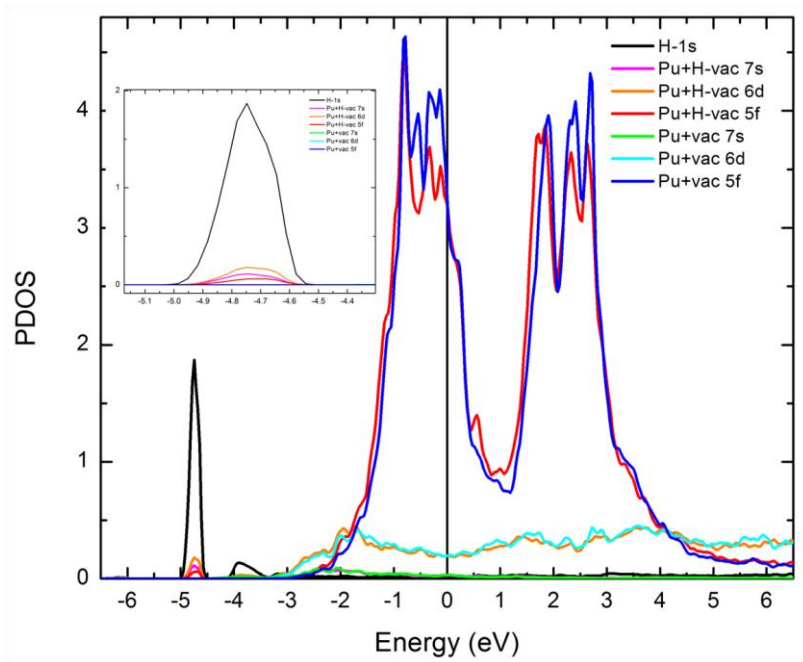


Figure 3.12: PDOS for a Pu atom located at 1nn distance relative to the H atom (H-vac) and vacancy (vac) for the final quasi-1nn distance to the Ga atom SOC relaxed structure. Insert shows expanded PDOS to amplify the hybridization of the H  $1s$  and Pu-1nn  $5f6d7s$ . Image from Ref. 108

## Chapter 4

### Atomic O adsorption on Ga stabilized $\delta$ -Pu (111) surface

#### 4.1 Computational Details

Similar to the bulk calculations, the surface calculations employed DFT and FP-L/APW+lo basis method as implemented within the *WIEN2k* code [99]. The PBE formulation of the GGA exchange-correlation functional [97] was used. APW+lo basis functions was used to describe the  $s$ ,  $p$ ,  $d$ , and  $f$  states ( $l=0, 1, 2, 3$ ), and the LAPW basis is used for all other higher orders of angular momentum states up to  $l_{wf}^{max} = 10$  in the expansion of the wave functions. Additional LO were added to the Pu  $6s$  and  $6p$  semi-core states.

The surface was modeled based on parameters from the bulk study presented in Chapter 3[108]. To maintain a Ga concentration in the surface geometry consistent with the bulk geometry, a periodic slab model with a  $p(4 \times 2)$  surface geometry was constructed. Past theoretical studies have shown that a Pu slab with at least 3 atomic layers is sufficient to model the adsorption of impurities [111, 112, 113]. Thus a slab with a thickness of four atomic layer was employed (cf. Figure 4.1 and Figure 4.2). For the 3.125 at. % Ga  $\delta$ -Pu (111) surface, the slab contains 31 Pu atoms and 1 Ga atom and the theoretical lattice constant of  $4.523 \text{ \AA}$  obtained from the bulk study was used for the theoretical lattice constants for the slab, yielding lattice parameters of  $a = 12.794 \text{ \AA}$  and  $b = 6.397 \text{ \AA}$ . A vacuum region of  $15.9 \text{ \AA}$  was applied to the third dimension, hence  $c = 23.710 \text{ \AA}$ . For the 9.375 at. % Ga  $\delta$ -Pu (111) surface, the slab

contained 29 Pu atoms and 3 Ga atoms and the theoretical lattice constant of 4.493 Å from the bulk study was used for the theoretical lattice constants for the slab. Subsequently yielding lattice parameters of  $a = 12.708$  Å and  $b = 6.354$  Å and a vacuum region of 15.9 Å was applied in the z-direction, then  $c = 23.710$  Å. Also from the bulk study, the Ga atoms were placed at fourth nearest neighboring distance from each other in the surface, since this was the most preferred distance in the bulk structure. The bulk study indicated that with the inclusion of Ga, the ground state structure was AFM (with the exception at the Ga-site), thus the surface was modeled with an AFM-like configuration for the Pu atoms. AFM-like here implies that the magnetic configuration is not strictly AFM since there are an odd number of Pu atoms. The *WIEN2k* parameters were kept consistent with previous oxygen adsorption studies [79]. For O adsorption study, the parameters comprised of a RMT of 1.127 Å, 1.032 Å, and 0.635 Å for Pu, Ga, and O, respectively, and a planewave kinetic energy cutoff of  $K_{\max}^2 = 163$  eV for the expansion of the wave function in the interstitial region. The molecular O<sub>2</sub> total energy, which was used for the calculation of the adsorption energy, was calculated in a 13.23 Å box and at the  $\Gamma$  k-point.

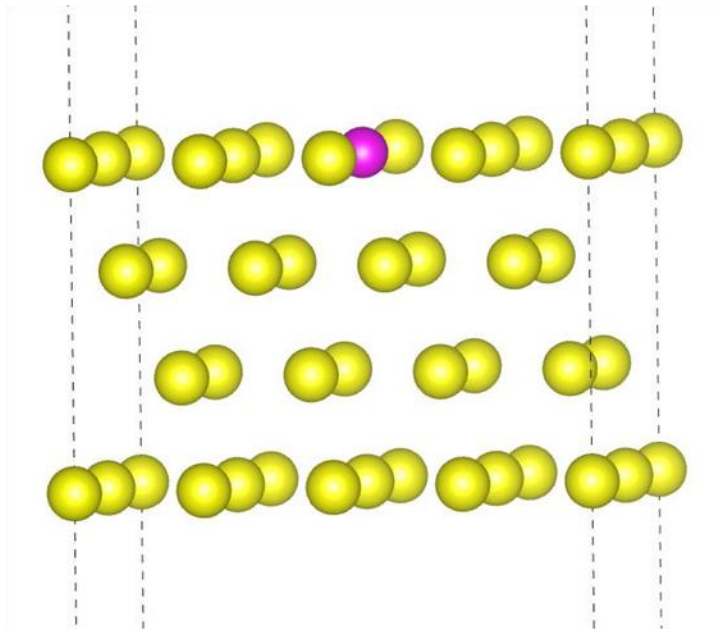


Figure 4.1: 3.125 at. % Ga stabilized  $\delta$ -Pu surface, with Ga located in the topmost surface. Pu atoms are yellow, while Ga atoms are purple.

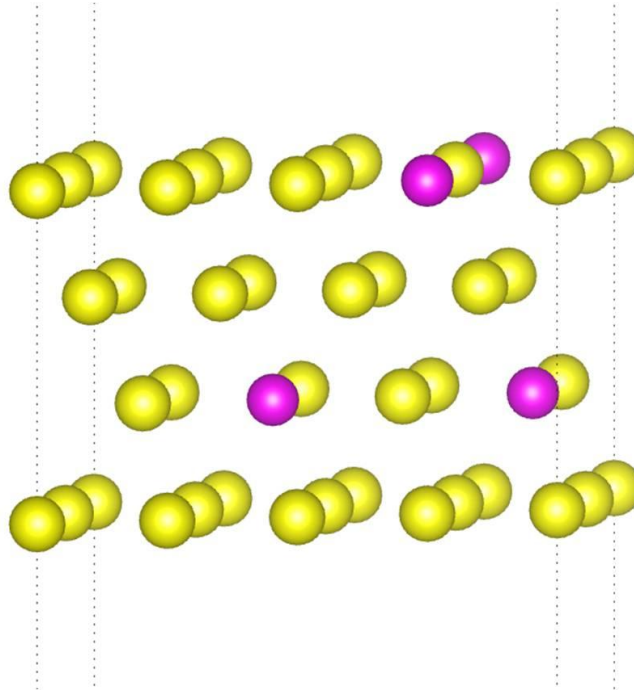


Figure 4.2: 9.375 at. % Ga stabilized  $\delta$ -Pu surface, with Ga located in the topmost surface and in the sub-surface.

Full geometry relaxations were performed at the scalar relativistic level, no-spin-orbit coupling (NSOC), by minimizing the total energy with respect to the atomic positions. The relaxations were terminated when the maximum Hellman-Feynman force on each atom was less than  $0.051 \text{ eV/\AA}$ . After the scalar relativistic relaxations, a single calculation was performed with the inclusion of spin-orbit-coupling (SOC) using the optimal scalar relativistic geometries. As mentioned above, currently *WIEN2k* does not have the capability to perform a Hellman-Feynman force computation with the inclusion of SOC. However, prior studies indicate that the equilibrium scalar relativistic and SOC-inclusive geometries are quite similar [79,

105]. SOC interactions were included via a second variational scheme using the scalar relativistic eigenstates as a basis with all eigenstates with energies below 61.2 eV included [103]. SOC effects were added only to the Pu atoms.

For adsorption sites on a 3.125 at. % Ga surface, the effects of Ga on the adsorption mechanisms can be probed by placing Ga on the surface layer (case 1) or sub-surface layer (case 2). Our initial assessments indicated that at both the NSOC and SOC levels of theory, the slab total energies for case 1 and case 2 were nearly degenerate. Hence since our focus for this work was to probe the effect that Ga would have to on-surface adsorption, we found it instructive to consider case 1. Figure 4.1 depicts the slab model for case 1. From the figure, it is obvious that the adsorbate may approach a Pu-terminated (Pu-rich) surface or a PuGa-terminated surface, which due to the Ga impurity on the surface will increase the number of adsorption sites. Also adsorption of a single O adsorbate on each face was considered, resulting in an adsorbate surface coverage of 0.125 ML.

The O adsorbate was initially placed at four high-symmetry adsorption sites: top (one-fold coordination), bridge (two-fold coordination), hollow hcp, and hollow fcc (both hollow sites are three-fold coordination). These four initial adsorption geometries correspond to adsorption on the Pu-terminated surface. Due to the presence of Ga, there were eight initial adsorption geometries on the PuGa-terminated surface: all the four sites on the Pu-terminated surface plus top site on Ga, bridge site between a Pu and Ga atom, and two hollow sites that included a Ga atom

in the three-fold coordination. Figure 4.3 depicts the adsorption sites for which the Ga atom is a coordination atom. The subsurface octahedral and tetrahedral interstitial sites were also investigated. Again, due to the presence of Ga, multiple interstitial sites were inspected, which included interstitial sites that systematically moved away from the Ga impurity within the slab (Figure 4.4). To view initial Pu-terminated sites and PuGa-terminated sites that included the adsorbate to be coordinated with a Pu-rich environment see Appendix C on page 206.

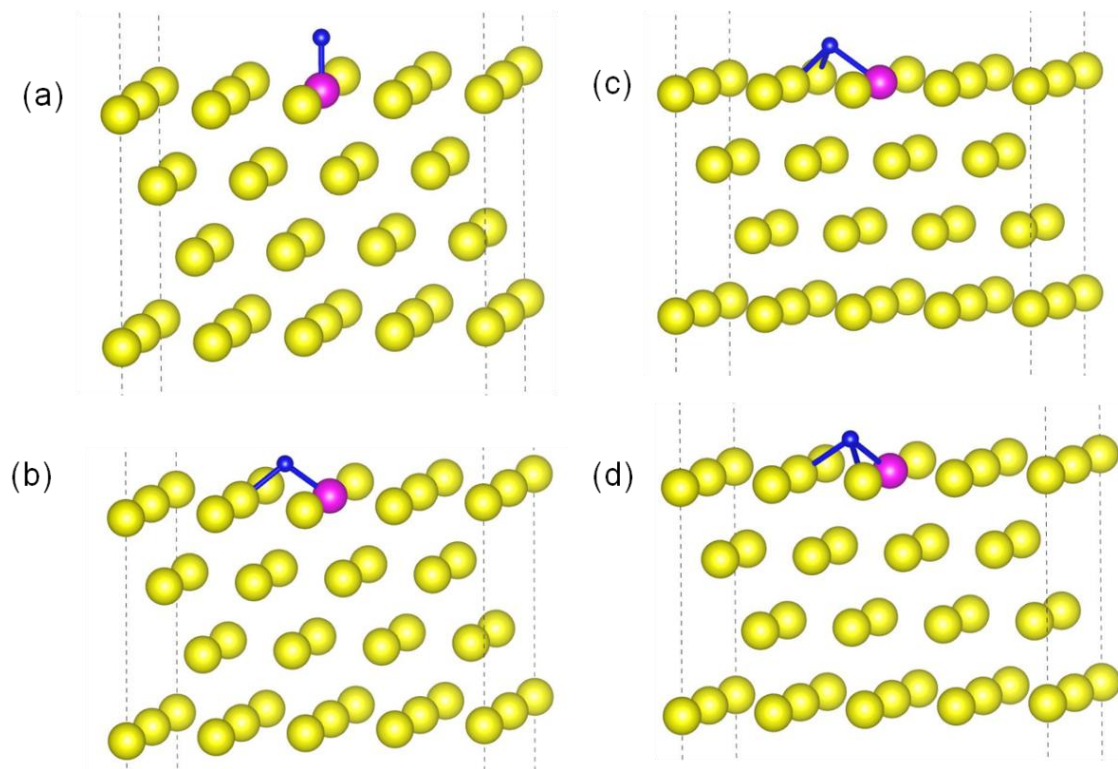


Figure 4.3: 3.125 at. % Ga slab initial sites for adsorbate (blue) on PuGa-terminated surface. On top of Ga (a), bridge between Pu and Ga (b), and hollow sites, hcp (c) and fcc (d), with Ga as a nearest neighboring atom. Similar sites for the adsorbate were also taken into consideration for a Pu-rich environment for both the Pu-terminated and PuGa-terminated surface, which can be seen in Appendix C.

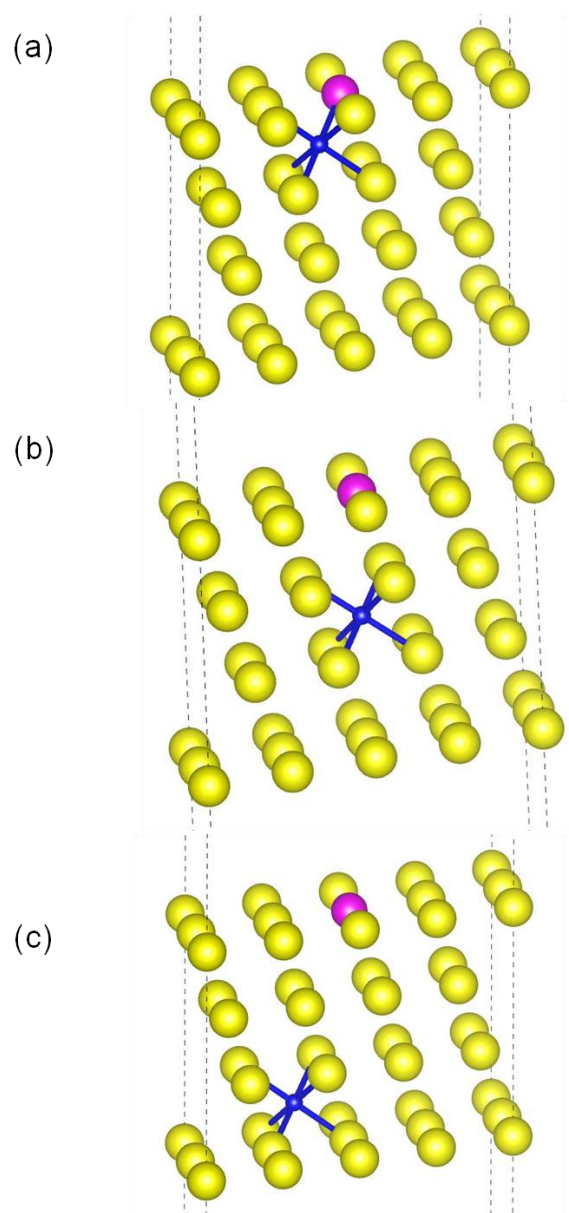


Figure 4.4: Initial octahedral interstitial sites with O adatom for 3.125 at. % Ga surface. Sites include positions where the O atom regressed further away from the Ga atom [(a)-(c)]. A similar regression of the O atom from the Ga atom was also studied for the tetrahedral sites, which can be observed in Appendix C.

Adsorption sites for 9.375 at. % Ga slab considered are similar to the 3.125 at. % Ga surface where the adsorbate is approaching a Pu-terminated (Pu-rich) surface or a PuGa-terminated surface. Also similar to the low Ga concentration slab, a single adsorbate on each surface was considered, which resulted in an adsorbate surface coverage of 0.125 ML. The adsorbate was initially placed at four high-symmetry adsorption sites: top (one-fold coordination), bridge (two-fold coordination), hollow hcp, and hollow fcc (both hollow sites are three-fold coordination) for the Pu-terminated surface. Due to the presence of Ga located within the sub-surface, a fifth site was taken into consideration, a hollow hcp over a Ga atom. On the PuGa-terminated surface, a total of nine initial adsorption geometries were considered: two top sites on a Pu or Ga atom, two bridge sites between a Pu and Pu or Ga atom, two hollow hcp sites coordinated with or without a Ga atom, three hollow fcc sites coordinated with or without a Ga atom and where the adatom is over a Ga atom in the subsurface. Figure 4.5 shows the adsorption sites for the PuGa-terminated surface for when the Ga atom is a coordination atom. Interstitial sites, octahedral and tetrahedral sites, were also explored. Also, similar to the 3.125 at. % surface, due to the presence of Ga, multiple interstitial sites were investigated, which included interstitial sites that were either in a Pu-rich or PuGa environment (Figure 4.6). To view Pu-terminated sites and PuGa-terminated sites that included the adsorbate to be coordinated with a Pu-rich environment see Appendix D on page 212.

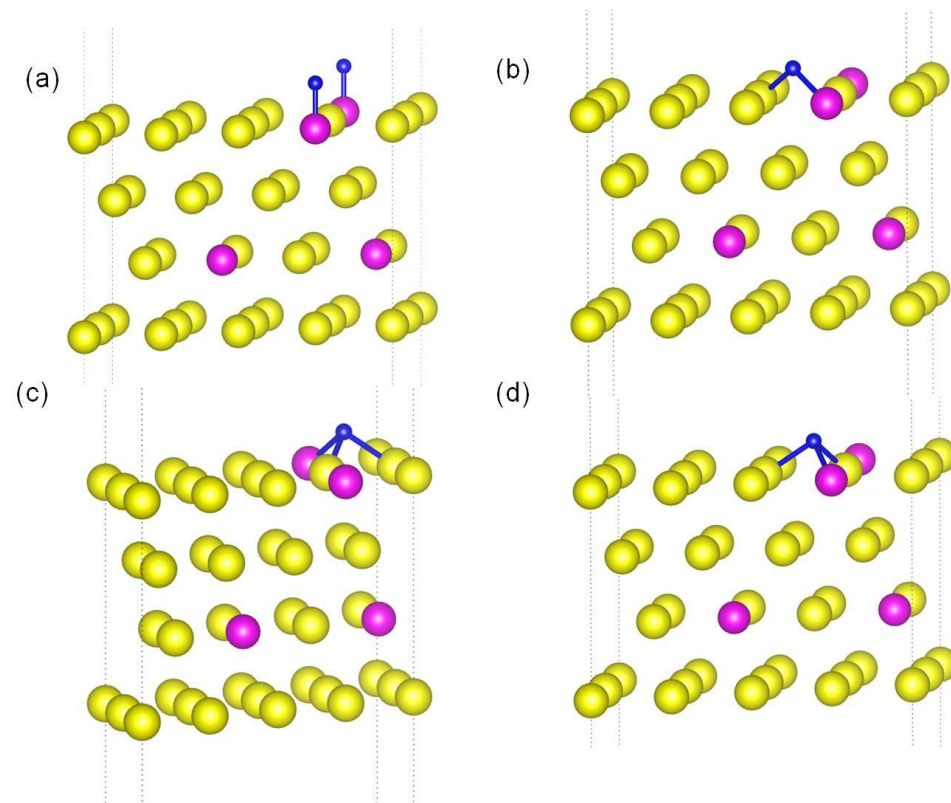


Figure 4.5: 9.375 at. % Ga initial sites for O atom for PuGa-terminated surface. On top of Ga (a), bridge between Pu and Ga (b), and hcp (c) and fcc (d) sites, with Ga as a nearest neighboring atom. Similar sites were also investigated for the Pu-rich environment for the Pu-terminated and PuGa-terminated surface, which may be viewed in Appendix D.

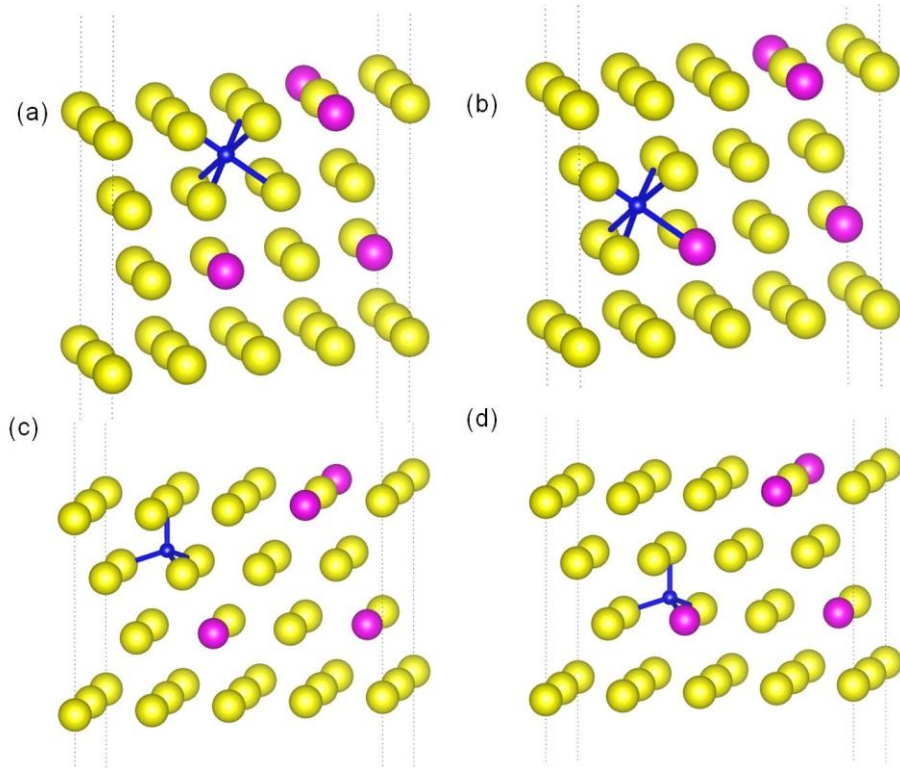


Figure 4.6: 9.375 at. % Ga surface initial octahedral interstitial sites when O atom is far from Ga (a) and near Ga (b). Initial tetrahedral interstitial sites when O atom is far from Ga (c) and near Ga (d).

Finally, *chemisorption energy* is given by  $E_c = E_{PuGa+O} - E_{PuGa} - \frac{1}{2}E_{O_2}$ , where  $E_{PuGa+O}$  is the total energy of the Pu-Ga surface with X adatom after relaxation,  $E_{PuGa}$  is the total energy of the relaxed clean Pu-Ga surface, and  $E_{O_2}$  is the total energy of the  $O_2$  molecule. Therefore, if  $E_c < 0$ , then binding is favorable, otherwise it is unfavorable. We will also report relaxation energy,  $E_r$ , which is defined as  $E_r = E_{relax} - E_{unrelax}$ . Here,  $E_{relax}$  is the total energy of the fully relaxed slab-

adsorbate geometry (no constraints) and  $E_{unrelax}$  is the total energy of the slab-adsorbate geometry where only the adsorbate was allowed to relax and the slab atomic positions were constrained.

## 4.2 Results and Discussions

### Oxygen adsorption on 3.125 at. % Ga stabilized $\delta$ -Pu (111) surface

#### 4.2.1 Relaxation and stability of 3.125 at. % Ga $\delta$ -Pu (111) surface

Relaxation of the bare Pu-Ga surface (that is, no adsorbate present) yielded  $\Delta d_{12}/d_o = -1.1\%$ ,  $\Delta d_{23}/d_o = 3.7\%$ , and  $\Delta d_{34}/d_o = -3.2\%$ , where  $d_o$  is the bulk optimized interlayer distance and  $\Delta d_{ij}$  is the interlayer separation between layer  $i$  and layer  $j$  (the topmost layer is layer 1). The  $d_1$  layer had the Ga atom and after relaxation the Ga atom remained planar with very small local lateral distortions ( $\sim 0.001$  Å). Comparing the PuGa-terminated surface to the previous 3.125 at. % Ga bulk results [108], we observe that the local distortion induced by Ga is similar. Analysis is shown in Table 4.1. Specifically, the ratio between the relaxed bond lengths to the unrelaxed bond lengths of the Pu-Ga and Pu-Pu bonds in the first nearest neighbor shell around the Ga,  $d_{relax}/d_{fcc}$ , were 0.977 and 0.982, respectively. For the bulk, both ratios were 0.978. Also, the previous study of bulk Pu-Ga yielded average Pu-Ga and Pu-Pu bond contractions of 0.069 Å, whereas the corresponding bond contractions on the surface were 0.072 Å (Pu-Ga bonds) and 0.059 Å (Pu-Pu bonds). Although a bond length contraction was noticed in both systems, short-range disorder was more prevalent in the surface. This is evidenced by the normalized Pu-Ga and Pu-Pu bond

length standard deviations (measurement of structural disorder) of 0.018 and 0.019, respectively, for the surface, whereas little or no deviation was seen in the bulk. The contraction seen in the topmost Pu-rich surface layer is due to the missing neighbors of atoms. Overall, there were little or no lateral relaxations of the Pu-Ga surface.

Table 4.1: Structural analysis of the first nearest neighboring shell around the Ga atom in the 3.125 at. % Ga bulk and surface systems. The division of the bond length distance in the final relaxed structure by the bond length distance of the pristine structure is defined by  $d_{relax}/d_{fcc}$ ,  $\sigma$  is the standard deviation of the normalized bond lengths, and the average bond length contractions are tabulated. Bulk data was obtained from Ref. 108.

System	Bond Length Type	$d_{relax}/d_{fcc}$	$\sigma$	Average Bond length contractions (Å)
Bulk	Pu-Ga	0.978	0.000	0.069
	Pu-Pu	0.978	0.001	0.069
Surface	Pu-Ga	0.977	0.018	0.072
	Pu-Pu	0.982	0.019	0.059

The *surface relaxation energy*, which is defined as the total energy after geometry relaxation minus the total energy of the slab with the atoms fixed at their bulk terminated position was -0.19 eV (that is, relaxation of the atomic positions lowers the slab total energy by 0.19 eV). In comparison, the relaxation of a p(4x2)  $\delta$ -Pu (111) slab (pure Pu slab; no Ga) was also investigated and the total energy was lowered by 0.11 eV. Thus Ga provides the same stabilizing effect on the surface as it does in bulk  $\delta$ -Pu. Currently, there is no experimental data in the literature on the relaxation of Ga-stabilized  $\delta$ -Pu metal so the observations regarding the effects of Ga on surface relaxations cannot be fully validated. To further probe the stability of the  $\delta$ -Pu surface by Ga we computed the *formation energy* defined as  $E_f = E_{slab} - (m/32)*E_{Pu-bulk} - (n/8)*E_{Ga-bulk}$ , where  $E_{slab}$  was the total energy of the Pu-Ga surface,  $E_{Pu-bulk}$  was the total energy of the Pu-bulk,  $E_{Ga-bulk}$  is the total energy of the orthorhombic Ga bulk,  $m$  is the number of Pu atoms in the surface, and  $n$  is the number of Ga atoms in the surface. The computed values of  $E_f$  for the 0, 3.125, and 9.375 at. % Pu-Ga surfaces were 0.40 eV, 0.36 eV and 0.27 eV/atom, respectively. Thus the order of decreasing surface stability is 9.375 at. % Ga > 3.125 at. % Ga > Pu. Also, the *surface energy*, defined as  $\gamma = [1/(2A)]*[E_{slab} - E_{bulk}]$ , where  $A$  is the surface area of the slab,  $E_{slab}$  is the total energy of the surface, and  $E_{bulk}$  is the total energy of the bulk, was computed for each system. The surface energies for the 0, 3.125, and 9.375 at. % Ga surfaces were computed to be 1.24 J/m<sup>2</sup>, 1.23 J/m<sup>2</sup>, and 1.19 J/m<sup>2</sup>, respectively. Again the order of decreasing surface stability is 9.375 at. %

Ga > 3.125 at. % Ga > Pu. Collectively, the two trends in  $E_f$  and  $\gamma$  further supports our earlier assertion that the inclusion of Ga coupled with increasing Ga concentrations stabilizes the surface.

#### 4.2.2 Adsorption on Pu-terminated surface

Table 4.2 shows the results of the O adsorbed on the Pu-terminated surface. Reported in the Table 4.2 are the relaxation energy and the adsorption energies at the NSOC and SOC levels of theory, optimized perpendicular distance of the adsorbate from the surface, and the nearest neighbor distances of the adsorbate from the surface atoms.

We observe that the top site was the least favorable site, with SOC chemisorption energy of -3.55 eV, which has been seen in previous works [8,9]. It can also be seen in Table 4.2 that the chemisorption energies for hcp, fcc, and bridge-to-fcc sites at the NSOC level differ by a few tenths of an eVs (-4.50 eV to -4.90 eV range). With the inclusion of SOC, the chemisorption energies slightly decreased by 0.08-0.15 eV, supporting previous assertions that equilibrium scalar relativistic and SOC-inclusive geometries are quite similar and that SOC energies are slightly more stable than NSOC energies [79, 105]. The most preferred site, after relaxation of the slab indicated that the initial bridge site had a final hollow fcc site, with three-fold coordination and yielded a SOC chemisorption energy of -4.98 eV. This supports the conclusions from Atta-Fynn's and Ray's [79, 80] work that the bridge site will mediate the lowest energy pathway from a stable hollow site to a neighboring hollow

site. The final geometry showed that there were oxygen-induced local distortions (Figure 4.7). The bond length of the atoms forming the bridge site expanded from 3.20 Å to 3.56 Å coupled with contractions in all interlayer spacings. This implies that the bridge-to-fcc site adsorbate configuration is achieved at the expense of introducing local structural distortions on the surface Pu atoms. Oxygen induced distortions have been seen theoretically from the recent work of Taylor [81], but Taylor's results correspond to high adsorbate coverage (1 ML compared to 0.125 ML in this work). Experimentally however, the stability of the  $\delta$ -Pu surface has been noted by Cox [114], which concluded that a 3.40 at. % Ga stabilized  $\delta$ -Pu surface had an induced surface phase transformation to the  $\alpha$ -phase (room temperature phase of Pu), but the author did not clearly state whether the observed effect was due to sample preparation or the presence of oxygen on the surface. The final distance of the adatom from the slab was 1.11 Å for the bridge-to-fcc site, resulting in an average neighboring Pu-O distance of 2.25 Å. We note that the Pu-O distance in bulk PuO<sub>2</sub> is 2.36 Å [6]. All distances of the O atom from the surface was lower than those reported in previous published works, with the exception of the top site. For example, in Atta-Fynn's and Ray's [79] work were the atomic positions of the slab atoms were constrained and only the oxygen adsorbate was allowed to relax, the reported distances were 1.84 Å for the top site, and 1.23 Å for the fcc site. Compared to this work, the distances are 1.86 Å for the top site, and 1.07 Å and 1.11 Å for the two different final fcc sites. These differences suggest that constrained-free

atomic relaxations are necessary to accurately describe the adsorption geometries.  
To view initial and final positions of the oxygen adatom, see Appendix C on page 206.

Table 4.2: Results for the Pu-terminated surface which includes relaxation energy,  $E_r$ , chemisorption energy,  $E_c$ , at the NSOC and SOC level of theory, and distance of the adatom from the surface,  $r_{slab-O}$ , and distance of the adatom to the nearest neighboring atoms,  $r_{Pu-O}$ .

Pu-terminated			NSOC	SOC		
Initial site	Final site	$E_r$ (eV)	$E_c$ (eV)	$E_c$ (eV)	$r_{slab-O}$ (Å)	$r_{Pu-O}$ (Å)
top	top	-0.27	-3.46	-3.55	1.86	1.86
hcp	hcp	-0.27	-4.50	-4.65	1.31	2.26, 2.26, 2.36
fcc	fcc	-0.55	-4.80	-4.91	1.07	2.23, 2.24, 2.27
bridge	fcc	-0.97	-4.90	-4.98	1.11	2.20, 2.24, 2.30

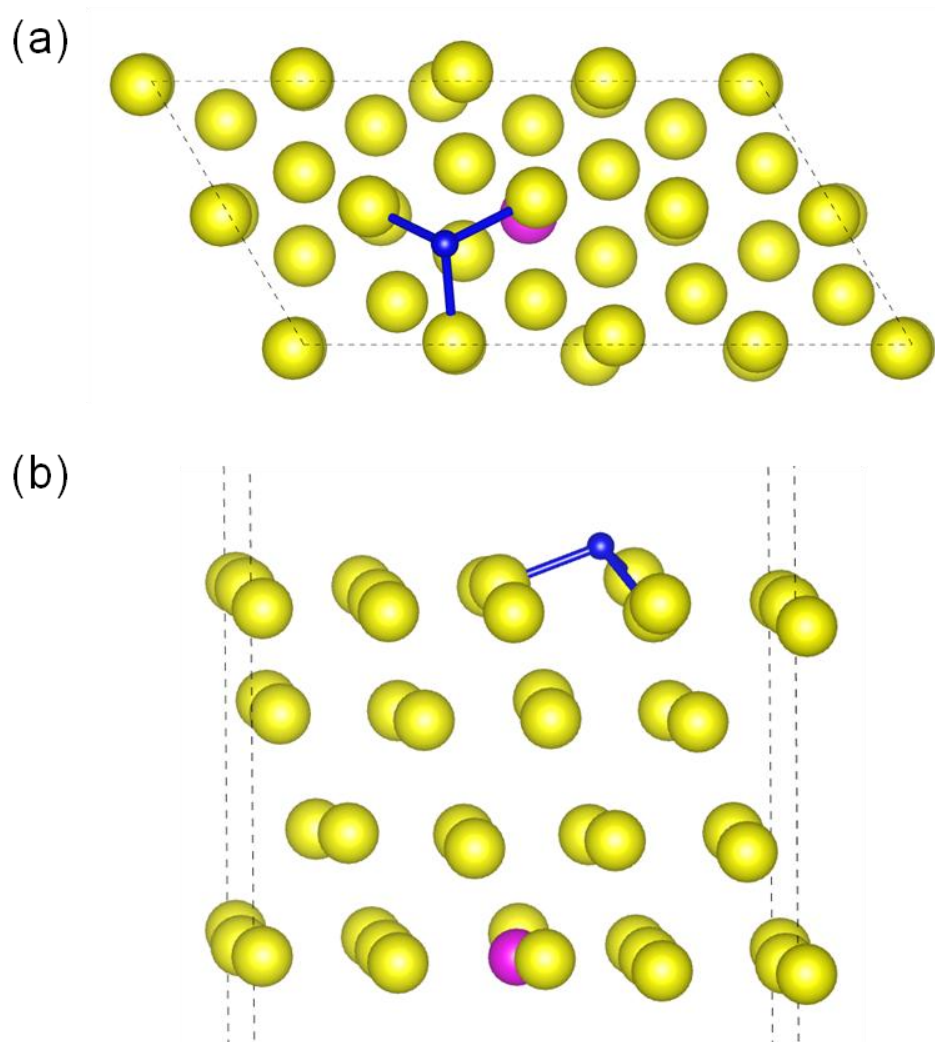


Figure 4.7: Top (a) and side (b) view of the final geometries after O adsorption for the Pu-terminated bridge-to-fcc site. Pu atoms are yellow, Ga atom is purple, and O atom is blue.

#### 4.2.3 Adsorption on PuGa-terminated surface

Table 4.3 shows the results for O adsorbed on the PuGa-terminated surface. Note that in Table 4.3, we have adopted the nomenclature of site-Pu, site-Ga, or site-PuGa, thus indicating whether the initial site has Pu, Ga, or both (PuGa) atoms as nearest neighboring atoms. This convention is similar for the final site. It can be clearly seen that the preferred sites are sites that have all Pu atoms as nearest neighboring atoms. The most favorable site being bridge-Pu-to-fcc site had a SOC chemisorption energy of -5.06 eV, where the bridge site was a mediator for the O adatom to migrate to a hollow site. The sites, top-Pu, fcc-Pu, and bridge-Pu, are all comparable in value from similar sites on the Pu-terminated surface. The difference in chemisorption energies ranges from 0.03 to 0.08 eV. The hcp-Pu site has a chemisorption energy difference of 0.18 eV from the hcp site on the Pu-terminated surface; this could be due to the fact that the relaxation energy for the hcp-Pu site for the PuGa-terminated surface yielded -0.55 eV, while the hcp site for the Pu-terminated surface yielded a value of -0.27 eV. Therefore, more relaxation of the PuGa-surface occurred, which may be explained by the misfitting Ga atom present on the surface. Either way, all PuGa-terminated Pu-rich surface sites were similar to the Pu-terminated surface sites and had equivalent final geometric sites.

Table 4.3: Results for the PuGa-terminated surface which includes relaxation energy,  $E_r$ , chemisorption energy,  $E_c$ , at the NSOC and SOC level of theory, and distance of the adatom from the surface,  $r_{slab-O}$ , and distance of the adatom to the nearest neighboring atoms,  $r_{X-O}$ , where  $X$  is the atom that is nearest to the adatom. If atom is not designated by parenthesis it is assumed that it is a Pu atom.

PuGa-terminated			NSOC	SOC		
Initial site	Final site	$E_r$ (eV)	$E_c$ (eV)	$E_c$ (eV)	$r_{slab-O}$ (Å)	$r_{X-O}$ (Å)
top-Pu	top-Pu	-0.24	-3.36	-3.50	1.86	1.86
top-Ga	top-Ga	-0.43	-1.69	-1.62	1.80	1.80 (Ga)
hcp-Pu	hcp-Pu	-0.55	-4.82	-4.83	1.02	2.23, 2.23, 2.29
hcp-PuGa	hcp-PuGa	-0.27	-3.76	-3.85	1.17	2.16, 2.16, 2.22 (Ga)
fcc-Pu	fcc-Pu	-0.51	-4.83	-4.94	1.11	2.23, 2.23, 2.34
fcc-PuGa	fcc-PuGa	-0.33	-4.01	-4.09	1.16	2.18, 2.21 (Ga), 2.25
bridge-Pu	fcc-Pu	-1.05	-4.95	-5.06	1.07	2.24, 2.26, 2.28
bridge-PuGa	four-fold	-0.69	-3.92	-4.01	0.89	2.16 (Ga), 2.21, 2.31, 2.93

We also observe from Table 4.3 that the participation of Ga in the adsorption process leads to an increase in the chemisorption energies near Ga-sites. Thus all sites with a Ga-O bond *are less* favorable compared to Pu-O bond-only sites. The SOC chemisorption energies are -1.62 eV, -3.85 eV, -4.01 eV, and -4.09 eV for the top-Ga, hcp-PuGa, bridge-PuGa, and fcc-PuGa, respectively. Nevertheless, the pattern is similar to the Pu-terminated surface whereas the fcc site is the most favorable site, and this consistent increase in chemisorption energy implies that oxygen prefers an all Pu atom environment (very little Ga influence). To buttress this point, we carried out dimer formation energy calculations and the order of binding energies stability were Pu-O > Ga-O > Pu-Ga > Pu-Pu. Therefore, the Ga-O bond is relatively weaker than the Pu-O bond, which agrees with our assertions. This may be explained by fact that Pu is more electropositive than Ga. To view initial and final positions of the O adatom, see Appendix C on page 206.

#### 4.2.4 Interstitial adsorption

Table 4.4 shows the results for the interstitial sites. Note that site-1 is near the Ga, site-2 is in the middle of the four-layers, and site-3 is far away from the Ga (Figure 4.4). The results demonstrate that even with oxygen in an all Pu environment, the chemisorption energies are still not as favorable as on-surface oxygen adsorption. Thus establishing that O atom prefers a three-fold on-surface coordination environment. The octahedral-1 and tetrahedral-1 sites, where a Ga atom is participating in bonding with the O adatom are least favorable, with SOC

chemisorption energy of -4.02 eV. In addition to these unfavorable chemisorption energies, we also observed that the interlayer separation has an expansion in the  $d_{12}$  interlayer as opposed to the contraction seen in the slab with no O adsorbate. The  $d_{12}$  interlayer has a Ga atom located in layer 1. There is also a decrease in the expansion of the  $d_{23}$  interlayer and an increase in contraction in the  $d_{34}$  interlayer. The most favorable SOC chemisorption energy of -4.64 eV is the tetrahedral-3 site, which the final site was a four-fold site and the final position of the O atom was above the surface with a distance of 0.46 Å. This four-fold coordination was a distorted tetrahedral site with angles ranging from  $80^\circ$  to  $125^\circ$ , and differed from the PuGa-terminated bridge-PuGa-to-four-fold site. For the latter site, the four-fold coordination is in-plane to the PuGa surface and is a non-tetrahedral site, since the angles significantly differ from a tetrahedral configuration. The interlayer separation of the tetrahedral-3 site, showed a contraction in  $d_{12}$  and  $d_{34}$ , while an expansion in  $d_{23}$ , but this expansion was significantly smaller, with a percent difference of 0.6%, then when no O adsorbate is present (percent difference of 3.7%). All interstitial sites showed an expansion of the bond lengths of the nearest neighboring atoms from the initial 2.26 Å and 1.96 Å for the octahedral and tetrahedral sites, respectively, which elucidates the stress/strain that the system experiences from the O atom being in the sub-surface. Overall, all final interstitial sites also were distorted since angles differed by percent error of 1.06% to 26.60% for the final tetrahedral sites and 0.01% to 9.95% for the octahedral sites. Thus the tetrahedral interstitials sites were more

distorted than the final octahedral sites. Also the final tetrahedral-3 to a four-fold geometry showed the O atom was protruding out of the surface, and was no longer a sub-surface site. Therefore we can conclude that on-surface O adsorption is preferred over interstitial adsorption. To view initial and final sites of the O adatom, see Appendix C on page 206.

Table 4.4: Results for the interstitials sites which includes relaxation energy,  $E_r$ , chemisorption energy,  $E_c$ , at the NSOC and SOC level of theory, and distance of the adatom from the surface,  $r_{slab-O}$ , and distance of the adatom to the nearest neighboring atoms,  $r_{X-O}$ , where  $X$  is the atom that is nearest to the adatom. If atom is not designated by parenthesis it is assumed that it is a Pu atom.

Interstitials			NSOC	SOC		
Initial site	Final site	$E_r$ (eV)	$E_c$ (eV)	$E_c$ (eV)	$r_{slab-O}$ (Å)	$r_{X-O}$ (Å)
octahedral-1	octahedral*	-0.39	-4.09	-4.02	-1.28	2.31, 2.34, 2x2.38, 2.42, 2.55 (Ga)
octahedral-2	octahedral*	-0.43	-4.45	-4.40	-3.95	2x2.39, 2x2.40, 2.41, 2.42
octahedral-3	octahedral*	-0.38	-4.65	-4.55	-1.15	2x2.37, 2.39, 2.41, 2.42, 2.43
tetrahedral-1	four-fold	-0.77	-4.00	-4.02	-0.05	2.12 (Ga), 2x2.21, 2.46
tetrahedral-2	tetrahedral*	-0.41	-4.10	-4.03	-3.26	3x2.25, 2.27
tetrahedral-3	four-fold	-0.38	-4.66	-4.64	0.46	2x2.22, 2.28, 2.77

\*After relaxation the final interstitial site was a distorted interstitials site.

#### 4.2.5 Adsorption Probabilities

A simple Boltzmann distribution of the adsorption energies was computed to further quantify the on-surface versus sub-surface/interstitial adsorption probabilities on the Pu-terminated surface and interstitial sites. This was calculated using  $P[E_i]/P[E_{i+1}] = e^{(E_i - E_{i+1})/kBT}$  subject to the normalization condition that the sum of the Boltzmann probabilities is unity, where  $E_i$  denotes the adsorption energy at adsorption site  $i$  ( $i = \text{top, bridge, hcp, fcc, etc.}$ ). Increasing  $i$  corresponds to increasing (unfavorable) chemisorption energies. For instance, when the oxygen atom is approaching the Pu-terminated surface,  $E_l = -4.98$  eV, which corresponds to the bridge-Pu-to-fcc site and the final  $E$  would be the least favorable chemisorption site, tetrahedral-1 or octahedral-1 with  $E_c = -4.02$  eV. We assumed  $T = 300$  K. The Boltzmann distribution illustrated that 93% of the time the oxygen atom will adsorb at an on-surface site, specifically the fcc site. Similarly for the PuGa-terminated surface, the Boltzmann distribution showed a much larger on-surface adsorption probability of 99%. This suggests, assuming that the adsorption energies corresponds to at room temperature values, that oxygen diffusion must be activated, unless a significant amount of oxygen dosing is applied to the surface.

#### 4.2.6 Adsorbate-induced work function changes

The results on the adsorbate-induced work-function changes with respect to the clean Pu-Ga surface, which is given by  $\Delta\phi = \phi^{adatom/PuGa} - \phi^{PuGa}$ , are shown in Table 4.5 for the NSOC and SOC level of theory. The interstitial sites are not shown since

the changes in work function were negligible (on the order of 0.01 eV). The least preferred sites have the largest change in work function (i.e. top site), while the most preferred sites have lowest change in work function (i.e. fcc site). These trends agree well with previous works [77, 79, 80]. The work function shifts are explained as follows: partial transfer of electrons from the Pu-Ga surface to the O adsorbate occurs since O is more electronegative than both Pu and Ga; this results in an induced surface dipole formation; the magnitude of induced surface dipole moment is proportional to the change in work function [115]. Another indicator was the change in magnetic moment. For instance, prior to adsorption the initial magnetic moment of the top site Pu was  $3.97 \mu_B$ . After O adsorption at the top site, the Pu magnetic moment decreased to  $3.29 \mu_B$ . Similar reduction was seen for other adsorption sites, such as the Pu-terminated bridge-to-fcc site where the average magnetic moment (averaged over the Pu atoms coordinated to oxygen) decreased from  $3.96 \mu_B$  before adsorption to  $3.84 \mu_B$  after adsorption. These reductions are signatures of charge transfer and substantiate the observed changes in the work functions, as reported in Table 4.5.

Table 4.5: Changes in work function,  $\Delta\phi$ , at the NSOC and SOC levels of theory.

The work function for the clean relaxed Pu slab was 3.29 eV and 3.37 eV, respectively, at the NSOC and SOC level of theory. Experimental work function for Ga stabilized  $\delta$ -Pu is 3.2 eV [116].

		NSOC	SOC
		$\Delta\phi$	$\Delta\phi$
Initial site		(eV)	(eV)
Pu-terminated	top	0.28	0.28
	hcp	0.16	0.15
	fcc	0.10	0.09
	bridge	0.12	0.11
PuGa-terminated	top-Pu	0.33	0.33
	top-Ga	0.22	0.22
	hcp-Pu	0.09	0.08
	hcp-PuGa	0.11	0.10
	fcc-Pu	0.10	0.09
	fcc-PuGa	0.12	0.12
	bridge-Pu	0.11	0.11
	bridge-PuGa	0.07	0.06

#### 4.2.7 Electronic structure analysis

We commence the discussions on the electronic structure by focusing on the adsorption configurations for the least preferred top site and most preferred bridge-to-fcc site on the Pu-terminated surface. Figure 4.8 depicts the PDOS for the aforementioned sites. Note that Pu bare (Ga bare) are the Pu (Ga) atoms PDOS before adsorption and Pu+O (Ga+O) are the Pu (Ga) atoms PDOS after adsorption with O. PDOS for Pu and Ga are coordinated with O. The PDOS in Figure 4.8(a) shows hybridization and a decrease in intensity of the Pu *5f* and *6d* electrons with the O *2p* when compared to the bare relaxed Pu atoms. The O *2p* states are also at lower energies, which is in good agreement with Atta-Fynn's and Ray's work [79, 80]. For the bridge-to-fcc site [Figure 4.8(b)], the O *2p* states shift to an even lower energy state around 5 eV below the Fermi energy. This shift of the O *2p* states to lower energies for the favorable adsorption sites was also observed in Ref. 79 and 80. In general both adsorption sites showed a decrease in the *5f* and *6d* states in the vicinity of the Fermi level, thus indicating a net electron transfer from Pu to O. The hcp and fcc sites also showed this decrease in *5f* and *6d* electrons around the Fermi energy (not shown).

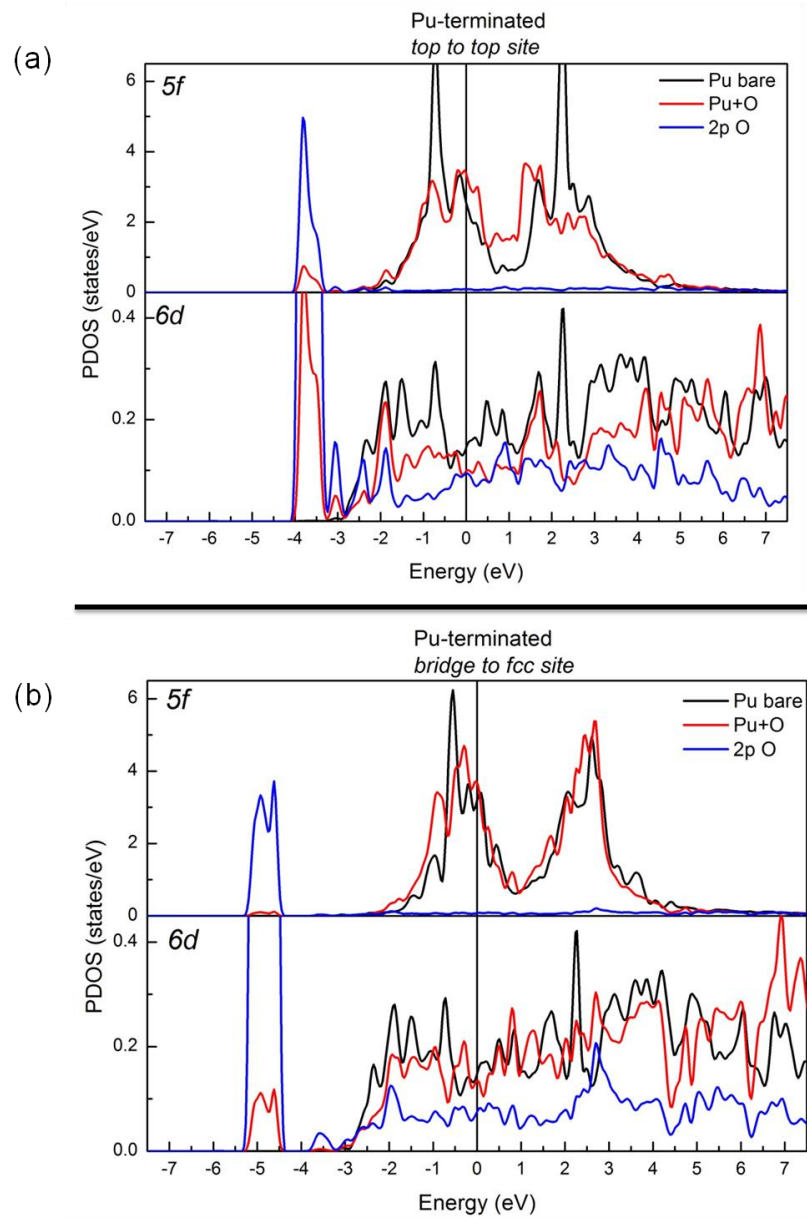


Figure 4.8: PDOS for the SOC level of theory for the least favorable site, top site (a), and most favorable site, bridge-to-fcc site (b), for when the O adsorbate is approaching the Pu-terminated surface.

Figure 4.9 shows the PDOS for the least and most preferred sites for the PuGa-terminated surface when Ga forms or does not form a bond with O after adsorption. For the case where Ga forms a bond with the O adatom, the Ga  $4s4p$  states hybridize with the O  $2p$ , especially for the top-Ga site [Figure 4.9(a)]. Furthermore, for the fcc-PuGa [Figure 4.9(b)] the Pu  $6d$  intensity is comparable to the intensity for the  $6d$  states for the Pu-terminated PDOS results. The degree of intensity for the  $5f$  is similar to the Pu bare  $5f$  and with a slight decrease of intensity in the  $6d$  states. The O  $2p$  states are located at lower energies in the fcc-PuGa adsorption site compared to the top-Ga adsorption site. A drop of the Ga  $4p$  states at the Fermi energy can also be seen. In the case where Ga does not form a bond with O, the top-Pu site PDOS [Figure 4.9(c)] is similar to the Pu-terminated top site for the Pu  $5f$  electrons, but the degree of hybridization of the Pu  $6d$  at the Fermi energy is more evident than the Pu-terminated PDOS shown in Figure 4.8(a). This feature is better described if we only examine the Pu atoms before adsorption [Pu bare in Figure 4.8(a) and Figure 4.9(c)]. For instance, for the bare Pu atoms in Figure 4.8(a), the PDOS shows a higher degree of intensity for the  $5f$  and  $6d$  states than the PuGa-terminated top-Pu site. This can be further explained by the fact that the Ga atom for this top-Pu site is a nearest neighboring atom, and from the previous bulk Pu-Ga work [108], the Ga  $4p$  states hybridizes with Pu  $6d$  states and also slightly delocalizes the  $6d$  electrons, while the Pu  $5f$  remain unchanged. Therefore, even within the surface, the Ga atom enhances the ability of the  $6d$  electrons to participate

in bonding over the  $5f$  electrons, which also aids in the stabilization of the surface (see discussion in Section 3.2.2, page 54). Subsequently, since the Pu  $6d$  electrons are readily available, due to the Ga atom present on the surface, this allows for the O  $2p$  orbitals to hybridize strongly with the Pu  $6d$  orbitals.

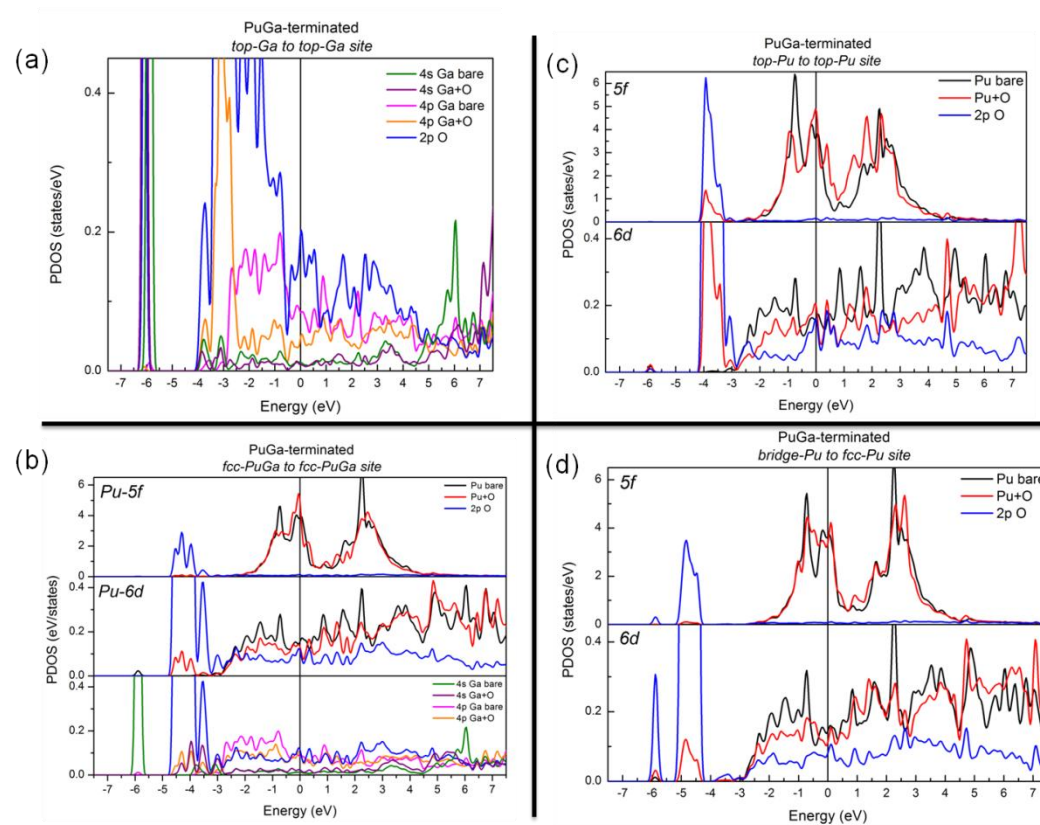


Figure 4.9: PDOS for the SOC level of theory for the least favorable site, top-Ga and top-Pu site [(a) and (c), respectively], and most favorable site, fcc-PuGa and bridge-Pu site [(b) and (d), respectively], for when the O adsorbate is approaching the PuGa-terminated surface.

For Figure 4.9(d), for the bridge-Pu-to-fcc-Pu site, the degree of intensity of the  $5f$  electrons are similar to the Pu bare  $5f$  electrons and hybridization and further broadening is observed in the Pu  $6d$  states, which can also be explained by the presence of the Ga atom at the surface. Also we observe a shift of the O  $2p$  to lower energies for the more favorable site, similarly to PDOS in Figure 4.8, but there is splitting of the O  $2p$  into sub-bands, which is not seen in the Pu-terminated PDOS. This splitting of the O  $2p$ , can be described by an indirect effect with the Ga atom present on the surface. Figure 4.10 shows the PDOS for Pu  $6d$  states and the nearest neighboring Ga atom  $4p$  states before and after adsorption. The nearest neighboring Ga atom is at a distance of 3.15 Å. Observing Figure 4.10 is that even though the Ga atom is not coordinated with the O adatom (O-Ga bond length is 5.22 Å for the bridge-Pu and 4.00 Å for the top-Pu site), the hybridization that is occurring between the Pu  $6d$  and Ga  $4p$  allows for this splitting to occur. This splitting of the O  $2p$  is not observed in previous works done by Atta-Fynn and Ray [79, 80] with a pure Pu surface. Therefore, the presence of Ga seems to decrease the propensity of the Pu  $5f$  states to hybridize with the O  $2p$  states, whereas allowing the Pu  $6d$  to be hybridized with the O  $2p$  states, while also splitting the O  $2p$  states into sub-bands.

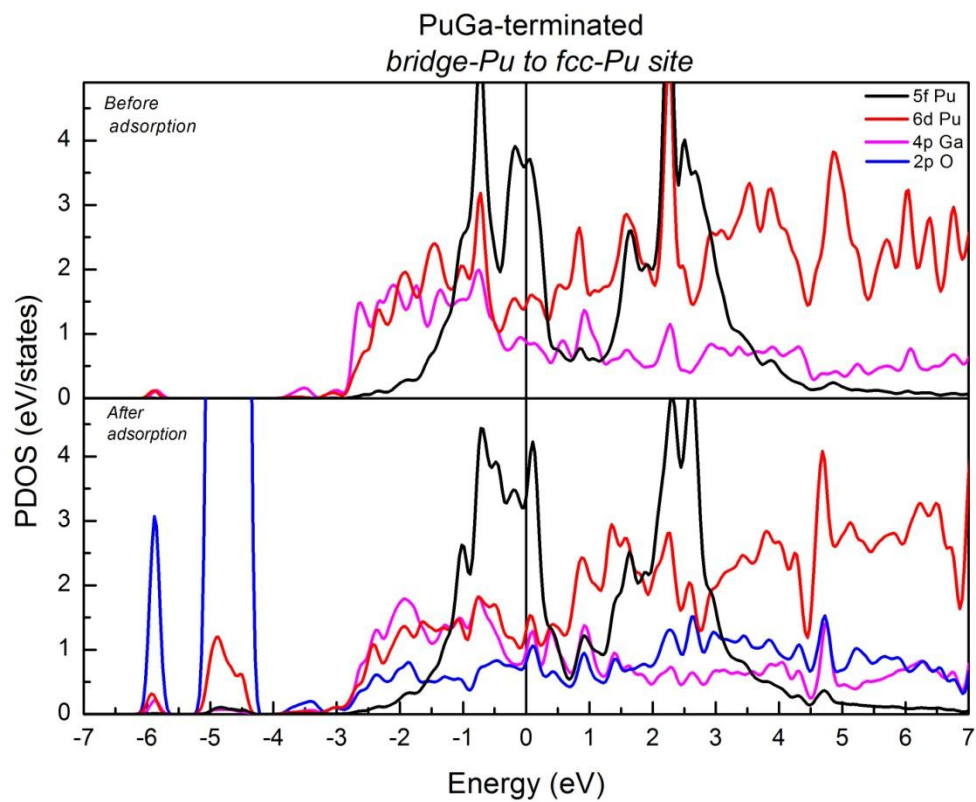


Figure 4.10: PDOS of Pu  $5f$  and  $6d$  states and nearest neighboring Ga atom  $4p$  states before and after O adsorption. O

$4p$  states are also plotted.

The above can be clearly seen further in Figure 4.11, which shows the least and most favorable interstitial sites. Figure 4.11(a) and Figure 4.11(c), show that when a Ga-O bond is formed, the Pu *5f* and O *2p* hybridizations is negligible, while the Ga *4s4p* and Pu *6d* and O *2p* states is significant, with more pronounce splitting of the O *2p* states. When the local environment is all Pu atoms [Figure 4.11(b) and Figure 4.11(d)], we see a shift of the O *2p* states to lower energies below the Fermi energy, coupled with very little hybridization between the Pu *5f* and O *2p* states, while there is some hybridization of the Pu *6d*, and no splitting of the O *2p*. Furthermore, Figure 4.11(b) and (d) show that the Pu *5f* and *6d* slightly become more broadened when compared to the PDOS for the bare Pu *5f* and *6d* states. These findings further support the notion that O prefers an all Pu environment and that the splitting of the O *2p* states is due to the presence of Ga.

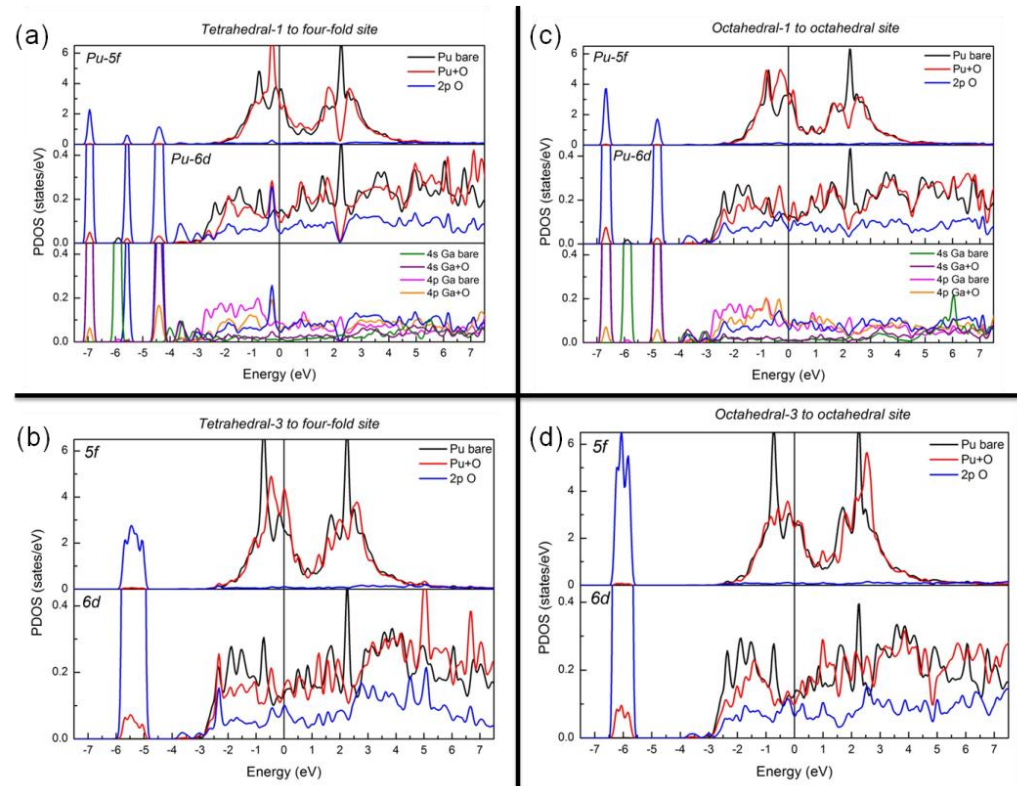


Figure 4.11: PDOS for the SOC level of theory for the least favorable interstitial site, tetrahedral-1 and octahedral-1 [(a) and (c), respectively], and most favorable site, tetrahedral-3 and octahedral-3 site [(b) and (d), respectively], for when the O adsorbate is initially placed in an interstitial site.

Finally a three-dimensional difference charge density plot is shown in Figure 4.12 for the Pu-terminated bridge-to-fcc site and for the PuGa-terminated bridge-PuGa-to-four-fold site. The difference charge density was computed as  $\Delta n(r) = n(\text{Pu-Ga} + \text{O}) - n(\text{Pu-Ga}) - n(\text{O})$ , where  $n(\text{Pu-Ga} + \text{O})$  is the total charge density of the Pu-Ga system with adsorbate O,  $n(\text{Pu-Ga})$  is the total charge density of the Pu-Ga slab, and  $n(\text{O})$  is the charge density of the O atom. In the computations of  $n(\text{Pu-Ga} + \text{O})$ ,  $n(\text{Pu-Ga})$ , and  $n(\text{O})$ , respective positions of the constituent atoms remained invariant.  $\Delta n(r)$  provides a real space picture for assessing the redistribution of electron density due to the adsorption process. In Figure 4.12(a), we notice electron density accumulation around the O atom (red regions) and electron density depletion around the Pu (blue regions). The electron density redistribution is further evidence by the data reported in Table 4.6, which are the net valence partial charges (computed inside the muffin tin spheres) for the O adsorbate and the neighboring Pu atoms. For the Pu atoms, the net valence partial charges were calculated by taking the difference between the partial charges after O adsorption and the partial charges with no O present. For O, the difference is between the partial charge in the adsorbed state and the partial charges of the isolated atomic oxygen. A net reduction in the charge on all Pu atoms can be clearly seen in Table 4.6, while a corresponding increase can be seen in the O atom. This is in agreement in the charge density redistribution plot in Figure 4.12(a). Interesting enough, Figure 4.12(b), where the O atom is four-fold coordinated with three Pu atoms and one Ga atom, shows charge

accumulation around the O atom while the Pu and Ga atoms are losing charge, while the net valence partial charges in Table 4.6 indicate that the charge transfer effects are still prevalent when Ga is involved in the bonding process, the net valence partial charge is less than the aforementioned site. Therefore, although the interaction is still there, the Ga atom seems to suppress Pu atoms to transfer significantly more charge to the O atoms.

Table 4.6: Net valence partial charges for the Pu-terminated bridge-to-fcc site and PuGa-terminated bridge-PuGa-to-four-fold site.

Surface	Initial site	Atom	Net Valence charge
Pu-terminated	bridge	Pu	-0.049
		Pu	-0.029
		Pu	-0.019
		O	0.266
PuGa-terminated	bridge-PuGa	Pu	-0.045
		Pu	-0.062
		Pu	-0.038
		Ga	0.008
		O	0.186

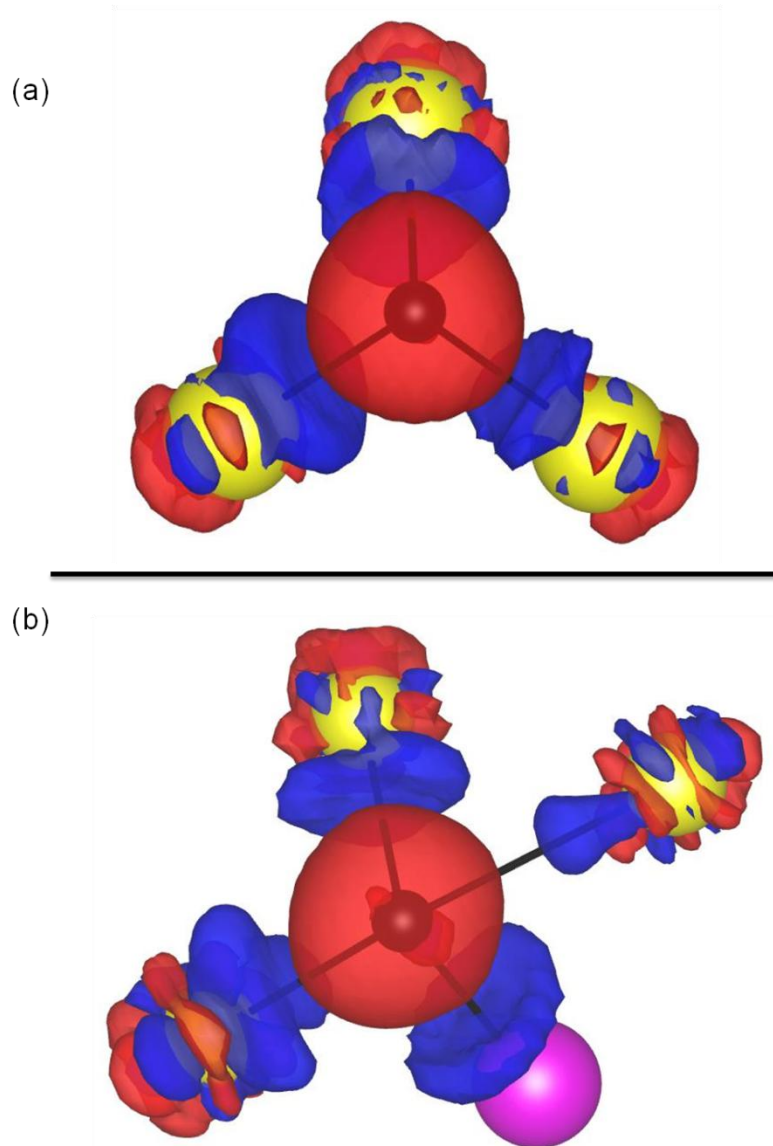


Figure 4.12: Three-dimensional  $\Delta n(r)$  for the bridge-to-fcc site (a) for the Pu-terminated surface, and for the PuGa-terminated surface the bridge-PuGa-to-four-fold site (b). Only the coordination environment around the O-atom is shown. Regions of red indicate charge accumulation, while regions of blue indicate charge depletion. Isosurface level is  $0.0337 \text{ e}^-/\text{cubic } \text{\AA}$ .

## 4.3 Results and Discussions

Oxygen adsorption on 9.375 at. % Ga stabilized  $\delta$ -Pu (111) surface

### 4.3.1 Relaxation and stability of 9.375 at. % Ga $\delta$ -Pu (111) surface

We commence our results and discussion on the relaxation of the bare Pu-Ga surface, which yielded  $\Delta d_{12}/d_o = -4.4\%$ ,  $\Delta d_{23}/d_o = -2.8\%$ , and  $\Delta d_{34}/d_o = -2.7\%$ , where  $d_o$  is the bulk optimized interlayer distance and  $\Delta d_{ij}$  is the interlayer separation between layer  $i$  and layer  $j$  (the topmost layer is layer 1). The  $d_1$  layer had one Ga atom and the  $d_3$  layer had two Ga atoms. Also after relaxation very small local lateral distortions were observed ( $\sim 0.009$  Å) and all Ga atoms remained in-planer to their respective layer. Comparing the PuGa-terminated surface to the previous 9.375 at. % Ga bulk results [108], we observe that the local distortion induced by Ga is similar. Table 4.7 shows the structural analysis of the surface compared to the bulk. When calculating the ratio between the relaxed bond lengths to the unrelaxed bond lengths,  $d_{fcc}/d_{unrelax}$ , of the Pu-Ga and Pu-Pu bonds in the first nearest neighbor shell around the Ga, this yielded an average of 0.985 and 0.983, respectively. For the bulk, the ratios for Pu-Ga and Pu-Pu bonds were 0.993 and 0.996, respectively. Also, the bulk Pu-Ga yielded an average Pu-Ga and Pu-Pu bond contractions of 0.022 Å and 0.013 Å, respectively, whereas the corresponding bond contractions on the surface were 0.049 Å (Pu-Ga bonds) and 0.036 Å (Pu-Pu bonds). Therefore, the bond length contraction was more prevalent in the surface than the bulk. In addition, the short-range disorder observed on the surface was more so than the bulk

counterpart. The normalized Pu-Ga and Pu-Pu bond length standard deviations, which is a measurement of structural disorder, for the surface was 0.019 and 0.042, respectively, whereas in the bulk the standard deviations were 0.012 (Pu-Ga bonds) and 0.010 (Pu-Pu bonds). Therefore, like the bulk, the surface better retained the overall crystal structure, while compensating the structural disorder. Also, there were little or no lateral relaxations of the Pu-Ga surface.

Table 4.7: Structural analysis of the first nearest neighboring shell around the Ga atom in the 9.375 at. % Ga bulk and surface system. The division of the bond length distance in the final relaxed structure by the bond length distance of the pristine structure is defined by  $d_{relax}/d_{fcc}$ ,  $\sigma$  is the standard deviation of the bond lengths, and the average bond length contractions are tabulated. Bulk data was obtained from Ref. 108.

System	Bond Length Type	$d_{relax}/d_{fcc}$	$\sigma$	Average Bond length contractions (Å)
Bulk	Pu-Ga	0.993	0.012	0.022
	Pu-Pu	0.996	0.010	0.013
Surface	Pu-Ga	0.985	0.019	0.049
	Pu-Pu	0.983	0.042	0.036

Overall, the 9.375 at.% Ga surface was structurally more stable than the 3.125 at. % Ga; the ratios of the Pu-Ga and Pu-Pu bonds between the relaxed and unrelaxed structure were lower and the bond length contractions were higher than the 9.375 at.% Ga surface.

The stability of the surface was further proven by the dropped in *surface relaxation energy* to 0.12 eV/Ga-atom from 0.19 eV/Ga-atom for the 3.125 at. % Ga surface. Therefore, this decrease in surface relaxation energy from the lower Ga concentrated surface to the higher Ga concentrated surface indicates that Ga provides the same stabilizing effect on the surface, by retaining the symmetry of the (111) surface. Similar effect was found in bulk  $\delta$ -Pu, where the relaxation energy dropped from 0.14 eV/Ga-atom to 0.05 eV/Ga-atom for the 3.125 and 9.375 at. % Ga concentration [108]. Also we showed in Section 4.2.1 on page 106, which the stability of the surface increased with increasing Ga concentration by the observation of decreasing formation energies and surface energies as the Ga concentration increased. Thus we conclude with that fact that the inclusion of Ga not only stabilizes the bulk, but also stabilizes the surface.

#### *4.3.2 Adsorption on Pu-terminated surface*

Table 4.8 shows the results of O adsorbed on the Pu-terminated surface. Reported in Table 4.8 are the relaxation energies, adsorption energies at the NSOC and SOC levels of theory, the optimized perpendicular distance of the adsorbate from the surface, and the nearest neighbor distances of the adsorbate from the surface

atoms. Note that “site over atom” refers to the O atom is placed over either a Pu or Ga atom in the sub-surface. This distinction is made since when the O is approaching this side of the surface, two Ga atoms are located within the second layer from the O atom.

Table 4.8: Relaxation energy,  $E_r$ , chemisorption energy,  $E_c$ , at the NSOC and SOC level of theory, and distance of the adatom from the surface,  $r_{slab-O}$ , and distance of the adatom to the nearest neighboring Pu atoms,  $r_{Pu-O}$ , for the Pu-terminated surface sites.

Pu-terminated			NSOC	SOC		
Initial site	Final site	$E_r$ (eV)	$E_c$ (eV)	$E_c$ (eV)	$r_{slab-O}$ (Å)	$r_{Pu-O}$ (Å)
top	top	-0.48	-3.40	-3.33	1.86	1.86
hcp over Pu	hcp over Pu	-0.85	-4.90	-4.74	0.93	2.22, 2.25, 2.28
hcp over Ga	hcp over Ga	-0.58	-4.57	-4.54	1.38	2.24, 2.28, 2.29
fcc	fcc	-0.99	-5.13	-5.06	0.97	2.23, 2.24, 2.29
bridge	four-fold	-0.94	-4.62	-4.47	0.97	2.21, 2.22, 2.58, 2.62

The least favorable site was the top site, with SOC chemisorption energy of -3.33 eV; which has been seen in previous works [79, 80]. In comparison to O adsorption on the 3.125 at. % Ga (111) surface, the adsorption energy increased by 0.15 eV. The most favorable site is the fcc over a Pu atom site, which SOC chemisorptions energy yielded -5.06 eV. Also from Table 4.8 the chemisorption energies between the NSOC and SOC level of theory slightly increased by 0.03-0.16 eV, thus supporting reports that equilibrium scalar relativistic and SOC-inclusive geometries are quite similar [79, 105]. For the top, hcp over Pu/Ga, and fcc over Pu sites the O atom remained at the initial sites, while distorting the local environment. Interesting enough, unlike the bridge site in the 3.125 at. % Ga surface, where the initial bridge site of the O adsorbate moved to a final fcc site, the final site for the O atom for 9.375 at. % Ga bridge site was four-fold coordinated. Therefore, contrasting from the 3.125 at. % Ga surface, the bridge site did not help mediate the O atom to the lowest energy pathway, instead the final geometry for the 9.375 at. % Ga surface had oxygen-induced local distortions. The bond length of the atoms forming the bridge site expanded from 3.18 Å to 3.79 Å and was coupled with contractions in all interlayer spacings. This expansion in the bridge site was 0.25 Å greater than the expansion of the bridge site seen in the 3.125 at. % Ga concentration slab. As seen in our previous work for O adsorption on the 3.125 at. % Ga surface, oxygen induced distortions are noted and have also been seen from the recent work

of Taylor [81]. However, due to the high adsorbate coverage of 1 ML in Taylor's results as opposed to 0.125 ML in this work, the amount of distortion seen were not  $\alpha$ -like as proposed by Taylor. The final distance of the adatom from the slab was 0.97 Å for the bridge-to-four-fold site, resulting in an average neighboring Pu-O distance of 2.41 Å, where the O adatom was closer to the slab and Pu-O distances were longer than the 3.125 at. % Ga results, which had a final distance of 1.11 Å and an average Pu-O bond length of 2.25 Å. In comparison to the 3.125 at. % results, we see that the final distance of the O adatom remains the same for the top site, but decreases for all other similar sites (i.e. hcp/fcc over Pu and bridge sites).

For the hcp over Ga, the chemisorptions energy was the least favorable of the hollow sites and the distance of the O adatom from the surface was greater than all other hollow sites, with a distance of 1.38 Å. In addition, the average Pu-O bond lengths also increased for the hcp over Ga site from the other hollow sites, from 2.25 Å to 2.27 Å. Therefore, the presence of Ga in the second layer within the slab from the adsorbate affected the adsorption of O even though the local coordination environment was Pu-rich. The effects of Ga will be elucidated in the next section. As seen in the previous work for the 3.125 at. % Ga surface adsorption study, all distances of the O atom from the surface were lower than those reported in previous published adsorption studies, with the exception of the top site [79]. Therefore, we conclude here that to achieve an appropriate description of the distance of the O from the slab and any structural distortions that may be present, constrained-free atomic

relaxations are *necessary* to accurately describe the adsorption geometries. Initial and final sites are presented in Appendix D on page 212.

#### 4.3.3 Adsorption on PuGa-terminated surface

Table 4.9 shows the results for O adsorbed on the PuGa-terminated surface, where when the O is approaching this surface, Ga is located in the topmost surface and two Ga atoms are located in the third layer from the O atom. Note that in Table 4.9, we have adopted the nomenclature of site-Pu, site-Ga, or site-PuGa, thus indicating whether the initial site has Pu, Ga, or both (PuGa) atoms as coordination atoms to the O atom. The final site does not make this distinction, since the last column indicates the final coordinating atoms with O.

Table 4.9: Results for PuGa-terminated surface sites, which include relaxation energy,  $E_r$ , chemisorption energy,  $E_c$ , at the NSOC and SOC level of theory, and distance of the adatom from the surface,  $r_{slab-O}$ , and distance of the adatom to the nearest neighboring atoms,  $r_{X-O}$ , where  $X$  is the atom that is nearest to the adatom. In the last column if atom is not designated by parenthesis it is assumed that it is a Pu atom.

PuGa-terminated			NSOC	SOC		
Initial site	Final site	$E_r$ (eV)	$E_c$ (eV)	$E_c$ (eV)	$r_{slab-O}$ (Å)	$r_{X-O}$ (Å)
top-Pu	fcc-Pu	-2.09	-5.08	-4.96	1.15	2.19, 2.26, 2.34
top-Ga	top-Ga	-0.76	-1.89	-1.64	1.82	1.82(Ga)
hcp-Pu	hcp-Pu	-0.76	-4.90	-4.80	1.15	2.20, 2.26, 2.35
hcp-PuGa	fcc-Pu	-1.80	-5.07	-5.01	1.02	2.18, 2.27, 2.29
fcc-Pu	fcc-Pu	-0.99	-5.02	-4.92	1.07	2.22, 2.23, 2.32
fcc-PuGa	hcp-Pu	-1.54	-4.97	-4.79	1.08	2.16, 2.26, 2.37
fcc-Pu over Ga	fcc-Pu over Ga	-0.82	-4.89	-4.76	0.96	2.22, 2.26, 2.27
bridge-Pu	four-fold	-1.04	-4.74	-4.58	1.10	2.21, 2.23, 2.44, 3.00
bridge-PuGa	hcp-Pu	-1.90	-4.90	-4.75	1.12	2.22, 2.26, 2.31

The least favorable site was the top-Ga site, with SOC chemisorptions energy of -1.64 eV and with the farthest distance from the slab of 1.82 Å for the PuGa-terminated surface. The most favorable site was the hcp-PuGa-to-fcc site, similar to the Pu-terminated surface adsorption, with SOC chemisorptions energy of -5.01 eV and distance from the slab of 1.02 Å. There is also an increase of chemisorptions energies from the NSOC to SOC level of theory for all sites. Similar initial adsorption sites for the PuGa-terminated surface as to the Pu-terminated surface, specifically the hcp-Pu, fcc-Pu, and bridge-Pu sites, yielded a decrease in chemisorptions energy in the range of 0.06 eV to 0.14 eV. For the initial top-Pu site, the top-Pu site for the Pu-terminated surface resulted that the O adatom remained at the top site, whereas for the PuGa-terminated top-Pu site the O adatom migrated to a final fcc site. The chemisorptions energy difference between these two sites is 1.63 eV. Thus, due to the Ga presence on the topmost surface and Ga presented within the sub-surface, it enables the O atom to relax from the top-Pu site to a final fcc site, which was not observed in the 3.125 at. % Ga case either. Additionally by observing the last column in Table 4.9, only the top-Ga site had the final site where the O adatom was coordinated with a Ga atom. Therefore, in all other final sites, the O adatom relaxed to a Pu-rich environment, regardless if a Ga atom was initially coordinated with O. This distinction was not seen in the 3.125 at. % Ga results, since the O atom remained coordinated with a Ga atom in all final sites when it was initially placed in a Pu-Ga environment. Hence, the presence of the additional Ga

atoms affected the surface chemistry of the 9.375 at. % Ga, which subsequently effected the final position of O. These results indicates the effect of Ga being located in the sub-surface greatly affected the final relax position.

To further probe these effects, additional locations of the Ga within the sub-surface were investigated. Figure 4.13 illustrates these two additional surfaces. Since the most favorable site was the hcp-PuGa-to-fcc site, for the surfaces presented in Figure 4.13, we only computed the O adatom at the hcp-PuGa site. For the surface in Figure 4.13(a), two possible hcp-PuGa sites were investigated, the O atom over either a Pu or Ga atom located in the sub-surface. The SOC chemisorption energies are shown in Table 4.10. Table 4.10 indicates that when the O atom is initially placed in a Pu-Ga coordinated environment along with being located over a Ga atom in the sub-surface, the chemisorptions energy was not favorable and the O atom was not able to migrate to a Pu-rich environment. Furthermore, when the O atom was located over a Pu atom in the sub-surface and the Ga atoms were either in the second or third layer, the O atom was able to relax to a Pu-rich environment and these chemisorptions energies were more favorable. The fourth case, where the Ga atoms are located in the fourth layer, the O atom remained in its initial site and the chemisorptions energy was not as favorable and this is probably due to the fact, that at this distance the Ga atoms in the fourth layer are screened from the layer that is interacting with the O adatom. This was observed in the bulk study [108], which showed that when two Ga atoms were located at sixth nearest neighboring shells

apart, the Ga atoms were no longer interacting with each other and the stability of the structure was compromised. Therefore, the location of the Ga atoms within the surface and sub-surface is decisive on determining the migration of the O adatom to a Pu-rich environment. Lastly, this effect of O migrating to a Pu-rich region can be explained by the dimer formation energy (Pu-O binding energy is greater than Ga-O), which was discussed at the end of Section 4.2.3 on page 115. To view the final and initial sites, see Appendix D on page 212.

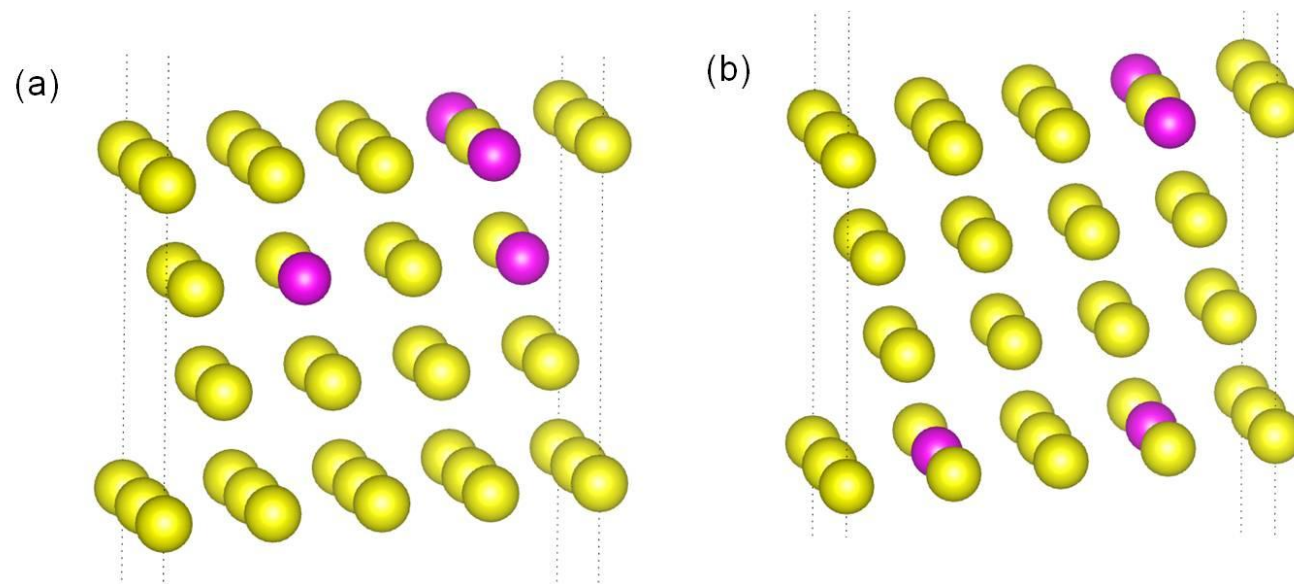


Figure 4.13: Two Ga atoms located in the second layer (a) and fourth layer (b) with respect to the PuGa-terminated surface.

Table 4.10: SOC chemisorption energies for when two Ga atoms are located in a different layer.

Location of 2 Ga	Initial Site	Final Site	SOC E <sub>c</sub> (eV)
2nd-layer	hcp-PuGa over Ga	hcp-PuGa over Ga	-4.16
2nd-layer	hcp-PuGa over Pu	fcc-Pu over Pu	-4.97
3rd-layer	hcp-PuGa over Pu	fcc-Pu over Ga	-5.01
4th-layer	hcp-PuGa over Pu	hcp-PuGa over Pu	-4.26

#### 4.3.4 Interstitial adsorption

Table 4.11 shows the results for the interstitial sites. Note that site-1 is far from the Ga atom and site-2 is near the Ga atom (Figure 4.6). Structural deformations of the O atom in an interstitial site were manifested by expansions of the bond lengths for the coordinating atoms from the initial 2.25 Å and 1.95 Å for the octahedral and tetrahedral sites, respectively. Final bond lengths were in the range of 2.32 Å to 2.57 Å and 2.16 Å to 2.27 Å for the octahedral and tetrahedral sites, respectively. Also the final site of a four-fold coordination shown for the initial tetrahedral-2 site was a distorted tetrahedral site with angles ranging from 95° to 121° and differed from the four-fold final sites for the on-surface adsorption. For the latter sites, the four-fold coordination is in-plane to the topmost surface and is a non-tetrahedral site, where the angles differ significantly from a tetrahedral configuration of 109.5°. Also all other final interstitial sites also were a distorted, since angles differed by 0.40% to 13.28% for the final tetrahedral sites and 0.38% to 13.79% for the octahedral sites. Thus the distortions were about the same for the final tetrahedral and octahedral sites. The distortion for the final octahedral sites were slightly worse than the distortions seen for the 3.125 at. % Ga surface results, but the final tetrahedral sites were not as distorted as the 3.125 at. % Ga surface results.

The chemisorption energies results indicate that regardless of whether O is in a Pu-rich region or Pu-Ga region, the chemisorptions energies are not as favorable as to the on-surface results. Hence, O prefers to be three-fold on-surface coordinated,

likewise seen in previous works [78, 79, 80]. Furthermore, when the results are compared to similar interstitial sites in the 3.125 at. % Ga surface, the chemisorption energies for the 9.375 at. % Ga surface have significantly increase. For instance, for the 9.375 at. % Ga surface, the Pu-rich environment for the octahedral-1 and tetrahedral-1 sites yielded SOC chemisorption energies of -4.22 eV and -4.02 eV, respectively, whereas similar sites for the 3.125 at. % Ga surface were -4.55 eV and -4.64 eV, respectively. Alternatively, for the Pu-Ga interstitial environment, the octahedral-2 and tetrahedral-2 sites SOC chemisorptions energies were -3.54 eV and -3.12 eV, respectively, for the 9.375 at. % Ga surface, and similar sites in the 3.125 at. % Ga surface yielded SOC chemisorption energy of -4.02 eV for both Pu-Ga interstitial sites. Therefore, for the 9.375 at. % Ga surface the degree of least favorability of interstitial adsorption is more evident than the O adsorption on 3.125 at. % Ga surface. Thus, the presence of additional Ga within the sub-surface discourages formation of a sub-surface oxide, hence concluding that for the Pu-Ga surface O adsorption prefers to be an on-surface phenomenon. Images of the initial and final sites are in Appendix D on page 212.

Table 4.11: Relaxation energy,  $E_r$ , chemisorption energy,  $E_c$ , at the NSOC and SOC level of theory, and distance of the adatom from the surface,  $r_{slab-O}$ , and distance of the adatom to the nearest neighboring atoms,  $r_{X-O}$ , where  $X$  is the atom that is nearest to the adatom, for the interstitials sites. In last column, if atom is not designated by parenthesis it is

assumed that it is a Pu atom.

Interstitials		NSOC	SOC			
Initial site	Final site	$E_r$ (eV)	$E_c$ (eV)	$E_c$ (eV)	$r_{slab-O}$ (Å)	$r_{X-O}$ (Å)
octahedral-1	octahedral*	-0.60	-4.49	-4.22	-1.17	2.34, 2.36, 3x2.44, 2.47
octahedral-2	octahedral*	-0.48	-3.76	-3.54	-3.73	2.32, 2.35, 2x2.36, 2.37, 2.57(Ga)
tetrahedral-1	tetrahedral*	-0.82	-4.26	-4.02	-2.13	2.23, 2x2.25, 2.27
tetrahedral-2	four-fold	-0.68	-3.36	-3.12	-3.24	2.16, 2.17, 2.19, 2.26(Ga)

\*Final sites were distorted interstitials sites.

#### *4.3.5 Adsorption Probabilities*

Finally, when computing the simple Boltzmann distribution as defined in Section 4.3.5 on page 154, we found that for the Pu-terminated on-surface adsorption probability was 99%, whereas for the PuGa-terminated on-surface adsorption probability was 82%. These probabilities differ from the 3.125 at. % Ga on-surface adsorption probabilities, which were 93% for the Pu-terminated and 99% for the PuGa-terminated surface. Overall these probabilities indicate that for the 3.125 at. % Ga probabilities, the Pu-terminated surface had more potential to have O diffusion into the sub-surface, if O was able to overcome the potential barrier. For the PuGa-terminated surface the majority of O would be adsorb on the surface. Now for the 9.375 at. % Ga probabilities, the probability of on-surface adsorption increased for the Pu-terminated surface, while the PuGa-terminated surface probability decreased. This indicates that due to the presence of Ga in the second layer from the adsorbate, when the adsorbate is approaching the Pu-terminated surface, Ga enhanced the ability of the adsorption to remain on-surface. For the PuGa-terminated surface, the presence of Ga on the topmost surface and on the third layer from the adatom, allowed the adatom to migrate from a PuGa environment to a Pu-rich environment on the surface, which was not seen in the 3.125 at. % Ga adsorption results, and since the next sub-surface layer was all Pu atoms, the ability of O to diffuse in the sub-surface becomes slightly more possible than the PuGa-terminated results from the 3.125 at. % Ga case. For this reason, the inhibition of O diffusion into the sub-

surface might be achieved with the presence of Ga being in subsequential layers from the reactive top-most layer. Either way the high probabilities indicate that O diffusion is an activated process, or a significant amount of O dosing would be need. In addition, the surface chemistry of the Pu-Ga surface can greatly influence the adsorption of O on the surface, even at these low atomic concentrations of Ga.

#### 4.3.6 *Electronic structure analysis*

Our discussion on the electronic structure will focus on adsorption sites that were the least and most preferred sites for both the Pu-terminated and PuGa-terminated surfaces. In Figure 4.14, the PDOS are shown for the Pu-terminated top and fcc site. Note that the PDOS illustrates that the Pu bare (Ga bare) are the Pu (Ga) atoms PDOS before adsorption and Pu+O (Ga+O) are the Pu (Ga) atoms PDOS after adsorption with O and only the atoms that are coordinated with O are plotted. The PDOS for the top site [Figure 4.14(a)] shows that the O  $2p$  states are at a higher energy, while the Pu  $5f$  states are slightly shifted below the Fermi energy from the Pu bare  $5f$  states. The Pu  $6d$  states are hybridizing with the O  $2p$ , while splitting of the O  $2p$  states into sub-bands are noted. For the Pu-terminated fcc site PDOS [Figure 4.14(b)], the O  $2p$  states have shifted to lower energies and there is a decrease in intensity of the Pu  $5f$  and  $6d$  states, with hybridization with the O  $2p$  states. Similarly we see the O  $2p$  states splitting into sub-bands. Figure 4.14(b) also shows a decrease of intensity of the Pu  $5f6d$  states at the Fermi level. The trend of the O  $2p$  states to lower energies with favorable chemisorption energy is in good agreement with

previous works [14,15,29]. Interesting though is that the splitting feature of the O  $2p$  states observed in Figure 4.14 is also featured in the 3.125 at. % Ga adsorption results, but these features were observed only for when the adatom was adsorbed on the PuGa-terminated surface. Further analysis is shown in Figure 4.15, which shows the nearest neighboring Ga atom to the Pu atom for the top site. The bond distance for Pu-Ga was 3.17 Å and the Ga was a distance of 4.76 Å from the O atom. In Figure 4.15, we notice that although Ga is not directly participating in bonding with the O atom, it does have slight influence on the electronic structure of the Pu atom. Therefore, due to the increase of Ga atoms in the 9.375 at. % Ga surface, this allowed for the Pu  $6d$  states to readily participate in bonding through an indirect influence from the Ga. This was shown in the previous bulk results [108], which indicated that with increasing Ga concentrations the Pu  $6d$  states decreased in intensity, by hybridizing with the Ga  $4p$  electrons. Even though Ga is not present in the Pu-terminated surface, the Pu atoms that are coordinated with the O are within nearest neighboring distance to a Ga atom located in the sub-surface. Hence, Ga enables the Pu  $6d$  states to hybridize with the O  $2p$  states.

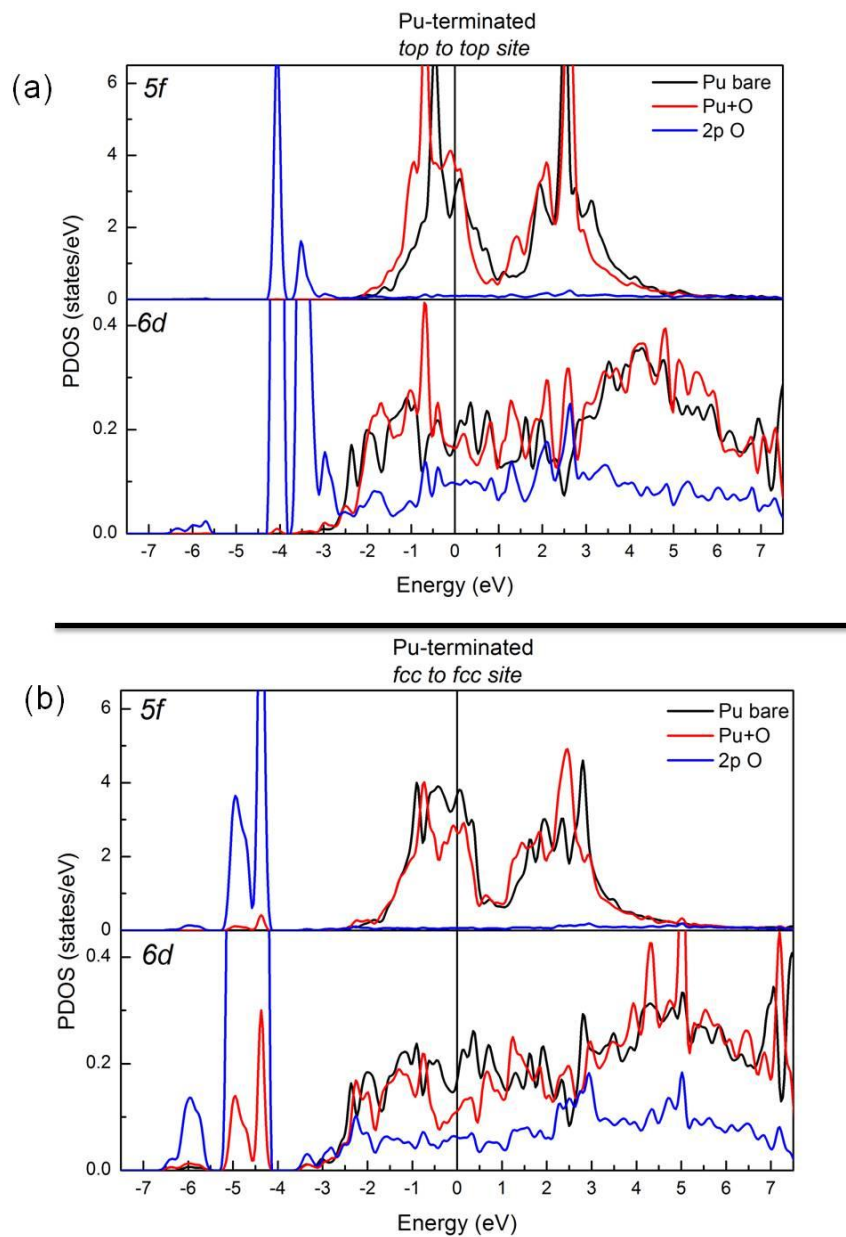


Figure 4.14: PDOS for the SOC level of theory for the least favorable site, top site (a), and most favorable site, fcc site (b), for when the O adsorbate is approaching the Pu-terminated surface.

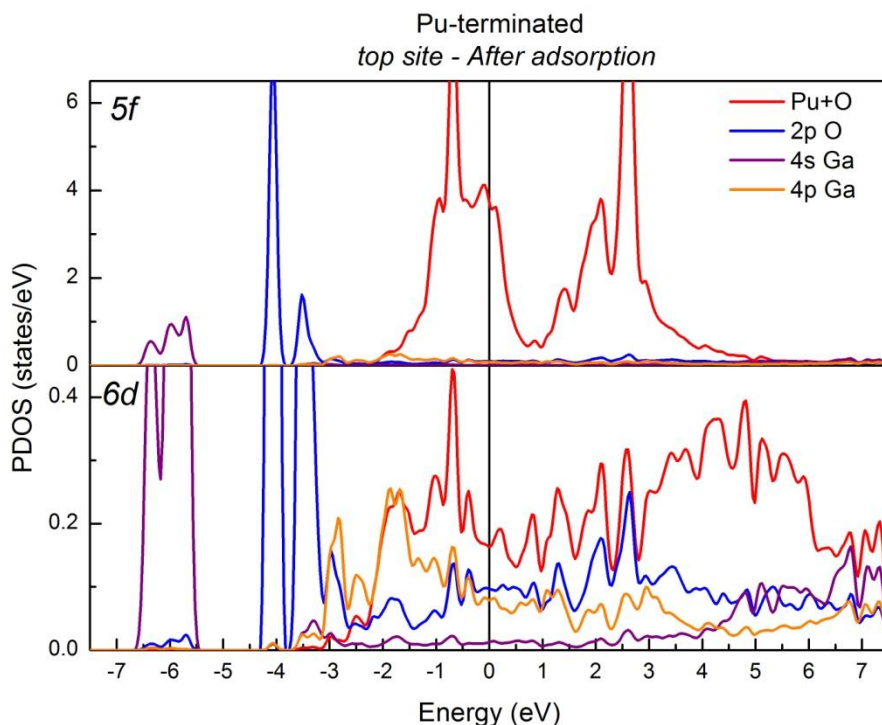


Figure 4.15: PDOS for the Pu  $5f$  and  $6d$  state and nearest neighboring Ga atom  $4s$  and  $4p$  states, and O  $2p$  states for the Pu-terminated top site after adsorption.

For the least and most energetically favorable sites for the PuGa-terminated surface, the top-Ga site [Figure 4.16(a)] PDOS shows strong hybridization of the Ga  $4s4p$  states with the O  $2p$  states, with also a decrease in intensity at the Fermi level for the Ga  $4p$  states. These features are similar to the features observed for the top-Ga site for the 3.125 at. % Ga results. For the most favorable site, hcp-PuGa-to-fcc site [Figure 4.16(b)] PDOS depicts that the O  $2p$  states hybridizing with the Pu  $5f$  and  $6d$  states, with a reduction of magnitude of the Pu  $5f$  and  $6d$  states. These features were not observed in the 3.125 at. % Ga results, instead the Pu  $5f$  states

retained the degree of intensity, thus indicating that Ga was suppressing the Pu  $5f$  electrons to hybridize with the O. This claim cannot be concluded for the PuGa-terminated surface, but like we discussed above the presence of Ga enhanced the ability of the Pu  $6d$  to hybridize with the O  $2p$ , in addition to slightly affecting the  $5f$  electrons indirectly. To further elaborate, as mentioned in Section 1.3 on page 6, there are strong hybridized  $d-f$  character in pure  $\delta$ -Pu (no Ga present) [42, 43] and that the postulation that with the inclusion of Ga the “stabilization mechanism” of  $\delta$ -Pu to room-temperature is provided by the fact that the presence of Ga tends to shift the Fermi level a way that decreases the  $f$ -bonding nature, subsequently enhancing the  $d$ -bonding characteristics [44]. Also in Pu<sub>3</sub>Ga it was observed that there was covalent bonding in the Pu  $d-f$  state with the Ga  $p$  state [46]. Moreover our previous bulk study indicated that the Pu  $5f$  states remained unaffected in the presence of Ga, while the Pu  $6d$  states hybridized with Ga  $4p$  states with increasing Ga concentrations [108]. Thus, by observing the nearest neighboring Ga atom PDOS (Figure 4.17) in conjunction with the PDOS in Figure 6b, we observe that Ga only had minimal effect on the  $5f$  electrons before O absorption, whereas after O absorption the Ga enhanced the  $d$ -bonding in Pu, while also indirectly affecting the Pu  $5f$  states. As result that the 9.375 at. % Ga is close to the boundary of forming Pu<sub>3</sub>Ga, the presence of the O adatom contributed slightly to allowing the slight indirect hybridization of Pu  $5f$  and  $6d$  states with the Ga  $4p$  states.

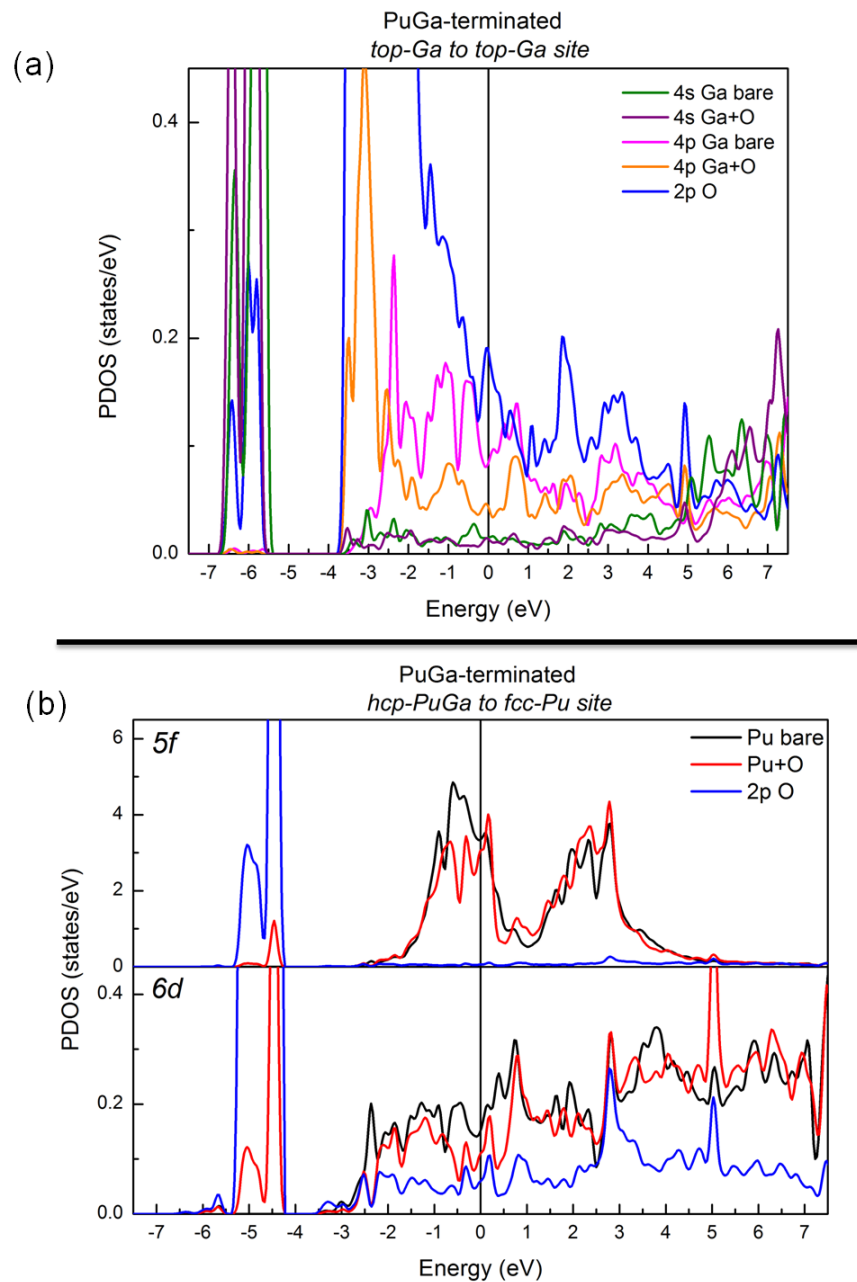


Figure 4.16: PDOS for the SOC level of theory for the least favorable site, top-Ga (a), and most favorable site, hcp-PuGa-to-fcc (b), for when the O adsorbate is approaching the PuGa-terminated surface.

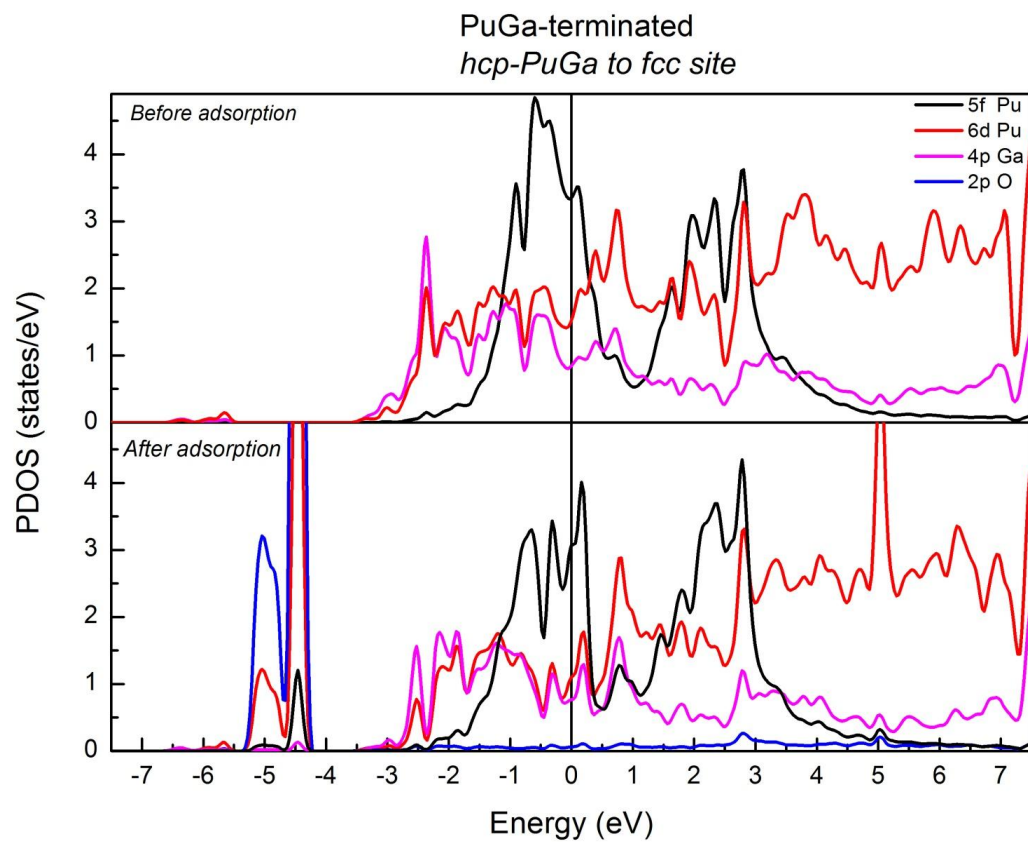


Figure 4.17: PDOS for hcp-PuGa to fcc site before and after O adsorption with nearest neighboring Ga atom plotted.

Pu-Ga bond is 3.18 Å and Ga-O bond was 4.09 Å.

In Figure 4.18(a), the most favorable interstitial site, octahedral-1 and tetrahedral-1, where the O atom is in a Pu-rich environment, did not demonstrate the O  $2p$  states splitting into sub-bands. The PDOS for these two sites are similar to the 3.125 at. % Ga cases of where the O adatom is in a Pu-rich environment; there are similar trends, such as the Pu  $5f$  and  $6d$  states become slightly more broaden when compared to the bare Pu  $5f6d$  sates. Not shown in Figure 4.18(a) is that after adsorption the nearest neighboring Ga atom to the Pu atoms that are coordinated with the O atom PDOS shows that the Ga  $4p$  states are *not* hybridizing with the Pu  $6d$  at the lower energy regimen with the O  $2p$  states, but the Ga  $4p$  states are hybridizing with Pu  $6d$  states at higher energies. Therefore, the indirect influence of Ga on the Pu  $6d$  states is not seen here. The trends of the 3.125 at. % Ga adsorption results, for when Ga is a coordinating atom to the O adatom remain the same for the 9.375 at. % Ga interstitial results. Figure 4.18(b), show that the Pu  $5f$  states are consistent when compared to the bare Pu  $5f$  states, whereas we see here that the Ga  $4s$  and  $4p$  and Pu  $6d$  states are hybridizing with the O  $2p$ . Therefore, in the interstitial sites, when a Ga atom is participating in bonding with the O atom, the Pu  $5f$  states have no or little interaction with the O  $2p$  states, while the Pu  $6d$  states slightly hybridize with the O  $2p$  states. In summary, when the O adatom was adsorb on an on-surface site, the addition of more Ga in the slab, enhance the ability of the Pu  $6d$  and somewhat the Pu  $5f$  states to hybridized with the O  $2p$  states, but this was not seen in the interstitial adsorption sites. In comparison to when the O adatom is absorbed on a pure Pu slab,

previous results indicated no splitting of the O  $2p$  states into sub-bands, while hybridization of the Pu  $6d$  and O  $2p$  with admixture of Pu  $5f$  states and a reduction of the  $5f$  PDOS, which could possibly lead to further broadening of the  $5f$  electrons, were noted [79].

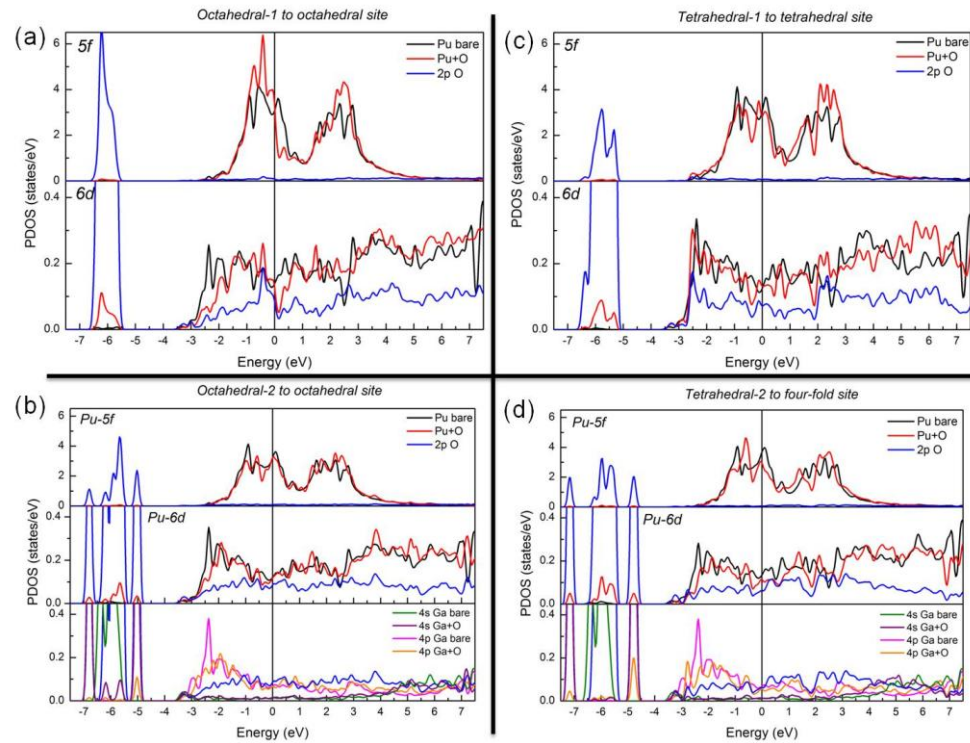


Figure 4.18: PDOS for the SOC level of theory for the most favorable interstitial site, tetrahedral-1 and octahedral-1 [(a) and (c), respectively], and least favorable site, tetrahedral-2 and octahedral-2 site [(b) and (d), respectively], for when the O adsorbate is initially placed in an interstitial site.

Representative three-dimensional difference charge density plots of the most favorable site, the Pu-terminated fcc site, and a site where Ga and O are bonded, the tetrahedral-2 site, are shown in Figure 4.19. The difference charge density was computed as stated in Section 4.2.7. Figure 4.19 provides a real space picture for assessing the redistribution of electron density after the adsorption process. In Figure 4.19(a), we notice electron density accumulation around the O atom (red regions) and electron density depletion around the Pu (blue regions). Figure 4.19(b), where the O atom is four-fold coordinated with three Pu atoms and one Ga atom, shows charge accumulation around the O atom while the Pu and Ga atoms are losing charge. To further quantify the charge accumulation of O, we observe that the net valence partial charges, which are calculated within the muffin tin spheres, showed that for the O atom in both systems had a net valence charge of 0.20. Thus, verifying that the O atom is accumulating charge from its surrounding neighbors.

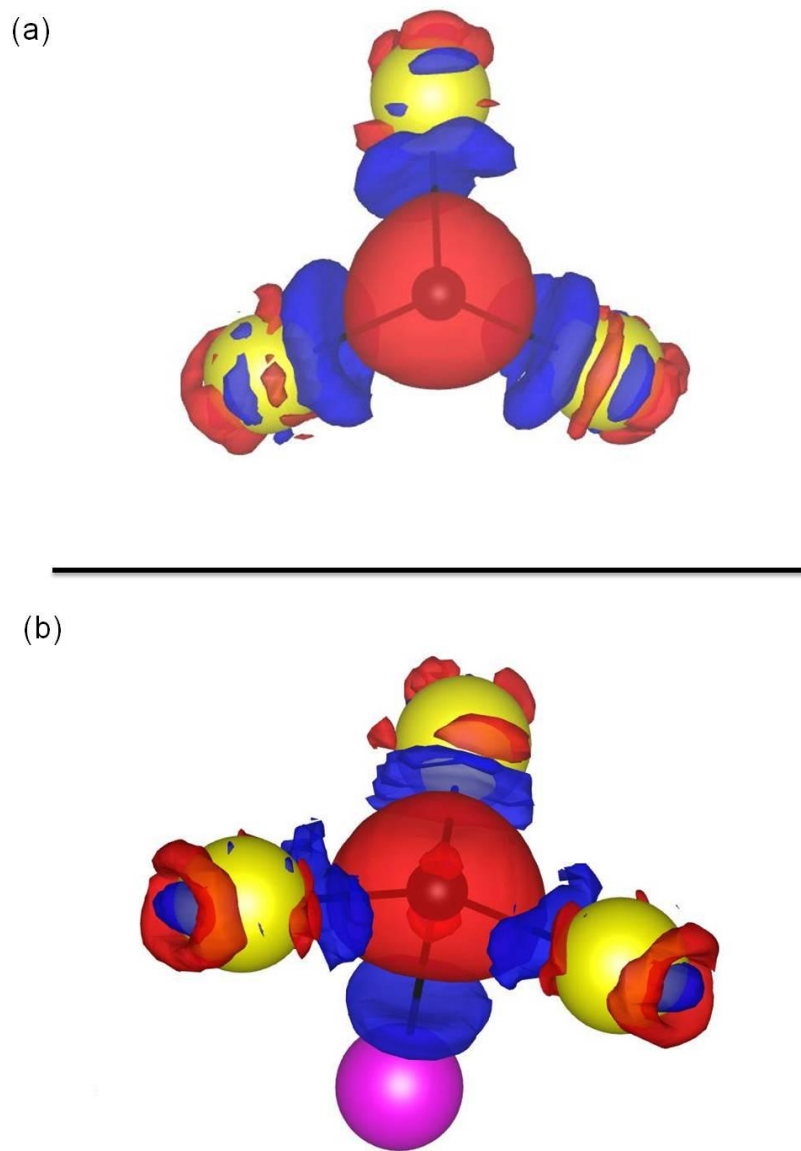


Figure 4.19: Three-dimensional  $\Delta n(r)$  for the Pu-terminated fcc site (a), and for the interstitial tetrahedral-2 site (b). Only the coordination environment around the O-atom is shown. Red indicates charge accumulation (positive), blue indicates charge depletion (negative). Isosurface level is  $0.0337 \text{ e}^-/\text{cubic } \text{\AA}$ .

Also in Table 4.12, the results on the adsorbate-induced work-function changes with respect to the clean Pu-Ga surface, calculated by the equation in Section 4.2.6 on page 121. The work function changes for the interstitials sites are not shown, because  $\Delta\phi$  was negligible (on the order of 0.01 eV). The least preferred sites, Pu-terminated top site and PuGa-terminated top-Ga site have the largest change in work function, while the most preferred sites, hcp and fcc, have the lowest change in work function. These trends agree well with previous works [78, 79, 80]. Thus, the electron charge transfers seen in Figure 4.19 agree with the change in the net valence increase for the O adatom and for the adsorbate-induced work-function shifts

Table 4.12: Changes in work function,  $\Delta\phi$ , at the NSOC and SOC levels of theory. The work function for the clean relaxed Pu-Ga slab was 3.32 eV and 3.39 eV, respectively, at the NSOC and SOC level of theory. Experimental work function is 3.2 eV for stabilized  $\delta$ -Pu [36].

		NSOC	SOC
		$\Delta\phi$	$\Delta\phi$
Initial site		(eV)	(eV)
Pu-terminated	top	0.25	0.25
	hcp over Pu	0.07	0.06
	hcp over Ga	0.13	0.13
	fcc over Pu	0.09	0.07
	bridge	0.04	0.05
PuGa-terminated	top-Pu	0.06	0.05
	top-Ga	0.18	0.17
	hcp-Pu	0.11	0.10
	hcp-PuGa	0.09	0.09
	fcc-Pu	0.09	0.09
	fcc-PuGa	0.09	0.08
	fcc over Ga	0.07	0.07
	bridge-Pu	0.08	0.08
bridge-PuGa	0.12	0.11	

## Chapter 5

### Atomic H adsorption on Ga stabilized $\delta$ -Pu (111) surface

#### 5.1 Computational Details

DFT and the FP-L/APW+lo basis method as implemented within the *WIEN2k* code was used to carry out the calculations [99]. PBE formulation of the GGA to exchange-correlation functional [97] was also used. To describe the *s*, *p*, *d*, and *f* states ( $l=0, 1, 2, 3$ ), APW+lo basis functions were employed, along with the LAPW basis for all other higher orders of angular momentum states up to  $l_{wf}^{max} = 10$  in the expansion of the wave functions. Additionally, the Pu  $6s$  and  $6p$  semi-core states had local orbitals (LO) added to them.

The surface was constructed identically to the surfaces used for the oxygen adsorption study. In addition, the hydrogen adsorbate was placed in sites that were identical to the oxygen initial sites. To see initial sites and final sites after relaxation, see Appendix E on page 220 and Appendix F on page 226 for the 3.125 and 9.375 at. % Ga surface sites, respectively. The *WIEN2k* parameters were kept consistent with previous adsorption studies on a pure Pu surface and a Pu-Ga surface [79, 80, 117, 118]. The *WIEN2k* parameters were a RMT of 1.127 Å, 1.032 Å, and 0.318 Å for Pu, Ga, and H, respectively, and a planewave kinetic energy cutoff of  $K_{max}^2 = 212$  eV for the expansion of the wave function within the interstitial region. Due to previous theoretical works [108] and a k-point convergence test on the surface, a k-point mesh of 2x4x1 and a temperature broadening parameter of  $k_B T = 0.068$  eV were chosen.

The convergence criteria for the total energy and charge were  $1.36 \times 10^{-4}$  eV and  $1 \times 10^{-3} e^-$ , respectively. The molecular H<sub>2</sub> total energy, which was used for calculating the adsorption energy, was computed in a 10.58 Å box and at the  $\Gamma$  k-point.

Full geometry relaxations were performed at the scalar relativistic level of theory. The relaxations of the atomic positions were terminated when the maximum Hellman-Feynman force on each atom was less than 0.051 eV/Å. A single-point calculation was performed with the inclusion of SOC on the optimal scalar relativistic geometries. SOC interactions were implemented through a second variational scheme using the scalar relativistic eigenstates as a basis with all eigenstates with the inclusion of energies below 61.2 eV [103]. SOC effects were only included on the Pu atoms.

*Chemisorption energy* was calculated by  $E_c = E_{PuGa+H} - E_{PuGa} - 1/2 * E_{H2}$ , where  $E_{PuGa+H}$  is the total energy of the Pu-Ga surface with H adatom after relaxation,  $E_{PuGa}$  is the total energy of the relaxed bare Pu-Ga surface with no adsorbate, and  $E_{H2}$  is the total energy of the H<sub>2</sub> molecule. Therefore, if  $E_c < 0$ , then binding is favorable, otherwise it is unfavorable. We also report *relaxation energy*,  $E_r$ , which is defined as  $E_r = E_{relax} - E_{unrelax}$ . Here,  $E_{relax}$  is the total energy of the fully relaxed slab-adsorbate geometry (no constraints) and  $E_{unrelax}$  is the total energy of the slab-adsorbate geometry where only the adsorbate was allowed to relax and the slab atomic positions were constrained.

## 5.2 Results and Discussions

### 5.2.1 Adsorption on Pu-terminated surface

Table 5.1 shows the results for the H atom approaching a Pu-terminated surface. Note that “site over X” indicates that the H atom was coordinated with all Pu atoms, but the location of the hydrogen atom was over X atom in the sub-surface (X could be Pu or Ga). From the table, the H adsorbate was not as reactive as the O adsorbate, since chemisorption energies ranged from -3.33 to -5.06 eV for O adsorption. For the 3.125 at. % Ga surface, the top site was the least favorable and the hcp site was the most favorable with SOC chemisorption energy of 0.12 eV and -0.76 eV, respectively. For the 9.375 at. % Ga surface, the top site was the least favorable and the fcc site was the most favorable with SOC chemisorption energy of 0.14 eV and -0.80 eV, respectively. These results are similar with previous theoretical work of atomic H adsorption on  $\delta$ -Pu (111) surface [84], which concluded that the most preferred site was a hollow three-fold coordinated site. Regardless of Ga concentration, H atom prefers to be absorbed at a hollow site. Interesting enough for the 3.125 and 9.375 at. % Ga surfaces the chemisorption energy for the most favorable site are fairly similar in value (difference of 0.04 eV), but the distance of the H adatom from the surface increased from the lower Ga concentrated surface to the higher Ga concentrated surface, from 1.27 Å to 1.33 Å. There was also an increase in average Pu-H bond length, 2.25 Å to 2.30 Å. Note that the bond length of Pu-H in the PuH<sub>2</sub> is 2.31 Å [6].

Table 5.1: Relaxation energy,  $E_r$ , chemisorption energy,  $E_c$ , at the NSOC and SOC level of theory, and distance of the H atom from the surface,  $r_{slab-H}$ , and bond length of H atom to the nearest neighboring Pu atoms,  $r_{Pu-H}$ , for the Pu-terminated surface sites on the 3.125 and 9.375 at. % Ga slabs.

Pu-terminated				NSOC	SOC		
at. % Ga	Initial site	Final site	$E_r$ (eV)	$E_c$ (eV)	$E_c$ (eV)	$r_{slab-H}$ (Å)	$r_{Pu-H}$ (Å)
3.125	top	top	-0.17	0.22	0.12	2.16	2.16
	hcp	hcp	-0.20	-0.69	-0.76	1.27	2.23, 2x2.26
	fcc	fcc	-0.20	-0.67	-0.73	1.27	2.22, 2.26, 2.27
	bridge	bridge	-0.22	-0.52	-0.53	1.44	2x2.19
9.375	top	top	-0.26	0.22	0.14	2.20	2.20
	hcp over Pu	hcp over Pu	-0.25	-0.67	-0.71	1.31	2.26, 2x2.27
	hcp over Ga	hcp over Ga	-0.26	-0.62	-0.71	1.42	2.23, 2x2.28
	fcc	fcc	-0.20	-0.69	-0.80	1.33	2.27, 2x2.31
	bridge	three-fold	-0.35	-0.46	-0.53	1.49	2.21, 2.22, 2.93

In addition, all distances of the H adatom from the surface increased for the 9.375 at. % Ga surface from the 3.125 at. % Ga surface. Also no migration of the hydrogen atom was observed in the 3.125 at. % Ga surface. For the 9.375 at. % Ga surface, only one site, bridge-to-three fold site, there was some migration of the hydrogen atom. This three-fold site had one long bond length of Pu-H, 2.93 Å, and two short bond lengths, 2.21 Å and 2.22 Å. Thus the migration of hydrogen for this surface was minimal. This is in contrast with the O results, which showed significant migration of the O adatom when placed in a bridge site, bridge-to-fcc site and bridge-to-four-fold site for the 3.125 and 9.375 at. % Ga surfaces, respectively. The bridge site is usually considered a pathway of an adsorbate between two hollow sites, which was observed in the case for oxygen, but not for hydrogen.

### *5.2.2 Adsorption on PuGa-terminated surface*

Table 5.2 shows the results for when hydrogen is approaching the PuGa-terminated surface. Note that terminology used in Table 5.2 to designate a site is site-Pu or site-PuGa. This indicates that the hydrogen atom was either coordinated with all Pu atoms (site-Pu) or coordinated with both Pu and Ga atoms (site-PuGa) and all of these sites correspond to the hydrogen atom placed over a Pu atom in the sub-surface. In addition, similar to the Pu-terminated surface, the “site over X” corresponds to the same type of site as indicated above.

Table 5.2: Relaxation energy,  $E_r$ , chemisorption energy,  $E_c$ , at the NSOC and SOC level of theory, and distance of the H atom from the surface,  $r_{slab-H}$ , and bond length of the H atom to the nearest neighboring atoms,  $r_{X-H}$ . In the last column if atom is not designated by parenthesis it is assumed that it is a Pu atom.

PuGa-terminated			NSOC	SOC			
at. % Ga	Initial site	Final site	$E_r$ (eV)	$E_c$ (eV)	$E_c$ (eV)	$r_{slab-H}$ (Å)	$r_{X-H}$ (Å)
3.125	top-Pu	three-fold	-0.96	-0.52	-0.48	1.38	2.18, 2.26, 2.89
	top-Ga	top-Ga	-0.19	0.20	0.19	1.66	1.66(Ga)
	hcp-Pu	hcp-Pu	-0.22	-0.75	-0.79	1.30	2.26, 2x2.27
	hcp-PuGa	hcp-PuGa	-0.13	-0.15	-0.23	1.20	2x2.16, 2.19(Ga)
	fcc-Pu	fcc-Pu	-0.21	-0.76	-0.78	1.28	2.23, 2x2.27
	fcc-PuGa	fcc-PuGa	-0.21	-0.39	-0.41	1.09	2.08(Ga), 2.19, 2.20
	bridge-Pu	three-fold	-0.27	-0.58	-0.59	1.44	2.19, 2.21, 2.97
	bridge-PuGa	four-fold	-0.37	-0.21	-0.18	1.14	1.78(Ga), 2.27, 2.82, 2.98
9.375	top-Pu	top-Pu	-0.29	0.24	0.14	2.09	2.09
	top-Ga	top-Ga	-0.24	0.23	0.18	1.67	1.67(Ga)
	hcp-Pu	hcp-Pu	-0.24	-0.61	-0.70	1.30	2.24, 2.25, 2.27
	hcp-PuGa	hcp-PuGa	-0.26	-0.20	-0.33	1.20	2.08(Ga), 2.23, 2.24
	fcc-Pu	fcc-Pu	-0.29	-0.66	-0.70	1.28	2.23, 2.26, 2.27
	fcc-PuGa	fcc-PuGa	-0.28	-0.22	-0.31	1.13	1.95(Ga), 2x2.24
	fcc over Ga	fcc over Ga	-0.23	-0.55	-0.64	1.32	2.19, 2x2.28
	bridge-Pu	bridge-Pu	-0.29	-0.39	-0.48	1.50	2.23, 2.24
bridge-PuGa	four-fold	-0.41	-0.12	-0.16	1.16	1.80(Ga), 2.26, 2.83, 2.97	

We commence this discussion by first discussing the differences for each Ga concentration between the Pu-terminated and PuGa-terminated similar sites. For the 3.125 at. % Ga surface, we see that for the top-Pu site, the H atom migrated to a three-fold site and significant relaxation was observed in the slab, with relaxation energy of -0.96 eV. This was not observed with the top site on the Pu-terminated surface. This migration explains why the top-Pu site had SOC chemisorption energy of -0.48 eV and the H atom was closer to the slab with a distance of 1.38 Å. For all other sites similar to the Pu-terminated surface, i.e. initial sites hcp-Pu, fcc-Pu, and bridge-Pu, and although the initial bridge-Pu site had a final three-fold site, the SOC chemisorptions energies and distances from the surface are similar. Energy differences ranged from 0.03-0.06 eV and largest difference in  $r_{\text{slab-H}}$  is 0.03 Å. Therefore, the presence of one Ga at the surface allowed some migration of the hydrogen atom on the surface.

For the sites that included a Ga atom coordinated with the H atom, we observe no apparent migration of the H atom to a Pu-rich environment. Minimal migration was observed for the initial site of bridge-PuGa to four-fold site. In the final four-fold site the longest bond length of the H atom was a Pu-H bond of 2.98 Å and the shortest bond length was a Ga-H bond of 1.78 Å. Regardless, in comparison to all sites where the H atom is located in a Pu-rich environment, the PuGa environment is not favorable, since SOC chemisorption energies yielded 0.19 eV for the top-Ga, -0.18 eV for the bridge-PuGa, -0.23 eV for the hcp-PuGa, and -0.41 eV

for the fcc-PuGa initial sites. Between the “most” favorable site-PuGa and the most favorable site-Pu the energy difference is 0.38 eV, therefore similar to O, the H atom prefers to be coordinated with all Pu atoms. To further probe this conclusion, calculations of binding energies of dimers indicated that from most to least preferred binding energy showed this pattern, Pu-H > Ga-H > Pu-Ga > Pu-Pu. This is indicative that Pu-H bond is stronger than Ga-H and this due to Pu being more electropositive than Ga.

For the 9.375 at. % Ga surface, similar sites for the Pu-terminated surface, the PuGa-terminated surface implies that the Pu-terminated surface was more susceptible to H, since SOC chemisorption energies were higher for the PuGa-terminated surface. Some sites were similar in SOC chemisorption energy, such as the top-Pu site with 0.14 eV and the hcp-Pu site with 0.70 eV, but there was a 0.1 eV difference between the two fcc sites (-0.80 for the Pu-terminated fcc site and -0.70 for the PuGa-terminated fcc-Pu site). We also observe that for the fcc over Ga site, the SOC chemisorption energy increased from the similar fcc-Pu site. Similar for the 3.125 at. % Ga results, all sites that included a Ga as a coordinated atom were not favorable to the Pu-rich sites, with SOC chemisorptions energies of 0.18 eV for the top-Ga site, -0.16 for the bridge-PuGa site, -0.31 eV for the fcc-PuGa site, and -0.33 eV for the hcp-PuGa site. Therefore, with inclusion of more Ga in the surface, this further substantiates that hydrogen prefers a Pu-rich environment. The bridge-PuGa-to-four-fold site showed minor movement of the H atom, while no movement of the

H atom to another site was observed. The fact that there wasn't any migration of the H from the top-Pu site to a hollow site, which was seen in the 3.125 at. % Ga surface case, is because the distance of the Pu atom to Ga atom was around 5.50 Å. In the 3.125 at. % Ga surface top-Pu to three-fold case was due to the fact that the Ga atom was a first nearest neighbor from the Pu atom that the H was interacting to. The distance was 3.20 Å apart. Thus the influence of Ga was stronger in the lower concentrated slab. This was not the case for O adsorption on the 9.375 at. % Ga surface, since the results showed that when oxygen was approaching the PuGa-terminated surface, all initial sites that initially had Ga coordinated with the oxygen atom, the oxygen atom migrated to a Pu-rich environment. Therefore, this indicates the importance of surface chemistry for O adsorption. In our current work with H, the presence of more Ga seems to constrain the H atom, since in the 3.125 at. % GA surface results showed some movement of the H atom to another site. Hence, either the presence of more H or additional energy would be needed to relax the H atom to a Pu-rich environment. Lastly, the presence of more Ga increased SOC chemisorptions energies from the 3.125 at. % Ga surface for the sites that were coordinated with all Pu atoms, thus demonstrating that Ga slightly inhibits reactivity of Pu and H.

### *5.2.3 Interstitial adsorption*

Table 5.3 shows the results for an H atom in an interstitial site. The terminology for this table is as follows, unless otherwise noted, interstitial-1 is

coordinated with both Pu and Ga atoms, interstitial-2 is only coordinated with Pu atoms and is located in the middle of the slab, and interstitial-3 is only coordinated with Pu atoms and is located between the topmost and sub-surface layers.

Table 5.3: Relaxation energy,  $E_r$ , chemisorption energy,  $E_c$ , at the NSOC and SOC level of theory, and distance of the H atom from the surface,  $r_{slab-H}$ , and bond length of the H atom to the nearest neighboring atoms,  $r_{X-O}$ , for the interstitials sites. In last column, if atom is not designated by parenthesis it is assumed that it is a Pu atom.

Interstitials			NSOC	SOC			
at. % Ga	Initial site	Final site	$E_r$ (eV)	$E_c$ (eV)	$E_c$ (eV)	$r_{slab-H}$ (Å)	$r_{X-H}$ (Å)
3.125	octahedral-1	octahedral*	-0.26	-0.54	-0.52	-1.40	2.22, 2.23, 2,27, 2,29, 2.30, 2.59 (Ga)
	octahedral-2	octahedral*	-0.22	-0.46	-0.44	-3.99	4x2.33, 2x2.35
	octahedral-3	octahedral*	-0.25	-0.67	-0.66	-1.31	2.30, 2x2.31, 2x2.32, 2.34
	tetrahedral-1	tetrahedral*	-0.20	-0.19	-0.19	-0.60	1.90(Ga), 2.08, 2x2.11
	tetrahedral-2	tetrahedral*	-0.21	-0.16	-0.18	-3.31	2x2.09, 2.10, 2.12
	tetrahedral-3	tetrahedral*	-0.25	-0.33	-0.31	-0.64	3x2.10, 2.11
9.375	octahedral-1 <sup>†</sup>	octahedral*	-0.21	-0.24	-0.34	-3.90	2.25, 2.26, 2x2.28, 2.29, 2.40(Ga)
	octahedral-2 <sup>‡</sup>	octahedral*	-0.18	-0.51	-0.58	-1.27	2.25, 2.29, 2.30, 2.31, 2x2.33
	tetrahedral-1 <sup>†</sup>	tetrahedral*	-0.32	-0.02	-0.09	-3.22	1.88(Ga), 2x2.09, 2.11
	tetrahedral-2 <sup>‡</sup>	tetrahedral*	-0.27	-0.21	-0.24	-1.92	2x2.10, 2x2.11

\*Final sites were distorted interstitial sites.

<sup>†</sup>Refers to interstitial site that is coordinated with a Ga and Pu atom and hydrogen atom located in the middle of the slab.

<sup>‡</sup>Refers to interstitial site that is coordinated with only Pu atoms.

Although H is known to occupy an octahedral site in PuH<sub>2</sub> [6] and a recent theoretical study showed that the octahedral site was slightly more energetically favorable than on-surface adsorption for a  $\delta$ -Pu (111) surface [87], this work showed that there were no interstitial sites that were favorable compared to on-surface adsorption. The “most” favorable interstitial site for the 3.125 at. % Ga surface is the octahedral-3 site, where H is coordinated with all Pu atoms, and has SOC chemisorption energy of -0.66 eV. This site had an energy difference of 0.13 eV and 0.10 eV for the most energetically favorable PuGa-terminated and Pu-terminated surface sites, respectively. For the tetrahedral sites, all SOC chemisorption energies increased. Furthermore, for the 9.375 at. % Ga surface, adsorption interstitial sites were *even more* unfavorable from the 3.125 at. % Ga surface. In addition, when the H was coordinated with a Ga atom, SOC chemisorption energies were not favorable, with the most unfavorable energy of -0.09 eV for the 9.375 at. % Ga surface tetrahedral-1 site. Therefore, H prefers on-surface adsorption and this conclusion was similar to the oxygen adsorption results.

All interstitial final sites were slightly distorted interstitial sites, with percent error of the angles ranging from 0.04% to 6.63%. Distortions of the oxygen interstitial adsorptions were more prominent with percent error ranging from 0.05% to 26.60%. In addition an expansion of the interstitial sites was observed. This included that the bond lengths increased from the initial bond lengths of 1.95 Å and 2.25 Å for the tetrahedral and octahedral interstitial sites, respectively. Nevertheless,

due to the presence of Ga in the surface, hydrogen interstitial sites were unfavorable, thus an activation energy would be required for the mobility of the hydrogen into the sub-surface.

A simple Boltzmann distribution (as described in Section 4.2.5 on page 121) also determined that for the 3.125 at. % Ga surface the probability of the H absorbing at an on-surface site was 77% and 55% for the Pu-terminated and PuGa-terminated surfaces, respectively. For the 9.375 at. % Ga surface the probability of H absorbing at an on-surface site was 93% and 51% for the Pu-terminated and PuGa-terminated surfaces, respectively. Therefore, the increase of Ga in the higher concentrated slab showed an increase and more favorability to an on-surface adsorption for the Pu-terminated site, while the PuGa-terminated surface made insignificantly difference for the probability of the H adsorbing at an on-surface site.

#### *5.2.4 Electronic structure analysis*

PDOS was calculated for the SOC level of theory and selective cases are shown in Figure 5.1. We first discuss the PDOS for the when the H atom is approaching the Pu-terminated surface (Figure 5.1). Figure 5.1 shows PDOS for the Pu bare (no absorption) and Pu+H (after adsorption) *5f* and *6d* states with the H *1s* state after adsorption for the least and most favorable cases for the 3.125 and 9.375 at. % Ga surface results. One key difference between the 3.125 and 9.375 at. % Ga surfaces are that the Pu bare *5f* electrons show more degree of intensity for the 9.375 at. % Ga [Figure 5.1(c) and (d)] than the 3.125 at. % Ga surface. Therefore, the

presence of more Ga slightly localizes the  $5f$  electrons in the surface. After H adsorption, the least favorable cases, top site [Figure 5.1(a) and (c)] both indicate a decrease in intensity of the  $5f$  states and hybridization of the Pu  $6d$  with H  $1s$  states, and a slight drop in magnitude around the Fermi energy. Figure 5.1 also indicates that the H  $1s$  states move to lower energy from the least preferred case (top site) to the most preferred case, a hollow three-fold coordinated site. There is no significant features of hybridization of the Pu  $5f$  with the H  $1s$  states, as opposed to minimal hybridization seen in the results for O adsorption on the Pu-Ga surfaces.

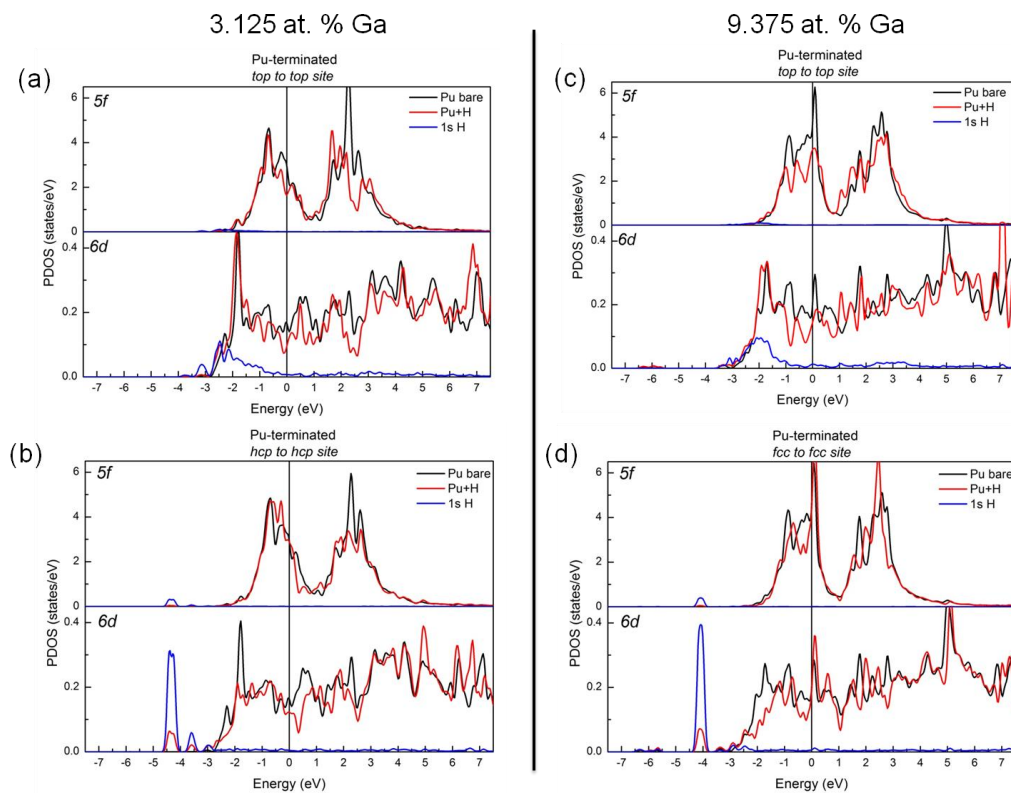


Figure 5.1: PDOS for the SOC level of theory for the least favorable site, top site [(a) and (c)], and most favorable site, hcp (b) and fcc (d) sites, for the 3.125 and 9.375 at. % Ga surfaces, respectively. PDOS is for the case when the H atom is approaching the Pu-terminated surface.

Figure 5.2 shows the PDOS for the least favorable site, top-Ga, and the most favorable sites for the 3.125 and 9.375 at. % Ga surfaces for when the H atom is approaching the PuGa-terminated surface. Similar to the Pu-terminated surface, the Pu bare *5f* electrons became more localized with the addition of more Ga in the surface. Furthermore, for the top-Ga site, hybridizations between the Ga *4s* and *4p* and H *1s* are noted for both Pu-Ga surfaces. Figure 5.2(b) and (c) show slight broadening of the Pu *5f* and *6d* states, with a slight drop of states in the vicinity of the Fermi energy, similar to the PDOS for the Pu-terminated surface. After adsorption, the PDOS for the 3.125 and 9.375 at. % Ga slabs for the hcp-Pu and fcc-Pu sites, respectively, show insignificant difference between the two. In fact weak hybridizations of the Pu *6d* and H *1s* occur around the same energy range of approximately below -4 eV. Therefore, the presence of additional Ga on the surface (i.e. the 9.375 at. % Ga surface) the electronic features after adsorption of H on the PuGa-terminated surface was not affected significantly. This is contrary to the oxygen adsorption studied that showed that for the 3.125 at. % Ga surface, the Ga atom enable the Pu *6d* to participate in bonding while inhibiting the Pu *5f* states to hybridize with the O *2p* states [25]. When the Ga concentration increased to the 9.375 at. % Ga surface it was more evident that the Ga enhanced the ability of the Pu *6d* states to hybridize with the O *2p* states, while also slight hybridization with the Pu *5f* states and O *2p* states occurred.

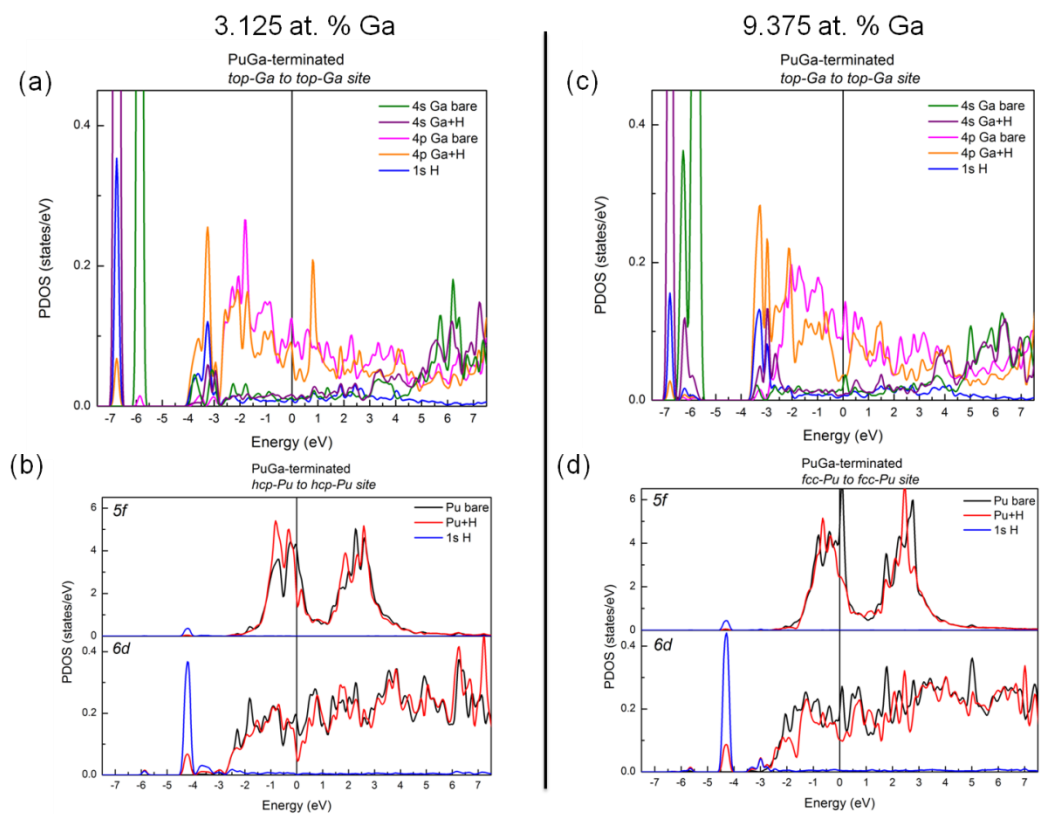


Figure 5.2: PDOS for the SOC level of theory for the least favorable site, top-Ga [(a) and (c)], and most favorable site, hcp-Pu (b) and fcc-Pu (d), for the 3.125 and 9.375 at. % Ga surfaces for when the H atom is approaching the PuGa-terminated surface.

The PDOS for the least and most favorable interstitial sites are shown in Figure 5.3. Likewise, the cases for the Pu-terminated and PuGa-terminated discussed above, the Pu bare *5f* electrons are more in magnitude for the 9.375 at. % Ga surface as compared to the 3.125 at. % Ga surface. Another feature is that the PDOS are quite similar between to the two surfaces. For instance, in Figure 5.3(a) and (c), we observe after H adsorption that the Pu *5f* states are decreased in the vicinity of the Fermi energy, with slight broadening of the Pu *5f*, and hybridization of the Pu *6d* and Ga *4p* with the H *1s*. Therefore due to the close proximity of the Ga atom to the Pu atoms, it is clear here that the Ga atom enhances the ability of the Pu *6d* electrons to bond with the H. This is similar to our discussion above for the O adsorption study and also discussed earlier in the bulk study. To summarize, the bulk study indicated that with increasing Ga concentration the Pu *5f* electrons remained unaffected by the Ga atom while there was an increase in broadening of the Pu *6d* and hybridizations of the Pu *6d* with the Ga *4p* [108]. For the most favorable interstitial sites the PDOS are also similar to each other between the two different Pu-Ga surfaces. Figure 5.3(b) and (d) illustrate a decrease in states for the Pu *5f* and *6d* states, while weak hybridization of the H *1s* and Pu *6d*. Nonetheless, the features observe in the interstitial sites PDOS are similar to the PDOS for the Pu-terminated and PuGa-terminated PDOS for the most favorable sites when comparing the different Pu-Ga surfaces. Therefore, unlike the O adsorption study that did show that the presence of more Ga affected the electronic structure, we cannot make the same case here for the

hydrogen adsorption. To reiterate, the PDOS results indicate that the presence of more Ga at the surface does not affect the electronic structure properties when compared to a lower Ga concentrated surface.

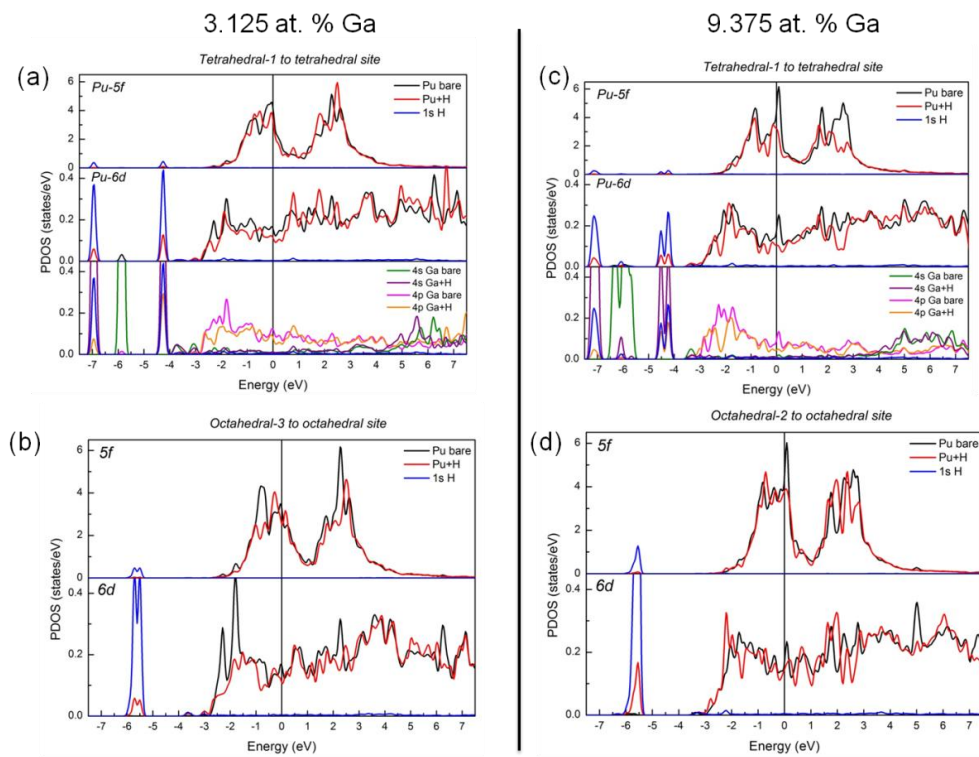


Figure 5.3: PDOS for the SOC level of theory for the least favorable interstitial site, tetrahedral-1 [(a) and (c)], and most favorable site, octahedral-3 and octahedral-2 site [(b) and (d)] for the 3.125 and 9.375 at. % Ga surfaces for when the H adsorbate is initially placed in an interstitial site.

In all PDOS (Figure 5.1, Figure 5.2, and Figure 5.3) we see a consistent decrease of the Pu  $5f$  electrons after adsorption, without any evidence of hybridization with the H  $1s$  electrons. Figure 5.4 shows the Pu  $5f$  and  $6d$  states for a pure  $\delta$ -Pu surface, and for the 3.125 and 9.375 at. % Ga surfaces before adsorption. For the 3.125 and 9.375 at. % Ga surface, we plotted a Pu atom that was in the Pu-terminated surface. Also the  $6d$  states have been amplified (x10) so it may be better compared with the highly large intensity of the  $5f$  electrons. Illustrated in Figure 5.4, for the pure  $\delta$ -Pu surface, we observe that there is significant coupling between the Pu  $5f$  and  $6d$  everywhere. It has been seen previously that theoretically there exist strong  $5f$ - $6d$  hybridization in the actinides [42, 43]. With the inclusion of Ga, we observe that while the coupling is still present, it does decrease with the addition of more Ga. For instance, in the 3.125 at. % Ga surface there exist coupling between the  $5f$  and  $6d$  states that begins at around 1.8 eV below the Fermi level, while for the 9.375 at. % Ga surface the coupling begins at around 1.2 eV below the Fermi level. Therefore, the presence of Ga enables the Pu  $5f$  and  $6d$  to decouple in some regions in the valence band, which enables Pu  $6d$  to hybridize with H  $1s$ . Near the Fermi level the coupling still exist, so when hydrogen is adsorb onto the surface, it hybridizes with Pu  $6d$  and in turn indirectly affects by decreasing the Pu  $5f$  states.

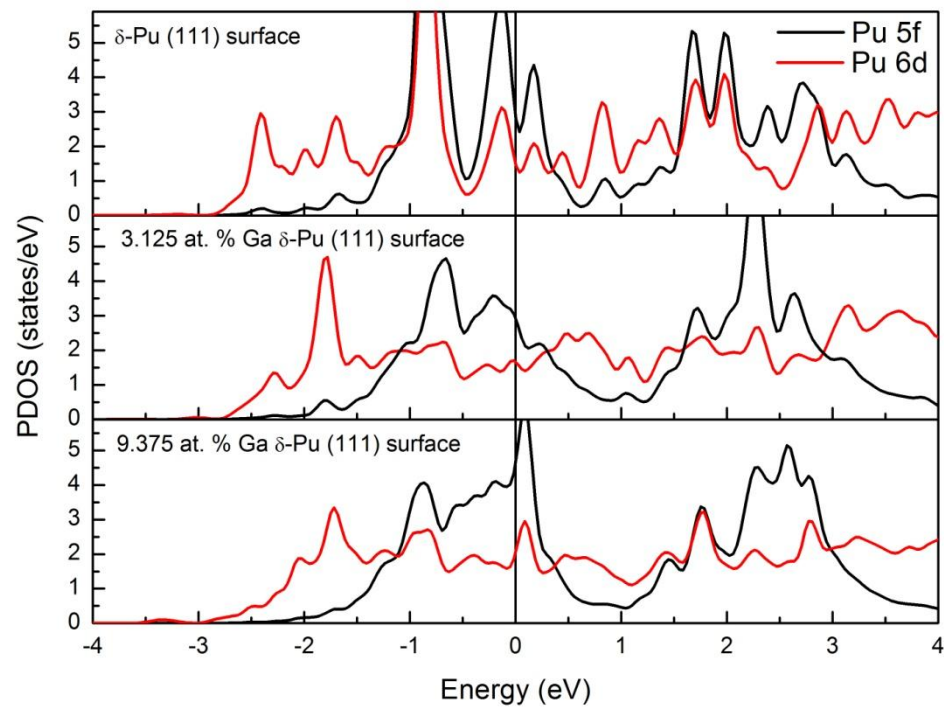


Figure 5.4: PDOS for Pu 5f and 6d for the pure  $\delta$ -Pu (111) surface and 3.125 and 9.375 at. % Ga  $\delta$ -Pu (111) surface.

Only a Pu atom for the Pu-terminated surface was plotted. The Pu 6d have been amplified (x10) to see features.

Figure 5.5 illustrates a real space picture to aid the analysis of the redistribution of electron density after the H adsorption process. This three-dimensional difference charge density plots were calculated similarly to the O charge density plots. For Figure 5.5 it was computed by  $\Delta n(r) = n(\text{Pu-Ga} + \text{H}) - n(\text{Pu-Ga}) - n(\text{H})$ , where  $n(\text{Pu-Ga} + \text{H})$  is the total charge density of the Pu-Ga system with H adatom,  $n(\text{Pu-Ga})$  is the total charge density of the Pu-Ga slab, and  $n(\text{H})$  is the charge density of the H atom. The most favorable sites for the Pu-terminated and PuGa-terminated were plotted for the 3.125 and 9.375 at. % Ga surfaces. In Figure 5.5, we define electron density accumulation as the red regions and electron density depletion as the blue regions. From Figure 5.5, we observe that all Pu atoms are losing charge, while the Ga atoms are losing some charge but not as significant. The change in work function confirmed this observation by the fact that there was more charge transfer occurring on the Pu-terminated sites than the PuGa-terminated sites. The change in work function shown in Table 5.4 for the Pu-terminated hcp and fcc sites for the 3.125 and 9.375 at. % Ga surfaces, respectively, was 0.05 eV, while for the PuGa-terminated fcc-PuGa site for both surfaces was 0.02 eV. Therefore, although the results for both Pu-Ga surfaces were quite similar, the Ga did inhibit some charge transfer to the H atom.

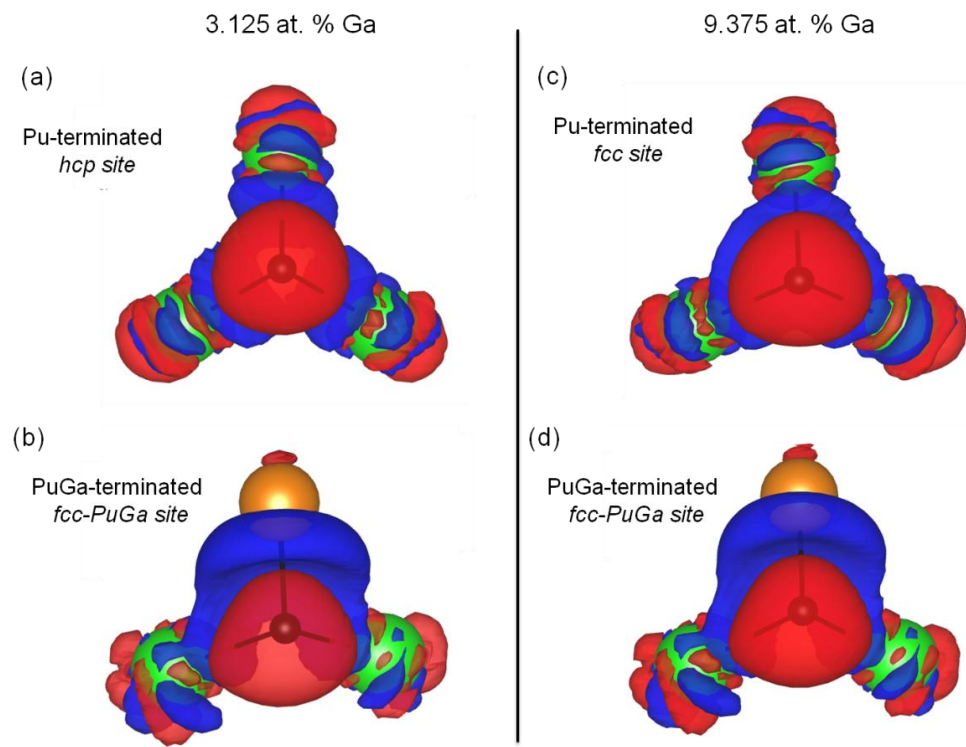


Figure 5.5: Three-dimensional  $\Delta n(r)$  for the hcp site (a) and fcc site for the Pu-terminated surface, and the fcc-PuGa site [(b)-(d)] for the PuGa-terminated 3.125 and 9.375 at. % Ga surface, respectively. Only the coordination environment around the H-atom is shown. Red indicates charge accumulation, while blue indicates charge depletion. Isosurface level is  $0.0121 \text{ e}^-/\text{cubic } \text{\AA}$ . Green is Pu atoms, orange is Ga atom, and H is the center atom.

Table 5.4: Changes in work function,  $\Delta\phi$ , at the NSOC and SOC levels of theory.

The work function for the clean relaxed Pu-Ga slab was 3.32 eV and 3.39 eV, respectively, at the NSOC and SOC level of theory. Experimental work function is 3.2 eV for stabilized  $\delta$ -Pu [116].

at. % Ga		Initial site	NSOC $\Delta\phi$ (eV)	SOC $\Delta\phi$ (eV)	
3.125	Pu-terminated	top	0.28	0.27	
		hcp	0.05	0.04	
		fcc	0.05	0.05	
		bridge	0.07	0.07	
	PuGa-terminated	top-Pu	0.06	0.05	
		top-Ga	0.03	0.02	
		hcp-Pu	0.05	0.04	
		hcp-PuGa	0.05	0.04	
		fcc-Pu	0.03	0.04	
		fcc-PuGa	0.02	0.02	
		bridge-Pu	0.07	0.06	
		bridge-PuGa	0.02	0.01	
	9.375	Pu-terminated	top	0.25	0.25
			hcp-Pu	0.04	0.05
hcp-Ga			0.07	0.08	
fcc			0.05	0.05	
bridge			0.08	0.08	
PuGa-terminated		top-Pu	0.28	0.27	
		top-Ga	0.02	0.01	
		hcp-Pu	0.06	0.05	
		hcp-PuGa	0.04	0.03	
		fcc-Pu	0.05	0.05	
		fcc-PuGa	0.02	0.02	
		fcc over Ga	0.06	0.06	
		bridge-Pu	0.10	0.09	
		bridge-PuGa	0.00	0.00	

## Chapter 6

### Conclusions

In conclusions, we have studied the effect of Ga concentrations on the structural, energetic, and electronic properties of *fcc* bulk Pu and oxygen and hydrogen adsorption on Pu-Ga alloy (111) surfaces. For the bulk study, we observed that the lowest magnetic energy structure was of anti-ferromagnetic (AFM) spin order, regardless of Ga concentration. This AFM arrangement was AFM-like, due to the fact that there was no magnetic moment on the Ga atom. In the 6.25 at. % Ga and 9.375 at. % Ga structures, where more than one Ga atom is existed in the supercell, the Ga atoms prefer to occupy substitutional *fcc* locations that are separated by four nearest neighboring shells. With increasing Ga concentrations, the equilibrium lattice constant decreased, which was in agreement with experimental data. However, the bulk modulus showed no well-defined trend with increasing Ga concentration. The alloy formation energies for the Pu-Ga systems decreased with increasing Ga concentration; thus implying the inclusion of Ga in  $\delta$ -Pu is exothermic.. Additionally, upon relaxation, the stability and retention of the *fcc* structure increased with increasing Ga concentration, while introducing slight short range disordered. This was also in agreement with experimental data.

The PDOS showed that at 3.125 at. % Ga, there is little or no effect to the Pu valence electrons when Ga is a nearest neighbor to Pu, but with increasing Ga concentration the first nearest neighbor Pu atom *6d* and *7s* electrons showed further

broadening with slight hybridization with the Ga  $4p$  electrons at 9.375 at. % Ga concentration. Charge density difference plots indicated  $4sp$  hybridization in the Ga atom due to polarization of the Ga valence orbitals by the strong electric fields of the nearby Pu atoms; the observed hybridizations were validated by the examination of the atomic partial charges inside the muffin tin sphere.

We also studied vacancies and hydrogen-vacancies in the 3.125 at. % Pu-Ga structure. Vacancies were formed by removing a single Pu atom. Vacancies were placed at first, second, and fourth nearest neighboring distance from the Ga atom in the supercell. Each vacancy within the Pu-Ga bulk was unstable, implying to be endothermic, irrespective of the location of the vacancy relative to Ga. When hydrogen was placed inside the vacancy, there were significant atomic relaxations for when the hydrogen-vacancy was placed at first nearest neighbor to the Ga atom. Minimal atomic relaxations were observed when the hydrogen vacancy was placed at second or fourth nearest neighboring distance from the Ga atom. Atomic relaxations for the first nearest neighbor hydrogen-vacancy structure indicated that the vacancy region appears to widen on the Ga-H side and contract on the Pu-H side. Strong interactions with the nearest neighboring Pu atom to the hydrogen were quantified as the partial charge calculations indicated that the H atom accumulates charge from the nearest neighboring Pu atom. PDOS showed slight hybridization of the H  $1s$  and Pu  $5f6d7s$  electrons with a decreased intensity for the Pu  $5f$  electrons. All hydrogen-vacancy complexes had formation energies that were exothermic; therefore hydrogen

stabilized the vacancy complexes in the Pu-Ga bulk structure. This in turn may drive super-abundant vacancy formation.

The stabilization of the surface with the presence of Ga is shown through the decrease of formation and surface energies with increasing Ga concentrations. Structural comparisons to the bulk and surface showed that while the *fcc* (111) surface was retained there were significantly more short-range disorder around the Ga atom. This could be due to the missing neighbors of the topmost surface. For O adsorption on the 3.125 at. % Ga surface, results indicated that the O atom prefers an all Pu-rich environment with a three-fold coordination and the highest SOC chemisorption energy was -5.06 eV. When the adsorption configuration included a Ga-O bond, chemisorption energies were less favorable compared to the configuration with only Pu-O bonds. Therefore, oxygen did not prefer to be near Ga. In addition, O impacted the geometric stability of the surface. Relaxation of the O to another final site was observed and proved that the initial bridge site was a pathway to most energetically favorable hollow site. O also preferred to adsorb on the surface, since the interstitial sites were not as favorable as the surface sites.

In addition, the PDOS showed broadening of the *5f* and *6d* states and hybridization of Pu *5f* and *6d* states with the O *2p* states at the Fermi energy for when the O interacts with an all Pu environment, thus implying the high reactivity of Pu with O. This was in agreement with past theoretical efforts on O adsorption on pure  $\delta$ -Pu. When O was coordinated with a Ga atom, the PDOS implied that the Ga atom

inhibits the ability for the Pu atoms'  $5f$  to hybridize with the O  $2p$  orbitals, while enhancing the ability of the  $6d$  orbitals to hybridize with O  $2p$  orbitals. This was in agreement with the bulk study, since in the bulk study there was slight hybridization of the Ga  $4p$  with the Pu  $6d$  states.

For oxygen adsorption on the 9.375 at. % Ga surface, similar to the 3.125 at. % Ga results, oxygen preferred a Pu-rich environment with three-fold coordination and the *fcc* site was the most favorable site. The *fcc* site chemisorption energy was -5.06 eV. Additionally, when the O adsorbate was approaching the PuGa-terminated surface, the O atom migrated to a Pu-rich environment, which was not seen for the surface with a lower Ga concentration. Therefore, the inclusion of more Ga at the surface implies that the surface chemistry is extremely important in determining the adsorption of O onto the surface. Interstitial sites were not as favorable as on-surface sites, which was similar to the 3.125 at. % Ga surface adsorption results. Therefore, with the presence of one O on the surface, O adsorption is an on-surface phenomenon. Thus, the presence of Ga discourages the formation of an oxide layer on  $\delta$ -Pu. Structural distortions were detected and the final O sites had expanded Pu-O bond lengths and surrounding Pu-Pu distances.

Electronic properties showed that the Ga  $4p$  states indirectly influenced the Pu  $6d$  to hybridize with the O  $2p$  states, inducing the O  $2p$  states to split into sub-bands, which were seen in all on-surface PDOS. The O  $2p$  sub-bands splitting was only seen for when O was coordinated with a Ga atom for the 3.125 at. % Ga surface

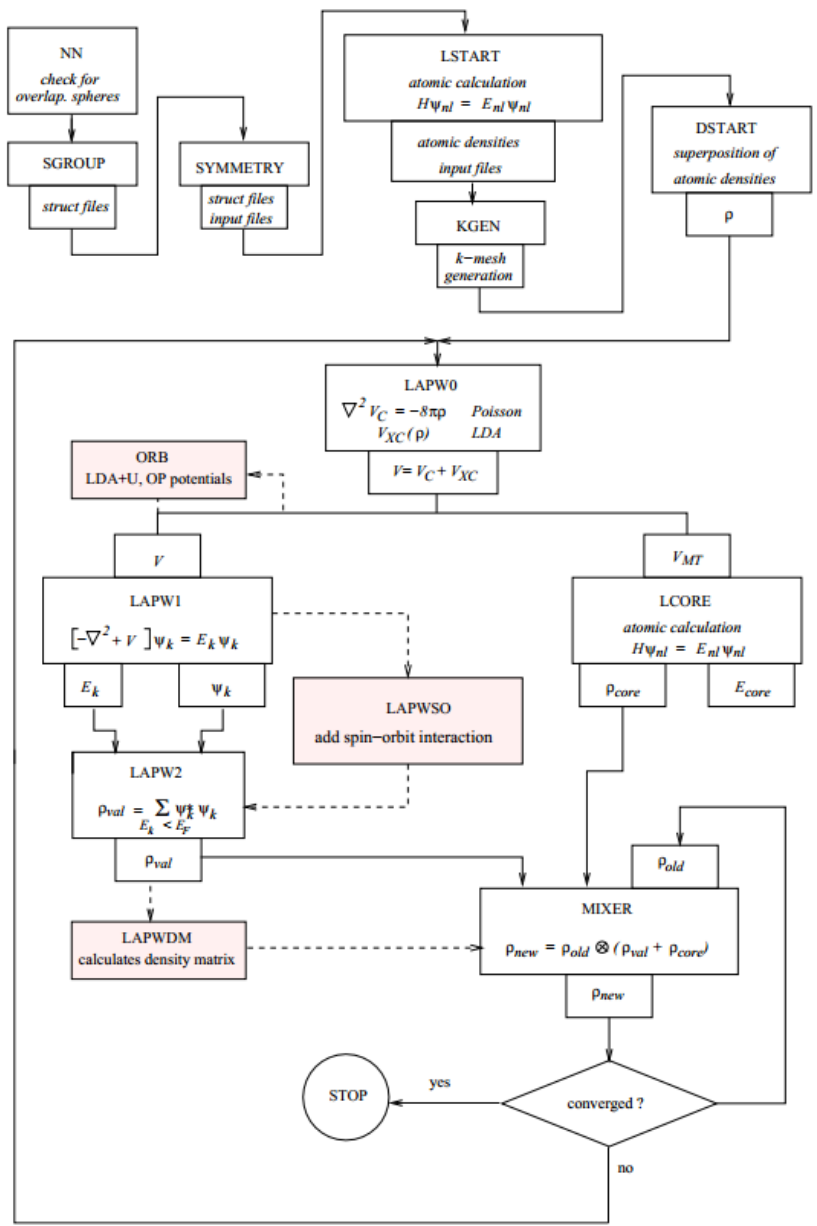
results. Hence the presence of more Ga in the surface influenced the electronic structure of the Pu *6d* states. Slight admixture of the Pu *5f* with the O *2p* and Pu *6d* were also observed and this could be due to the strong influence of the Ga *4p*. This is similar to the bulk results, since at the 9.375 at. % Ga bulk structure, further broadening of the Pu *6d* states were noted, along with hybridization of the Pu *6d* and Ga *4p*. These effects were not seen in the interstitial sites when O was coordinated to all Pu atoms. Finally, charge density difference plots showed that O accumulated charge from both the Pu and Ga atoms, which is due to the high electronegativity of O. Adsorbate-induced work function changes verified this charge transfer. This was also similar to the 3.125 at. % Ga surface results.

Hydrogen adsorption on the Pu-Ga (111) surface showed that the H atom preferred to be in a Pu-rich environment and three-fold coordinated in a hollow site for both the 3.125 and 9.375 at. % Ga surfaces, with chemisorption energies of -0.76 eV and -0.80 eV, respectively. These chemisorption energies signify that the reaction of H with the Pu-Ga surface is not as volatile as the reaction of O. Migration of the H atom upon relaxation was limited to some cases, but local structural distortion for the surface was observed. Movement of the H atom was inhibited as the concentration of the Ga increased in the surface, since there was no significant relaxation of the H to relocate from being in a Pu-Ga environment to a Pu-rich environment, which was seen in the O adsorption study. Sites that included the H to be coordinated to both Pu and Ga atoms were unfavorable when compared to sites where the H atom was

coordinated to all Pu atoms. These conclusions are similar to the O adsorption study. Likewise to the O adsorption, H does not prefer to be over-coordinated, since all interstitial sites were unfavorable. In addition, interstitial final sites were slightly distorted and expansions of the Pu-H bond lengths were noted.

Finally, electronic structure eluded that regardless of Ga concentration there were no significant change to the PDOS, but showed a decrease and slight broadening of the Pu *5f* and weak hybridization of the Pu *6d* and H *1s* states. Also when Ga participated in bonding, the H *1s* hybridized with the Ga *4p* and Pu *6d* states. Charge density difference plots illustrated charge accumulation on the H atom, whereas there was charge depletion from the Pu atoms. There was slight charge transfer from the H to the Ga, which was shown by the low work function changes.

Appendix A  
Program Flow of *WIEN2k*



Kohn-Sham equations as implemented in *WIEN2k*.<sup>iii</sup>

<sup>iii</sup> Image acquired from [http://www.wien2k.at/reg\\_user/textbooks/usersguide.pdf](http://www.wien2k.at/reg_user/textbooks/usersguide.pdf) on page 44.

## Appendix B

### Three-Dimensional Charge Density Difference Plot

First, one must compute the charge density difference of each different system. For instance, charge density of system+interacting-atom, charge density of system, and charge density of interacting atom. Using the executable file, `wien2venus.py` (download from the *WIEN2k* website), this will make a three-dimensional grid of the charge density. The user must specify the grid. For example, at the prompt type “`./wien2venus.py 100 100 100,`” where you specify x, y, and z. After calling the executable file for each charge density, `*.rho3d` file will be created. Collect all `*.rho3d` files into the same directory. Using the program `diff_charge_density_vesta.f` (see below), this will compute the difference and write a file `*.rho`, which can be opened using the program VESTA. Within the program `diff_charge_density_vesta.f` must change block that sets `*.rho3d` as F1, F2, and F3. F1 corresponds to system+interacting-atom, F2 corresponds to system, and F3 corresponds to interacting-atom. There is an example written in the program below. Then, after making the changes to F1, F2, and F3, compile and execute the program. After opening `*.rho` in VESTA, link the structure file of the system+interacting-atom structure. The following program was developed by Dr. Raymond Atta-Fynn.

Program: diff\_charge\_density\_vesta.f

c Simple f77 code to compute difference charge density

c Raymond Atta-Fynn, UT Arlington Physics

c April 7, 2013

```
implicit none
double precision x(3,5),tmp,tmp2(3),tmp3(3)
integer          i, j, nat, nx, ny, nz
character        a*1, a2*4, F1*50, F2*50, F3*50
```

c Edit this block

```
F1 = 'PuGa.rho3d'
F2 = 'Pu_only.rho3d'
F3 = 'Ga_only.rho3d'
```

c End block

```
open(1,file=F1,status='old')
open(2,file=F2,status='old')
open(3,file=F3,status='old')
open(4,file='diff.rho',status='unknown')
```

```
read(1,*)a2
read(2,*)a
read(3,*)a
write(4,'(A4)')a2
```

```
read(1,*)(tmp2(i),i=1,3)
read(2,*)tmp,tmp,tmp
read(3,*)tmp,tmp,tmp
write(4,'(3(f10.6,2X))')(tmp2(i),i=1,3)
```

```
read(1,*)(tmp3(i),i=1,3)
read(2,*)tmp,tmp,tmp
read(3,*)tmp,tmp,tmp
write(4,'(3(f10.6,2X))')(tmp3(i),i=1,3)
```

```

read(1,*)nx, ny, nz, tmp, tmp, tmp
read(2,*)nx, ny, nz, tmp, tmp, tmp
read(3,*)nx, ny, nz, tmp, tmp, tmp
write(4,'(3(I3,2X),3(f10.6,2X))')nx, ny, nz, (tmp2(i),i=1,3)

nat = nx*ny*nz

do i=1,nat/5
  read(1,*)(x(1,j),j=1,5)
  read(2,*)(x(2,j),j=1,5)
  read(3,*)(x(3,j),j=1,5)
  write(4,'(5(E15.8,X))')(x(1,j)-x(2,j)-x(3,j),j=1,5)
end do

write(*,*)
write(*,*)'Output written to diff.rho'
write(*,*)

close(1)
close(2)
close(3)
close(4)

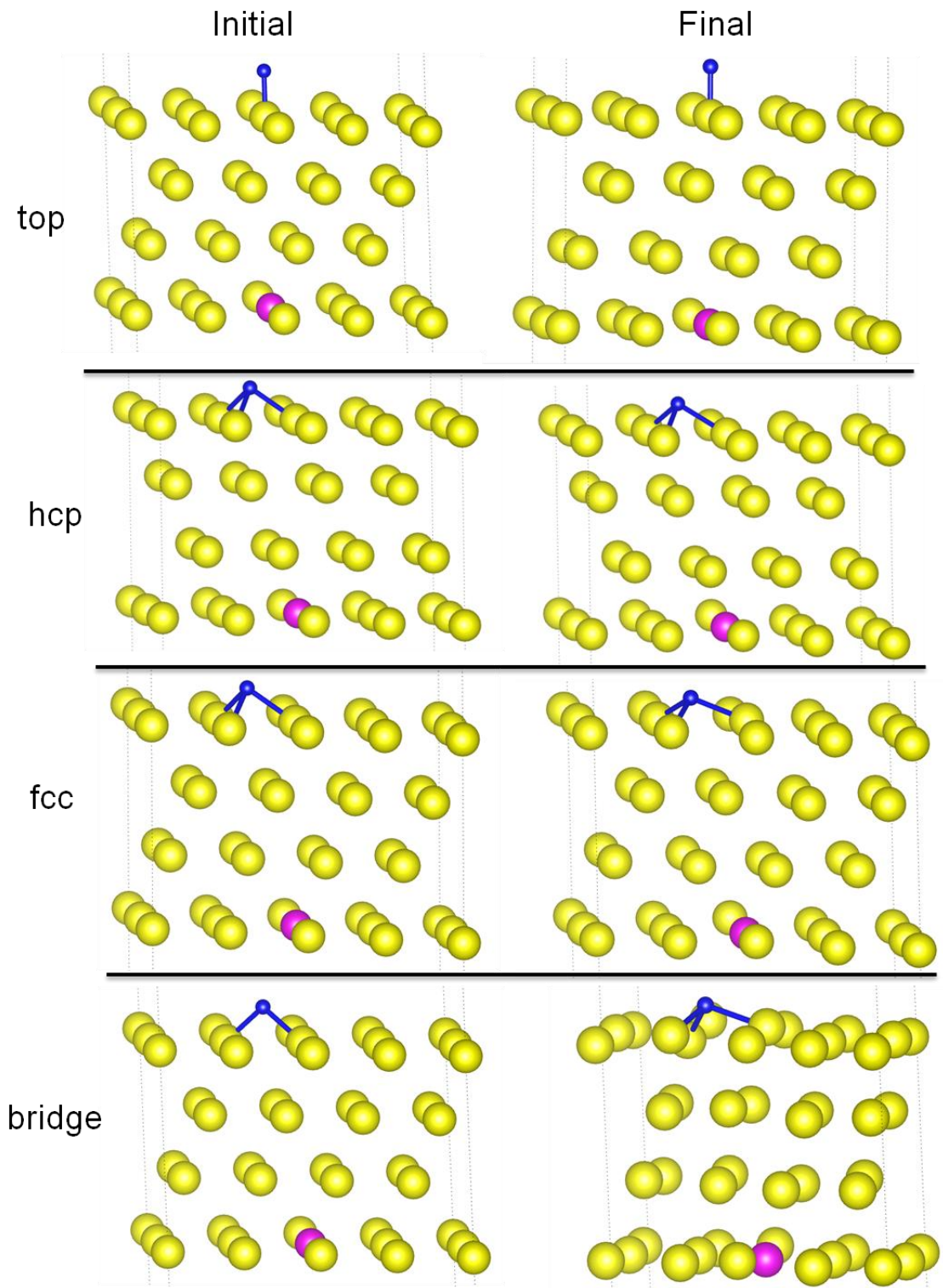
stop
end

```

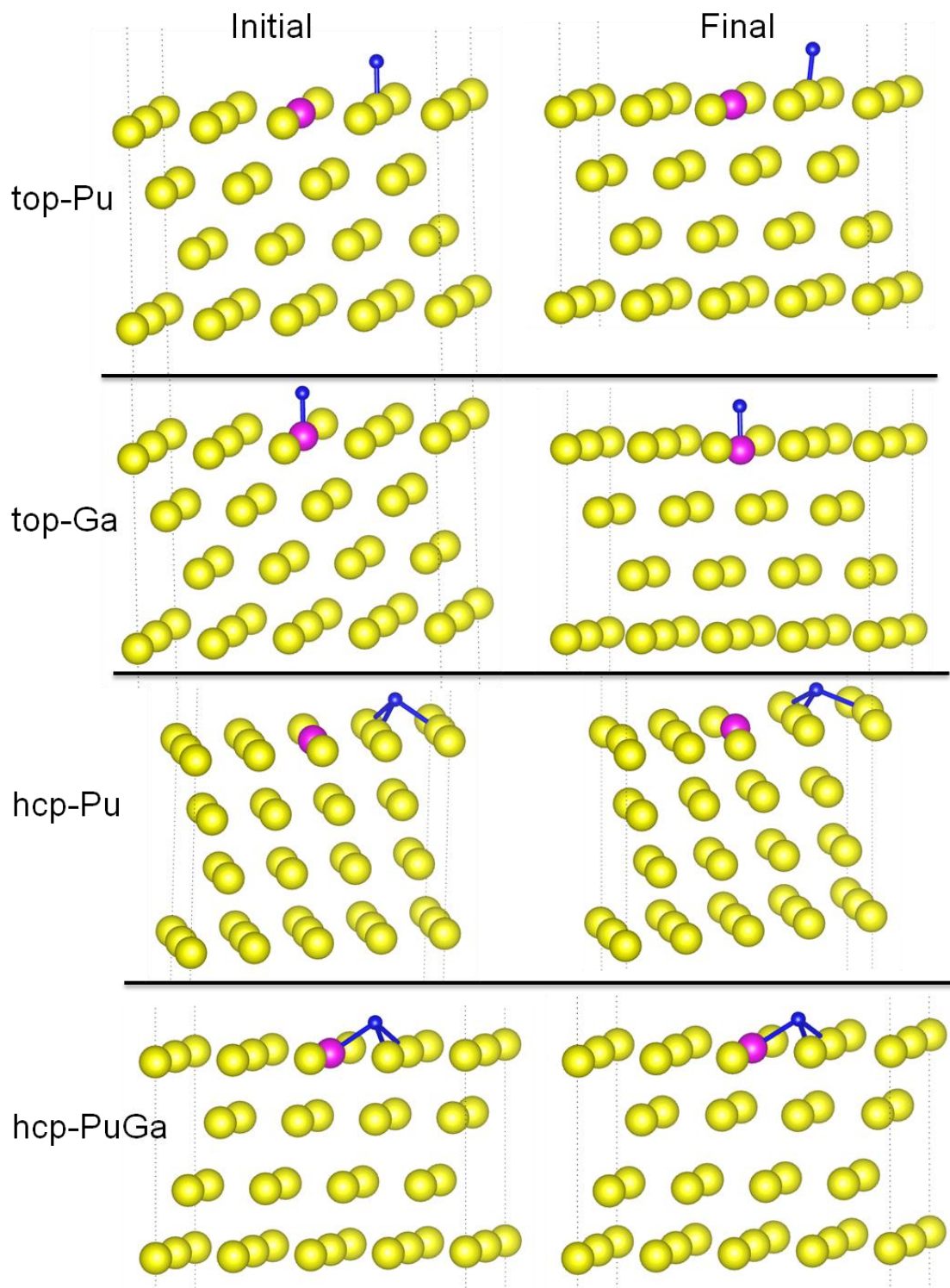
## Appendix C

Initial and final positions for O adsorption on 3.125 at. % Ga  $\delta$ -Pu (111) surface

Pu-terminated sites



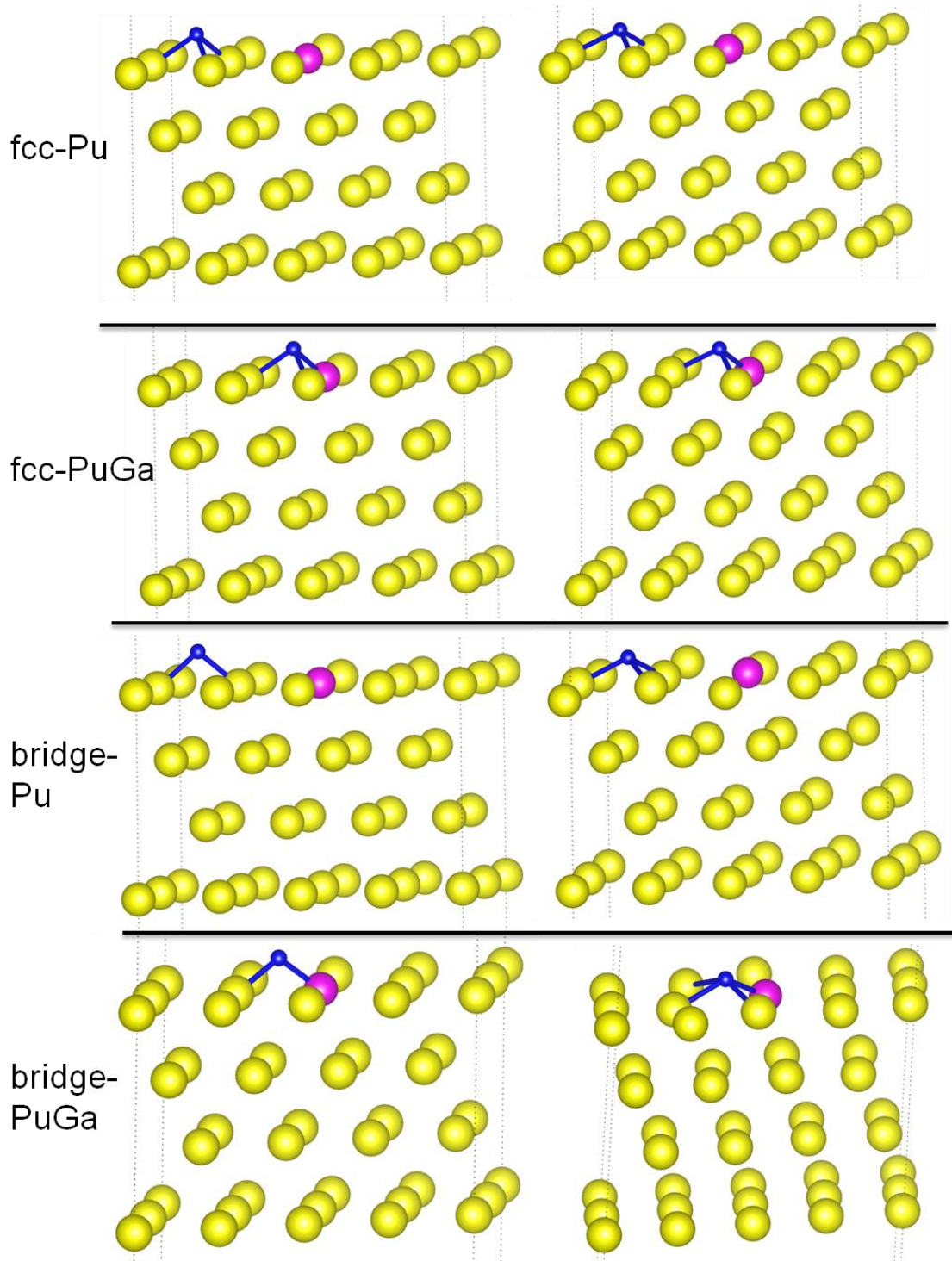
PuGa-terminated sites



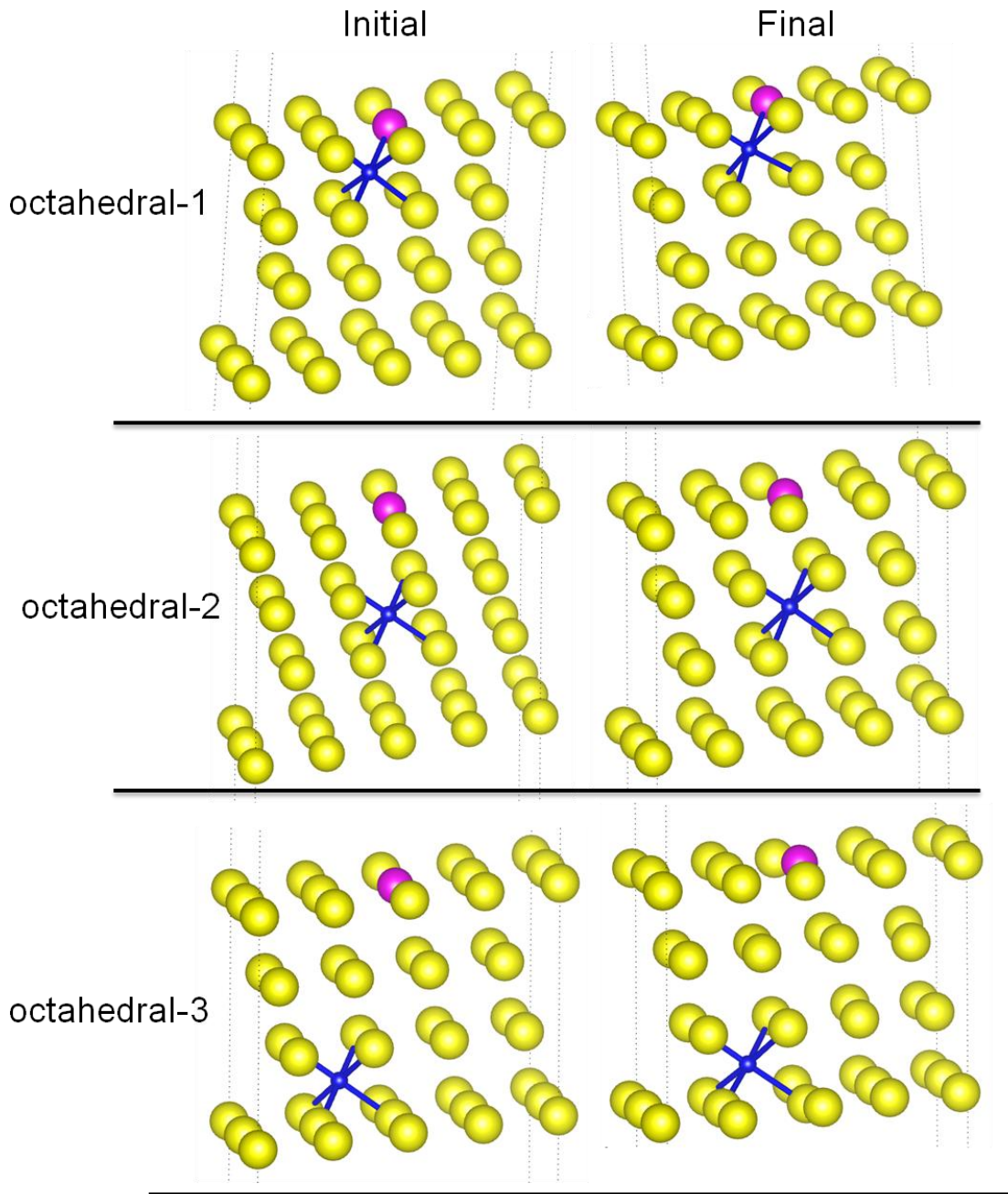
PuGa-terminated sites

Initial

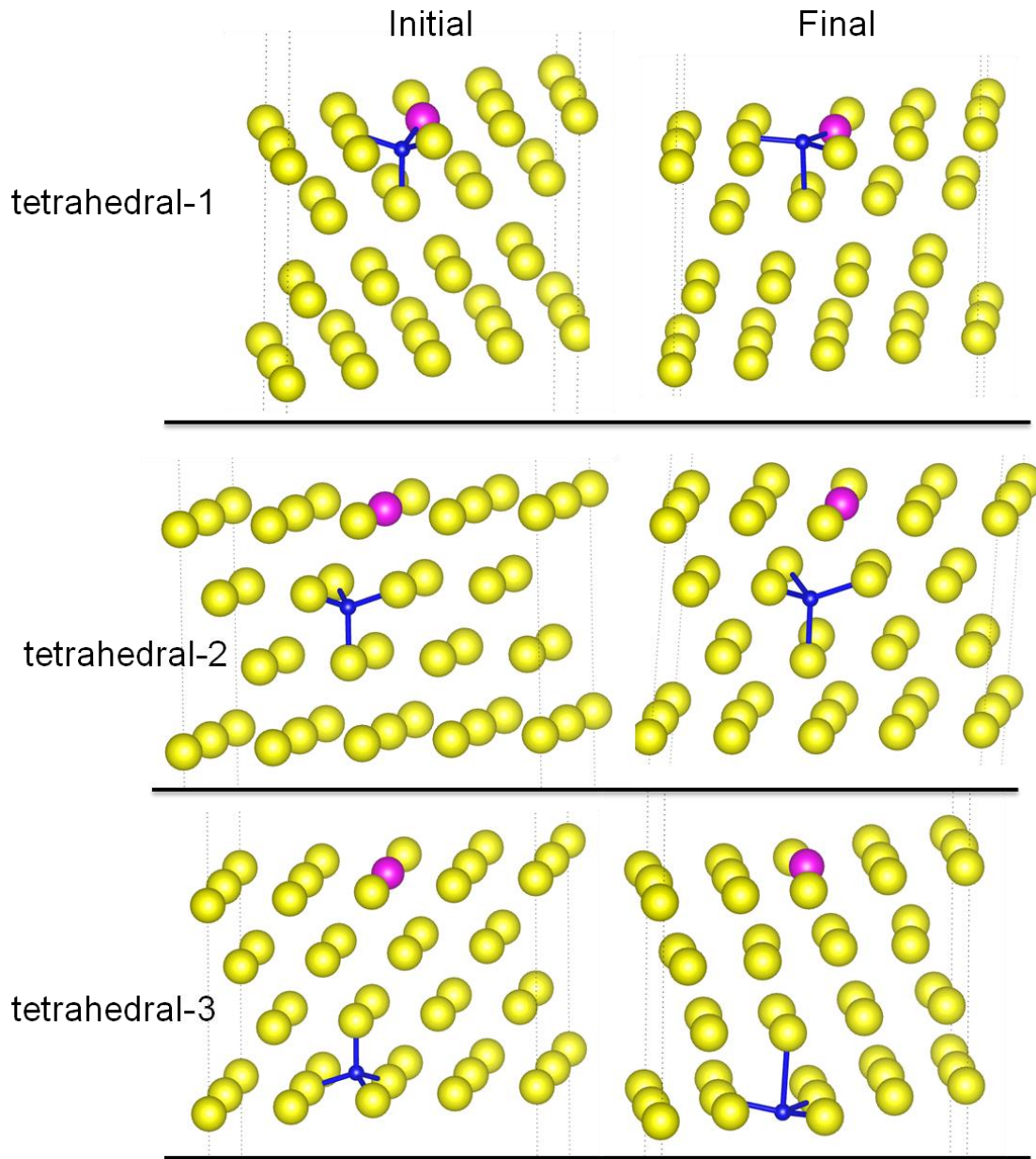
Final



Interstitials sites



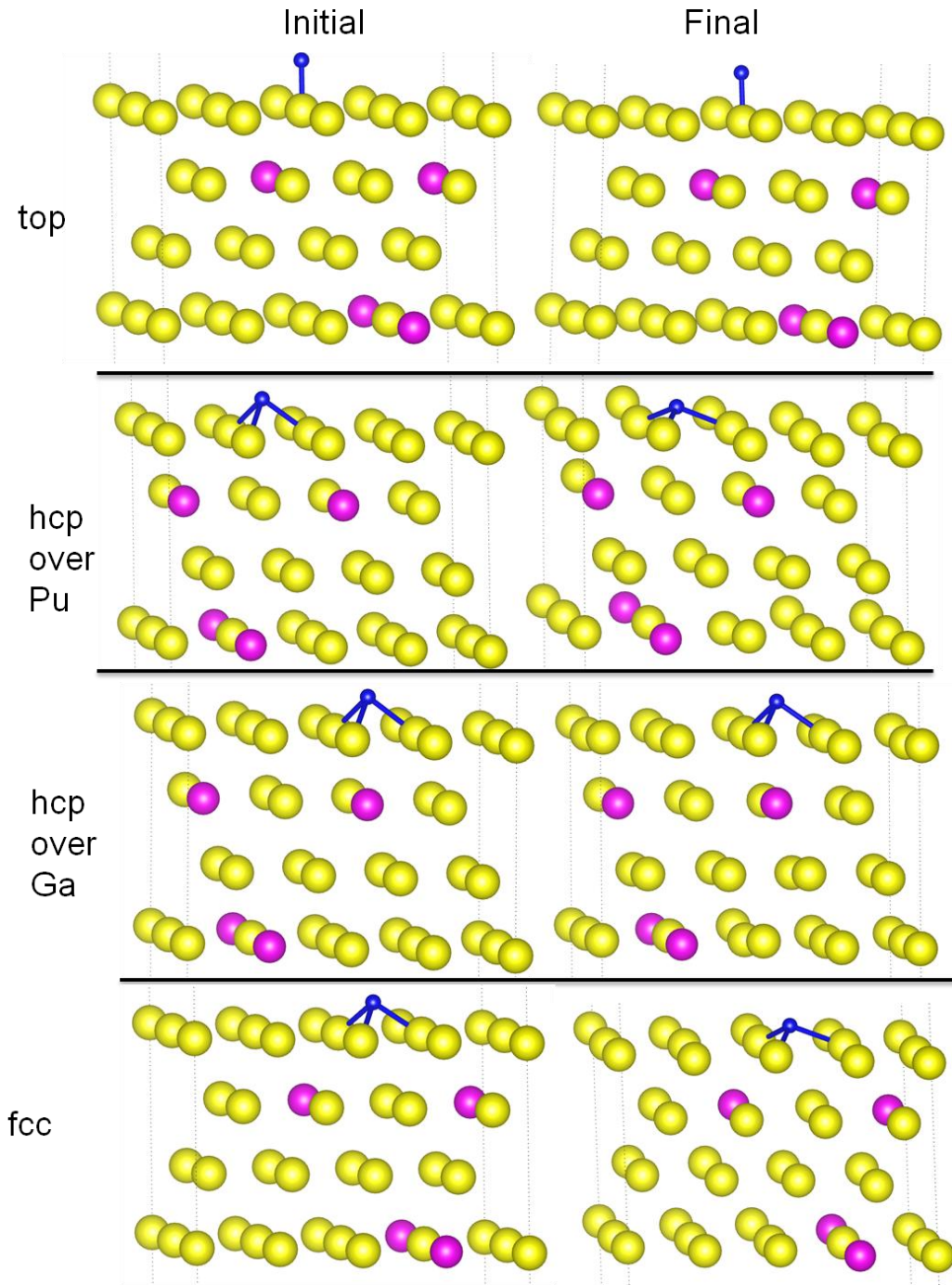
Interstitials sites



## Appendix D

Initial and final positions for O adsorption on 9.375 at. % Ga  $\delta$ -Pu (111) surface

Pu-terminated sites

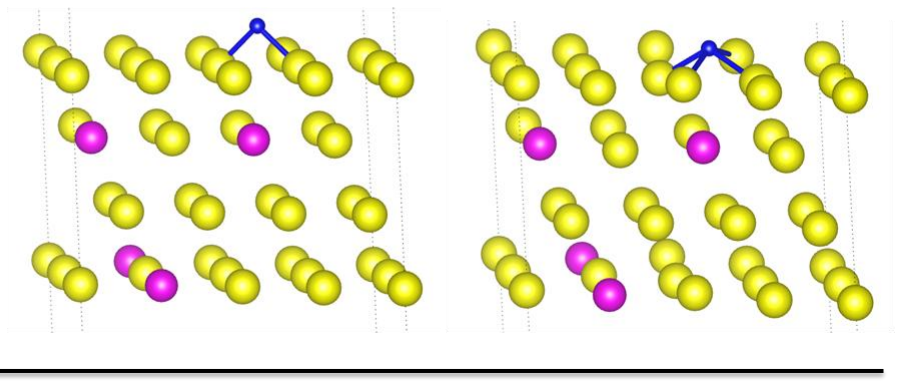


Pu-terminated sites

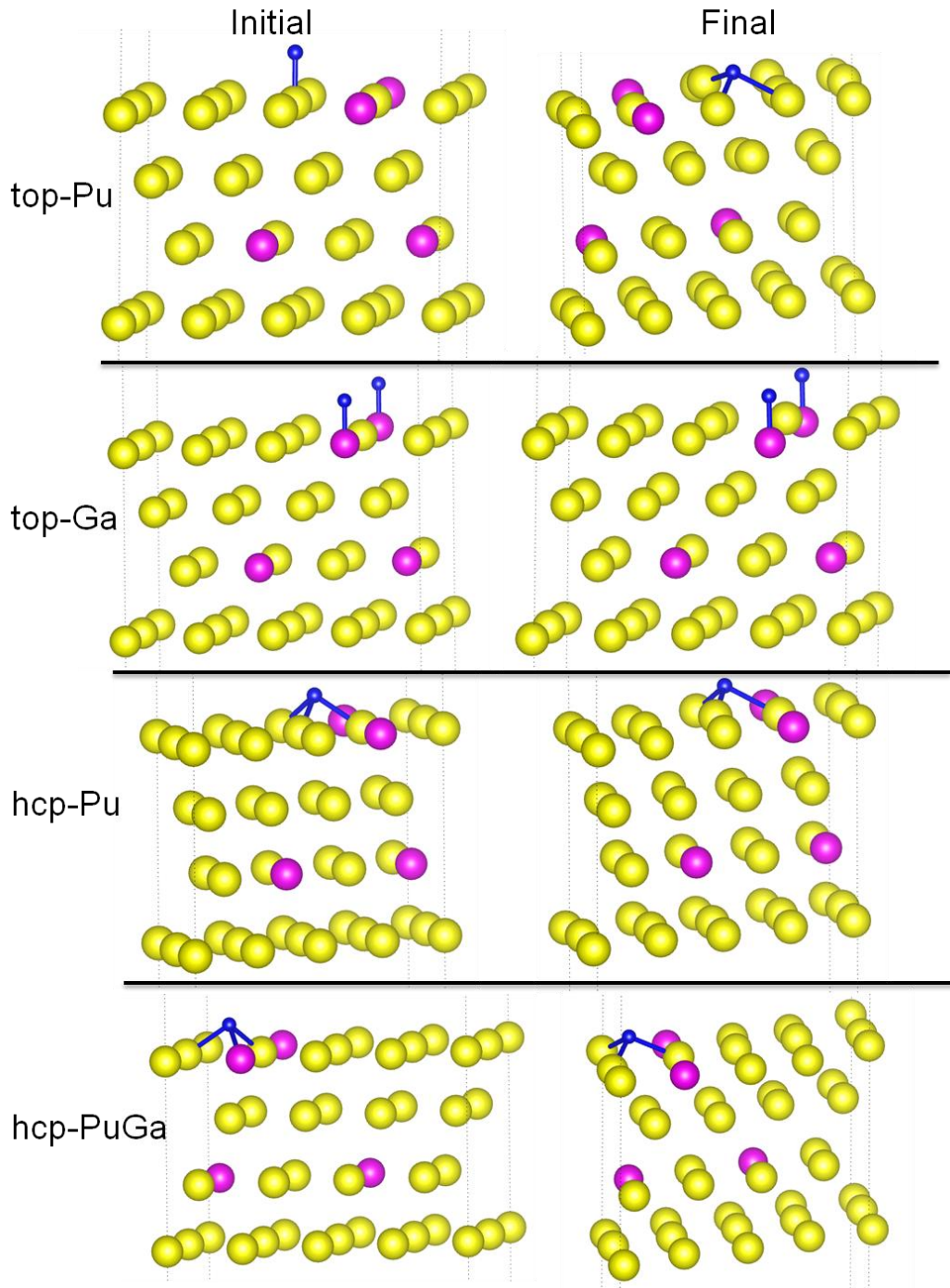
Initial

Final

bridge



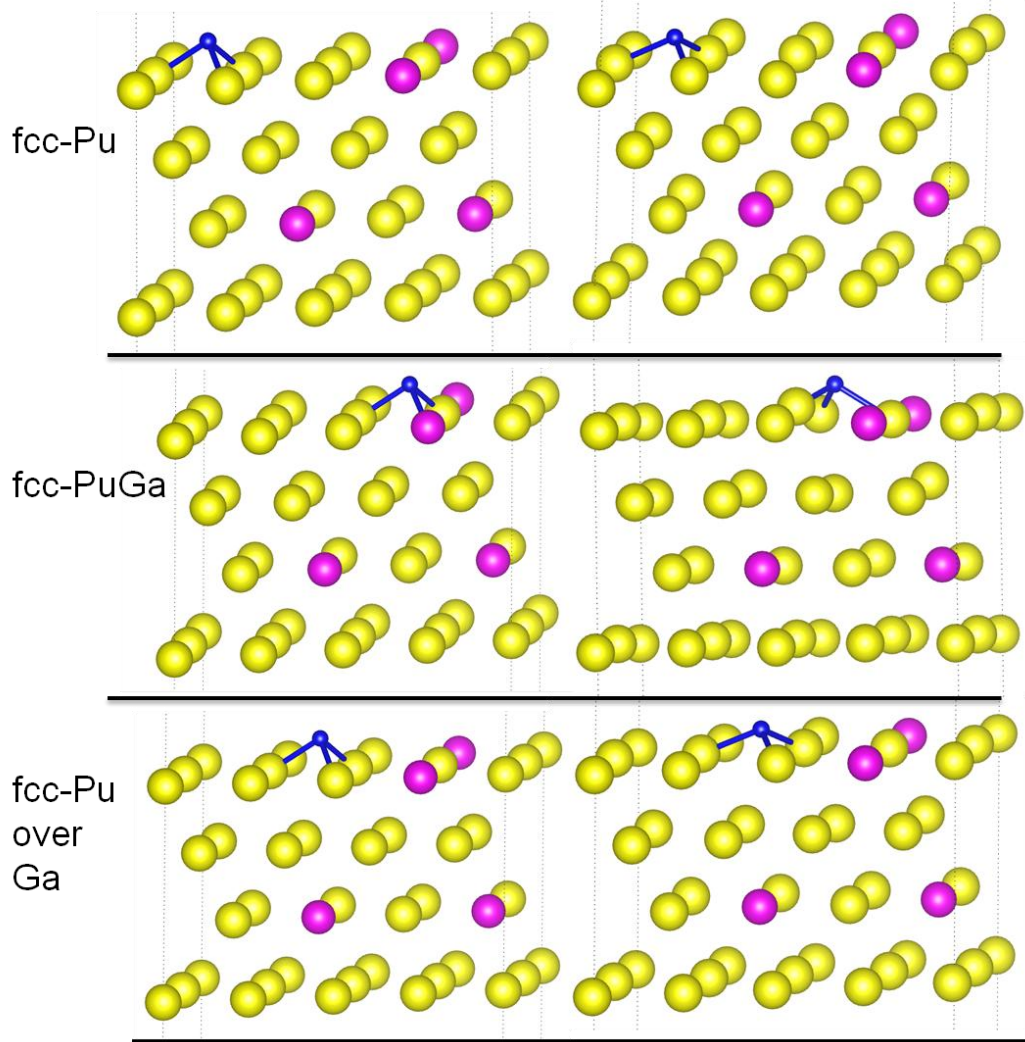
PuGa-terminated sites



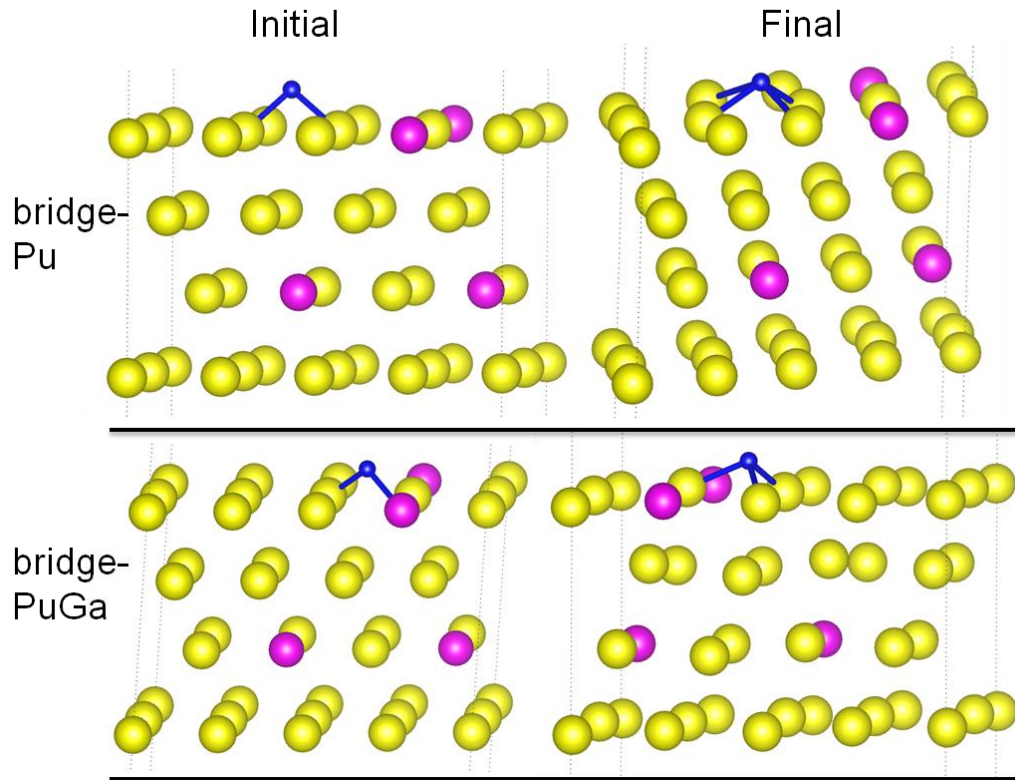
PuGa-terminated sites

Initial

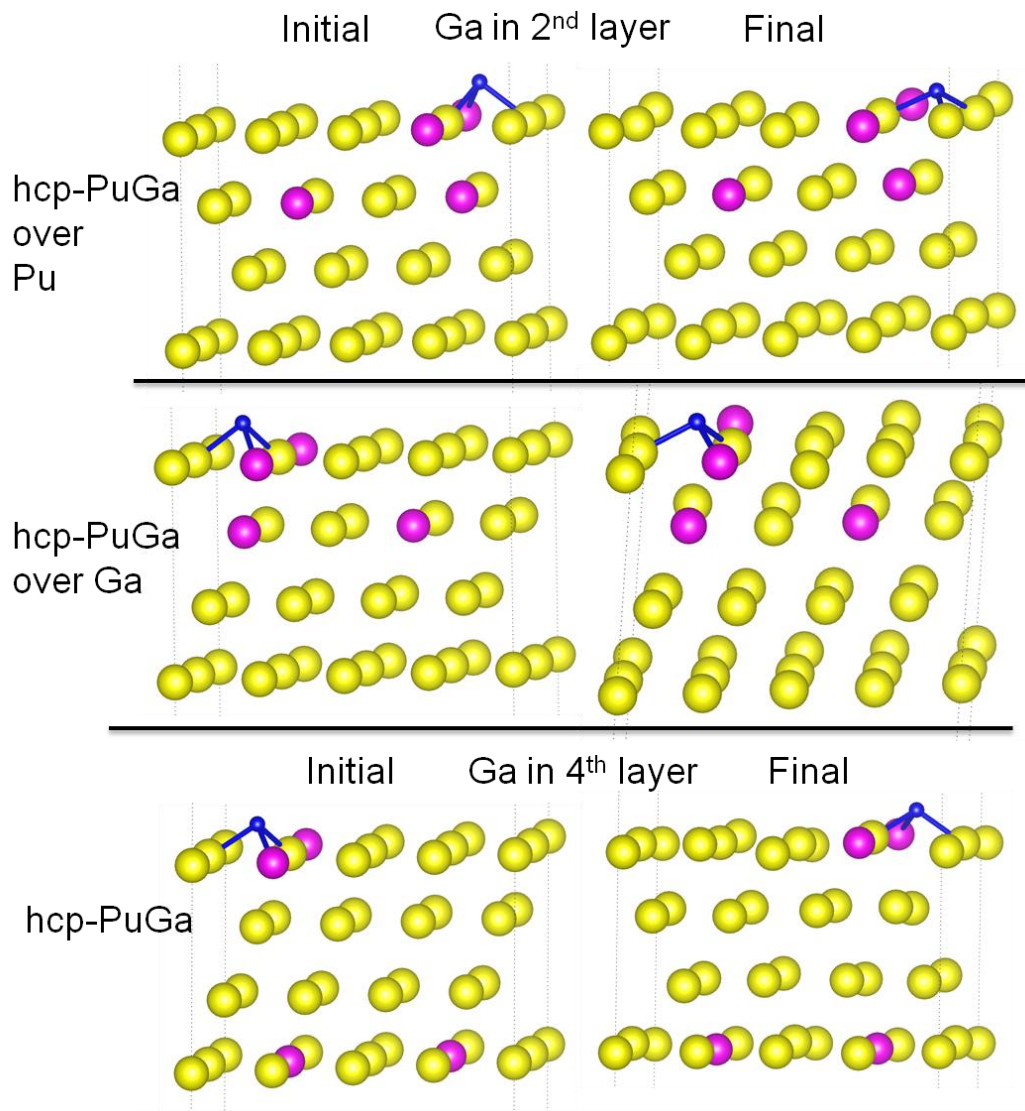
Final



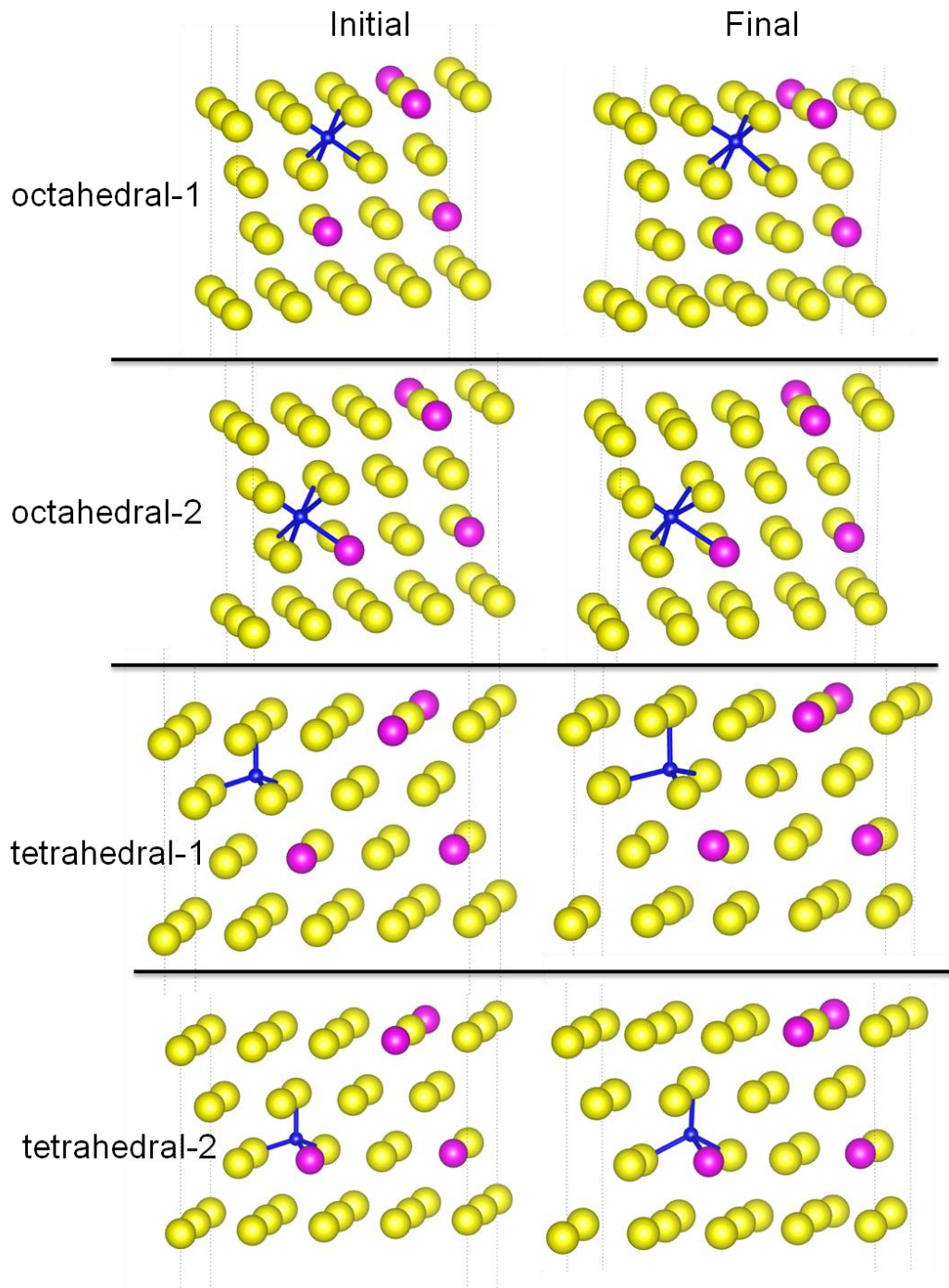
PuGa-terminated sites



PuGa-terminated sites for Ga placed in different layers



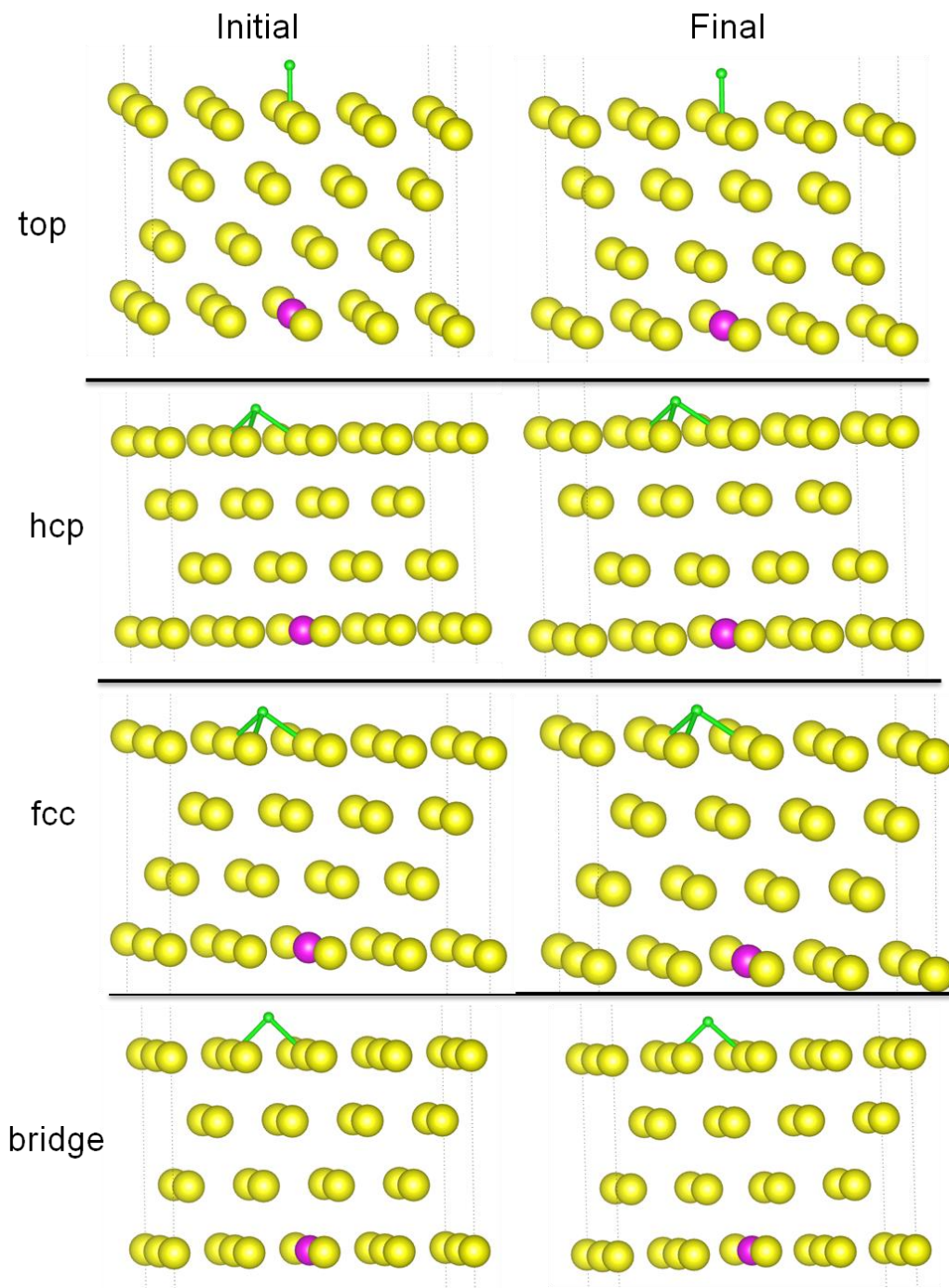
Interstitials sites



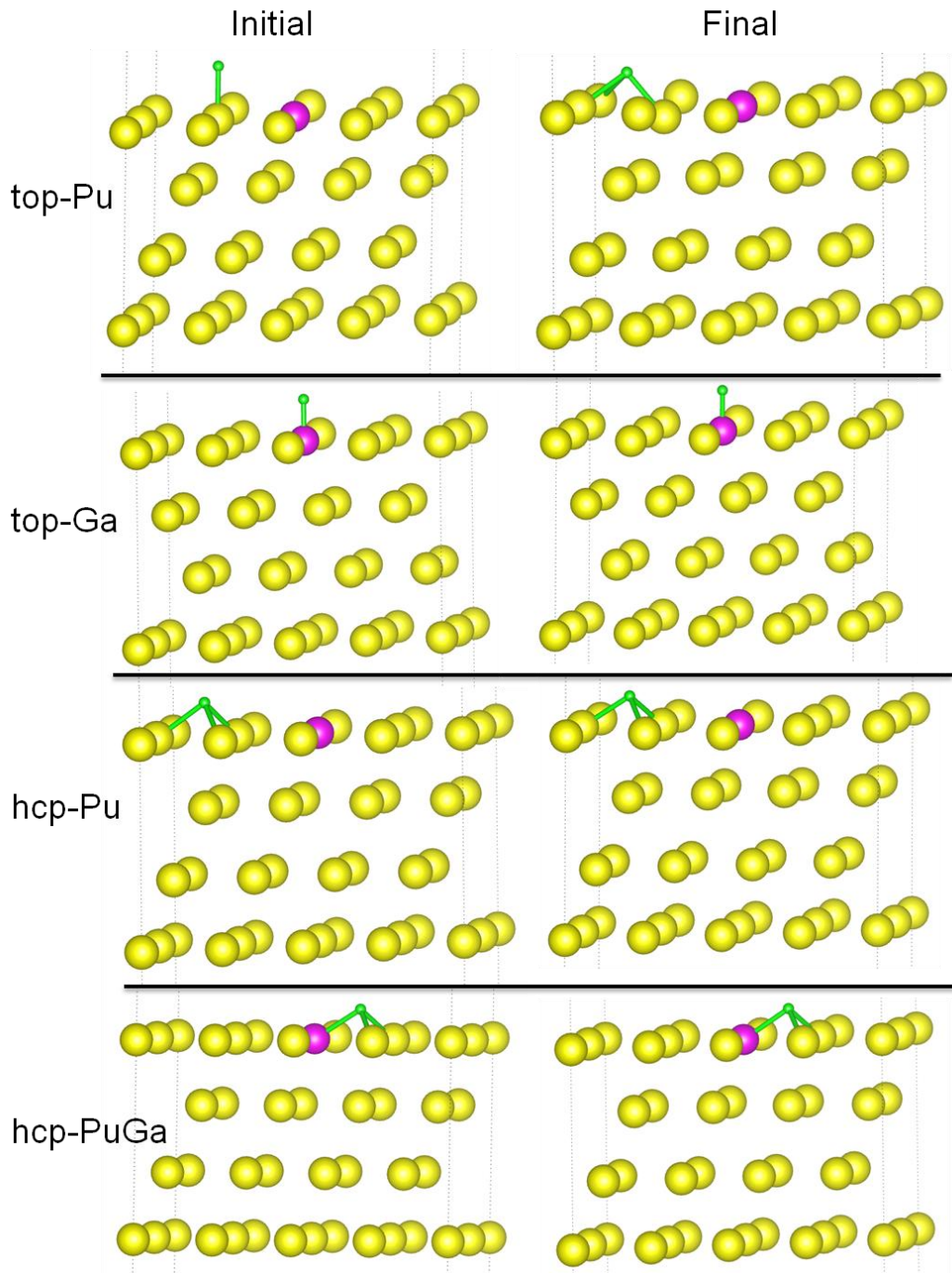
## Appendix E

Initial and final positions for H adsorption on 3.125 at. % Ga  $\delta$ -Pu (111) surface

Pu-terminated sites



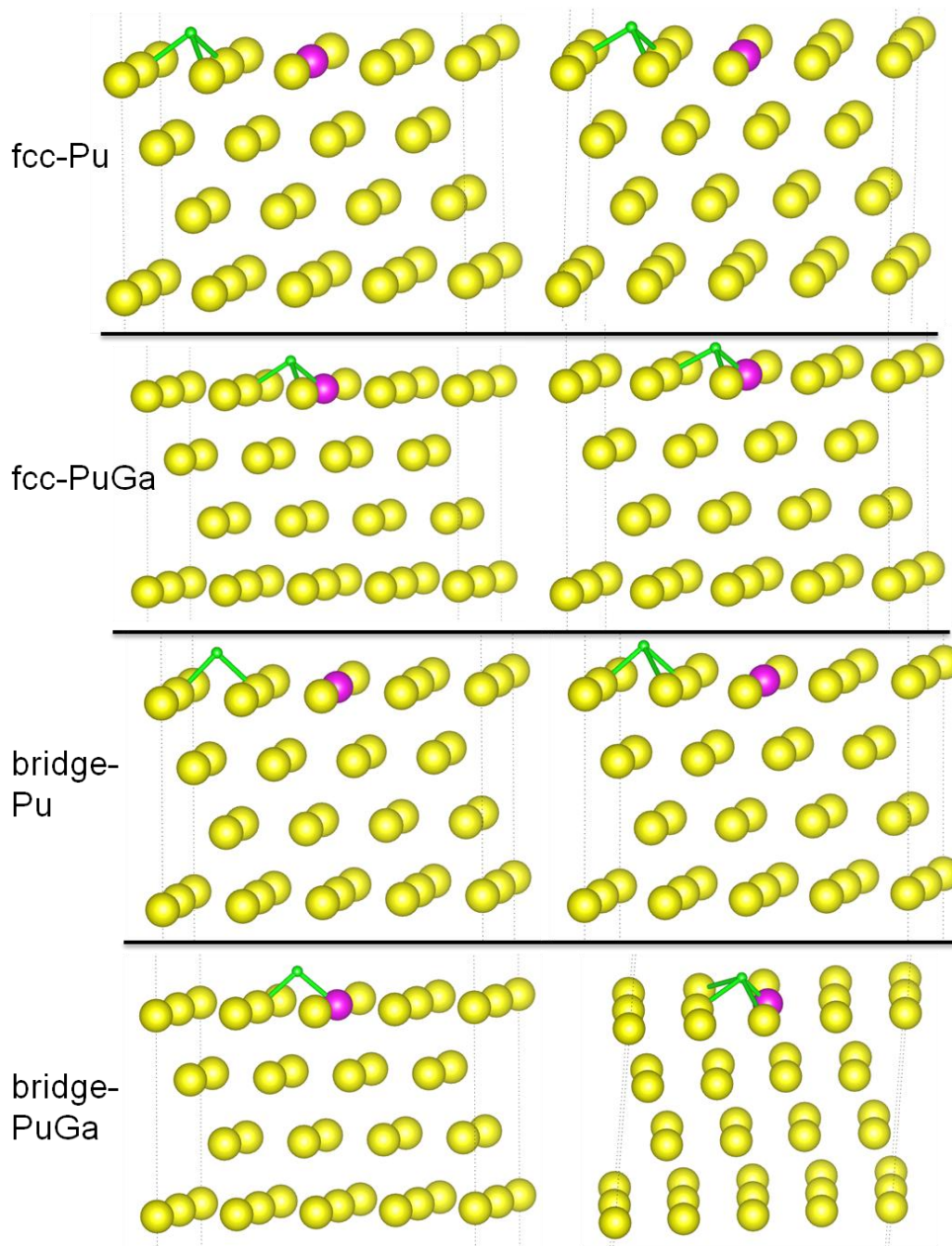
PuGa-terminated sites



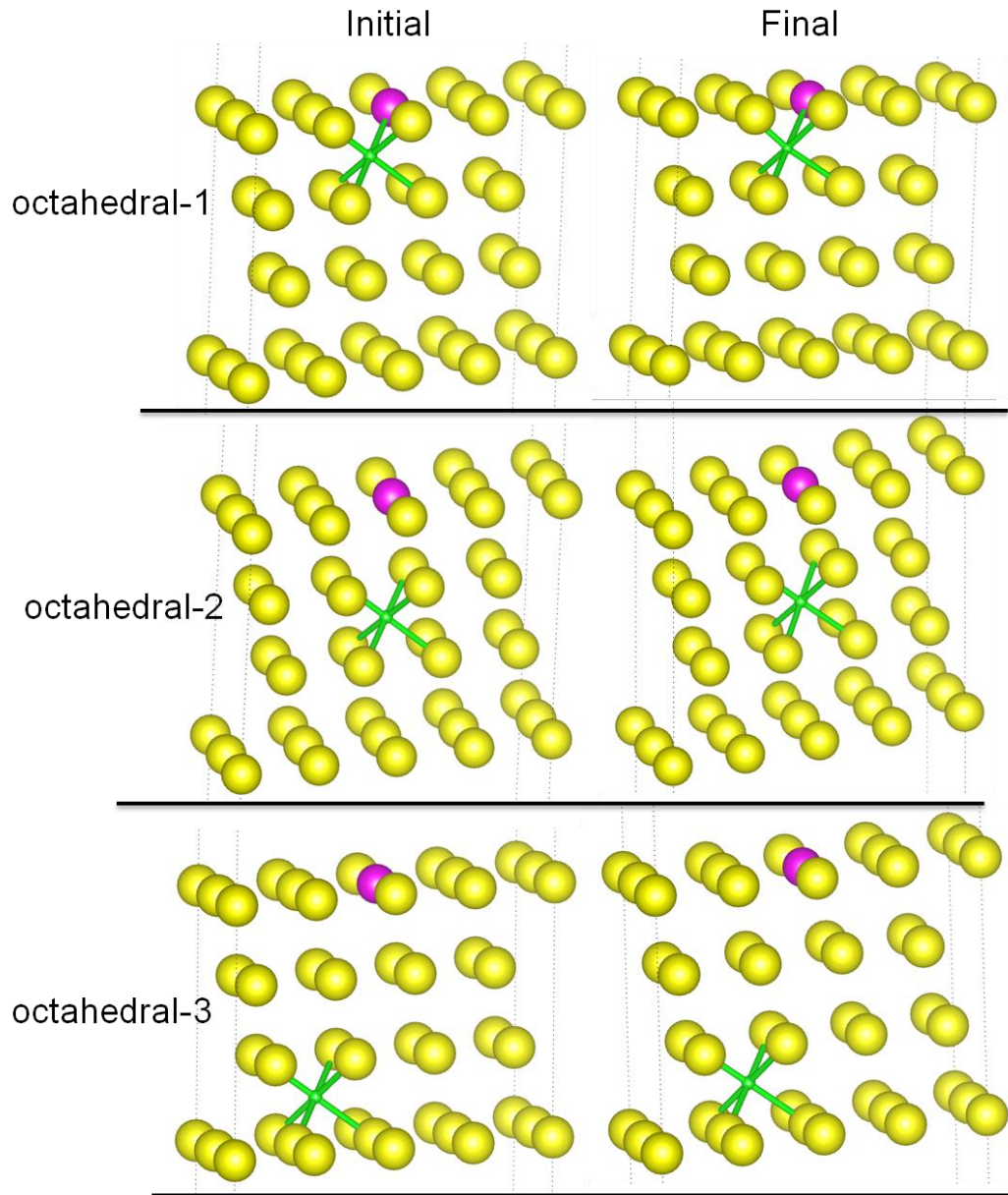
PuGa-terminated sites

Initial

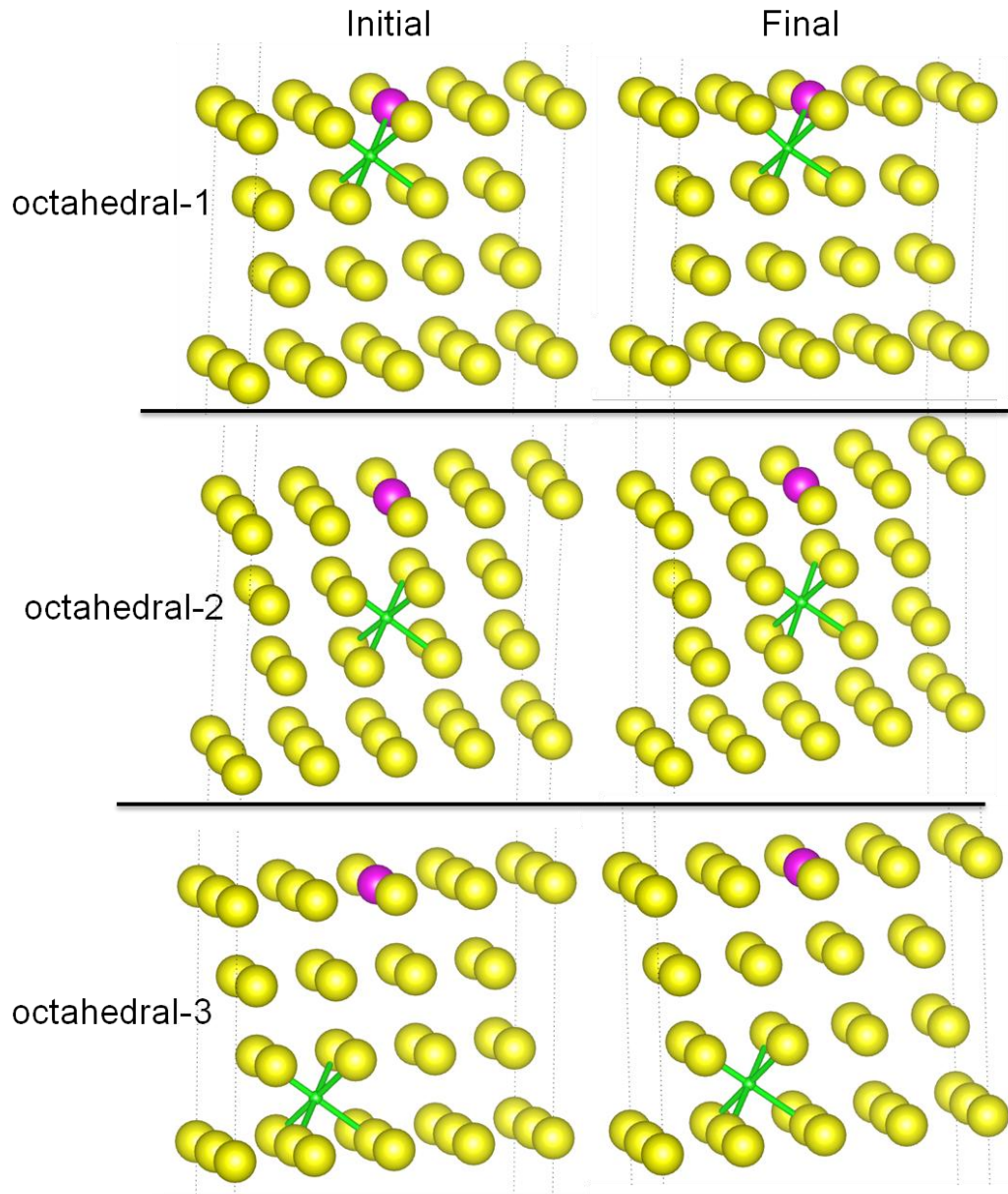
Final



Interstitials sites



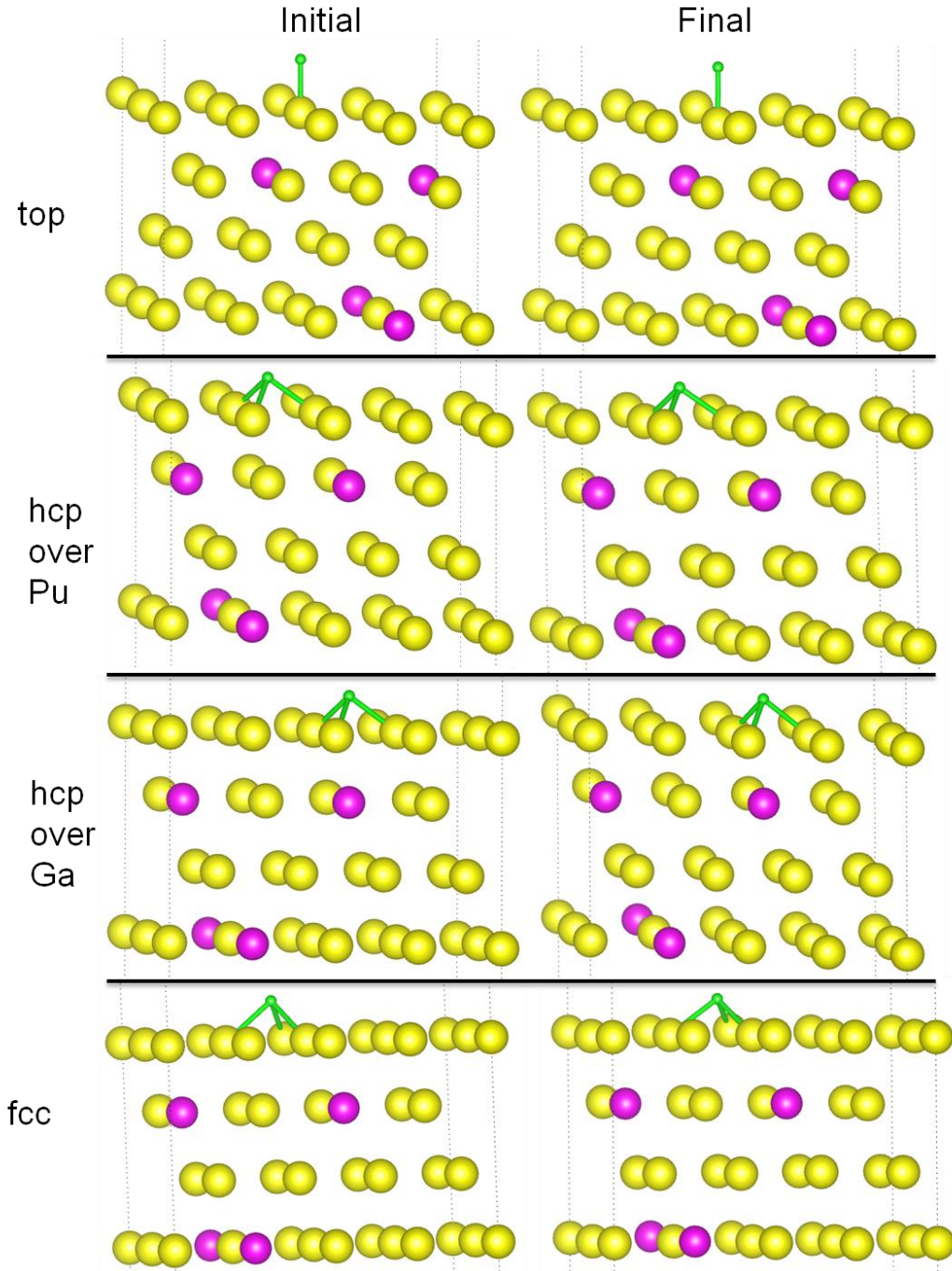
Interstitials sites



## Appendix F

Initial and final positions for H adsorption on 9.375 at. % Ga  $\delta$ -Pu (111) surface

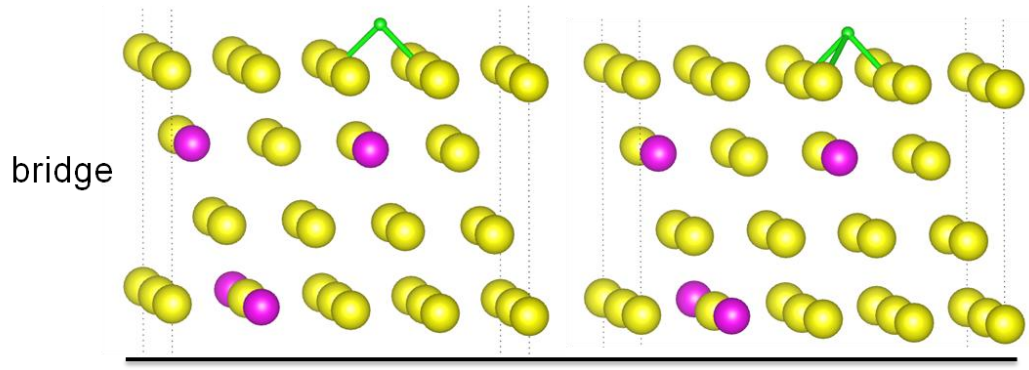
Pu-terminated sites



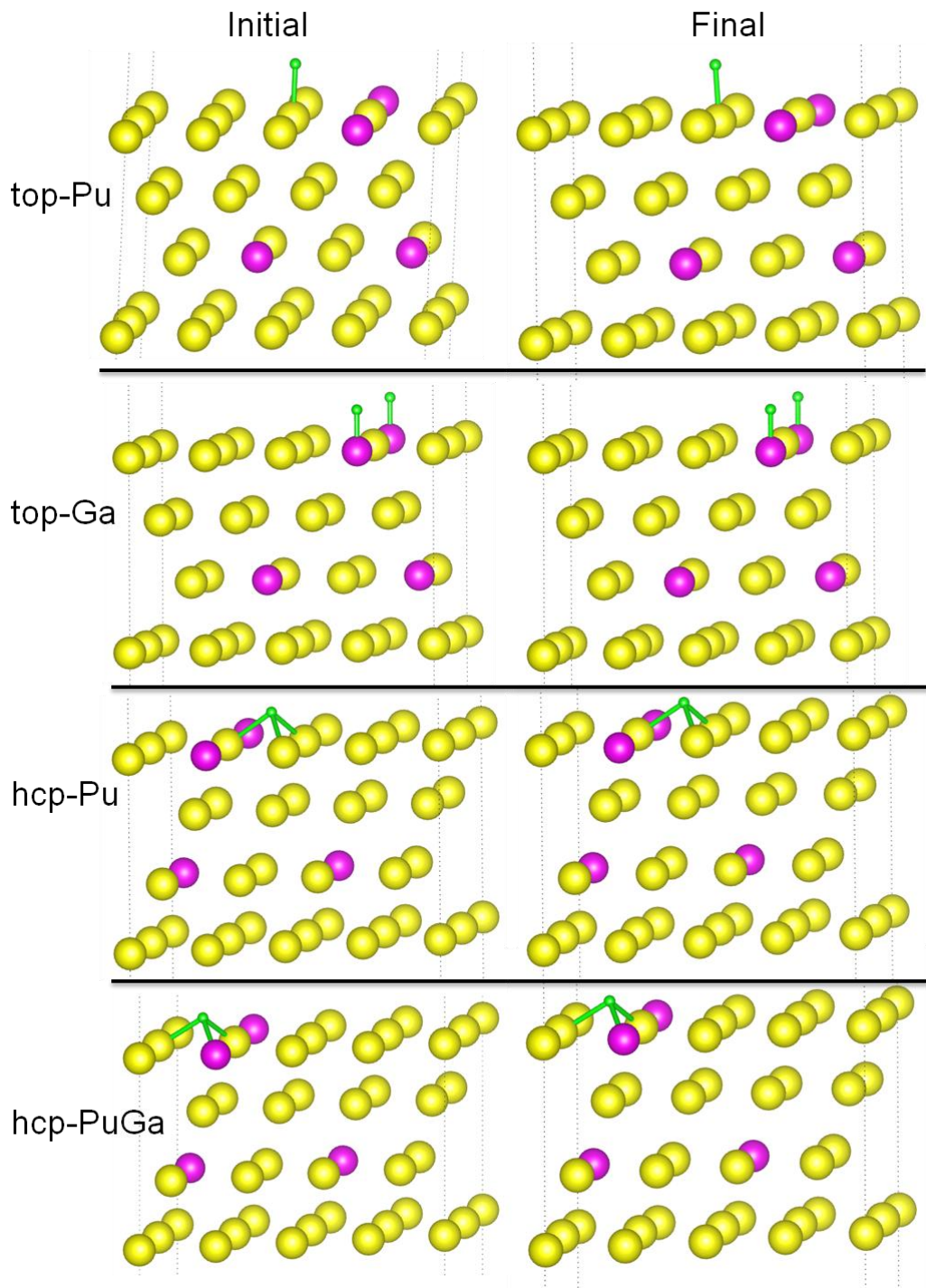
Pu-terminated sites

Initial

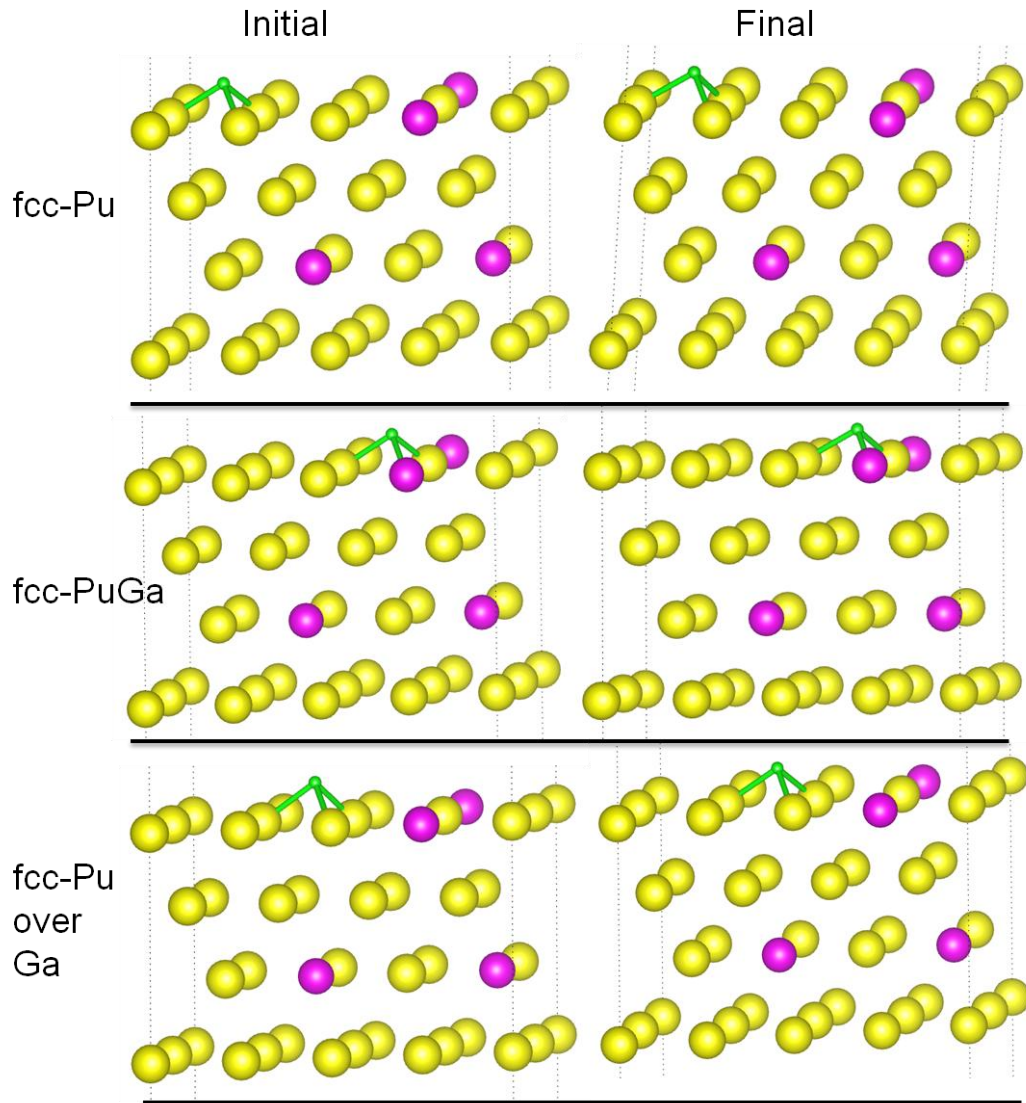
Final



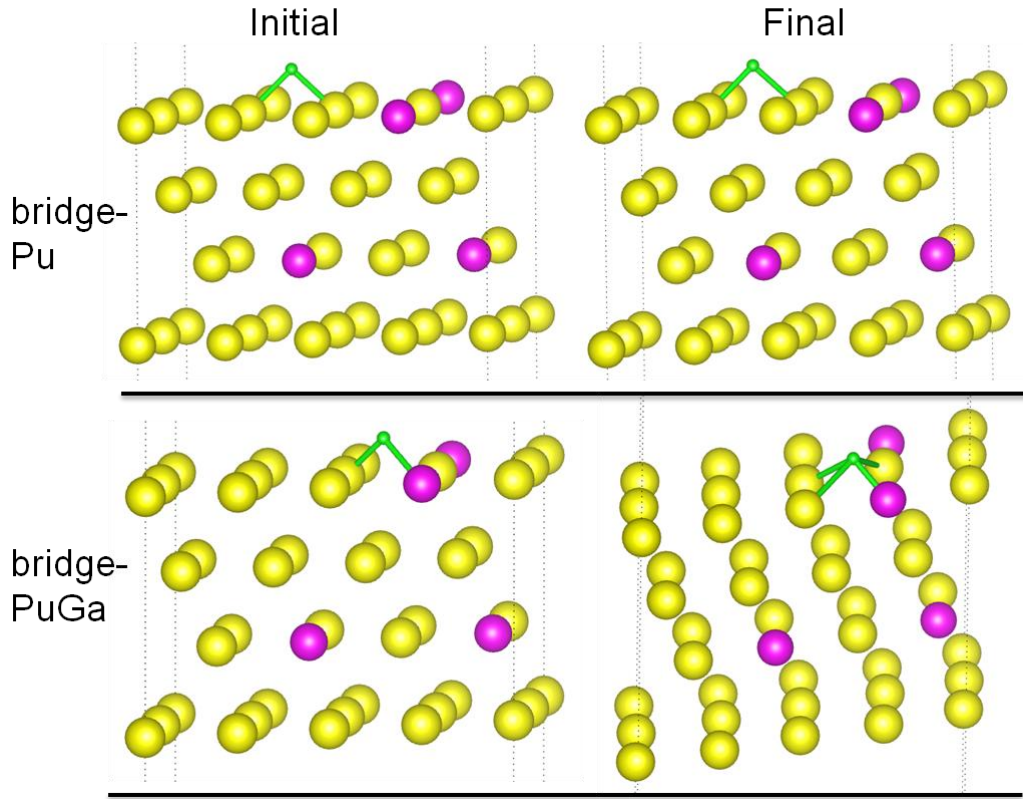
PuGa-terminated sites



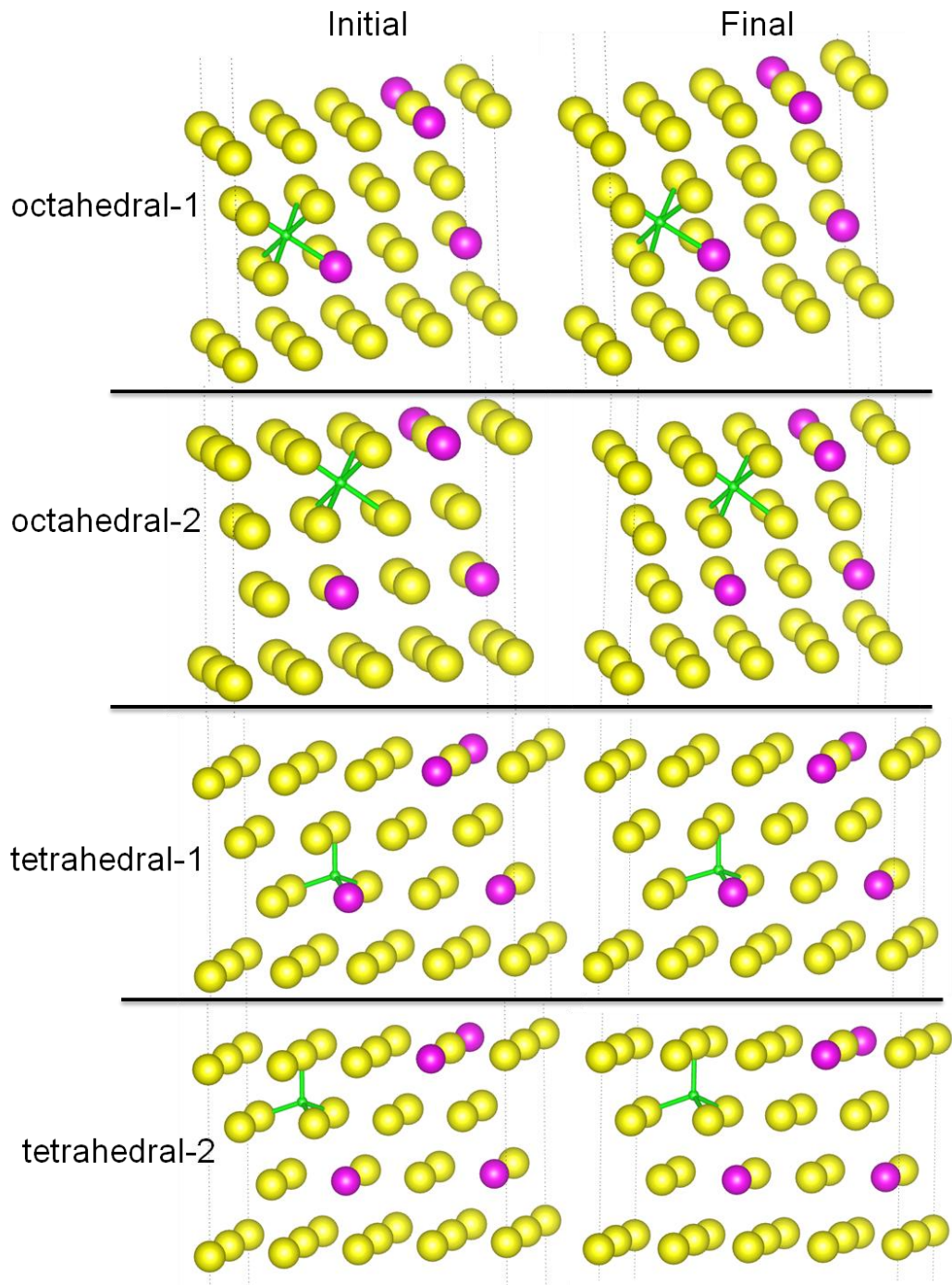
PuGa-terminated sites



PuGa-terminated sites



Interstitials sites



## References

- 1 A. F. Michaudon and I. G. Buican, Los Alamos Science Number 26, 4-9 (2000).
- 2 Los Alamos Science Number 26, 16-23 (2000).
- 3 A. M. Boring and J. L. Smith, Los Alamos Science Number 26, 90-127 (2000).
- 4 Plutonium Handbook, A Guide to Technology, edited by O. J. Wick (American Nuclear Society, Lagrange Park, IL, 1980), Vol. 1.
- 5 D. A. Young, Phase Diagrams of the Elements (University of California Press, Berkeley, 1991).
- 6 D. L. Clark, S. S. Hecker, G. D. Jarvinen, and M. P. Neu, *Plutonium Chapter 7*, LA-UR-05-7306.
- 7 J. C. Lashley, A. Lawson, R. J. McQueeney, and G. H. Lander, Phys. Rev. B **72**, 054416 (2005).
- 8 M. Janoschek, P. Das, J. M. Lawrence, F. Trouw, D. Abernathy, M. D. Lumsden, M. Ramos, J. N. Mitchell, G. Lander, and E. D. Bauer, Plutonium Futures The Science 2014, Las Vegas, NV, September 7-12, 2014, 35.
- 9 B. Sadigh, P. Söderlind, W. G. Wolfer, Phys. Rev. B **68**, 241101(R) (2003).
- 10 J. Bouchet, R. C. Albers, M. D. Jones, and G. Jomard, Phys. Rev. Lett. **92**, 095503 (2004).
- 11 M. Pénicaud, J. Phys. Cond. Matt. **12**, 5819 (2000); **14**, 3575 (2002).
- 12 P. Söderlind, Phys. Rev. B **77**, 085101 (2008).

- 13 P. Söderlind, A. Landa, and B. Sadigh, *Phys. Rev. B* **66**, 205109 (2002).
- 14 P. Söderlind, *Europhys. Lett.* **55**, 525 (2001).
- 15 A. L. Kutepov and S. G. Kutepova, *J. Phys.: Condens. Matter* **15**, 2607 (2003).
- 16 M. F. Islam and A. K. Ray, *Journal of Computational and Theoretical Nanoscience* **6**, 1458-1467 (2009).
- 17 P. Söderlind, G. Kotliar, K. Haule, P. M. Oppeneer, and D. Guillaumont, *MRS Bulletin* **35**, 883 – 888 (2010).
- 18 S. P. Chen, *Philosophical Magazine* **89**, 1813 – 1822 (2009).
- 19 S. Y. Kavrasov and G. Kotliar, *Phys. Rev. Lett.* **84**, 3670 (2000).
- 20 A. B. Shick, V. Drchal, and L. Havela, *Europhys. Lett.* **69** (4), 588-594 (2005).
- 21 R. Atta-Fynn and A. K. Ray, *Europhysics Letters* **85**, 27008 (2009).
- 22 C. A. Marianetti, K. Haule, G. Kotliar. and M. J. Fluss, *Phys. Rev. Lett.* **101**, 056403 (2008).
- 23 J. H. Shim, K. Haule, and G. Kotliar, *Nature* **446**, 513-516 (2007).
- 24 L. V. Pourovskii, M. I. Katsnelson, A. I. Lichtenstein, L. Havela, T. Gouder, F. Wastin, A. B. Shick, V. Drchal, and G. H. Lander, *Europhys. Lett.* **74** (3), 479-485 (2006).
- 25 “Mixed Oxide (MOX) Fuel,” World Nuclear Association (2011) Retrieved April 10, 2012 <http://www.world-nuclear.org/info/inf29.html>.
- 26 <http://saturn.jpl.nasa.gov/multimedia/products/pdfs/power.pdf>

- 27 F. H. Ellinger, C. C. Land, and V. O. Struebing, *J. Nucl. Mater.* **12**, 226-236 (1964).
- 28 L. E. Cox, R. Martinez, J. H. Nickel, S. D. Conradson, and P. G. Allen, *Phys. Rev. B* **51**, 751-755 (1995).
- 29 Ph. Faure, B. Deslandes, D. Bazin, C. Tailland, R. Doukhan, J. M. Fournier, and A. Falanga, *J. Alloys and Compounds* **244**, 131-139 (1996).
- 30 R. B. Fischer, *High-Pressure Science and Technology*, 287-291 (1979).
- 31 S. S. Hecker, *Los Alamos Science*, Nov. 26, 2000, pg. 293
- 32 A. J. Schwartz, H. Cynn, K. J. M Bloaum, M. A. Wall, K. T. Moore, W. J. Evans, D. L. Farber, J. R. Jeffries, and T. B. Massalski, *Progress in Materials Science* **54**, 909-943 (2009).
- 33 S. S. Hecker, D. R. Harbur, and T. G. Zocco, *Progress in Materials Science* **49**, 429-485 (2004).
- 34 P. Deloffre, J. L. Truffier, and A. Falanga, *J. Alloys and Compounds* **271-273**, 370-373 (1998).
- 35 N. Richard, Ph. Faure, P. Rofidal, J. L. Truffier, and D. Bazin, *J. of Alloys and Compounds* **271-273**, 879-882 (1998).
- 36 C. H. Booth, Yu Jiang, S. A. Medling, D. L. Wang, A. L. Costello, D. S. Schwartz, J. N. Mitchell, P. H. Tobash, E. D. Bauer, S. K. McCall, M. A. Wall, and P. G. Allen, *J. Appl. Phys.* **113**, 093502 (2013).

- 37 B. Sadigh and W. G. Wolfer, Phys. Rev. B **72**, 205122-1 – 205122-12 (2005).
- 38 G. Robert, A. Pasturel, and B. Siberchicot, J. Alloys and Comps. **444-445**, 191-196 (2007).
- 39 P. Söderlind, A. Landa, J. E. Klepeis, Y. Suzuki, and A. Migliori, Phys. Rev. B **81**, 224110 (2010).
- 40 J. D. Becker, J. M. Wills, L. Cox, and B. R. Cooper, Phys. Rev. B **58**, 5143 – 5145 (1998).
- 41 K. T. Moore, P. Söderlind, A. J. Schwartz, and D. E. Laughlin, Phys. Rev. Lett. **96**, 206402 (2006).
- 42 R. Jullien, E. Galleani d'Agliano, and B. Coqblin, J. Low Temp. Phys. **10**(5/6), 685 (1973).
- 43 R. Jullien, E. Galleani d'Agliano, and B. Coqblin, Phys. Rev. B **6**(6), 2139 (1972).
- 44 J. van Ek, P. A. Sterne, and A. Gonis, Phys. Rev. B **48**, 16280 – 16289 (1993).
- 45 P. Weinberger, A. M. Boring, and J. L. Smith, Phys. Rev. B **31**, 1964 – 1970 (1985).
- 46 J. D. Becker, J. M. Wills, L. Cox, and B. R. Cooper, Phys. Rev. B **54**(24), R17265(R) (1996).
- 47 P. Söderlind and A. Landa, J. Nucl. Mater. **448**, 310-314 (2014).

- 48 *Ageing Studies and Lifetime Extension of Materials*, ed. L. Mallinso, Springer, US, 23-52 (2001).
- 49 J. M. Haschke, T. H. Allen, and L. A. Morales, *Los Alamos Science* Number 26, 252 – 273 (2000).
- 50 J. M. Haschke, T. H. Allen, and J. L. Stakebake, *J. Alloys and Compounds* **243**, 23 – 25 (1996).
- 51 J. M. Haschke, T. H. Allen, and L. A. Morales, *J. Alloys and Compounds* **314**, 78 – 91 (2001).
- 52 J. M. Haschke and J. C. Martz, *J. Alloys and Compounds* **266**, 81 -89 (1998).
- 53 G. L. Voelz as told to I. G. Buican, *Los Alamos Science* Number 26, 74 – 89 (2000).
- 54 K. A. Dunn, G. T. Chandler, C. W. Gardner, M. R. Louthan, J. W. McClard, and L. M. Worl, Report SRNL-STI-2009-00729 (2009)
- 55 J. M. Haschke and T. H. Allen, *J. Alloys and Compounds* **320**, 58-71 (2001).
- 56 H. G. Garcia Flores, P. Roussel, D. P. Moore, and D. L. Pugmire, *Surf. Sci.* **605**, 314-320 (2011).
- 57 A. J. Nelson and P. Roussel, *J. Vac. Sci. Technol. A* **31**(3), 031406 (2013).
- 58 M. T. Butterfield, T. Durakiewicz, E. Guziewicz, J. J. Joyce, A. J. Arko, K. S. Graham, D. P. Moore, and L. A. Morales, *Surf. Sci.* **571**, 74-82 (2004).

- 59 D. L. Pugmire and H. G. Garcia Flores, *Plutonium Futures The Science 2014*, Las Vegas, NV, September 7-12, 2014, 355.
- 60 *Plutonium 1965: Proceedings of the 3<sup>rd</sup> International Congress on Plutonium*, eds. A. E. Kay and M. B. Waldron, 575 (1965).
- 61 J. M. Haschke, A. E. Hodges III, R. L. Lucas, *J. of the Less-Common Metals* **133**, 155-166 (1987).
- 62 I. B. Johns, United States Atomic Energy Commission, MDDC-717 (1944).
- 63 G. W. McGillivray, J. P. Knowles, I. M. Findlay, M. J. Dawes, *J. Nucl. Mater.* **385**, 212- 215 (2009).
- 64 R. N. R. Mulford and G. E. Sturdy, *J. Am. Chem. Soc.* **77**, 3449-3452 (1955).
- 65 R. N. R. Mulford and G. E. Sturdy, *J. Am. Chem. Soc.* **78**, 3897-3901 (1956).
- 66 F. Brown, H. M. Ockenden, and G. A. Welch, *J. Chem. Soc.* **3**, 3932-3936 (1955).
- 67 J. L. Stakebake, *J. Electrochem. Soc.* **128**, 2383-2388 (1981).
- 68 J. L. Stakebake, *J. Alloys and Compounds* **187**, 271-283 (1992).
- 69 L. N. Dinh, J. M. Haschke, C. K. Saw, P. G. Allen, W. McLean II, *J. Nucl. Mater.* **408**, 171-175 (2011).
- 70 S. Richmond, J. S. Bridgewater, J. W. Ward, and T. H. Allen, *IOP Conf. Ser.: Mater. Sci. Eng.* **9**, 012036 (2010).

- 71 C. D. Taylor and D. Moore, Plutonium Futures - The Science 2010, Keystone, CO, September 19-23, 2014, 234.
- 72 G. Robert, A. Pasturel, and B. Siberchicot, Europhys. Lett. **71**(3), 412 – 417 (2005).
- 73 M. Robinson, S. D. Kenny, R. Smith, and M. T. Storr, J. Nucl. Mater. 423, 16 – 21 (2012).
- 74 D. S. Schwartz, S. Richmond, A. I. Smith, A. Costello, and C. D. Taylor, Mater. Res. Soc. Symp. Proc. **1444**, 183 – 187 (2012).
- 75 S. Richmond, J. Anderson, and J. Abes, Plutonium Futures – The Science, September 19-23, 2010, Keystone, CO 206 – 207.
- 76 K. Watanabe, J. Nucl. Mater. 136, 1 (1985).
- 77 M. N. Huda and A. K. Ray, International Journal of Quantum Chemistry **105**, 280-291 (2005).
- 78 M. N. Huda and A. K. Ray, Eur. Phys. J. B. **40** 337-346 (2004).
- 79 R. Atta-Fynn and A. K. Ray, Phys. Rev. B **75**, 195112 (2007).
- 80 R. Atta-Fynn and A. K. Ray, Physica B **400**, 307-316 (2007).
- 81 C. D. Taylor, Surf. Sci. **618**, 101 – 108 (2013).
- 82 M. F. Islam and A. K. Ray, Phys. Status Solidi B **248**(1), 193-202 (2011).
- 83 O. Eriksson, Y. G. Hao, B. R. Cooper, G. W. Fernando, L. E. Cox, J. W. Ward, and A. M. Boring, Phys. Rev. B **43**(6), 4590-4597 (1991).

- 84 M. N. Huda and A. K. Ray, *Physica B* **352**, 5-17 (2004).
- 85 M. N. Huda and A. K. Ray, *Physica B* **366**, 95-109 (2005).
- 86 M. N. Huda and A. K. Ray, *Phys. Rev. B* **72**, 085101 (2005).
- 87 C. D. Taylor, S. C. Hernandez, M. F. Francis, D. S. Schwartz, and A. K. Ray, *J. Phys.: Condens. Matter* **25**, 265001 (2013).
- 88 K. Balasubramanian, T. E. Felter, T. Anklam, T. W. Trelenberg, W. McLean II, *J. Alloys and Compounds* **444-445**, 447-452 (2007).
- 89 M. Born and R. Oppenheimer, *Annalen der Physik* **389**(20), 457-484 (1927).
- 90 R. G. Parr and W. Yang, *Density-Functional Theory of Atoms and Molecules*, (Oxford: Oxford University Press, 1989).
- 91 P. Hohenberg and W. Kohn, *Physical Review B* **136** (3B), B864-+ (1964).
- 92 Richard M. Martin, *Electronic Structure Basic Theory and Practical Methods*, Cambridge University Press, Cambridge, UK 2004.
- 93 W. Kohn and L. J. Sham, *Physical Review* **140** (4A), 1133-1138 (1965).
- 94 P. A. M. Dirac, *Proc. Cambridge Philos. Soc.* **26**, 376 (1930).
- 95 O. Gunnarsson and B. I. Lundqvist, *Physical Review B* **13**(10), 4274 (1976).
- 96 J. P. Perdew and W. Yue, *Phys. Rev. B.* **33**, 8800 (1986).
- 97 J. P. Perdew, K. Burke, and M. Ernzerhof, *Phys. Rev. Lett.* **77**, 3865 (1996)
- 98 J. P. Perdew, H. A. Chevary, S. H. Vosko, K. A. Jackson, M. R. Pederson, D. J. Singh, and C. Fiolhais, *Phys. Rev. B* **46**(11), 6671-6687 (1992).

- 99 P. Blaha, K. Schwarz, G. K. H. Madsen, D. Kvasnicka, and J. Luitz, *WIEN2k*, Vienna University of Technology, Austria, 2001, [www.wien2k.at](http://www.wien2k.at).
- 100 [www2.mpi-halle.mpg.de/theory\\_department/research/elk\\_code\\_development/](http://www2.mpi-halle.mpg.de/theory_department/research/elk_code_development/)
- 101 E. Sjöstedt, L. Nordström, and D. Singh, *Solid State Communications* **114**(19), 15-20 (2000).
- 102 G. K. H. Madsen, P. Blaha, E. Sjöstedt, and L. Nordström, *Phys. Rev. B* **64**, 195134 (2001).
- 103 D. D. Koelling and B. N. Harmon, *J. Phys. C: Solid State Phys.* **10**, 3107 (1977).
- 104 A. H. MacDonald, W. E. Pickett, and D. D. Koelling, *J. Phys. C: Solid State Phys.* **13**, 2675-2683 (1980).
- 105 X. Wu and A. K. Ray, *Phys. Rev. B* **72**, 045115 (2005).
- 106 L. R. Morss, N. M. Edelstein, J. Fuger, and J. Katz, *The Chemistry of the Actinide and Transactinide Elements 1-5* (New York: Springer) 2006.
- 107 R. L. Moment, *Plutonium and Other Actinides* (Amsterdam: North-Holland) 1976.
- 108 S. C. Hernandez, D. S. Schwartz, C. D. Taylor, and A. K. Ray, *J. Phys.: Cond. Matt.* **24**, 235502 (2014).
- 109 J. J. Joyce, T. Durakiewicz, K. S. Graham, E. D. Bauer, D. P. Moore, J. N. Mitchell, J. A. Kennison, R. L. Martin, L. E. Roy, and G. E. Scuseria, *J. Phys.: Conference Series* **273**, 012023 (2011).

- 110 VESTA: a three-dimensional visualization system for electronic and structural analysis, K. Momma and F. Izumi, *J. Appl. Crystallogr.* **41**, 653-658 (2008).
- 111 H. Gong and A. K. Ray, *Mater. Res. Soc. Symp.* **893**, 0893-JJ01-08.1 (2006).
- 112 H. Gong and A. K. Ray, *Surf. Sci.* **600**, 2231 (2006).
- 113 A. K. Ray, J. C. Boettger, *Phys. Rev. B.* **70**, 085418 (2004).
- 114 L. E. Cox, *Phys. Rev. B* **37**, 8480 (1988).
- 115 A. Soon, M. Todorova, B. Delley, and C. Stampfl, *Phys. Rev. B* **73**, 165424 (2006).
- 116 D. P. Moore, A. L. Broach, D. L. Pugmire, H. G. Flores, T. Durakiewicz, J. Joyce, *Actinides 2009*, July 12-17 2009, San Francisco, CA.
- 117 J. Wang and A. K. Ray, *J. Nucl. Mater.* **424**, 138-145 (2012).
- 118 R. Atta-Fynn and A. K. Ray, *Chem. Phys. Lett.* **470**, 233-239 (2009).

### Biographical Information

Ms. Sarah Christine Hernandez, a native Texan, graduated from Texas Christian University with a Bachelor of Science in May 2007, with a major in Physics and Astronomy and Mathematics. In August of 2009, Ms. Hernandez graduated with a Master of Science from Miami University of Ohio in Physics. She was mentored by Dr. Michael Pechan. Her thesis work involved the investigation of magnetostatics of exchange-coupled Permalloy nano-dots using the magnetic-optic Kerr effect.

In August of 2010, she began her graduate work for a PhD in Physics at the University of Texas at Arlington under the supervision of Dr. Asok Ray. She was awarded a Louis Stoke Alliance for Minority Participation Bridge to the Doctorate (LSAMP-BD) Fellowship during the years of 2010-2012. During her time at UTA she has had the opportunity to be a G.T. Seaborg Summer Fellow in the summers of 2011 and 2012 at Los Alamos National Laboratory, where her interest sparked in the field of actinide science. Soon after she began her theoretical work on the plutonium-gallium alloyed system, which has been funded through the Los Alamos National Laboratory LDRD program. She has published multiple papers on plutonium. She has also been supported through the UTA Physics Department GAAN scholarship. One day, she hopes to mentor a group that collaborates on both experimental surface techniques and theoretical projects.